Vector correlations in rotationally inelastic molecular collisions

vorgelegt von

M.Sc. (Physik) Mikhail Lemeshko

aus Rostow-am-Don, Russland

von der Fakultät II – Mathematik und Naturwissenschaften

der Technischen Universität Berlin

zur Erlangung des akademischen Grades

Doktor der Naturwissenschaften

Dr. rer. nat.

genehmigte Dissertation

Promotionsausschuss:

Vorsitzende: Prof. Dr. rer. nat. Sabine Klapp

Gutachter: Prof. Dr. rer. nat. Bretislav Friedrich

Gutachter: Prof. Dr. rer. nat. Thomas Möller

Gutachter: Priv.-Doz. Dr. rer. nat. Burkhard Schmidt

Tag der wissenschaftlichen Aussprache: 13. April 2011

The work described in this thesis has been carried out at the Fritz Haber Institute of the Max Planck Society in Berlin, Germany, under the supervision of Prof. Dr. Bretislav Friedrich

Nothing in this world can take the place of persistence. Talent will not; nothing is more common than unsuccessful people with talent. Genius will not; unrewarded genius is almost a proverb. Education will not; the world is full of educated derelicts. Persistence and determination alone are omnipotent. The slogan "press on" has solved and always will solve the problems of the human race.

Calvin Coolidge

Abstract

Mikhail Lemeshko,
Vector correlations in rotationally inelastic molecular collisions

The thesis presents an analytic model that describes scalar and vector properties of molecular collisions, both field-free and in fields. The model is based on the sudden approximation and treats molecular scattering as the Fraunhofer diffraction of matter waves from the hard-core part of the interaction potential. The theory has no fitting parameters and is inherently quantum, rendering fully state- and energy-resolved scattering amplitudes and all the quantities that unfold from them in analytic form. This allows to obtain complex polarization moments inherent to quantum stereodynamics, and to account for interference and other non-classical effects. The simplicity and analyticity of the model paves a way to understanding the origin of the features observed in experiment and exact computations, such as the angular oscillations in the state-to-state differential cross sections and the polarization moments, the rotational-state dependent variation of the integral cross sections, and change of these quantities as a function of the applied field.

The theory was applied to study the $\mathbf{k} - \mathbf{k}'$ vector correlation (differential cross section) for the following collision systems: Ar–NO($X^2\Pi$) and Ne–OCS($X^1\Sigma$) in an electrostatic field, Na$^+$–N$_2$($X^1\Sigma$) in a laser field, and He–CaH($^2\Sigma$), He–O$_2$($X^3\Sigma$), and He–OH($X^2\Pi$) in a magnetic field. The model was able to reproduce the behavior of the differential cross sections and their variation with field strength.

Combining the Fraunhofer model with the quantum theory of vector correlations made it possible to study three- and four-vector properties. The model results for the $\mathbf{k} - \mathbf{k}' - \mathbf{j}'$ vector correlation in Ar–NO($X^2\Pi$) and He–NO($X^2\Pi$) scattering were found to be in good agreement with experiment and exact computations. This allowed to demonstrate that the stereodynamics of such collisions is contained solely in the diffractive part of the scattering amplitude which is governed by a single Legendre moment characterizing the anisotropy of the hard-core part of the system's potential energy surface. The alignment moments obtained for He–OH($X^2\Pi$), He–O$_2$($X^3\Sigma$), and He–CaH($X^2\Sigma$) allowed to identify the fingerprints of diffraction, which can be used to discern diffraction-driven stereodynamics in future experiments and exact computations. Analytic results for the Ne–NO($A^2\Sigma$) system were found to be in good agreement with experiment and exact computations for low rotational energy transfer; the discrepancy found for higher excitation channels could be traced back to the breakdown of the sudden approximation. The model was also applied to the $\mathbf{k} - \mathbf{j} - \mathbf{k}'$ and $\mathbf{k} - \mathbf{j} - \mathbf{k}' - \mathbf{j}'$ correlations in rotationally inelastic Ar–NO($X^2\Pi$) scattering. It was shown that preparing the reagents with polarized angular momentum $\mathbf{j}$ makes it possible to significantly alter the collision dynamics and stereodynamics.

In the final part of the thesis the analytic theory was extended to the study of multiple scattering of matter waves propagating through atomic and molecular gases. The combination of the Fraunhofer model with the semiclassical approximation to account, respectively, for the repulsive and attractive part of the potential energy surface resulted in a simple analytic formula, which agree well with experiment for the refraction of a Li beam passing through Xe gas.

Zusammenfassung

Mikhail Lemeshko,

Vector correlations in rotationally inelastic molecular collisions

In dieser Doktorarbeit wird ein analytisches Model präsentiert, das die skalaren und vektoriellen Eigenschaften von Molekülstößen beschreibt und auch auf die Einflüsse von externen Felder berücksichtigt. Das Model basiert auf der Sudden-Approximation und behandelt die molekulare Streuung als Beugung von Materiewellen am stark repulsiven Teil des Wechselwirkungspotentials in der Fraunhofernäherung. In diese Theorie werden keine Fitparameter eingebunden, sie ist rein analytisch auf der Quantenmechanik basierend. Sie gibt das volle Spektrum der zustands- und energieaufgelösten Streuamplituden wieder, aus denen alle weiteren physikalischen Eigenschaften abgeleitet werden. So können zum Beispiel komplexe Polarisationsmomente berechnet werden, die allein von der quantenmechanischen Stereodynamik herrühren, oder andere nichtklassische Effekte wie Interferenzen. Aufgrund dessen, dass das Model einfach und analytisch lösbar ist, ebnet es einen Weg den Ursprung von Verhaltensweisen zu verstehen, die in Experimenten und in exakten numerischen Berechnungen zu Tage treten.

Die Theorie wurde angewendet, um die $\mathbf{k} - \mathbf{k}'$ Vektorkorrelationen des differentiellen Wirkungsquerschnitts der folgenden Stoßsysteme zu untersuchen: Ar–NO($X^2\Pi$) und Ne–OCS($X^1\Sigma$) in einem elektrostatischen Feld, Na$^+$–N$_2$($^1\Sigma$) in einem Laserfeld und He–CaH($^2\Sigma$), He–O$_2$($^3\Sigma$) und He–OH($^2\Pi$) in einem magnetischen Feld. Die Theorie war in der Lage das Verhalten des differentiellen Querschnitts und dessen Veränderung durch die Feldstärke wiederzugeben.

Die Erweiterung des Fraunhofer Models durch die Einführung der Quantentheorie der Vektorkorrelationen machte es möglich Dreier- und Vierervektoreigenschaften zu untersuchen. Die Vorhersagen dieses Models für die $\mathbf{k} - \mathbf{k}' - \mathbf{j}'$ Vektorkorrelationen bei den Stößen zwischen Ar–NO($X^2\Pi$) und He–NO($X^2\Pi$) stimmen sehr gut mit experimentellen Daten und exakten Computersimulationen überein. Dies zeigte, dass die Stereodynamik solcher Kollisionen allein vom gebeugten Teil der Streuamplitude herrührt. Die Momente, die für verschiedene Ausrichtungen der Moleküle in den Systemen He–OH, He–O$_2$ und He–CaH ermittelt wurden, erlaubten es einen tieferen Einblick in den Beugungsmechanismus zu bekommen, was dazu benutzt werden kann, um beugungsinduzierte Stereodynamik zukünftiger Experimente und Computersimulationen zu verstehen. Resultate aus analytischen Rechnungen für das System Ne–NO($A^2\Sigma$) stimmten mit experimentellen Daten und exakten Simulationen für den rotationellen Energietransfer bei niedrigen Energien überein. Die Abweichungen bei höheren Energien konnten darauf zurückgeführt werden, dass die Sudden-Approximation keine gute Näherung mehr war. Das Model wurde auch auf die Vektorkorrelationen $\mathbf{k} - \mathbf{j} - \mathbf{k}'$ und $\mathbf{k} - \mathbf{j} - \mathbf{k}' - \mathbf{j}'$ der rotationell, inelastischen Streuung im Ar–NO($X^2\Pi$) System angewandt. Es wurde auch gezeigt, dass es die Präparation der Reaktanden in einen bestimmten polarisierten Drehimpulszustand $\mathbf{j}$ ermöglicht, die Stoßdynamik und die Stereodynamik signifikant zu erhöhen.

Im letzten Teil dieser Doktorarbeit wurde die analytische Theorie erweitert, um die Mehrfachstreuung von Materiewellen untersuchen zu können, die durch ein atomares oder molekulares Gas propagieren. Die Sythese des Fraunhofer Models mit einer semiklassichen Näherung, die eingeführt wurde, um den respektive repulsiven und den attraktiven Teil des PES, zu berücksichtigen, brachte eine einfache analytische Formel hervor, die gut mit den experimentellen Daten der Streuung eines Li Atomstrahls in einem Xenongasreservoir übereinstimmt.

Contents

1 Introduction

> I've heard people say that they don't want to
> learn Little Walter, or Sonny Boy, or anybody
> else, because they want to have their own style.
> And, some of them did have their own style –
> but it wasn't anything I would listen to without
> a gun to my head.
>
> Jerry Portnoy, "Blues harmonica masterclass"

1.1 Origin of vector correlations: nuclear reactions and spectroscopy

Like many other branches of modern atomic, molecular, and chemical physics, the field of vector correlations originated in nuclear physics. In 1940 Dunworth, a research student at the Clare College in Cambridge, suggested that there might be some correlations between the directions of successive emissions of two γ-quanta in a cascade nuclear decay [1]. Although the method of coincidence counting did not allow Dunworth to measure any significant correlation, in the appendix to his paper [1] he mentioned that he "...hopes to make a more accurate test of the spatial correlation of successively emitted γ-rays," being inspired by discussions with his colleague Pryce, who insisted that such a correlation should take place. The same year, the challenge was taken up by Hamilton at Harvard University, who provided a theoretical evidence for directional correlations in double γ-decays [2]. His effort was induced by discussions with Getting, who tried to experimentally reveal the $\gamma - \gamma$ coincidence in the Th nucleus decay, but never published any results on it.

1

In 1942 Kikuchi and collaborators from the University of Kaiserslautern experimentally observed hints to the angular correlations in the double γ-decay of the ^{38}Cl nucleus, but almost no correlations in the case of ^{24}Na [3]. However, these results were not confirmed by subsequent experiments of Beringer at Yale University, who showed that there is no correlations either for the ^{24}Na or for ^{38}Cl decays [4]. Another unsuccessful attempt was undertaken in 1946 by Good at MIT, who investigated the decay of ^{24}Na, ^{60}Co, and ^{88}Y nuclei and found no asymmetry in the angular distributions of γ-quanta [5]. The first conclusive proof of vector correlations in nuclear spectroscopy was obtained one year later by Brady and Deutsch at MIT, who experimentally observed pronounced anisotropy in γ-decay of ^{60}Co and ^{46}Sc nuclei [6].

The theory of this new phenomenon was thoroughly worked out in the late 40's in subsequent papers of Goertzel and Zinnes (New York University) [7, 8], Hamilton (Princeton) [9], Gardner (University of Birmingham) [10, 11], and Falkoff (University of Michigan) [12, 13, 14]. In 1951 Gulio Racah from the Institute for Advanced Study in Princeton published an article that started as follows "It is the purpose of this paper to show that the problem is much simpler than it seems, both from the algebraical and from the geometrical point of view" [15]. Indeed, nine years earlier, Racah was involved in the study of complex atomic spectra. For this purpose he generalized the vector operators of Condon and Shortley [16] by developing tensor operator algebra, and introduced what was later termed 'Racah coefficients,' used to switch between different angular momentum coupling schemes [17]. When applied to collision studies, this approach made it possible to separate the dynamical and geometrical properties, and therefore became a natural and straightforward tool to treat the angular correlations problem. About the same time similar theories were independently developed by Lloyd, also working at the Institute for Advanced Study [18], and Fano (National Bureau of Standards, Washington DC) [19]. In 1953 Biedenharn and Rose from Oak Ridge National Laboratory combined different earlier theoretical developments and formulated the general theory of angular correlations of nuclear radiations [20]. With an emphasis on interpretation of different formulations of the theory, Ref. [20]
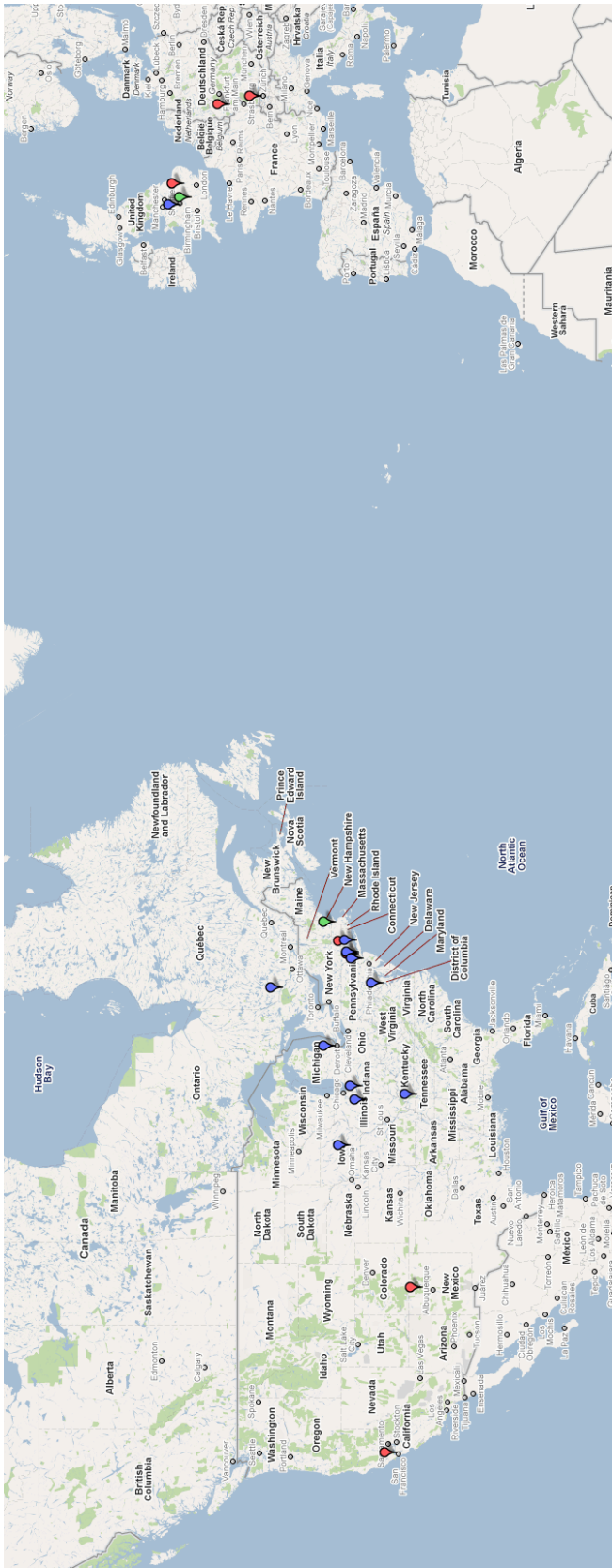
Figure 1.1: Geography of nuclear vector correlations. The main institutions involved in experimental research, in random order [red labels]: Cambridge (Dunworth, Pryce), Harvard (Hamilton), University of Kaiserslautern (Kikuchi), Yale (Beringer), MIT (Good, Brady, Deutsch). Theoretical groups [blue labels]: New York University (Goertzel, Zinnes), Princeton (Hamilton), University of Birmingham (Gardner), University of Michigan (Falkoff), IAS Princeton (Racah, Lloyd), National Bureau of Standards (Fano), Oak Ridge National Laboratory (Biedenharn, Rose, Simon, Welton), Harvard (Abraham, Pound), Purdue (Steffen), State University of Iowa (Coester), Oxford (Satchler, Brink, Rose), University of Illinois (Blatt), Atomic Energy of Canada Limited (Kennedy, Sharp), Brookhaven National Laboratory (Jacob, Wick). The institutions involved both in experiment and theory are labeled by green.

3

is a classic source on vector correlations in nuclear spectroscopy until now. Later, the theory was generalized to account for effects of external magnetic and electric fields on the angular correlations by Abraham and Pound (Harvard) [21], Steffen (Purdue) [22], and Coester (State University of Iowa) [23], and to treat triple nuclear decays by Satchler (Oxford) [24]. In 1967 Rose and Brink developed a theory of angular distributions of gamma-rays, based on phase-defined reduced matrix elements [25]. Theory of vector correlations in nuclear spectroscopy in its semiclassical and quantum formulations was reviewed by Biedenharn in Ref. [26].

Racah's approach separating geometry from dynamics was also used to develop the theory of nuclear scattering. In 1952 Blatt and Biedenharn drastically simplified formulae for nuclear reaction cross sections, by performing explicit summations over magnetic quantum numbers [27]. The resulting expressions, involving Racah coefficients, are applicable to spin-conserving and spin-changing collisions proceeding via a scattering resonance, both for neutral and charged particles. In 1953 Simon and Welton from Oak Ridge National Laboratory combined the S-matrix technique with the Racah formalism to treat binary nuclear reactions, $a + X \rightarrow Y + b$, with particle a colliding with nucleus X to produce nucleus Y and particle b [28, 29]. Their approach accounted for the polarization of reagents and products spin states, and therefore amounted to the first theory of vector correlations in nuclear scattering. Later, the theory was simplified by Satchler [30] and Kennedy and Sharp (Atomic Energy of Canada Limited, Chalk River, Ontario) [31], and generalized to the relativistic case by Jacob and Wick from Brookhaven National Laboratory (Upton, New York) [32]. Over the next 20 years, a significant progress has been made in experimental investigation of angular distributions of γ-rays emitted from oriented nuclei [33], angular correlations in inelastic nucleon scattering [34], and vector correlations in collisions of polarized particles and nuclei, such as polarization transfer and spin correlations [33, 35, 36, 37].

Nuclear theory of vector correlations came handy in atomic physics 20 years later when Fano and Macek adapted it to study polarization of emitted light in atomic and electronic collisions [38]. Later, vector correlations turned into a flourishing part of

atomic physics. Extensively studied are shell polarization effects in collisions of atoms with electrons, atoms, and ions [39, 40, 41, 42, 43], modifying atom-atom collisions by laser fields [44], and electron-photon angular correlations resulting from electron impact of atoms or molecules [45].

The geography of the development of vector correlations in nuclear reactions and spectroscopy is illustrated in Fig. 1.1.

1.2   Vector correlations in molecular dynamics

The actual birth of the field of reaction dynamics is marked by the invention of the crossed molecular beam technique [46, 47], which allowed to leap from measuring macroscopic rate constants to detailed understanding of molecular collisions. The first study was performed by Bull and Moon at Birmingham, who investigated the formation of CsCl by impact of CCl_4 on Cs [48], however their work remained disregarded for a long time. One year later Taylor and Datz at Oak Ridge National Laboratory performed a study for the K+HBr→KBr+H reaction, using the hot-wire surface ionization detector [49]. Although the traditional surface ionization detector is about equally sensitive to K and KBr, they found that a platinum alloy is much more effective for K than for KBr. The difference in the signals from two separately heated wires made it possible to distinguish very small amounts of KBr produced in the reaction from the background of elastically scattered K atoms. Within the next decade, the pioneering work of Taylor and Datz was followed by numerous scattering studies [50], with the Herschbach group leading the 'alkali age' research.

In the end of the 1960's Herschbach and co-workers designed the first 'universal' crossed-beam apparatus, provided with an electron-impact mass spectrometer detector [51]. This made it possible to detect any chemical species and led reaction dynamics out of the 'alkali age' into the 'chemical age' [52]. The study of vector correlations in molecular dynamics rapidly became a flourishing field involving many groups all over the globe, as illustrated in Fig. 1.2.

Early crossed molecular beam experiments dealt almost solely with the most readily accessible $\mathbf{k} - \mathbf{k}'$ vector correlations, or differential cross sections (DCS), which were measured for a large number of reactions [53]. By that time the analysis of chemical reactions largely profited from Newton diagrams, introduced into the field by Herschbach and widely used until now. The diagrams were named in such a way because for kinematic analysis Newton's law suffice: in the asymptotic translational states the beam molecules are too far apart to interact and therefore have constant velocities [52].

In the early 70's experimental techniques were already up to tackling more complex vector properties [54]. For instance, deflection by electric field gradient (analogous to the Stern-Gerlach magnet) was used to measure angular momentum polarization of products (the $\mathbf{k} - \mathbf{j}'$ correlation) in K+HBr, Cs+HBr, Cs+HI, and Cs+CH$_3$I reactions [55, 56]. That technique also allowed the first experimental study of scattering-angle resolved product polarization (the $\mathbf{k} - \mathbf{k}' - \mathbf{j}$ three-vector correlation), which was performed by Herschbach's group in 1974 [57]. This showed that in the Cs+CH$_3$I reaction the CsI product's $\mathbf{j}'$ vector is not azimuthally symmetric about $\mathbf{k}$, but rather strongly aligned perpendicular to the $\mathbf{k} - \mathbf{k}'$ plane. The newly formed product molecule thus tends to rotate in the plane containing the initial asymptotic trajectories of the reactants and the final trajectories of the products. Successive model calculations found that such an alignment is weak in the statistical regime [58] and becomes stronger when impulsive repulsion occurs between the reaction products [59].

In 1975 Case and Herschbach adapted the theory of vector correlations used in nuclear physics [26] to treat chemical stereodynamics [58]. Their theoretical approach was used to account for two-vector [61], three-vector [58], and four-vector correlations [60, 62]. Herschbach and co-workers developed statistical [63] and impulsive [64, 65] methods to recover DCS's and angular-resolved product polarization (the $\mathbf{k} - \mathbf{k}' - \mathbf{j}'$ distribution), carried out trajectory calculations to illustrate the angular momentum disposal in exchange reactions [66], and worked out classical and quantum theory for resonance fluorescence measurements [67].
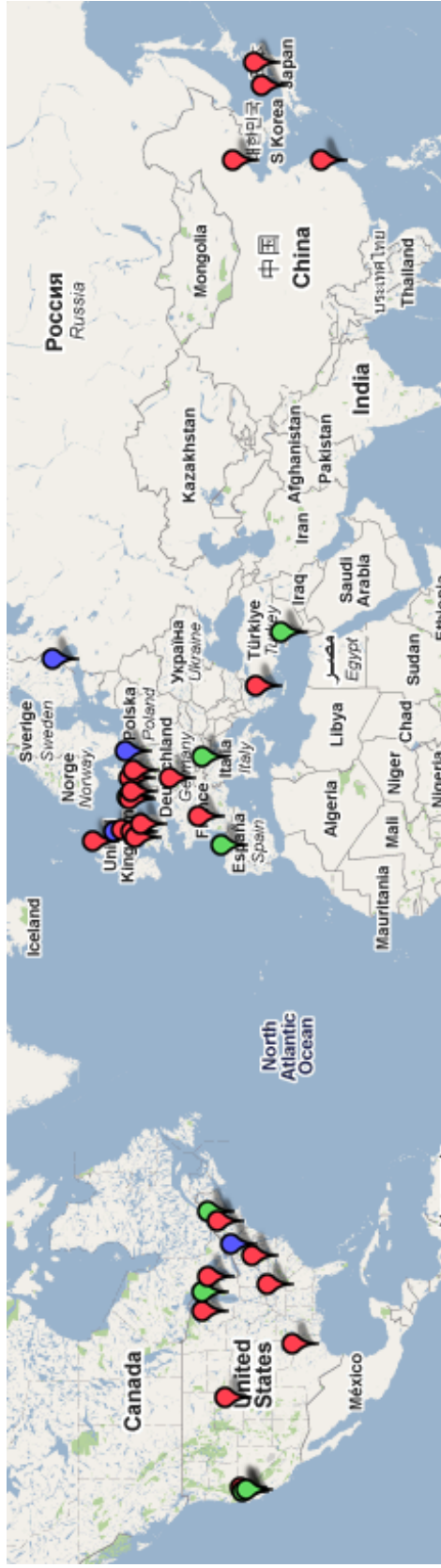
Figure 1.2: Geography of vector correlations in molecular dynamics. The main institutions involved in experimental research, in random order [red labels]: Harvard (Herschbach), Stanford (Zare), Cornell University (Houston), University of Chicago (Farrar, Lee), Rice University (Brooks, Jones), University of California, Los Angeles (Bernstein), University of California, Santa Barbara (Martin), JILA (Nesbitt), Wayne State University (Suits, Vasyutinskii), Ohio State UniVersity (McBane), University of North Carolina (Miller), Brookhaven National Laboratory (Hall), Sandia National Laboratories (Chandler), Oxford (Simons, Brouard, Vallance), Bristol (Orr-Ewing, Ashfold, Dixon), University of Sussex (Wynn, McCaffery), Leeds (Whithaker), Ioffe Physico-Technical Institute (Vasyutinskii), Madrid (Aoiz, Bañares, Herrero), Institute of Electronic Structure and Laser, Hellas (Rakitzis, Toomes, Kitsopoulos), University of Perugia (Aquilanti), National Taiwan University, Taipei (Liu), Max-Planck-Institut für Strömungsforschung, Götingen (Schinke), Radboud University Nijmegen (Parker, ter Meulen, Groenenboom), Vrije UniVersiteit Amsterdam (Stolte), University of Bielefeld (Loesch, Stienkemeier). Theoretical groups [blue labels]: Harvard (Herschbach), Stanford (Zare), University of Maryland (Alexander, Klos), Madrid (Aoiz, Bañares, Herrero, Aldegunde), University of Leeds (de Miranda), Oxford (Clary), University College London (Clary), University of Exeter (Althorpe), Heriot-Watt University, Edinburgh (McKendrick), Fritz Haber Institute, Berlin (Friedrich, Lemeshko), University of Perugia (Aquilanti), Vrije UniVersiteit Amsterdam (Stolte). The institutions involved both in experiment and theory are labeled by green.

7

In the case of an atom-diatom collision, there are six vector directions that can be specified or observed experimentally. These are the directions of the initial and final relative velocity vectors, $\mathbf{k}$ and $\mathbf{k}'$, initial and final orientations of the molecular axis, $\mathbf{r}$ and $\mathbf{r}'$, and the rotational angular momentum vectors of reagents and products, $\mathbf{j}$ and $\mathbf{j}'$. Although the directions of $\mathbf{r}$ and $\mathbf{r}'$ can be controlled by means of nonresonant electric, magnetic, or laser fields, most experiments deal with correlations between the $\mathbf{k}$, $\mathbf{j}$, $\mathbf{k}'$, $\mathbf{j}'$ vectors, which form a 'hierarchy pyramid,' Fig. 1.3, first established by Herschbach and co-workers [60]. Different pairs of the $\mathbf{k}$, $\mathbf{j}$, $\mathbf{k}'$ and $\mathbf{j}'$ vectors form six *two-vector correlations*, each a function of a single angle between the vectors [61]. Most familiar is the product angular distribution in the center-of-mass frame, $\mathbf{k} - \mathbf{k}'$, i.e. the differential cross section (DCS), which has been obtained in many theoretical models and experimental results. The single angle in this case is the center-of-mass scattering angle ϑ. Other two-vector correlations are, e.g. the $\mathbf{j} - \mathbf{j}'$ correlation (rotational tilt), the $\mathbf{k} - \mathbf{j}$ correlation (reagent-polarization-dependent reaction probability), and the $\mathbf{k} - \mathbf{j}'$ correlation (product-polarization-resolved reaction probability). The four vectors are also related by four *three-vector correlations*, each specified by three angles. Among those, the reagent-polarization-dependent differential reaction probability (the $\mathbf{k} - \mathbf{j} - \mathbf{k}'$ correlation), the product-polarization-resolved differential reaction probability (the $\mathbf{k} - \mathbf{k}' - \mathbf{j}'$ correlation), and
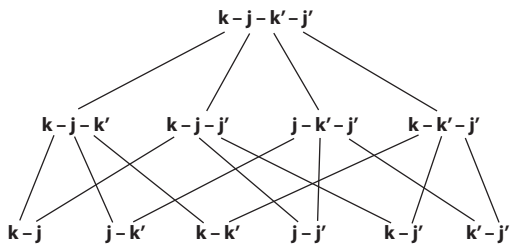
Figure 1.3: Hierarchy of angular correlations for an arom+diatom collision. $\mathbf{k}$ and $\mathbf{k}'$ denote initial and final relative velocity vectors, $\mathbf{j}$ and $\mathbf{j}'$ the rotational angular momenta of reactant and product molecules. Lines indicate how lower order correlations represent special cases of higher order correlations. Adapted from Ref. [60].
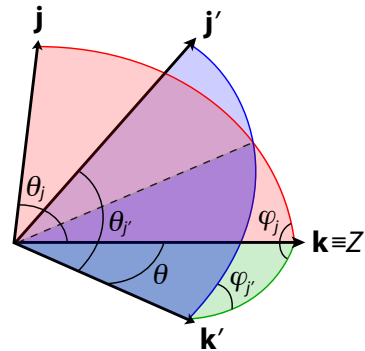
Figure 1.4: Four-vector correlation between $\mathbf{k}, \mathbf{j}, \mathbf{k}', \mathbf{j}'$ vectors, described by three polar and two dihedral angles.

the approach-direction-dependent rotational tilt (the $\mathbf{k} - \mathbf{j} - \mathbf{j}'$ correlation). Three-vector correlations are characterized by three angles, one of them dihedral. Also, there is a single $\mathbf{k} - \mathbf{j} - \mathbf{k}' - \mathbf{j}'$ *four-vector correlation* given by three polar and two dihedral angles which can be defined in a number of ways, e.g. as shown in Fig. 1.4.

An interest in measuring reactive DCS and the $\mathbf{k} - \mathbf{k}' - \mathbf{j}'$ correlation has been stimulated by the development of rigorous spectroscopic techniques, so-called 'pump-probe' methods, described in more detail in Chapter 2. In these methods, the 'pump' laser pulse prepares a reagent in an initial state, e.g. dissociating a precursor molecule and thereby creating an atomic or molecular fragment with a well-defined velocity $\mathbf{k}$, or polarizing the initial angular momentum vector $\mathbf{j}$ via the electronic excitation. After a collision with a target molecule, the second, 'probe,' laser is used to detect the collision products via laser-induced fluorescence (LIF) or resonance-enhanced multi-photon ionisation (REMPI). Being widely used to measure scalar properties, this method was also applied to study differential cross sections for a number of reactions, such as e.g. $H+H_2O/D_2O \rightarrow OH/OD + H_2/HD$ [68]. Brouard and co-workers used the 'pump-probe' technique to measure the $\mathbf{k} - \mathbf{j}'$ correlation in the $O+N_2O \rightarrow NO+NO$ reaction [69], showing that the rotational angular momentum of NO tends to align perpendicularly to the relative velocity of the reagents. Hall and coworkers measured the $\mathbf{k}' - \mathbf{j}'$ correlation in $H+O_2 \rightarrow OH+O$ [70], observing substantially different angular momentum polarization for two Λ-doublet states of the OH product: the $\mathbf{j}'$ vector tends to align perpendicularly to $\mathbf{k}'$ for OH $\Pi(A')$, while its distribution is nearly unpolarized for the A'' level. A similar result was obtained by Brouard *et al.* for the angular polarization of OH produced in the $O+CH_4 \rightarrow OH+CH_3$ reaction [71, 72]. At the same time, measurements of the $\mathbf{k} - \mathbf{k}' - \mathbf{j}'$ correlation in the $H+CO_2 \rightarrow OH+CO$ reaction showed the angular momentum polarization of OH to be significantly stronger for the A'' than for the A' state [73, 74]. Zare and co-workers looked into the DCS's and $\mathbf{k} - \mathbf{k}' - \mathbf{j}'$ three-vector correlation in the $Cl+CH_4 \rightarrow HCl+CH_3$ reaction, showing that the angular momentum $\mathbf{j}'$ of the product HCl molecule tends to align parallel to $\mathbf{k}'$ for forward and sideways scattering, and perpendicular to $\mathbf{k}'$ for the

backscattered HCl [75]. Zare's group also measured a set of polarization moments for the DCl molecule produced in the Cl+CD$_4 \rightarrow$ DCl + CD$_3$ and Cl+C$_2$D$_6 \rightarrow$ DCl+C$_2$D$_5$ reactions [76, 77]. Wynn and co-workers undertook an attempt to look into the $\mathbf{k} - \mathbf{j} - \mathbf{k}' - \mathbf{j}'$ correlation in collisions of Li$_2$ with Ar and Xe [78, 79] using two-colour sub-Doppler circular dichroism, which is so far the only experiment pertaining to a four-vector correlation. However, this technique did not allow to extract any polarization moments from the experimental data and measurement of four-vector correlations in molecular collisions still remains a challenging task.

Velocity-map imaging of scattering products (REMPI-VMI) [80, 81] was used by a number of groups to measure the reactive DCS's of such collision systems as H+D$_2$ [82], O+D$_2$ [83], and Cl+C$_4$H$_{10}$ [84]. The REMPI-VMI technique was used by Chandler and co-workers to observe state-resolved DCS's in rotationally inelastic collisions of Ne+CO [85], Ne+ND$_3$ [86], and of HCl with rare gases and molecules [87]. A few different groups investigated state-resolved DCS's of Ar+NO collisions [88, 89, 90]. Using different laser polarizations in REMPI detection Chandler and coworkers measured the scattering-angle resolved rotational alignment and orientation of the NO($X^2\Pi$) molecule after a collision with Ar (the $\mathbf{k} - \mathbf{k}' - \mathbf{j}'$ correlation) [91, 92, 93]. Recently, Chandler's group performed the first vector correlation experiment with molecules in excited electronic states, looking into the collisions of Ne with NO($A^2\Sigma$) [94]. The problem of the ground-state molecules is that the forward-scattered products are indistinguishable from rotationally excited molecules of the initial molecular beam which do not undergo collisions. This makes the background extraction extremely difficult, rendering the small-angle scattering almost inaccessible for ground-state molecules. On the other hand, the electronic excitation transfers the molecules into a single rotational state, absent in the initial molecular beam, such as the ($A^2\Sigma, N = 1/2, J = 0$) state of NO, allowing for accurate measurements in the forward scattering region. Liu and coworkers developed the three-dimensional ion velocity imaging technique [95] that allowed to measure state-correlated pair-resolved DCS's for the F+CD$_4 \rightarrow$DF+CD$_3$ process [96]. Mapping of the CD$_3^+$ ions resulted

in the 3D velocity distribution of the CD_3 reaction products, and also yielded the vibrational state and the preferred scattering direction of the coincidentally formed DF fragment.

In usual collision experiments molecules rotate freely with the directions of the internuclear axes being uniformly distributed, and restricting molecular rotations was a long-term challenge. Experiments with symmetric top molecules, which can be oriented by a weak electrostatic field of a hexapole, were pioneered by groups of Brooks and Bernstein in the mid-1960's [97, 98]. They used the hexapole technique to study the $\mathbf{k} - \mathbf{r}$ correlation in a number of reactions, e.g. showing that the reactivity of $K+CH_3I$ [99] and $Rb+CH_3I$ [100, 101] is substantially larger if the atom collides with the I end of the molecule. On the other hand, things were shown to be different for $K+CF_3I$ [102], where the reaction favors the K atom hitting the CF_3 end of the molecule. Parker, Stolte and co-workers investigated steric effect in $He+CH_3F$ (Ref. [103], pp. 41-50) and $Ca+CH_3F$ [104] collisions, and the influence of an electrostatic field on the reactivity of $NO+O_3$ [105] and $Ba+N_2O$ [106]. The hexapole technique was used to probe the changes of the integral cross sections in rotationally inelastic collisions with oriented reagents, i.e. the $\mathbf{k} - \mathbf{r}$ correlation. By selecting the initial states with a hexapole field, and then orienting the molecular axis by a static electric field, ter Meulen and co-workers observed that O- and H-ended collisions of $OH(X)$ with Ar gave different preferences for yielding low and high j' levels [107, 108]. Stolte and co-workers have observed an oscillatory dependence of the steric asymmetry in collisions of $NO(X)$ with He and Ar [109, 110]. Hexapole state selection was also used by Stolte's group to measure DCS for collisions of He and D_2 with NO in a single Λ-doublet level [111, 112].

For a long time orientation of molecules other than symmetric tops with an electrostatic field was considered to be impractical, since it was believed that orientation of a molecular dipole in the laboratory frame would require extremely high field strengths [113]. A good example from those days is Brook's paper, published in Science in 1976 [114], one of whose sections is entitled 'Brute force – how not to orient

molecules'. Brooks referred to attempts to orient molecular dipoles by strong fields as to the 'brute force' methods, and estimated the field strength required to suppress rotation and align HCl to be 12 MV/cm, which is experimentally unfeasible. The 'brute force' techniques were juxtaposed to the 'smart' orientation methods, based on picking suitable molecules, such as symmetric tops whose dipole moments are not averaged out by rotation.

Only in the 1990's it was understood that orientation of any polar molecule is possible upon rotational cooling to its ground state, $J = 0$. First experiments were done by Loesch and Remscheid who investigated the steric effect in K+CH$_3$I collisions [115], and by Friedrich and Herschbach, who oriented a non-symmetric-top molecule (ICl) for the first time [116]. Later the Loesch group investigated the influence of the reagent orientation on velocity and angular distributions of the products in K+CH$_3$Br [117], K+ICl [118], Li+HF→LiF+H [119], and K+C$_6$H$_5$I [120] reactions (for a review see Ref. [121]). Friedrich and co-workers looked into the effect of an electrostatic field on Ar+ICl collisions and found that the field suppresses rotationally inelastic scattering [122].

Alternatively, the polarization of the reactants' angular momentum can be controlled by the absorption of linearly polarized light, as proposed by Zare [123]. This technique was used by Loesch and Stienkemeier to study the Sr+HF→SrF+H and K+HF→KF+H reactions [124]. They found that at low energies reactivity of Sr with HF is favored by the HF bond being perpendicular to the Sr approach direction, whereas K+HF is favored by the HF bond being parallel to the approach direction. However, at higher collision energies the reactivity of Sr+HF becomes better for the 'parallel geometry,' whereas the reactivity of K with HF is insensitive to the alignment of the HF bond. Zare and co-workers studied the steric effect in reactions of Cl with stretch-excited CH$_4$ and CHD$_3$ by varying the direction of approach of the Cl atom relatively to the C–H stretching bond with different polarizations of the infrared excitation laser [125].

Another way of polarizing reagents is to remove a part of the M manifold by

selective photodissociation of the molecule. It was pioneered by de Vries *et al.* who polarized a beam of IBr and looked into its reaction with metastable Xe* to produce XeI* and XeBr* [126]. It was found that the reaction cross section is larger when the Xe* atom approaches parallel to the plane of rotation of IBr, and smaller for for the perpendicular approach direction.

In the 1930's it was predicted that the angular momentum of a molecule can be aligned naturally due to collisions with surrounding gas [127, 128], or, as later pointed by Ramsey, if a molecular beam crosses a gas target [129]. This effect was demonstrated only many years later in supersonic expansions for such molecules as Na_2 [130], Li_2 [131], I_2 [132, 133], and CO_2 [134], seeded in an excess of a light carrier gas, and now is proved to be a general phenomenon. In 1995 Herschbach and co-workers presented a model treatment and quasiclassical trajectory calculations of collisional alignment, taking into account single collisions [135]. In 1994 Aquilanti and co-workers provided the first experimental evidence for the strong dependence of alignment on the final molecular speed, by measuring the variation of paramagnetism of O_2 seeded in different carrier gases [136, 137]. McKendrick and co-workers measured polarization of the fluorescence emitted in collision-induced electronic relaxation of SiCl and SiF, disclosing information on the $\mathbf{j} - \mathbf{j}'$ correlation [138]. Brouard and co-workers proposed to use Zeeman quantum beat spectroscopy (see Chapter 2) to get insight into changes of angular momentum polarization in molecular collisions, i.e. the $\mathbf{j} - \mathbf{j}'$ correlation [139]. The technique was applied to study the angular momentum depolarization of electronically excited $NO(A^2\Sigma)$ and $OH(A^2\Sigma)$ radicals in collisions with a number of partners. It was found that for collisions of NO(A) with He and Ar, collisional depolarization is a relatively minor process, compared to the rotational energy transfer, due to very weak long-range forces in these systems [140]. On the other hand, collisions of OH(A) with water molecules [141], as well as with Ar and He atoms [142, 143] are accompanied by significant depolarization, whose rate is comparable, if not larger, than the rate for the energy transfer. Both quasiclassical and quantum theories were developed to describe depolarization of $^{2s+1}\Sigma$ radicals in

collisions with closed-shell atoms by Aoiz, de Miranda and co-workers [144].

Substantial progress in the theoretical understanding of vector correlations was made in the 1990's with the advance of quantum mechanical (QM) and quasiclassical trajectory (QCT) calculations (see Chapter 3). The first consistent QM description of four-vector correlations in atom-diatom collisions was given by de Miranda and Clary [145]. The main focus was on the reactive $A + BC \rightleftharpoons AB + C$ collisions, but the derived equations could also be used for inelastic scattering. In Ref. [145] the relations between the alignment moments and scattering matrices were presented, both in the angular momentum and helicity representations, which made it possible to connect the stereodynamics treatments with the close-coupling scattering calculations and extract all the information about the stereodynamics from the latter. In the subsequent years the quantum approach was applied to the H+D$_2$ [146, 147], Na+HF→NaF+H [148], Li+HF→LiF+H [149] collisions, to the four-atom reaction H$_2$+OH⇌H$_2$O+H [150], and to reactive F+H$_2$ and D+H$_2$ scattering at low and ultralow energies [151, 152]. In the mid-1990's Aoiz and co-workers developed a unified semiclassical description of the $\mathbf{k} - \mathbf{k'} - \mathbf{j'}$ three-vector correlation in photoinitiated bimolecular reactions [153]. The method was successfully applied to study the stereodynamics of the F+H$_2$ [154], O+H$_2$ →OH+H [155], Cl+HD→HCl+D [156], H+H$_2$O→OH+H$_2$ [157], O+H$_2$ →OH+H [158], O+HD [159], Li+HF→LiF+H [160] reactions, and the effect of molecular orientation on the reactivity of H+DCl [161]. In addition, Aoiz, de Miranda, and co-workers developed a unified description of classical and quantum stereodynamics [162, 163, 164], and investigated the effect of initial molecular polarization on reactivity [165, 166, 167].

There is another broad field lying beyond studying scalar properties of chemical reactions: vector correlations in molecular photodissociation, a process that can be viewed as the second half of a full collision. An atom-diatom reaction, $A + BC \rightarrow AB + C$, usually proceeds via an intermediate complex $(ABC)^*$, later decaying into the reaction products:

$$A + BC \rightarrow (ABC)^* \rightarrow AB + C \tag{1.1}$$
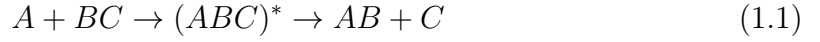
The 'second half' of the reaction might be simulated using photodissociation of the ABC molecule via the same $(ABC)^*$ excited state:

$$ABC + \hbar\omega \rightarrow (ABC)^* \rightarrow AB + C \tag{1.2}$$
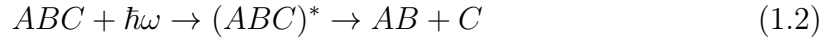
The decay of the $(ABC)^*$ complex in these two processes is driven by the same Hamiltonian, the only difference is how the complex was formed. In the case of thermal collisions, many partial waves take part in the process, and averaging over those is unavoidable. On the other hand, an excitation by a photon obeys the dipole selection rule, $\Delta J = 0, \pm 1$. As a consequence, the number of angular momentum states needed to describe the photodissociation process is substantially smaller than in the case of a full-collision. Also, the decay of a complex can be understood much better in a photodissociation than in a collision experiment, e.g. the energy of an intermediate complex can be easily controlled by variation of the photolysis wavelength, which is more problematic in scattering studies.

Three vectors are involved into the photolysis process: the transition dipole moment of the parent molecule, $\boldsymbol{\mu}$, the relative velocity vector of the fragments, $\mathbf{k}$, and the rotational angular momentum of the fragment, $\mathbf{j}$. In a photodissociation experiment the polarization vector of the photolysis laser, $\mathbf{E}$, defines a direction in the laboratory frame, relatively to which all other vectors are measured.

The most familiar vector correlation is the one between the recoil velocity $\mathbf{k}$ and the polarization vector $\mathbf{E}$, first described by Herschbach and Zare in 1963 [168]:

$$\frac{d\sigma}{d\theta}(\theta) = \frac{\sigma}{4\pi}\left[1 + \beta P_2(\cos\theta)\right], \tag{1.3}$$

where $-1 \leq \beta \leq 2$ is the anisotropy parameter, and θ is the angle between $\mathbf{E}$ and $\mathbf{k}$, $d\sigma/d\theta$ and σ are differential and integral photodissociation cross sections.

A more complicated vector correlation is the $\mathbf{E} - \boldsymbol{\mu} - \mathbf{k}$ one. The transition

dipole moment $\boldsymbol{\mu}$ of a diatomic molecule can point in either parallel or perpendicular direction to the molecular axis. These cases correspond to parallel and perpendicular transitions. In the dipole approximation, the probability for absorbing a photon is proportional to $\cos^2 \theta$, with θ being the angle between $\boldsymbol{\mu}$ and $\mathbf{E}$. Therefore, photons preferentially excite the molecules with dipole moments parallel to the polarization vector, and the resulting excited molecules are aligned in the laboratory frame. Since the relative velocity of the fragments $\mathbf{k}$ is normally directed along the internuclear axis, molecular alignment after the absorption of a photon also implies the alignment of $\mathbf{k}$. Therefore, the angular distribution of the photofragments, $I(\theta)$, is proportional to $\cos^2 \theta$ for a parallel transition and to $\sin^2 \theta$ for a perpendicular transition. More generally:

$$I(\theta) \propto \frac{1}{4\pi} \left[1 + \beta P_2(\cos \theta) \right], \tag{1.4}$$

where the anisotropy parameter β ranges between -1 for a perpendicular transition and $+2$ for a parallel transition.

Another possible correlation describes the orientation or alignment of the angular momentum $\mathbf{j}$ of the photofragment relatively to $\mathbf{E}$ and $\boldsymbol{\mu}$. The $\mathbf{E} - \boldsymbol{\mu} - \mathbf{j}$ correlation was first observed by van Brunt and Zare in 1968 [169]. As an example we can consider a triatomic molecule, such as H_2O, with $\boldsymbol{\mu}$ perpendicular to the plane defined by three atoms. In such a case the photon will mainly excite molecules that lie in the plane perpendicular to $\mathbf{E}$. Since the recoil directions of the H and OH fragments also lie in a plane, the angular momentum vector of OH will be preferentially directed parallel to $\mathbf{E}$.

While both $\mathbf{k}$ and $\mathbf{j}$ correlate with $\boldsymbol{\mu}$ and $\mathbf{E}$, they also correlate with each other, giving rise to the $\mathbf{k} - \mathbf{j}$ correlation. A peculiar feature of the $\mathbf{k} - \mathbf{j}$ correlation is that it completely belongs to the molecular frame and is independent of the choice of the laboratory frame. While $\mathbf{E} - \mathbf{k}$ and $\mathbf{E} - \mathbf{j}$ correlations are diminished by overall rotation in the lab frame before a molecule dissociates, the $\mathbf{k} - \mathbf{j}$ correlation is not established before the bond breaks, rendering the molecular rotation before dissociation irrelevant. This allows to gather additional information about the bond

rupture and the dissociation dynamics. The $\mathbf{k} - \mathbf{j}$ correlation was first observed in 1986 independently in four different laboratories [170, 171, 172, 173].

By applying external fields, one can orient or align the molecular axis $\mathbf{r}$ in the laboratory frame, which allows to look at the $\mathbf{r} - \mathbf{k}$ correlation and explore the photodissociation in the molecular frame. Using electric fields to orient molecules prior to photodissociation was proposed and demonstrated for N_2–HF and HF–HCl complexes by Roger Miller and co-workers [174, 175, 176]. In 1997 Stolte and co-workers combined hexapole state selection and orientation with two-dimensional ion imaging, which allowed to study photodissociation dynamics of fully-state selected oriented molecules [177].

In his 1986 Nobel lecture, Dudley Herschbach mentioned that about 500 review articles and definitely more than 5000 research papers have been published in the field of reaction dynamics by that time [52]. Having no opportunity to cover all the subjects of theory and experiment in this section, we provide a list of recent reviews on vector correlations in molecular dynamics, by different subjects: chemical reactions [178, 179, 180, 181, 182]; rotationally inelastic collisions [183]; orientation and alignment in stereochemistry and photodynamics [137, 184, 185, 186]; photodissociation [187, 188, 189, 190, 191, 192].

1.3 Scope and outline of the present thesis

Observing correlations among the vectors that characterize a collision can disclose all there is to know about *how* the collision proceeds [183]. Dudley Herschbach likened vector correlations to "forbidden fruit" whose "tasting" reveals what would otherwise remain hidden [181]. An example he frequently cites is the undoing of the azimuthal averaging about the initial relative velocity vector via a three-vector correlation, which reveals stereodynamical features lost by averaging over the initial distribution of impact parameters. The pioneering work of Herschbach and coworkers [58, 60, 67] on vector correlations in the domain of molecular collisions spurred an effort to extract

the information hidden in molecular dynamics computations, both quasiclassical and quantum, as these contain vector correlations as a default bonus [182]. However, even when characterized to the full by vector correlations, the *why* of collision stereodynamics can only be answered as well as the theoretical method applied to treat the collisions allows.

In this work we develop an analytic model of vector correlations in rotationally inelastic molecular collisions. The collision model is based on the Fraunhofer model of nuclear scattering of Drozdov and Blair [193, 194, 195], and was recently extended to treat molecular collisions in nonresonant fields [196, 197, 198, 199] and vector correlations in atom-diatom collisions [200, 201]. The Fraunhofer model has no fitting parameters and is inherently quantum, being able to account for interference, angular momentum selection rules, and other nonclassical effects. The complex scattering amplitudes furnished by the model allow to extract the characteristics of vector correlations that reflect the quantum stereodynamics, while its analiticity provides a particularly simple, yet perspicacious insight into experimentally observed dependences.

In Chapter 2 we survey the experimental techniques used to measure vector correlations, in particular the crossed molecular beam and pump-probe methods. Chapter 3 deals with the theory of molecular collisions. We present the concept of the potential energy surface, describe the close-coupling methods used to rigorously describe the field-free and field-dressed collision dynamics, and discuss different models employed to approximately solve the scattering problem. In Chapter 4 we present the theory of vector correlations, both in its quantum and semiclassical incarnations. The Fraunhofer model of molecular collisions and vector correlations is described in Chapters 5 and 6. We show that the molecular collision problem can be greatly simplified by means of the diffractive model, derive the expressions for elastic and inelastic scattering amplitudes, and discuss the limits of applicability of the Fraunhofer theory.

In Chapter 7 we extend the Fraunhofer theory to calculate differential and integral

cross sections of collisions of $^2\Pi$ molecules with closed-shell atoms, and exemplify it with the Ar–NO($X^2\Pi$) collisions. In Chapter 8 we study the effect of nonresonant fields on collisions of closed-shell molecules with closed shell atoms. In particular, we look into the simplest vector correlation, the differential cross section, in the Ne–OCS($X^1\Sigma$) scattering in an electrostatic field and Na$^+$–N$_2$($X^1\Sigma$) collisions in a laser field. In Chapter 9 we extend the Fraunhofer theory to the collisions of closed-shell atoms with $^2\Sigma$, $^3\Sigma$, and $^2\Pi$ molecules in a magnetic field, and exemplify it with the encounters of He with CaH($^2\Sigma$), O$_2$($^3\Sigma$), and OH($^2\Pi$).

Chapter 10 deals with a more complicated case of the $\mathbf{k} - \mathbf{k}' - \mathbf{j}'$ correlation. We use the model to obtain the alignment moments describing the polarization of the $\mathbf{j}'$ vector and compare them with experiment and exact computations. In Chapter 11 we look into the stereodynamics of He–NO ($X^2\Pi$), He–OH ($X^2\Pi$), He–O$_2$($X^3\Sigma$), and He–CaH($X^2\Sigma$) collisions. Comparison of the model and exact results allows to get insight into the mechanisms driving collisional stereodynamics and reveal diffractive contributions to scattering. In Chapter 12 we study vector correlations in collisions of Ne atoms with the electronically excited NO($A^2\Sigma$) molecule. By comparing our results with experiment and exact computations we show that the physical mechanisms behind the stereodynamics of the ground-state and excited-state NO molecules are substantially different. We discuss the $\mathbf{k} - \mathbf{j} - \mathbf{k}'$ and $\mathbf{k} - \mathbf{j} - \mathbf{k}' - \mathbf{j}'$ correlations in Chapter 13.

In Chapter 14 we apply the model to treat multiple scattering of matter waves. We extend the theory to account for the long-range attractive potential and derive analytic expressions for the refractive index of atomic and molecular gases. The main conclusions of this thesis are drawn in Chapter 15.

2 Experimental techniques

> A fool is a man who never tried an experiment in his life.
>
> Erasmus Darwin

In this section we briefly survey the state-of-the-art experimental techniques used to study vector correlations in molecular collisions. They can be broadly divided into two classes: crossed molecular beams (CMB) and pump-probe methods. In each case the molecules are prepared in well-defined state distributions with known vector properties, and then those properties are measured after the collision under controlled conditions.

Crossed molecular beams

In the CMB method the first step is to introduce or create the molecule of interest. While stable molecules such as CO, NO, NH_3, or I_2, can come out of a bottle, many nonstable species important in combustion and atmospheric chemistry, such as OH, NH, CN, or CH, are usually created using microwave or electric discharges, or laser photolysis of suitable precursors. Molecular beams are formed by expanding the molecular gas, usually seeded in an excess of a noble gas, into high vacuum [46]. Collisions in the expansion region result in rotational cooling of molecules, which is very efficient: rotational temperatures of a few Kelvin are achieved routinely. The rotational cooling comes along with the squeezing of transverse translational motion, with the energy redistributed into translation away from the nozzle. Thus, the CMB method restrain the rotational motion to a few lowest rotational states, without real state selection, which can be achieved by applying hexapole [99, 100] or quadrupole [202] focusing as the next step. Advantages of the CMB method include

an initial velocity selection and a small angular divergence which make it conductive to measurements of DCS.

After a collision, the molecular state population can be probed in a number of ways. The classic detection method is a rotatable mass spectrometer using electron impact ionization, with the time-of-flight (TOF) of the products from the scattering centre being recorded. Measuring the kinetic energy distribution via TOF spectroscopy for one of the reaction products recovers information about the undetected product due to energy and momentum conservation. However, providing very high resolution in the product scattering angle, TOF is not sensitive enough to the internal molecular state to observe state-resolved DCS, apart from some exceptional cases [203]. An alternative is to use spectroscopic detection techniques, such as laser-induced fluorescence (LIF) [204] or resonance-enchanced multi-photon ionization (REMPI) [205, 206], which allow to resolve product state populations. In principle, angle-resolved detection of products should be possible using a rotatable laser spectroscopic detector, but unfortunately the product densities in single quantum states are too low to allow for state-resolved DCS measurements with LIF or REMPI.

In the 1990's Welge and co-workers have developed a novel technique to detect H-atoms, which are often among the products of chemical reactions. This method has very high sensitivity and resolution and it was applied to study of the $H+D_2 \rightarrow HD+D$ reaction in crossed molecular beams [207]. In the experiment, a narrow velocity spread of H is achieved by pulsed laser photolysis of HI. The detection scheme is based on laser excitation of H (or D) atoms to a highly lying Rydberg state, immediately after they appear as reaction products and prior to escaping the collision volume. Afterwards, the translational and angular distributions of the nascent fragments is monitored by field ionization of the Rydberg atoms and TOF spectroscopy.

A very efficient way to resolve angular distributions and other vector properties of collisions is to apply the REMPI-Velocity Map Imaging method (REMPI-VMI) [81]. VMI is the extension of ion detection in which an ion lens is used to create a 2D image of the motions in the scattering plane. It was pioneered by Chandler and

Houston to measure 2D images of photodissociation, which can be thought of as a 'half-collision' [208]. REMPI-VMI was used in molecular beam experiments to measure DCS's of such reactions as $H+D_2$ [82], $O+D_2$ [83], and $Cl+C_4H_{10}$ [84]. Chandler and co-workers used REMPI imaging to observe state-resolved DCS for rotationally inelastic collisions of a number of systems, such as e.g. Ne–CO [85], HCl with rare gases and molecules [87], and Ne–ND_3 [86]. State-resolved DCS's of Ar–NO collisions were investigated by a number of groups [88, 89, 90]. Combining different probe laser polarizations Chandler and coworkers also measured $\mathbf{k} - \mathbf{k}' - \mathbf{j}'$ three-vector correlations (scattering-angle resolved rotational alignment and the orientation) of Ar–NO($X^2\Pi$) collisions [91, 92, 93]. Liu and coworkers developed a three-dimensional ion velocity imaging technique [95] that allowed to measure state-correlated pair-resolved DCS's for the $F+CD_4 \rightarrow DF+CD_3$ process [96]. Mapping the CD_3^+ ions they obtained the 3D velocity distribution of CD_3 reaction products, whose analysis also enabled to find out the vibrational state and the preferred scattering direction of coincidentally formed DF.

Combining molecular beams with Stark, Zeeman, Rydberg or optical deceleration [209] makes it possible to achieve complete state selection and beam velocity control. So far the Stark deceleration technique was employed to study scalar properties (integral cross-sections) of rotationally inelastic collisions of OH($X^2\Pi$) radicals with Xe, Ar, and He atoms, and D_2 molecules [210, 211, 212].

Control of chemical reactions is usually performed either by selecting a proper initial state (translational, vibrational, or rotational), or by orienting or aligning reacting molecules, thereby controlling their approach geometry with hexapole or quadrupole electric fields [213]. Experimental results on collisions with controlled reagents are surveyed in Sec. 1.2.

The achievement of higher number densities of molecular beams allowed to study photoinitiated reactions in CMB experiments. Polarized laser photolysis is used to create translationally aligned atoms in the beam, which subsequently exhibit collisions with molecules. The probe laser pulse measures the velocity distribution of products,

by making use of the Doppler effect, which allows to extract state-specific DCS's. Using this technique results in higher signal levels than traditional CMB experiments, but at the expense of greater uncertainty in the collision energy. This approach turned out to be ideally suited for three-atom reactions, $A + BC \rightarrow AB + C$, and was developed in groups of Simons and Brouard [214, 215], Hancock [216], Dagdigian [217], Zare [218, 219], and Hall [70].

Pump-probe techniques

Another broad class of experiments are the so-called 'pump-probe' experiments, which are usually carried out in a 'bulb' environment. The 'pump' laser pulse prepares a required initial state of a reagent, which subsequently undergoes collisions with surrounding 'target' molecules. After the collision with a target molecule, the second, 'probe,' laser is used to detect collision products via LIF of REMPI spectroscopy.

Vector properties were widely studied by the pump-probe technique for photoinitiated chemical reactions [220]. In this case the 'pump' laser pulse dissociates a precursor molecule, creating a fast atomic fragment with a well defined velocity $\mathbf{k}$, which then collides with a thermalized bath of the other reagent:

$$AX + h\nu \rightarrow A + X \tag{2.1}$$

$$A + BCD \rightarrow AB + CD \tag{2.2}$$

The product velocity is usually probed by the laser-induced fluorescence (LIF) technique. Products moving towards or away from the detection laser experience a blue or red Doppler shift in their LIF lines, which correspond to one-dimensional projection of the product velocity along the probe laser propagation direction. By repeating the experiment for different pump-probe laser geometries, one can reconstruct full 3D velocity distribution, and thereby obtain DCS. Since the transition probability at the probe step depends on the relative orientation of the laser polarization and the total angular momentum of the product, the method also provides information about

product angular momentum alignment. This method, combined with a formalism for transforming experimental data from the center-of mass to the laboratory frame [218, 220, 221], was applied to study vector properties of a number of reactions. Among them DCS's of H+H$_2$O and H+D$_2$O [68], $\mathbf{k} - \mathbf{j}'$ correlation in O+N$_2$O→NO+NO [69], $\mathbf{k}' - \mathbf{j}'$ correlation in H+O$_2$ →OH+O [70] and O+CH$_4$ →OH+CH$_3$ [71, 72], and $\mathbf{k} - \mathbf{k}' - \mathbf{j}'$ correlation in H+CO$_2$ →OH+CO [73, 74] reactions. A more sophisticated technique, the two-colour sub-Doppler circular dichroism, was used by Wynn and co-workers to look into the $\mathbf{k} - \mathbf{j} - \mathbf{k}' - \mathbf{j}'$ correlation in collisions of Li$_2$ with Ar and Xe [78, 79] which, however, did not allow to extract any alignment moments from the experimental data.

Zare and co-workers developed the so-called core extraction method based on REMPI-TOF spectroscopy [222], which allows to measure three-dimensional projections of product velocity distributions. This technique was used to look into DCS's and $\mathbf{k} - \mathbf{k}' - \mathbf{j}$ three-vector correlation in Cl+CH$_4$, Cl+CD$_4$, Cl+CHD$_3$, and Cl+C$_2$D$_6$ reactions [75, 76, 77, 125, 223].

Employing the REMPI-VMI technique within the pump-probe method has several advantages over laser-induced fluorescence detection. REMPI allows to detect a much wider range of species with higher velocity resolution than the Doppler-resolved LIF, and data acquisition times are shorter since each measurement is two-dimensional rather than one-dimensional. On the other hand the experiments must be carried out in a molecular beam and the density of products formed is much less than in the LIF experiments, leading to problems with sensitivity. So far applied only to photofragmentation studies, the pump-probe REMPI-VMI method might become a useful tool for studying reaction stereodynamics in the future [224].

Brouard and coworkers proposed to use the Zeeman quantum beat spectroscopy (ZQBS) to get insight into the polarization of angular momentum in molecular collisions, i.e. the $\mathbf{j} - \mathbf{j}'$ correlation, see e.g. Ref. [139] and Refs. therein. In this technique, a molecule placed in a weak magnetic field is excited to a coherent superposition of Zeeman levels by a short laser pulse. Precession of the excited state angular

momentum vector about the magnetic field direction leads to beats in the LIF decay of the excited species if the photon emission is detected through an appropriate linear polarizer. The Fourier transform of the LIF signal then gives information about angular momentum polarization. ZQBS was applied to study depolarization of electronically excited $OH(A^2\Sigma)$ radicals in collisions with water molecules [141], Ar and He atoms [142, 143], and also to depolarization of $NO(A^2\Sigma)$ in collisions with Ar and He [140]. Collisional depolarization was also studied by populating highly excited levels with Raman pumping and detecting final scattering states using LIF [225, 226].

Polarization spectroscopy (PS) [227] was recently adapted by McKendrick and coworkers to measure collisional depolarization [228]. In this technique pump and probe laser beams are tuned to the same transition (e.g. $A^2\Sigma - X^2\Pi$ (0,0) in OH), but their linear polarizations are rotated by 45° relatively to each other. While the pump pulse generates an alignment of the rotational angular momentum in the sample, the probe pulse generates a signal beam that co-propagates but has an orthogonal linear polarization. Any collision that affects the sample polarization will then result in a loss of the PS signal. The PS technique has been used by the McKendrick group to study the loss of alignment ($\mathbf{j} - \mathbf{j}'$ correlation) of $OH(X^2\Pi)$ in collisions with He and Ar [229, 230, 231].

The pump-probe technique, used for measuring DCS's in chemical reactions, was recently extended to look into the inelastic collision dynamics [232]. In the experiment, the molecules are first transferred to an isolated state by pump laser excitation. After the collision, the velocity distribution of scattering products is detected via REMPI-TOF/VMI or sub-Doppler LIF. While in practice the former detection method is limited to a few molecules by the viability of REMPI schemes, LIF suffers from poor velocity resolution due to the significant bandwidth of commercially available pulsed lasers. Using continuous-wave probe lasers for absorption spectroscopy allows for a high resolution, but is relatively insensitive compared to LIF and doesn't allow to measure very low product number densities. This may be overcome by using frequency-modulated spectroscopy (FMS). In this method the velocity distribution

of scattering products is measured by stimulated emission due to transitions to the electronic ground state, which in equivalent to absorption. The Doppler lineshapes are obtained by sweeping the laser frequency through the probe transition. Using two orthogonal photolysis laser polarizations makes it possible to extract Doppler profiles that are sensitive both to the speed and anisotropy of angular distribution. The DCS's are then obtained by fitting these Doppler profiles. This approach was used by Alagappan *et al.* to study DCS's of Ar–CN($A^2\Pi$) collisions [232].

Because of space limitations we refer the reader to recent reviews of experimental techniques employed in the field of collisional stereodynamics, by subject: crossed molecular beams [46, 47, 50]; pump-probe methods [179, 180, 215, 219, 233, 234, 235]; orientation and alignment [97, 121]; quantum beat spectroscopy [139, 236, 237].

3 Theory of molecular collisions

> I have yet to see any problem, however compli-
> cated, which, when you looked at it in the right
> way, did not become still more complicated.
>
> Poul Anderson

3.1 General theory

3.1.1 Potential energy surfaces

Historically, the concept of the potential energy surface (PES) emerged from the 1929 paper by London, who presented a semiempirical formula for the potential of the simplest reaction H+H$_2\rightarrow$ H$_2$+H [238]. Two years later Eyring and Polanyi extended London's approach to calculate PES's of several systems [239], and in 1936 Hirschfelder and co-workers performed a classical trajectory study of the reaction dynamics with the London surface [240]. It is worth mentioning that although started about 80 years ago, the dynamics of the simplest H+H$_2\rightarrow$ H$_2$+H reaction is not completely understood even today [241].

Theoretical treatment of molecular collisions requires the solution of the Schrö-dinger equation for the combined electronic and nuclear motions. However, in the limit when the two collision partners come together slowly, the electronic and nuclear motions can be separated, which constitutes the Born-Oppenheimer approximation – a key in the definition of PES. In this case, the total Hamiltonian of the system consists of the unperturbed molecular Hamiltonian, kinetic energy of relative motion,

and interaction potential:

$$H(\mathbf{r}, \xi_1, \xi_2) = H_0(\xi_1, \xi_2) - \frac{\hbar^2}{2\mu}\nabla_r^2 + V(\mathbf{r}, \xi_1, \xi_2), \qquad (3.1)$$

with ξ_1 and ξ_2 the internal coordinates of the two molecules, $\mathbf{r} = \{r, \theta, \varphi\}$ the relative, center-of-mass coordinates of the two molecules, and μ the reduced mass. Being much lighter, electrons of two molecules move much faster than nuclei and 'adapt' to the slowly changing internal and relative coordinates, thereby enabling the intermolecular potential $V(\mathbf{r}, \xi_1, \xi_2)$ to be determined independently for different values of $(\mathbf{r}, \xi_1, \xi_2)$. Analogously, giving that the timescale of molecular vibrations is much shorter than either the rotational period or the collision time, in most cases intermolecular potentials can be calculated with internuclear distances and bond angles fixed to their equilibrium values.

The PES's can be theoretically calculated in a variety of ways, with the ultimate level being a full *ab initio* quantum mechanical (QM) electronic structure calculation, which aims to be an 'exact' description of a particular system. Although recent development of computer technologies lead to tremendous progress in calculating *ab initio* PES's both for non-reactive [242, 243, 244] and reactive [245, 246, 247, 248] collisions, accurate potentials still represent a bottleneck of chemical reaction dynamics. For instance, no PES is available in the literature for rotationally inelastic collisions of two $^2\Pi$ molecules, such as OH or NO, not to mention scattering of two asymmetric tops or reactions of polyatomics. Another crucial point is that an analytic representation of the PES, obtained by fitting to calculated *ab initio* points, is usually a more difficult task than calculating the PES grid itself [248].

On the other hand, semiempirical or even simpler model surfaces are usually intended to capture the key features of the surface, with the benefits of simplicity and less computational expense. Simplified scattering models, e.g. those taking into account only the 'hard-shell' part of the molecular potential, not only require substantially less computational effort, but also provide qualitative insight into the scattering process. With a PES in hand one can calculate all the quantities observable in a scattering

experiment, either 'exactly' by quantum mechanical (QM) methods, or approximately by classical mechanics, the most rigorous level of which is a quasi-classical trajectory (QCT) calculation. Before introducing the Fraunhofer model of molecular collisions, which lies in the core of this thesis, we briefly survey exact and model techniques commonly used to describe molecular scattering.

3.1.2 Quantum theory of molecular collisions

The field-free case

The Hamiltonian, H, of a molecular system undergoing a binary molecular collision, A+B→A+B, consists of the Hamiltonian, H_0, of the individual molecules A and B, the kinetic energy term T, and the intermolecular interaction potential V:

$$H(\mathbf{r}, \xi_1, \xi_2) = H_0(\xi_1, \xi_2) + T + V(\mathbf{r}, \xi_1, \xi_2), \tag{3.2}$$

with ξ_1 and ξ_2 the internal coordinates of the two molecules, $T = -\hbar^2/(2\mu)\nabla_r^2$, $\mathbf{r} = \{r, \theta, \varphi\}$ the relative, center-of-mass coordinates of the two molecules, and μ the reduced mass. The Schrödinger equations pertaining to H and H_0 are

$$H\Phi(\mathbf{r}, \xi_1, \xi_2) = E\Phi(\mathbf{r}, \xi_1, \xi_2) \tag{3.3}$$

$$H_0\phi_n(\xi_1, \xi_2) = E_n\phi_n(\xi_1, \xi_2) \tag{3.4}$$

In the close-coupling formalism, the wavefunction is usually expanded in some complete orthogonal set of functions of molecular internal coordinates, ξ_1, ξ_2, angles θ, φ, and some unknown radial functions:

$$\Phi(\mathbf{r}, \xi_1, \xi_2) = \sum_n \frac{\Psi_n(r)}{r}\phi_n(\theta, \varphi, \xi_1, \xi_2) \tag{3.5}$$

The subscript n designates all the state labels of the system, such as angular momenta of the molecules, angular momentum of their relative motion, and projections thereof.

The sum in Eq. (3.5) is in principle infinite, but in practice it has to be truncated to a finite number of terms. Schrödinger equation (3.3) of the colliding system can be then recast as

$$\left[\frac{d^2}{dR} - \frac{l(l+1)}{R^2} + k_n^2 \right] \Psi_n(r) = \sum_{n'} V_{n,n'}(r) \Psi_{n'}(r), \tag{3.6}$$

with k_n the absolute value of the wavevector, such that $k_n^2 = 2m(E - E_n)/\hbar^2 \geq 0$, and

$$V_{n,n'}(r) = \frac{2\mu}{\hbar^2} \int \phi_n^*(\theta, \varphi, \xi_1, \xi_2) V(\mathbf{r}, \xi_1, \xi_2) \phi_{n'}(\theta, \varphi, \xi_1, \xi_2) d\tau_r, \tag{3.7}$$

where $d\tau_r$ indicates integration over all the variables except r.

The expansion set ϕ_n can be chosen in a number of different ways; however, it it convenient to use the functions that are eigenfunctions of the total angular momentum, which makes the potential matrix (3.7) block-diagonal. For two molecules with rotational eigenfunctions $\chi_{m_1\Omega_1}^{j_1}(\xi_1)$ and $\chi_{m_2\Omega_2}^{j_2}(\xi_2)$ the functions ϕ_n can be chosen as:

$$\phi_{j_1\Omega_1 j_2\Omega_2 j_{12}l}^{JM}(\theta, \varphi, \xi_1, \xi_2) = \sum_{m_{12}m} \sum_{m_1 m_2} \begin{pmatrix} j_1 & j_2 & j_{12} \\ m_1 & m_2 & -m_{12} \end{pmatrix} \chi_{m_1\Omega_1}^{j_1}(\xi_1) \chi_{m_2\Omega_2}^{j_2}(\xi_2)$$
$$\times \begin{pmatrix} j_{12} & l & J \\ m_{12} & m & -M \end{pmatrix} Y_{lm}(\theta, \varphi)(-1)^{-j_1+j_2-m_{12}-j_{12}+l-M} \left[(2j_{12}+1)(2J+1)\right]^{1/2}, \tag{3.8}$$

with $(\dots)$ 3j-symbols and $Y_{lm}(\theta, \varphi)$ the spherical harmonics. In the case of a closed-shell atom–molecule collision, $j_2 = m_2 = \Omega_2 = 0$, and Eq. (3.8) becomes:

$$\phi_{j_1\Omega_1 l}^{JM}(\theta, \varphi, \xi_1) = \sum_{m_1 m} \begin{pmatrix} j_1 & l & J \\ m_1 & m & -M \end{pmatrix} \chi_{m_1\Omega_1}^{j_1}(\xi_1)$$
$$\times Y_{lm}(\theta, \varphi)(-1)^{-j_1+l-M}(2J+1)^{1/2} \tag{3.9}$$

For the basis sets given by Eqs. (3.8) or (3.9) the field-free potential matrix (3.7) becomes diagonal in J and independent of M, which saves a lot of computational time. Substituting Eq. (3.8) into Eq. (3.7) we obtain the potential matrix:

$$
\begin{aligned}
V_{n,n'}(r) &= V^J_{j_1\Omega_1 j_2\Omega_2 j_{12} 2l; j_1'\Omega_1' j_2'\Omega_2' j_{12}' 2'l'}(r) \\
&= \sum_{p_1 p_1' p_2 p_2' p} (-1)^{j_1 - j_2 + j_{12} - l - j_1' + j_2' - j_{12}' + l'} \left[(2j_{12}+1)(2j_{12}'+1)(2l+1)(2l'+1) \right]^{1/2} \\
&\quad \times \begin{pmatrix} j_1 & j_2 & j_{12} \\ p_1 & p_2 & p \end{pmatrix} \begin{pmatrix} j_1' & j_2' & j_{12}' \\ p_1' & p_2' & p \end{pmatrix} \begin{pmatrix} j_{12} & l & J \\ -p & 0 & p \end{pmatrix} \begin{pmatrix} j_{12}' & l' & J \\ -p & 0 & p \end{pmatrix} \\
&\quad\quad \times V'_{j_1 p_1 \Omega_1 j_2 p_2 \Omega_2; j_1' p_1' \Omega_1' j_2' p_2' \Omega_2'}(r), \quad (3.10)
\end{aligned}
$$

with

$$
\begin{aligned}
&V'_{j_1 p_1 \Omega_1 j_2 p_2 \Omega_2; j_1' p_1' \Omega_1' j_2' p_2' \Omega_2'}(r) \\
&\qquad = \int \chi^{j_1*}_{p_1\Omega_1}(\xi_1) \chi^{j_2*}_{p_2\Omega_2}(\xi_2) V(r,0,0,\xi_1,\xi_2) \chi^{j_1'}_{p_1'\Omega_1'}(\xi_1) \chi^{j_2'}_{p_2'\Omega_2'}(\xi_2) d\xi_1 d\xi_2 \quad (3.11)
\end{aligned}
$$

Thus, for the field-free case the system of close-coupled equations (3.6) can be separated into a number of smaller systems corresponding to each J, which are then solved numerically with the following boundary condition:

$$
\Phi(\mathbf{r}, \xi_1, \xi_2) \underset{r\to\infty}{\sim} e^{ik_n z} \chi_n(\xi_1) \chi_n(\xi_2) + \sum_{n'} \chi_{n'}(\xi_1) \chi_{n'}(\xi_2) \frac{e^{ik_{n'} r}}{r} f_{n\to n'}(\theta, \varphi), \qquad (3.12)
$$

where $f_{n\to n'}(\theta, \varphi)$ is the scattering amplitude, which in computations is often expressed via the scattering matrix $S_{n,n'}$:

$$
f_{nn'}(\theta) = \frac{1}{2i(k_n k_{n'})^{1/2}} \sum_{\ell=0}^{\infty} (2\ell+1) \left[S^{(\ell)}_{nn'} - \delta_{nn'} \right] P_l(\cos\theta) \qquad (3.13)
$$

The computational effort needed to solve systems of close-coupled equations can be reduced by using different decoupling schemes, such as centrifugal sudden or infinite-order sudden approximatons, see Ref. [249] for details. However modern computers

are powerful enough to tackle collisional problems exactly for small molecules, even at thermal energies.

Effect of external fields

An external field breaks the spherical symmetry of the system, rendering the total angular momentum J no longer conserved, which does not allow to reduce the dimension of the collision problem. Volpi and Bohn were first to develop a quantum mechanical theory of field-dressed molecular collisions and to apply it to ultracold $^{17}O_2$–^3He scattering in magnetic fields [250]. Later Krems and Dalgarno extended the theory to ^1S-atom – $^2\Sigma$-molecule, ^1S-atom – $^3\Sigma$-molecule, $^2\Sigma$-molecule – $^2\Sigma$-molecule, and $^3\Sigma$-molecule – $^3\Sigma$-molecule collisions, proposing the fully uncoupled space-fixed basis representation of the wave function as the most convenient to treat molecular collisions in fields [251, 252]. This method was used by Krems, Tscherbul, and colleagues to study the He–NH$_3(X^3\Sigma)$ collisions in a magnetic field [253], collisions of CaD$(X^2\Sigma)$, ND$(X^3\Sigma)$, and OH$(^2\Pi)$ with helium in parallel and tilted electrostatic and magnetic fields [254, 255, 256], and He–CaH$(X^2\Sigma)$ collisions in a microwave laser field [257]. For review of recent developments in computations of molecular collisions in fields see Ref. [186].

Unfortunately, the tremendous computational effort needed to calculate molecular collisions in fields limits the exact computations to the cold and ultracold energy range where only few excitation channels are open, and simpler models are of great value in providing insight into the collision dynamics at thermal and hyperthermal energies.

3.2 Models of molecular collisions

3.2.1 Semiclassical approximation

Semiclassical models of molecular collisions have been widely used in the 1960's, when the computational power was insufficient for tackling scattering problems exactly.

The first study was undertaken by Lawley and Ross who applied the semiclassical theory to the problem of rotational excitation of a diatomic molecule by an atom [258]. The formalism was applied to the K–HBr system, in the regime when the energy transfer is a substantial fraction of the kinetic energy. They used different schemes for coupling of quantized angular momenta, treating the translational motion within the WKB approximation. Cross and Gordon applied semiclassical theory and the Born approximation to calculate total integral cross sections for dipole-dipole scattering at large impact parameters, exemplifying it by collisions of CH_3I molecules with CsBr, CsCl, and KCl [259]. This theory was later extended by Cross to small impact parameters [260]. Rabitz and Gordon derived explicit equations for first- and second-order rotationally inelastic transition probability for the general case of multipole potentials, and applied those to investigate energy and angular momentum transfer in HCN-HCN and ICN-ICN collisions [261]. Gislason and Herschbach used the semiclassical approximation to calculate small-angle differential cross sections in molecular collisions. Their results were found to be in a good agreement with experiment on $CsCl–SbCl_3$ scattering [262].

3.2.2 Quasiclassical trajectories methods

Quasiclassical trajectory (QCT) methods used to treat atom-diatom collisions are nowadays very similar to those developed in the mid-1960's by Karplus [263], and numerous reviews can be found in literature, see e.g. Refs. [264, 265]. The QCT method is based on calculating classical trajectories of atoms and molecules taking part in a collision by integrating classical equations of motion starting from some initial conditions. Many trajectories are calculated in this way and then averaged using the Monte-Carlo method; energy quantization is taken into account by a selection of initial and analysis of final trajectory conditions, therefore the method is "quasiclassical." Final distributions of coordinates and momenta, obtained as an outcome, give information about scalar and vector properties of a collision. Vector properties obtained within the QCT method are analyzed using classical probability

distributions and polarization moments. In the case of non-reactive scattering, the QCT approach was used e.g. to study low-temperature rotational relaxation of N_2 and CO molecules in collisions with He and Ne [266, 267, 268], and stereodynamics of inelastic Ar–NO collisions [269]. Semiclassical theory of vector correlations was extensively elaborated by Aoiz, de Miranda and coworkers and is described in detail in Refs. [162, 163, 164, 182].

3.2.3 Hard-shell models

Many of the key features of inelastic scattering are captured by even the most rudimentary 'hard shell' models. Such models are usually based on classical mechanics and vector properties of collisions are analyzed using classical probability density functions, as described in Sec. 3.2.2. The hard-shell models treat the PES as being infinitely repulsive inside and zero outside of the hard core part of the potential, as illustrated in Fig. 3.1. A fundamental premise is that no rotational energy can be exchanged if the collision does not exert torque on the diatomic molecule. In a hard (or 'sudden') collision the forces act along the surface normal of the hard shell, and the capacity to cause a rotational state change is related to the impact parameter. Within the hard-shape models the oscillatory shape of the DCS is usually considered to be arising from interference between different scattering trajectories.

The phase difference between trajectories arises due to different recoil points on the elliptical surface of the hard shell, and the position and frequency of the DCS oscillations is expressed in terms of the anisotropy of the ellipsoidal PES. Such an approach was used to calculate differential cross sections for a number of atom-molecule collision systems [270, 271, 272, 273], including the explanation of recent experimental results for Ar–NO($X^2\Pi$) collisions [274].

Khare *et al.* [275] developed a classical hard-shell model based on the conservation of the angular momentum projection on the 'kinematic apse,' which is defined as a unit vector of transferred momentum, $\mathbf{a}_k = (\mathbf{k}' - \mathbf{k})/|\mathbf{k}' - \mathbf{k}|$, see Fig. 3.1. For a hard shell, the kinematic apse points along the normal to the elliptical surface.

The kinematic apse model along with QCT computations was used by Pullman *et al.* to study the collisional relaxation and alignment of molecular rotation in atom-diatom collisions [135]. Conservation of the transferred momentum along the kinematic apse was recently used by Stolte and coworkers, who developed the so-called 'quasi-quantum treatment' (QQT) of molecular collisions [276, 277, 278]. The QQT method combines quantum wavefunctions with phase factors originating from different classical trajectories. Using this method the Stolte group described steric asymmetry (a particular case of $\mathbf{k} - \mathbf{r}$ correlation) and parity propensities in collisions of NO with He, Ar, and D_2.

Figure 3.1: Hard-shell collision model. The kinematic apse, $\mathbf{a}_k$, points along the transferred momentum, $\mathbf{a}_k = (\mathbf{k}' - \mathbf{k})/|\mathbf{k}' - \mathbf{k}|$.

Another 'hard-shell' model worth mentioning is the linear-to-angular momentum conversion model developed by McCaffery [279], which allowed to achieve good agreement with experiment for collision rates of rotationally inelastic $Na_2 + H_2$ and $C_2H_2O_2$–Ne collisions, vibrationally inelastic Cl_2–He collisions, and vibrationally-rotationally inelastic Li_2–Ne collisions.

A disadvantage of classical models is that they furnish scattering cross sections instead of scattering amplitudes, needed to obtain polarization moments, characterizing collisional stereodynamics. In 50's Drozdov [193] and Blair [194] came up with the idea to describe nuclear collisions as a Fraunhofer diffraction of matter waves, which makes the model inherently quantum. Later the Fraunhofer model was adapted by Faubel [195] to account for rotationally inelastic thermal atom-molecule collisions, and was extended by Lemeshko and Friedrich to account for collisions in electrostatic [196, 199], magnetic [198], and radiative [197] fields. The model can be also used to treat vector correlations in molecular collisions [200, 201] and is described in detail in the Chapters 5 and 6.

4 Theory of vector correlations

Life is hard but, fortunately, short.

Russian saying

4.1 Quantum theory of vector correlations

The first general quantum mechanical (QM) description of four-vector correlations in atom-diatom collisions was given by de Miranda and Clary [145]. The main focus was on the reactive collisions $A + BC \rightleftarrows AB + C$, but the derived equations can be also used for inelastic scattering. In Ref. [145] relations between alignment moments and scattering matrices were presented, both in angular momentum and helicity representations, which made it possible to connect stereodynamics treatments with close coupling scattering calculations and to extract all the information about the stereodynamics from the latter. The quantum approach was applied to H+D$_2$ [146, 147], Na+HF→NaF+H [148], Li+HF→LiF+H [149] collisions, to the four-atom reaction H$_2$+OH⇄H$_2$O+H [150], and to reactive F+H$_2$ and D+H$_2$ scattering at low and ultralow energies [151, 152]. In addition, Aoiz, de Miranda, and co-workers developed a unified description of classical and quantum stereodynamics [162, 163, 164], and investigated the effect of initial molecular polarization on reactivity [165, 166, 167]. The quantum theory of vector correlations was also applied to describe rotationally inelastic scattering, in particular to reveal DCS's and $\mathbf{k} - \mathbf{k}' - \mathbf{j}'$ vector correlations in Ar–NO [93] and to He–NO collisions [201], and collisional depolarization of $^{2s+1}\Sigma$ radicals in collisions with closed-shell atoms [144]. Both QM and QCT theories were developed to calculate DCS of He–NO collisions [280] and to tackle the problem of collisional depolarization of $^{2s+1}\Sigma$ radicals in collisions with closed shell atoms [144].

39

Pure state of a linear molecule

The rotational wavefunction of a linear molecule with the angular momentum j can be written in general form as:

$$|\Psi\rangle = \sum_{m=-j}^{j} c_m |jm\rangle, \tag{4.1}$$

where m is the projection of $\mathbf{j}$ on the Z axis of the chosen reference frame and c_m are complex expansion coefficients. The states $|jm\rangle$ are eigenstates of $\mathbf{j}^2$ and j_Z operators, and usually the c_m coefficients are normalized such that:

$$\sum_m |c_m|^2 \equiv 1 \tag{4.2}$$

The density operator corresponding to the pure, fully *coherent* state (4.1), is given by [281]:

$$\hat{\rho} = |\Psi\rangle\langle\Psi| = \sum_{m_a m_b} c_{m_a} c_{m_b}^* |jm_a\rangle\langle jm_b|, \tag{4.3}$$

with the corresponding density matrix,

$$\rho_{m_1 m_2} = \langle jm_1|\hat{\rho}|jm_2\rangle = \langle jm_1|\Psi\rangle\langle\Psi|jm_2\rangle = c_{m_a} c_{m_b}^*, \tag{4.4}$$

obeying the normalization condition,

$$\mathrm{Tr}(\rho) = \sum_m \rho_{mm} \equiv 1 \tag{4.5}$$

Mixed state of an ensemble of linear top molecules

If an ensemble of molecules is a mixture of N independently-prepared (i.e. *incoherent*) molecular states, no single wavefunction can describe the state of the ensemble, and there is a need to introduce the density matrix for the mixed system [281]. If the various pure molecular states, $n = 1, 2, \ldots, N$, appear in the final mixture with (real)

statistical weights $w_n = w_1, w_2, \ldots, w_N$, then the ensemble density matrix is given by [281]:

$$\rho_{m_1 m_2} = \sum_{n=1}^{N} w_n \rho_{m_1 m_2}^{(n)} = \sum_n w_n c_{m_1}^{(n)} c_{m_2}^{(n)*} \tag{4.6}$$

The usual normalization of the density matrix assumes Eq. (4.2) and $\sum_n w_n \equiv 1$, which implies

$$\mathrm{Tr}(\rho) = \sum_m \rho_{mm} = \sum_{mn} w_n \rho_{mm}^{(n)} = \sum_n w_n \mathrm{Tr}\left(\rho_{mm}^{(n)}\right) = 1 \tag{4.7}$$

Multipolar expansion of a density matrix

In this thesis we use the convention of de Miranda *et al.* [282] to define polarization moments a_q^k pertaining to vector correlations. The density matrix can be expanded as:

$$\rho_{m_1 m_2} = \sum_{kq} a_q^k \frac{2k+1}{2j+1} C(jkj, m_1 q m_2) \tag{4.8}$$

$$= \sum_{kq} a_q^k \frac{2k+1}{2j+1} (-1)^q C(jkj, m_2 - q m_1) \tag{4.9}$$

$$= \sum_{kq} a_q^k \left(\frac{2k+1}{2j+1}\right)^{1/2} \left[(-1)^q \left(\frac{2k+1}{2j+1}\right)^{1/2} C(jkj, m_2 - q m_1) \right] \tag{4.10}$$

$$= \sum_{kq} a_q^k \left(\frac{2k+1}{2j+1}\right)^{1/2} \langle jm_1 | (-1)^q \hat{T}_{k-q} | jm_2 \rangle \tag{4.11}$$

$$= \sum_{kq} a_q^k \left(\frac{2k+1}{2j+1}\right)^{1/2} \langle jm_1 | \hat{T}_{kq}^{\dagger} | jm_2 \rangle, \tag{4.12}$$

where $\hat{T}_{kq}$ are the multipole operators and $C(j_1 j_2 j, m_1 m_2 m)$ are Clebsch-Gordan coefficients. Here we used a symmetry property of the Clebsch-Gordan coefficients and Fano operators [283, 284], and we note that the multipoles differ from those defined by Fano [285] by a factor of $[(2k+1)/(2j+1)]^{1/2}$.

Since the expansion of Eq. (4.8) is written in terms of adjoints of the multipole

operators, the expansion is covariant. This means that if the polarization moments are rotated to a different reference frame, they change in exactly the same way as the $|jm\rangle$ basis sets.

Inversion of Eq. (4.8) leads to expression for the multipole moments:

$$a_q^k = \sum_{m_1 m_2} \rho_{m_1 m_2} C(jkj, m_1 q m_2), \tag{4.13}$$

and the fact that $C(j0j, m_1 0 m_2) = \delta_{m_1 m_2}$ implies:

$$a_0^0 = \sum_m \rho_{mm} = \mathrm{Tr}(\rho) \tag{4.14}$$

In the case of collision studies, polarization of angular momentum $\mathbf{j}$ is described by the density matrix with components consisting of scattering amplitudes for the states with different projections m:

$$\rho_{m_1 m_2} = \frac{1}{d\sigma/d\omega} f_{i \to f, jm_1}(\theta) f_{i \to f, jm_2}^*(\theta) \tag{4.15}$$

Since we are interested in angular dependence of the alignment moments, we normalized Eq. (4.15) by the differential cross section, which gives $\mathrm{Tr}(\rho) = 1$ at any scattering angle. The relations between the alignment moments obtained within the conventions of de Miranda and Zare [180, 283] are presented in Section 16.1.

4.2 Semiclassical theory of vector correlations

The classical description of vector correlations starts from defining the probability density function (PDF). The most familiar case is the $\mathbf{k} - \mathbf{k}'$ correlation, corresponding to product angular disctribution. It is proportional to DCS:

$$P(\theta) = \frac{2\pi}{\sigma} \frac{d\sigma}{d\omega}, \tag{4.16}$$

where σ and $d\sigma/d\omega$ are the integral and differential cross sections. The PDF is normalized as:

$$\int_0^\pi P(\theta) \sin\theta d\theta = 1 \tag{4.17}$$

Since the $\mathbf{k}$ and $\mathbf{k}'$ vectors are not quantized, classical and quantum descriptions of DCS coincide. However, the spatial distribution of quantized quantities, such as angular momenta, can be also described by PDF's within the classical approach. The PDF $P(\theta_j, \varphi_j)$ gives the probability of the angular momentum vector $\mathbf{j}$ lying along the direction specified by the spherical angles θ_j and φ_j, as shown in Fig. 1.4. The PDF can be expanded in terms of spherical harmonics $Y_{kq}(\theta_j, \varphi_j)$, or more conveniently, in terms of complex conjugates of the modified spherical harmonics $C_{kq}(\theta_j, \varphi_j) = [4\pi/(2k+1)]^{1/2} Y_{kq}(\theta_j, \varphi_j)$:

$$P(\theta_j, \varphi_j) = \sum_{k=0}^\infty \sum_{q=-k}^k \frac{2k+1}{4\pi} a_q^k(\mathbf{j}) C_{kq}^*(\theta_j, \varphi_j), \tag{4.18}$$

where the expansion coefficients $a_q^k(\mathbf{j})$ are the polarization moments, which can be obtained by inverting Eq. (4.18):

$$a_q^k(\mathbf{j}) = \int_0^{2\pi} \int_{-1}^1 P(\theta_j, \varphi_j) C_{kq}(\theta_j, \varphi_j) d(\cos\theta_j) d\varphi_j \tag{4.19}$$

Another PDF expansion, used e.g. in Ref. [182], is given by:

$$P(\theta_j, \varphi_j) = \sum_{k=0}^\infty \sum_{q=-k}^k \frac{2k+1}{4\pi} a_q^k(\mathbf{j}) C(jkj, j0j) C_{kq}^*(\theta_j, \varphi_j) \tag{4.20}$$

An analogous, 'symmetric' expression might be written for polarization of the internuclear axis $\mathbf{r}$:

$$P(\theta_r, \varphi_r) = \sum_{k=0}^\infty \sum_{q=-k}^k \frac{2k+1}{4\pi} a_q^k(\mathbf{j}) C(jkj, 000) C_{kq}^*(\theta_r, \varphi_r) \tag{4.21}$$

Please note that the same $a_q^k(\mathbf{j})$ moments feature in Eqs. (4.20) and (4.21). In the case of collisions involving molecules oriented or aligned by external fields [286], it is convenient to introduce $\mathbf{r}$-polarization moments $a_q^k(\mathbf{r})$, which are related to the $\mathbf{j}$-polarization moments $a_q^k(\mathbf{j})$ as:

$$a_q^k(\mathbf{r}) = a_q^k(\mathbf{j})C(jkj, 000) \qquad (4.22)$$

Semiclassical description of angular momentum polarisation combined with the QCT calculations was extensively used by Aoiz, de Miranda, and coworkers, and is described in detail in Refs. [162, 163, 164, 182].

5 The Fraunhofer model of molecular collisions

> Essentially, all models are wrong, but some are useful.
>
> George Box

The field-free Fraunhofer model was developed by Drozdov [193] and generalized by Blair [194] in the late 1950s to treat inelastic nuclear scattering. The model provided a much-sought explanation of the experimentally observed phase shifts between oscillations in the elastic and inelastic differential cross sections for the scattering of protons or α particles by medium-sized nuclei, later referred to as the "Blair phase rule." In 1984, the field-free Fraunhofer model was adapted by Faubel [195] to account for rotationally inelastic thermal collisions between helium atoms and N_2 and CH_4 molecules.

The Fraunhofer model relies on two approximations: (i) sudden approximation, that allows to express inelastic scattering amplitude in therms of the elastic one, and (ii) the elastic scattering amplitude is substituted by the amplitude of the Fraunhofer diffraction from a two-dimensional 'shadow' of the scatterer, as shown in Fig. 5.1. The Fraunhofer model takes into account only the sharp-edged hard-core part of the potential energy surface, comes close to the rigid shell approximation widely used in classical [287], [288, 289], [290], quantum [291], and quasi-quantum [276, 277, 278] treatments of field-free molecular collisions, where the collision energy by far exceeds the depth of any potential energy well. However, the Fraunhofer model is purely quantum and furnishes complex scattering amplitudes necessary to study quantum stereodynamics.
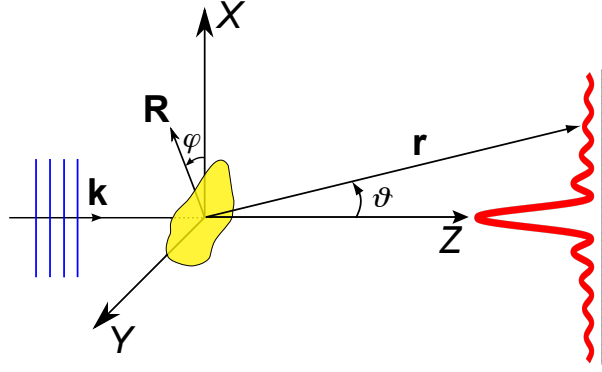
Figure 5.1: Schematic of Fraunhofer diffraction by an impenetrable, sharp-edged obstacle as observed at a point of radius vector $\mathbf{r}(X, Z)$ from the obstacle. Relevant is the shape of the obstacle in the XY plane, perpendicular to the initial wave vector, $\mathbf{k}$, itself directed along the Z-axis of the space-fixed system XYZ. The angle φ is the polar angle of the radius vector $\mathbf{R}$ which traces the shape of the obstacle in the X, Y plane and ϑ is the scattering angle. See text.

In optics, Fraunhofer (i.e. far-field) diffraction [292] occurs when the Fresnel number is small,

$$\mathscr{F} \equiv \frac{a^2}{r\lambda} \ll 1 \tag{5.1}$$

Here a is the dimension of the obstacle, $r \equiv |\mathbf{r}|$ is the distance from the obstacle to the observer, and λ is the wavelength, cf. Fig. 5.1. Condition (5.1) is well satisfied for nuclear scattering at MeV collision energies as well as for molecular collisions at thermal and hyperthermal energies. In the latter case, inequality (5.1) is fulfilled due to the compensation of the larger molecular size a by a larger de Broglie wavelength λ pertaining to thermal molecular velocities.

In this chapter we derive the equations involved in the Fraunhofer model for elastic and inelastic scattering and discuss the model limitations.

5.1 Formal theory for the elastic scattering

We consider a scattering target placed in the path of the beam described by a plane wave, $\exp{(i\mathbf{kr})}$, as sketched in Fig. 5.1. The wavefunction, which is the solution of

the Schrödinger equation with the scattering potential, has the asymptotic form:

$$\psi(\mathbf{r}) = e^{i\mathbf{k}\mathbf{r}} + \psi_{sc}(\mathbf{r}) \tag{5.2}$$

It consists of the transmitted plane wave and of the scattered wave, which is a diverging spherical wave:

$$\psi_{\text{sc}}(\mathbf{r}) = f(\theta, \phi)\frac{e^{ikr}}{r}, \tag{5.3}$$

with $f(\theta, \phi)$ the scattering amplitude [293]. Here and hereafter we use the notion of initial and final wavevectors, $\mathbf{k}$ and $\mathbf{k}'$, whose absolute values in the case of elastic scattering are equal to one another, $|\mathbf{k}| = |\mathbf{k}'| = k$.

On the other hand the wavefunction everywhere to the right of the absorber is completely specified by the value of the wavefunction and its derivative on a plane perpendicular to the beam placed immediately after the target. This connection is established via the free-space Green's function $g(\mathbf{r}_1, \mathbf{r}_2)$, which satisfies the differential equation:

$$(\nabla_1^2 + k^2)g(\mathbf{r}_1, \mathbf{r}_2) = \delta(\mathbf{r}_1 - \mathbf{r}_2), \tag{5.4}$$

where ∇_1^2 is the Laplace operator in the $\mathbf{r}_1$ coordinates, and $\delta(\mathbf{r}_1 - \mathbf{r}_2) \equiv \delta(x_1 - x_2)\delta(y_1 - y_2)\delta(z_1 - z_2)$ is the three-dimensional Dirac's delta-function. The free-space Green's function corresponding to an outgoing wave is:

$$g(\mathbf{r}_1, \mathbf{r}_2) = -\frac{1}{4\pi}\frac{e^{ik|\mathbf{r}_1 - \mathbf{r}_2|}}{|\mathbf{r}_1 - \mathbf{r}_2|} \tag{5.5}$$

Our goal to obtain the scattering wavefunction to the right from the obstacle, $\psi_{\text{sc}}(\mathbf{r_2})$, in terms of the wavefuncion on the plane perpendicular to the beam just after the obstacle, $\psi_{\text{sc}}(\mathbf{r_1})$. To do this, we multiply Eq. (5.4) by $\psi_{\text{sc}}(\mathbf{r_1})$ and integrate:

$$\int \mathbf{dr}_1 \psi_{\text{sc}}(\mathbf{r_1})(\nabla_1^2 + k^2)g(\mathbf{r}_1, \mathbf{r}_2) = \int \mathbf{dr}_1 \psi_{\text{sc}}(\mathbf{r_1})\delta(\mathbf{r}_1 - \mathbf{r}_2) \equiv \psi_{\text{sc}}(\mathbf{r_2}) \tag{5.6}$$

Analogously, we multiply by $g(\mathbf{r}_1, \mathbf{r}_2)$ and integrate the free-space Schrödinger

equation for $\psi_{sc}(\mathbf{r_1})$:

$$\int \mathbf{dr}_1 g(\mathbf{r}_1, \mathbf{r}_2)(\nabla_1^2 + k^2)\psi_{sc}(\mathbf{r_1}) = 0 \tag{5.7}$$

The difference between the two equations may be converted into a surface integral by means of the Gauss theorem:

$$\psi_{sc}(\mathbf{r_2}) = \int \mathbf{dr}_1 \left[\psi_{sc}(\mathbf{r_1})\nabla_1^2 g(\mathbf{r}_1, \mathbf{r}_2) - g(\mathbf{r}_1, \mathbf{r}_2)\nabla_1^2\psi_{sc}(\mathbf{r_1}) \right]$$
$$= \int dS_1 \left[\psi_{sc}(\mathbf{r_1})\mathbf{n}\boldsymbol{\nabla}_1 g(\mathbf{r}_1, \mathbf{r}_2) - g(\mathbf{r}_1, \mathbf{r}_2)\mathbf{n}\boldsymbol{\nabla}_1\psi_{sc}(\mathbf{r_1}) \right] \tag{5.8}$$

It is convenient to integrate over the surface of the semisphere, whose origin is chosen to be immediately after the scatterer and whose radius is much larger than both $\mathbf{r_2}$ and the scatterer dimensions, cf. Fig. 5.2. We can then use asymptotic forms for the scattering wavefunction and Green's function along the surface:

$$\psi_{sc}(\mathbf{r_1}) \to f(\theta_1, \phi_1)\frac{e^{ikr_1}}{r_1}, \tag{5.9}$$

and

$$g(\mathbf{r}_1, \mathbf{r}_2) \to -\frac{1}{4\pi}\frac{e^{ikr_1}}{r_1}e^{-ik(\mathbf{r}_1/r_1)\mathbf{r}_2} \tag{5.10}$$

In this case the two contributions to the surface integral cancel since the radial gradient of Eqs. (5.9) and (5.10) is the same. This means that $\psi_{sc}(\mathbf{r_2})$ is given solely by its value at the surface of the plane behind the scatterer.
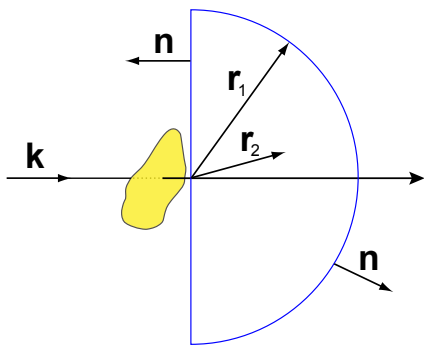
Figure 5.2: The semispherical surface used to evaluate the integral of Eq. (5.8)

We note that equation (5.8) for $\psi_{sc}(\mathbf{r_2})$ is an exact one. The Fraunhofer approximation is a result of the single assumption that $\mathbf{r_2} \gg \mathbf{r_1}$ for any point on the plane which gives a non-negligible contribution to the integral. This allows us to use the asymptotic form of the Green function (5.5)

in the integral along the plane:

$$g(\mathbf{r}_1, \mathbf{r}_2) \rightarrow -\frac{1}{4\pi}\frac{e^{ikr_2}}{r_2}e^{-i\mathbf{k}'\mathbf{r}_1} \tag{5.11}$$

Substituting (5.11) into (5.8) we obtain:

$$\psi_{\text{sc}}(\mathbf{r_2}) = \frac{e^{ikr_2}}{r_2}\left\{-\frac{1}{4\pi}\int_{\text{plane}}dS_1\left[\psi_{\text{sc}}(\mathbf{r_1})\mathbf{n}\boldsymbol{\nabla}_1 e^{-i\mathbf{k}'\mathbf{r}_1} - e^{-i\mathbf{k}'\mathbf{r}_1}\mathbf{n}\boldsymbol{\nabla}\psi_{\text{sc}}(\mathbf{r_1})\right]\right\}, \tag{5.12}$$

where the quantity in the curly brackets is by definition the scattering amplitude $f(\theta_2, \phi_2)$. We will use the convention in which $\mathbf{k}$ defines the space-fixed Z axis, and $\mathbf{k}'$ points in the direction of $\mathbf{r}_2$ lying in the XZ plane, i.e. $\mathbf{k}' \equiv k\mathbf{r}_2/r_2$. In this case the azimuthal scattering angle $\phi_2 = 0$ and we will denote the elastic scattering amplitude simply as $f(\vartheta)$.

To calculate the surface integral (5.12) we use $\psi_{sc}(\mathbf{r}_1)$ from Eq. (5.2)

$$\psi_{sc}(\mathbf{r}_1) = \psi(\mathbf{r}_1) - e^{i\mathbf{k}\mathbf{r}_1} \tag{5.13}$$

We assume that the obstacle is absolutely impenetrable, has sharp edges, and there is no diffraction near the edges. In this case $\psi(\mathbf{r}_1)$ coincides with a plane wave outside of the obstacle, and is zero within its 'shadow'. Consequently, $\psi_{sc}(\mathbf{r}_1)$ is zero everywhere on the plane, except in the shadow, where it equals $-e^{i\mathbf{k}\mathbf{r}_1}$. In this way the scattering occurs according to the Babinet principle: except for an overall change of phase, the scattering amplitude from a black absorber is equivalent to the amplitude resulting from an aperture of the same shape and size. Substituting (5.13) into (5.12) we obtain:

$$f(\vartheta) = \frac{1}{4\pi}\int_{\text{shadow}}dS_1\left\{(-\mathbf{n}i\mathbf{k}') - (\mathbf{n}i\mathbf{k})\right\}e^{-i\mathbf{k}'\mathbf{r}_1}$$
$$= \frac{ik}{4\pi}(1 + \cos\vartheta)\int_{\text{shadow}}dS_1 e^{-i\mathbf{k}'\mathbf{r}_1}, \tag{5.14}$$

since $\mathbf{n}$ points in the negative Z direction and $\mathbf{k} \perp \mathbf{r}_1$. We denote the two-dimensional coordinate in the plane of the obstacle by $\mathbf{R}$, with the shape of the shadow given by

$R(\varphi)$. For the scattering amplitude we obtain:

$$f(\vartheta) = \frac{ik}{4\pi}(1 + \cos\vartheta) \int_0^{2\pi} d\varphi \int_0^{R(\varphi)} e^{-ikR\sin\vartheta\cos\varphi} RdR \tag{5.15}$$

If we consider only the small-angle scattering, we can set $\sin\vartheta = \vartheta$ and $\cos\vartheta = 1$. Although this approximation looks quite rough, it does not lead to any significant errors even at $\vartheta = 90°$. The final expression for the Fraunhofer scattering amplitude reads:

$$f(\vartheta) = \frac{ik}{2\pi} \int_0^{2\pi} d\varphi \int_0^{R(\varphi)} e^{-ikR\vartheta\cos\varphi} RdR \tag{5.16}$$

We note that the Fraunhofer scattering amplitude, Eq. (5.16), is quite similar to the amplitude for Born scattering [293]. Either amplitude is a Fourier transform of the target's spatial characteristic – either its shape or its potential. Both the Fraunhofer and Born amplitudes comprise averages of the phase factor, $\exp(i\mathbf{kR})$, over the target's surface or volume [294].

We exemplify calculation of the elastic scattering amplitude by choosing an obstacle to be a black sphere/disk, characterized by the radius R_0. In this case Eq. (5.16) becomes:

$$f(\vartheta) = \frac{ik}{2\pi} \int_0^{R_0} RdR \int_0^{2\pi} d\varphi \; e^{-ikR\vartheta\cos\varphi} \tag{5.17}$$

The ntegral over ϕ amounts to the definition of the zero-order Bessel function [295]:

$$\int_0^{2\pi} d\varphi \; e^{-ikR\vartheta\cos\varphi} = 2\pi J_0(kR\vartheta) \tag{5.18}$$

The ntegral over R can be evaluated using the following property [295]:

$$\int dz' z' J_0(z') = z J_1(z), \tag{5.19}$$

which results in the following expression for the scattering amplitude for the black disk,

$$f_0(\vartheta) = i(kR_0^2)\frac{J_1(kR_0\vartheta)}{(kR_0\vartheta)} \tag{5.20}$$

5.2 The sudden approximation

The theoretical technique that allows to connect elastic and inelastic scattering is the energy *sudden approximation*. It is valid when the collision time is much smaller than the rotational period, as embodied by the inequality $\xi \ll 1$, where

$$\xi = \frac{\Delta E_{\mathrm{rot}} k R_0}{2 E_{\mathrm{coll}}} \approx \frac{B k R_0}{E_{\mathrm{coll}}}, \qquad (5.21)$$

is the Massey parameter, see e.g. Refs. [296],[297]. Here ΔE_{rot} is the rotational level spacing, B the rotational constant, E_{coll} the collision energy, $k \equiv (2mE_{\mathrm{coll}})^{1/2}/\hbar$ the wavenumber, m the reduced mass of the collision system,

and R_0 the radius of the scatterer. As a consequence, the actual scattering problem with non-degenerate energies can be replaced by one with degenerate levels, as shown in Fig. 5.3.

We assume every state to be the function of some internal coordinates, $\mathbf{r}_{\mathrm{int}}$. The statement that the collision time is much shorter than the rotational period means that the values of internal coordinates stay frozen during the collision. Since the internal coordinates do not change and there is no energy transfer, the scattering is characterized by an elastic scattering amplitude, $f_{\mathrm{el}}(\vartheta, \mathbf{r}_{\mathrm{int}})$, for a fixed value of $\mathbf{r}_{\mathrm{int}}$.
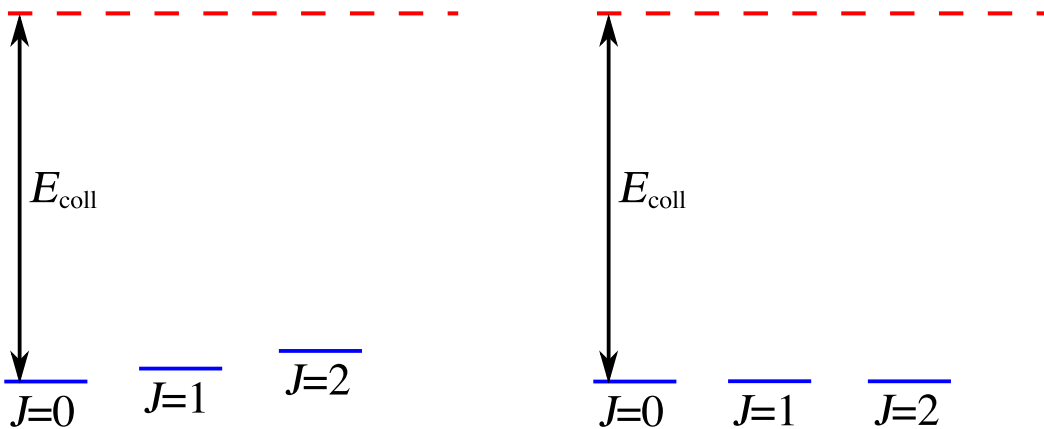

Figure 5.3: Replacing non-degenerate levels by degenerate ones, as a consequence of the sudden approximation.

Although different states are degenerate in energy, they still correspond to different internal coordinates, i.e. they have different wavefunctions. Therefore the scattering amplitude acting on the initial state $|\mathfrak{i}\rangle$, $f_{\text{el}}(\vartheta, \mathbf{r}_{\text{int}})|\mathfrak{i}(\mathbf{r}_{\text{int}})\rangle$, will project onto final states $|\mathfrak{f}\rangle$, which may differ from the initial state. This allows to represent the inelastic amplitude,

$$f_{\mathfrak{i}\to\mathfrak{f}}(\vartheta) = \langle\mathfrak{f}|f_{\text{el}}(\vartheta, \mathbf{r}_{\text{int}})|\mathfrak{i}\rangle, \tag{5.22}$$

for scattering into an angle ϑ from an initial, $|\mathfrak{i}\rangle$, to a final, $|\mathfrak{f}\rangle$, state in terms of the elastic scattering amplitude $f_{\text{el}}(\vartheta, \mathbf{r}_{\text{int}})$ at fixed values of the internal coordinates.

Eq. (5.22) can be rigorously derived within the Lippmann-Schwinger formalism as follows. The two-particle collision is driven by the Hamiltonian

$$H = T_{\text{kin}} + V(\mathbf{r}, \mathbf{r}_{\text{int}}) + H_0(\mathbf{r}_{\text{int}}), \tag{5.23}$$

where T_{kin} is the kinetic energy operator, $H_0(\mathbf{r}_{\text{int}})$ is the Hamiltonian of the internal states of the free collision partners, and $V(\mathbf{r}, \mathbf{r}_{\text{int}})$ is the interaction potential, which is both the function of internal coordinates $\mathbf{r}_{\text{int}}$ and of the distance and relative orientation $\mathbf{r}$ between the collision partners.

The formal expression for the transition amplitude from state $|\mathfrak{i}\rangle$ to state $|\mathfrak{f}\rangle$ is

$$f_{\mathfrak{i}\to\mathfrak{f}} = -\frac{2m}{4\pi\hbar^2}\left(\frac{k'}{k}\right)^{1/2}\langle\mathfrak{f}|\langle\mathbf{k}'|V + V\frac{1}{E - T - V - H_0(\mathbf{r}_{\text{int}}) + i\epsilon}V|\mathbf{k}\rangle|\mathfrak{i}\rangle, \tag{5.24}$$

with $1/(E - T - V - H_0(\mathbf{r}_{\text{int}}) + i\epsilon)$ the Green function of the intermediate state. The negligible change in internal coordinates during the collision is equivalent to omitting the $H_0(\mathbf{r}_{\text{int}})$ term in Eq. (5.24). However, the inner bracket expression $\langle\mathbf{k}'|\ldots|\mathbf{k}\rangle$ with $H_0(\mathbf{r}_{\text{int}}) = 0$ is by definition the elastic scattering amplitude, corresponding to fixed internal coordinates $\mathbf{r}_{\text{int}}$:

$$f_{\mathfrak{i}\to\mathfrak{f}} = -\frac{2m}{4\pi\hbar^2}\langle\mathfrak{f}|\langle\mathbf{k}'|V + V\frac{1}{E - T - V + i\epsilon}V|\mathbf{k}\rangle|\mathfrak{i}\rangle \equiv \langle\mathfrak{f}|f_{\text{el}}(\mathbf{k}', \mathbf{k}, \mathbf{r}_{\text{int}})|\mathfrak{i}\rangle \tag{5.25}$$

Here we also considered the absolute values of $\mathbf{k}$ and $\mathbf{k}'$ to be equal.

5.3   The inelastic scattering amplitude

Now we will use Eq. (5.22) to calculate the scattering amplitude for non-spherical obstacles. As was shown in Sec. 5.1, the elastic scattering amplitude is given by:

$$f(\vartheta) \approx \int e^{-ikR\vartheta\cos\varphi} d\mathbf{R}, \tag{5.26}$$

where φ is the polar angle of the radius vector $\mathbf{R}$ which traces the shape of the obstacle, $R \equiv |\mathbf{R}|$, and $k \equiv |\mathbf{k}|$ with $\mathbf{k}$ the initial wave vector. Relevant is the shape of the obstacle in the space-fixed XY plane, perpendicular to $\mathbf{k}$, itself directed along the space-fixed Z axis, cf. Fig. 5.1.

We consider nearly-circular targets, with a boundary $R(\varphi) = R_0 + \delta(\varphi)$ in the XY plane, with the anisotropy parameter $\delta \ll R_0$. In this case the scattering amplitude reads:

$$f(\vartheta) = \frac{ik}{2\pi} \int_0^{2\pi} d\phi \int_0^{R_0+\delta(\phi)} e^{-ikR\vartheta\cos\varphi} R dR \tag{5.27}$$

The radial integral yields:

$$\int_0^{R(\varphi)} e^{ixR} R dR = \frac{R(\varphi)}{ix} e^{iR(\varphi)x} + \frac{1}{x^2}\left[e^{ixR(\varphi)} - 1\right], \tag{5.28}$$

where we set $x = -k\vartheta\cos\varphi$. If the deformation $\delta(\varphi)$ is small, we can expand integral (5.28) in its powers of:

$$
\begin{aligned}
\int_0^{R(\varphi)} e^{ixR} R dR &= \frac{R_0+\delta(\varphi)}{ix} e^{iR_0 x}\left(1 + i\delta(\varphi)x - \frac{\delta^2(\varphi)x^2}{2} + \cdots\right) \\
&\quad + \frac{1}{x^2}\left[e^{iR_0 x}\left(1 + i\delta(\varphi)x - \frac{\delta^2(\varphi)x^2}{2} + \cdots\right) - 1\right] \\
&= \frac{R_0\, e^{R_0 x}}{ix} + \frac{1}{x^2}\left[e^{iR_0 x} - 1\right] + \delta(\varphi)R_0 e^{iR_0 x} \\
&\quad + \delta^2(\varphi)\left[e^{iR_0 x}\left(-\frac{R_0 x}{2i} + 1\right) - \frac{e^{iR_0 x}}{2}\right] + \cdots
\end{aligned}
\tag{5.29}
$$

In such a way the Fraunhofer scattering amplitude, Eq. (5.26), can be evaluated and

expanded in a power series in the deformation $\delta(\varphi)$,

$$f(\vartheta) = f_0(\vartheta) + f_1(\vartheta, \delta) + f_2(\vartheta, \delta^2) + \cdots , \tag{5.30}$$

with $f_0(\vartheta)$ the amplitude for scattering by a disk of radius R_0, as given by Eq. (5.20),

$$f_0(\vartheta) = i(kR_0^2)\frac{J_1(kR_0\vartheta)}{(kR_0\vartheta)}, \tag{5.31}$$

$f_1(\vartheta)$ the lowest-order anisotropic amplitude,

$$f_1(\vartheta) = \frac{ik}{2\pi} \int_0^{2\pi} \delta(\varphi)e^{-i(kR_0\vartheta)\cos\varphi}d\varphi, \tag{5.32}$$

and $f_2(\vartheta)$ the second order anisotropic amplitude:

$$f_2(\vartheta) = \frac{ik}{4\pi} \int_0^{2\pi} \delta^2(\varphi)\left(1 - ikR_0\vartheta\cos\varphi\right)e^{-i(kR_0\vartheta)\cos\varphi}d\varphi$$
$$= \frac{ik}{4\pi}\left[1 + x\frac{d}{d(kR_0\vartheta)}\right] \int_0^{2\pi} \delta^2(\varphi)e^{-i(kR_0\vartheta)\cos\varphi}d\varphi \tag{5.33}$$

In our model we employ only the first-order anisotropic amplitude $f_1(\vartheta)$; the second-order contribution (5.33) is given for reference purposes.

A key step required to maintain the analyticity of the Fraunhofer scattering amplitude, Eq. (5.32), is to present the shape of the atom-molecule potential in terms of a series in spherical harmonics,

$$R'(\theta', \phi') = \sum_{\kappa\nu} \Xi_{\kappa\nu}Y_{\kappa\nu}(\theta', \varphi'), \tag{5.34}$$

with $\Xi_{\kappa\nu}$ the Legendre moments. The polar and azimuthal angles θ' and φ' pertain to the body-fixed frame, defined, e.g., by the target's principal axes of inertia. However, what matters is the target's shape in the space fixed frame, see Fig. 5.1, which is given by

$$R(\alpha, \beta, \gamma; \theta, \varphi) = \sum_{\kappa\nu\rho} \Xi_{\kappa\nu}\mathscr{D}_{\rho\nu}^{\kappa}(\alpha\beta\gamma)Y_{\kappa\rho}(\theta, \varphi), \tag{5.35}$$

where (α, β, γ) are the Euler angles through which the body-fixed frame is rotated relative to the space-fixed frame, (θ, φ) are the polar and azimuthal angles in the space-fixed frame, and $\mathscr{D}^\kappa_{\rho\nu}(\alpha\beta\gamma)$ are the Wigner rotation matrices. We note that Blair [194] and Faubel [195] used the wrong rotation direction of Edmonds [298] (active vs. passive rotations). Here we use the correct convention, as, e.g. in Refs. [283, 284]. The term with $\nu = 0$ corresponds to a disk of radius R_0,

$$R_0 \approx \frac{\Xi_{00}}{\sqrt{4\pi}} \tag{5.36}$$

Since of relevance is the shape of the target in the XY plane, we set $\theta = \frac{\pi}{2}$ in Eq. (5.35). As a result,

$$\delta(\varphi) = R(\alpha, \beta, \gamma; \tfrac{\pi}{2}, \varphi) - R_0 = R(\varphi) - R_0 = \sum_{\substack{\kappa\nu\rho \\ \kappa \neq 0}} \Xi_{\kappa\nu} \mathscr{D}^\kappa_{\rho\nu}(\alpha\beta\gamma) Y_{\kappa\rho}(\tfrac{\pi}{2}, \varphi) \tag{5.37}$$

To calculate the integral (5.32) using Eq. (5.37), we use the expression for spherical harmonics at fixed $\theta = \pi/2$ [284]:

$$Y_{\kappa\rho} = \begin{cases} (-1)^{\frac{\kappa+\rho}{2}} e^{i\rho\varphi} \left(\frac{2\kappa+1}{4\pi}\right)^{\frac{1}{2}} \frac{[(\kappa+\rho)!(\kappa-\rho)!]^{\frac{1}{2}}}{(\kappa+\rho)!!(\kappa-\rho)!!} & \text{for } \kappa + \rho \text{ even} \\[2em] 0 & \text{otherwise} \end{cases} \tag{5.38}$$

And the integral representation of the Bessel function [295]:

$$\int_0^{2\pi} \cos(\rho\varphi) e^{-i(kR_0\vartheta)\cos\varphi} d\varphi = 2\pi(-i)^\rho J_\rho(kR_0\vartheta), \quad \text{for } \rho \geq 0 \tag{5.39}$$

In such a way we obtain the following expression for the first-order scattering amplitude:

$$f_1(\alpha, \beta, \gamma; \vartheta) = \frac{ikR_0}{2\pi} \sum_{\substack{\kappa\nu\rho \\ \kappa \neq 0}} \Xi_{\kappa\nu} \mathscr{D}^\kappa_{\rho\nu}(\alpha\beta\gamma) F_{\kappa\rho} J_{|\rho|}(kR_0\vartheta) \tag{5.40}$$

with the coefficient $F_{\kappa\rho}$ defined by

$$
F_{\kappa\rho} =
\begin{cases}
(-1)^\rho 2\pi \left(\frac{2\kappa+1}{4\pi}\right)^{\frac{1}{2}} (-i)^\kappa \frac{[(\kappa+\rho)!(\kappa-\rho)!]^{\frac{1}{2}}}{(\kappa+\rho)!!(\kappa-\rho)!!} & \text{for } \kappa + \rho \text{ even and } \kappa \geq \rho \\
\\
0 & \text{otherwise}
\end{cases}
\tag{5.41}
$$

For negative values of ρ, the factor $(-i)^\kappa$ is to be replaced by i^κ. Finally, by making use of Eq. (5.22), we obtain the inelastic scattering amplitude as

$$
f_{i\to f}(\vartheta) \approx \langle f|f_0 + f_1|i\rangle = \langle f|f_1|i\rangle = \frac{ikR_0}{2\pi} \sum_{\substack{\kappa\nu\rho \\ \kappa\neq 0 \\ \kappa+\rho \text{ even}}} \Xi_{\kappa\nu}\langle f|\mathscr{D}^\kappa_{\rho\nu}|i\rangle F_{\kappa\rho} J_{|\rho|}(kR_0\vartheta)
\tag{5.42}
$$

6 The Fraunhofer model of vector correlations

> Although this may seem a paradox, all exact
> science is dominated by the idea of approxima-
> tion.
>
> Bertrand Russell

Measurements and exact calculations of vector correlations allow to extract directional information on the angular momentum disposal, and thereby to obtain a complete information on *how* a given collision proceeds [66, 163, 164, 165]. However, even when characterized to the full by vector correlations, the *why* of collision dynamics can only be answered as well as the theoretical method applied to treat the collision allows [26, 179, 183]. Therefore, to understand the results of experiments and exact computations one needs to develop simple models, that allow to decompose a complicated scattering problem into smaller parts and figure out which of those govern the collision dynamics.

In this thesis we implement an analytic model of collision dynamics, capable of answering the *why* for a class of collisions in detail, and use it to develop an analytic model of vector correlations in such collisions [200, 201]. The collision model is based on the Fraunhofer scattering of matter waves [193, 194, 195] and is discussed in detail in Chapter 5. In short, the Fraunhofer model relies on the sudden approximation, which treats the rotational motion as frozen during the collision and thereby allows to replace the inelastic scattering amplitude with the elastic one. The elastic scattering amplitude itself is approximated by the amplitude for Fraunhofer diffraction of matter waves from a sharp-edged, impenetrable obstacle acting in place of the molecular scatterer

and captures forward scattering. At collision energies of hundreds of cm^{-1}, consistent with the sudden approximation, the shape of the scatterer is approximated by the repulsive core of the atom–molecule potential, with the attractive part disregarded. The Fraunhofer model renders fully state- and energy-resolved scattering amplitudes and all the quantities that unfold from them in analytic form. In this chapter we discuss the advantages and drawbacks of the Fraunhofer model of vector correlations.

In contrast to the widely used hard-shell models (cf. Sec. 3.2.3), the Fraunhofer model is entirely quantum and furnishes complex scattering amplitudes. With a realistic molecular wavefunction as an input, the model is able to account for the electronic state and quite involved energy level structure that some open-shell molecules have due to spin-rotation, spin-orbit, and spin-spin interactions. The model has no fitting parameters and is very simple, but only accounts for diffractive contributions to molecular scattering. In this way, a comparison of model results with exact theory and experiment allowed us to demonstrate that diffraction of matter waves from the 2D 'shadow' of the potential completely governs the stereodynamics of Ar–NO($X^2\Pi$) and He–NO($X^2\Pi$) collisions, see Chapters 10 and 11. On the other hand, analyzing discrepancies between model and exact results immediately reveals the effects originating from the breakdown of the sudden approximation, non-diffractive contributions to scattering, and the effect of the long-range branch of the potential. While the sudden approximation works better, and the effect of the attractive part of the PES becomes weaker at higher energies, the non-diffractive contributions to scattering don't vary much, since the 'hard egg' size and shape don't change drastically with the collision energy. Looking into the behavior of model and exact polarization moments at different collision energies allowed us to demonstrate the breakdown of the sudden approximation for Ne–NO($A^2\Sigma$) collisions at 470 cm^{-1}, see Chapter 12.

In optics, the diffractive oscillations scale with the size of the slit and the wavelength of light. The Fraunhofer differential cross sections and alignment moments originate completely from diffraction of matter waves, and so also scale with R_0/λ, where R_0 is the molecular size, and λ is the de Broglie wavelength. On the other hand,

the alignment moments coming from experiment or exact computations at different scattering energies do not coincide completely upon scaling, and the difference between those reveals the non-diffractive contribution to scattering.

Since, within the Fraunhofer model, the scatterer is two-dimensional, the model can only account for even-k (alignment) polarization moments with even q [200, 201]. The "extra symmetry" of the model causes odd-k (orientation) moments as well as odd-q alignment moments to vanish.

Interaction of open-shell molecules, such as $OH(X^2\Pi)$, with closed-shell atoms is described by two potential surfaces, corresponding to two projections of molecular electronic angular momentum onto the collision plane. Usually those potential energy surfaces are combined into a half-sum, V_{sum}, and half-difference, V_{diff}, potentials. In this case the former accounts for spin-conserving collisions, whereas the latter is responsible for the change of the spin state. The Fraunhofer model is able to account only for the V_{sum} potential, and is therefore limited to spin-conserving collisions. Comparing model and exact results allows to reveal the role of the electron spin for spin-conserved and parity-resolved channels.

7 Differential cross sections: the $\mathbf{k} - \mathbf{k}'$ vector correlation

> An ounce of action is worth a ton of theory.
>
> Friedrich Engels

7.1 Scattering of $^2\Pi$ molecules by closed-shell atoms

To exemplify the $\mathbf{k} - \mathbf{k}'$ vector correlation we consider a symmetric top-equivalent linear polar molecule, such as OH($^2\Pi$) or NO($^2\Pi$), colliding with a closed-shell atom, such as Ar or He. We treat the molecule as a pure Hund's case (a) species, characterized by a non-zero projection, Ω, of the electronic angular momentum on the molecular axis, whose definite-parity rotational wavefunction is given by

$$|j, m, |\Omega|, \epsilon\rangle = \frac{1}{\sqrt{2}}\left[|j, m, |\Omega|\rangle + \epsilon|j, m, -|\Omega|\rangle\right], \tag{7.1}$$

where the symmetry index ϵ distinguishes between the members of a given Ω doublet. The symmetry index takes the value of $+1$ for e levels and of -1 for f levels. The parity of the wave function is given by $\epsilon(-1)^{j-\frac{1}{2}}$ [299].

Interaction of a $^2\Pi$ molecule with a closed-shell atom is described by two potential energy surfaces, A' and A'', corresponding to two different orientations of molecules electronic angular momentum relatively to the collision plane [300]. For convenience the interaction is usually described by half-sum and half-difference of these potentials, V_{sum} and V_{diff}. While V_{sum} drives the inelastic scattering within the same spin-orbit manifold, $\Omega' = \Omega$, the difference potential V_{diff} is responsible for spin-changing collisions,

with $\Omega' \neq \Omega$. Since the Fraunhofer model is based on a single potential curve, V_{sum}, in this Chapter we focus only on the spin-conserving collisions. We consider a $^2\Pi$ molecule to be initially in the $\epsilon = -1(f)$ parity state,

$$|\mathfrak{i}\rangle = \frac{1}{\sqrt{2}}\left[|j, m, |\Omega|\rangle - |j, m, -|\Omega|\rangle\right], \tag{7.2}$$

and the final state of either e or f parity:

$$\langle\mathfrak{f}| = \frac{1}{\sqrt{2}}\left[\langle j', m', |\Omega|| + \epsilon'\langle j', m', -|\Omega||\right], \tag{7.3}$$

with the symmetric top wavefunctions given by Wigner rotation matrices:

$$|j, m, \Omega\rangle = \sqrt{\frac{2j + 1}{4\pi}}\mathscr{D}_{m\Omega}^{j*}(\varphi, \theta, \gamma = 0) \tag{7.4}$$

Substituting Eqs. (7.2), (7.3), and (7.4) into Eq. (5.42) we obtain the Fraunhofer scattering amplitude:

$$f_{\mathfrak{i}\to\mathfrak{f}}(\vartheta) = \frac{ikR_0}{4\pi}\sqrt{\frac{2j + 1}{2j' + 1}}J_{|\Delta m|}(kR_0\vartheta)$$

$$\times \sum_{\substack{\kappa \neq 0 \\ \kappa + \Delta m \text{ even}}} \Xi_{\kappa 0}F_{\kappa,\Delta m}C(j\kappa j'; m\Delta mm')C(j\kappa j'; |\Omega|0|\Omega|)\left\{\begin{array}{c}\left[(-1)^\kappa - (-1)^{\Delta j}\right] \\ \\ \left[(-1)^\kappa + (-1)^{\Delta j}\right]\end{array}\right\}, \tag{7.5}$$

where the first or second row of the expression in the curly brackets corresponds to a final state of, respectively, e or f parity. We note that within the Fraunhofer model $e \to e$ and $f \to f$ scattering amplitudes are equal to each other (so are $f \to e$ and $e \to f$ ones). Therefore Eq. (7.12) can be employed to molecules in the initial e-state.

7.2   Effect of an electrostatic field

The rotational states of a Hund's case (a) molecule with $j > 0$ and $m > 0$ can be oriented by coupling the opposite-parity members of an Ω doublet via the electric-dipole interaction. Such a coupling creates *precessing states*, in which the body-fixed electric dipole moment $\boldsymbol{\mu}$ precesses about the field vector. As a result, molecular rotation does not average out the dipole moment in first order. A precessing state is a hybrid of the two opposite-parity members of an Ω-doublet, and can be written as

$$|j, m, |\Omega|, w\rangle = \alpha(w)|j, m, |\Omega|, \epsilon = -1\rangle + \beta(w)|j, m, |\Omega|, \epsilon = 1\rangle, \qquad (7.6)$$

with $w \equiv \mu\varepsilon/\Delta$ an interaction parameter which measures the maximum potential energy of the electric dipole in terms of the Ω-doublet splitting, Δ, for $j = |\Omega|$. For a precessing state with $w \gg 1$, the coefficients $|\alpha(w)| = |\beta(w)| = 2^{-\frac{1}{2}}$, and the mixing of the states within an Ω doublet is perfect. A less perfect mixing, $|\alpha(w)| \neq |\beta(w)|$, obtains when $w \leq 1$. The wavefunction, Eq. (7.6), reduces for a precessing state with a perfect mixing to $|j, m, |\Omega|\rangle$. It is the inherent orientation of the precessing states along with their mixed parity that enters the Fraunhofer model for the scattering of Hund's case (a) molecules in an electric field. The directionality of the precessing states is illustrated in Figure 7.1. We assume the hybridization of j-states for a symmetric-top state to be negligible.

To account for an arbitrary direction of the electric field with respect to the initial wave vector $\mathbf{k}$, we introduce a field-fixed coordinate system $X^\sharp Y^\sharp Z^\sharp$, whose $Z^\sharp$-axis is defined by the direction of the electric field vector $\boldsymbol{\varepsilon}$. The symmetric top states are thus given by Wigner rotation matrices whose arguments are the angles $(\varphi^\sharp, \theta^\sharp, \gamma^\sharp)$ in the field-fixed frame:

$$|j, m, \Omega\rangle = \sqrt{\frac{2j+1}{4\pi}} \mathscr{D}^{j*}_{m\Omega}(\varphi^\sharp, \theta^\sharp, \gamma^\sharp = 0) \qquad (7.7)$$

In order to be able to apply Eq. (5.42) to collisions in the electrostatic field, we have
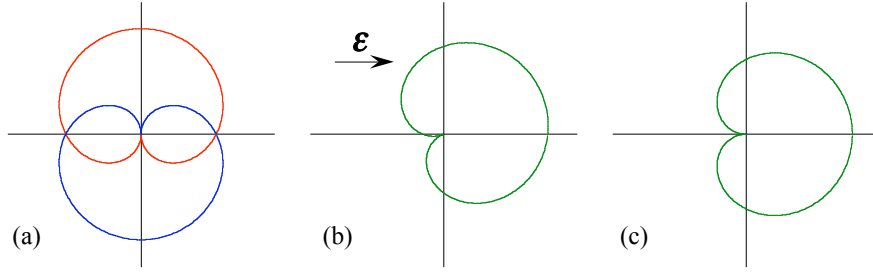
Figure 7.1: The moduli of the symmetric-top wavefunction for $j = m = \Omega = \frac{1}{2}$. Panel (a) shows the field-free wavefunctions, Eq. (7.1), for $\epsilon = 1$ (blue line) and $\epsilon = -1$ (red line). Panels (b) and (c) show the wavefunctions of the precessing states in the field, Eq. (7.6), for, respectively, an incomplete ($\alpha = 0.832$, $\beta = 0.555$) and perfect ($\alpha = \beta = \frac{1}{\sqrt{2}}$) mixing of the Ω doublet states. See text.

to transform Eq. (8.1) to the space-fixed frame XYZ. If the electric field vector is specified by the Euler angles $(\varphi_\varepsilon, \theta_\varepsilon, 0)$ in the XYZ frame, the symmetric top states take the form

$$\mathscr{D}^{j*}_{m\Omega}(\varphi^\sharp, \theta^\sharp, 0) = \sum_\xi \mathscr{D}^{j}_{\xi m}(\varphi_\varepsilon, \theta_\varepsilon, 0) \mathscr{D}^{j*}_{\xi\Omega}(\varphi, \theta, 0) \tag{7.8}$$

For transitions with $|\Omega| = |\Omega'|$, the initial and final precessing states can, therefore, be written as

$$|\mathfrak{i}\rangle = \sqrt{\frac{2j+1}{4\pi}} \sum_\xi \mathscr{D}^{j}_{\xi m}(\varphi_\varepsilon, \theta_\varepsilon, 0) \frac{1}{\sqrt{2}} \left\{ [\alpha(w) + \beta(w)] \, \mathscr{D}^{j*}_{\xi|\Omega|}(\varphi, \theta, 0) \right.$$
$$\left. + [-\alpha(w) + \beta(w)] \, \mathscr{D}^{j*}_{\xi-|\Omega|}(\varphi, \theta, 0) \right\}, \quad (7.9)$$

$$\langle \mathfrak{f}| = \sqrt{\frac{2j'+1}{4\pi}} \sum_{\xi'} \mathscr{D}^{j'*}_{\xi' m'}(\varphi_\varepsilon, \theta_\varepsilon, 0) \frac{1}{\sqrt{2}} \left\{ [\alpha'(w) + \beta'(w)] \, \mathscr{D}^{j'}_{\xi'|\Omega|}(\varphi, \theta, 0) \right.$$
$$\left. + [-\alpha'(w) + \beta'(w)] \, \mathscr{D}^{j'}_{\xi'-|\Omega|}(\varphi, \theta, 0) \right\} \quad (7.10)$$

By substituting from Eqs. (7.9) and (7.10) into Eq. (5.42), we finally obtain the scattering amplitude for inelastic collisions of symmetric-top molecules in precessing

states:

$$f_{i \to f}^w(\vartheta) = \frac{ikR_0}{4\pi} \sqrt{\frac{2j+1}{2j'+1}} \sum_{\substack{\kappa\rho \\ \kappa \neq 0 \\ \kappa+\rho \text{ even}}} \mathscr{D}_{-\rho,\Delta m}^{\kappa *}(\varphi_\varepsilon, \theta_\varepsilon, 0) \Xi_{\kappa 0} F_{\kappa\rho} J_{|\rho|}(kR_0\vartheta)$$

$$\times C(j\kappa j'; |\Omega|0|\Omega|) C(j\kappa j'; m\Delta m m') \left\{ [\alpha(w)\alpha'(w) + \beta(w)\beta'(w)] \left[(-1)^\kappa + (-1)^{\Delta j} \right] \right.$$

$$\left. + [\alpha(w)\beta'(w) + \alpha'(w)\beta(w)] \left[(-1)^\kappa - (-1)^{\Delta j} \right] \right\} \quad (7.11)$$

We note that if both the initial and final precessing states are perfectly mixed, the term in the curly brackets of Eq. (7.11) reduces to $2(-1)^\kappa$. The scattering amplitudes for different orientations of the electrostatic field ε with respect to the initial wave vector $\mathbf{k}$ are obtained from Eq. (7.11) by substituting the appropriate values of the angles: $\theta_\varepsilon = 0; \varphi_\varepsilon = 0$ for $\varepsilon \parallel \mathbf{k}$, and $\theta_\varepsilon = \frac{\pi}{2}; \varphi_\varepsilon = 0$ for $\varepsilon \perp \mathbf{k}$. Eq. (7.11) implies that the integral cross-sections, cf. Eqs. (8.14), for $j \to j'$ transitions are the same in the parallel and perpendicular fields. However, the partial integral cross sections for $j, m \to j', m'$ transitions do depend on whether the field is parallel or perpendicular to $\mathbf{k}$.

7.3 Scattering cross sections

We now consider the excitation of $NO(j = |\Omega| = \frac{1}{2}, f \to j', |\Omega|, e/f)$ by collisions with Ar, under conditions similar to those defined in Refs. [301, 302, 303, 304]: a hexapole state selector selects the $\epsilon = -1(f)$ state, Eq. (7.1), which adiabatically evolves into a partially oriented state, Eq. (7.6), when the collision system enters the electric field. The electric field of 16 kV/cm, directed parallel to the initial wave vector, $\varepsilon \parallel \mathbf{k}$, creates a precessing state, Eq. (7.6), whose hybridization coefficients are $\alpha = 0.832$ and $\beta = 0.555$. Next, a collision with an Ar atom excites the NO molecule to a final, field-free state, $|j', m', |\Omega|, \epsilon'\rangle$. The final, excited state is considered to be exempt from any effects of the electric field, as its Ω-doubling is large and hence $w < 1$. As a result,

$\beta'(w) = 1$ or $\alpha'(w) = 1$ for a final state of e or f parity, respectively. For a collision so defined, the scattering amplitude, Eq. (7.11) for $\boldsymbol{\varepsilon} \parallel \mathbf{k}$, takes the form:

$$
\begin{aligned}
f_{\mathrm{i} \to \mathrm{f}}^{w,\parallel}(\vartheta) = \frac{ikR_0}{4\pi} &\sqrt{\frac{2}{2j'+1}} J_{|\Delta m|}(kR_0\vartheta) \\
&\times \sum_{\substack{\kappa \neq 0 \\ \kappa + \Delta m \text{ even}}} \Xi_{\kappa 0} F_{\kappa,\Delta m} C(j\kappa j'; m\Delta m m') C(j\kappa j'; |\Omega|0|\Omega|) \\
&\times \left\{ \begin{array}{l} \beta(w)\left[(-1)^\kappa + (-1)^{\Delta j}\right] + \alpha(w)\left[(-1)^\kappa - (-1)^{\Delta j}\right] \\[2ex] \alpha(w)\left[(-1)^\kappa + (-1)^{\Delta j}\right] + \beta(w)\left[(-1)^\kappa - (-1)^{\Delta j}\right] \end{array} \right\},
\end{aligned} \tag{7.12}
$$

where the first or second row of the expression in the curly brackets corresponds to a final state of, respectively, e or f parity. The coefficients $\Xi_{\kappa 0}$ of the Ar-NO interaction potential, extracted from the data of Sumiyoshi *et al.* [305], are listed in Table 8.1 of the next Chapter. According to Ref. [305], the Ar-NO potential surface exhibits a global minimum of -115.4 cm^{-1} and, thus, the Fraunhofer model should be valid at collision energies $E_{\mathrm{coll}} > 400$ cm^{-1}. In Refs. [276, 277], the rigid shell QQT model was also used at these energies.

The state-to-state integral cross sections for spin-conserving collisions ($|\Omega'| = |\Omega| = \frac{1}{2}$) at a collision energy of 442 cm^{-1} are shown in Fig. 7.2, along with the close coupling calculations of Refs. [301, 302] and [303]. The analytic Fraunhofer model provides a simple interpretation of the features exhibited by the cross sections. First, let us consider the field-free case for an initial f state, i.e., for $\alpha(w = 0) = 1$ and $\beta(w = 0) = 0$ which corresponds to the scattering amplitude,

$$
\begin{aligned}
f_{\mathrm{i} \to \mathrm{f}}^{w=0}(\vartheta) \sim \; &J_{|\Delta m|}(kR_0\vartheta) \\
&\times \sum_{\substack{\kappa \neq 0 \\ \kappa + \Delta m \text{ even}}} \Xi_{\kappa 0} F_{\kappa,\Delta m} C(j\kappa j'; m\Delta m m') C(j\kappa j'; |\Omega|0|\Omega|) \left\{ \begin{array}{l} \left[(-1)^\kappa - (-1)^{\Delta j}\right] \\[2ex] \left[(-1)^\kappa + (-1)^{\Delta j}\right] \end{array} \right\}
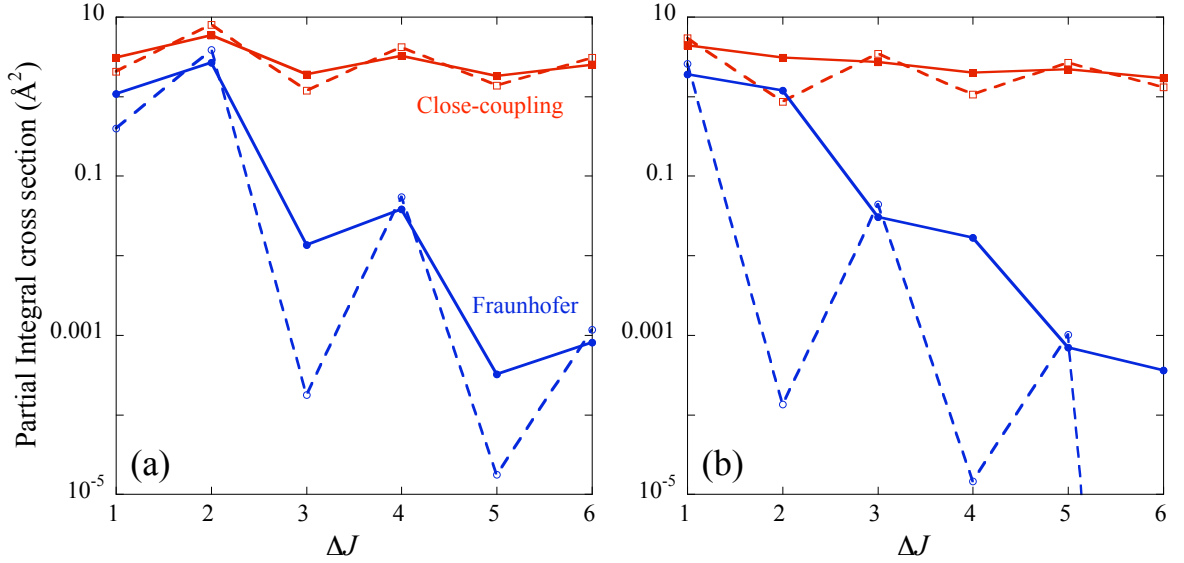\end{aligned}
$$

$$\tag{7.13}$$

Figure 7.2: Integral cross sections for the excitation of $NO(j = |\Omega| = \frac{1}{2}, f)$ in collisions with Ar to higher rotational levels of the $|\Omega| = \frac{1}{2}$ manifold. Panels (a) and (b) pertain, respectively, to parity-conserving and parity-breaking Ar-NO collisions. The results obtained from the Fraunhofer model are shown by blue curves, those obtained from the close-coupling calculations of Ref. [303] by red curves. Dashed lines pertain to field-free scattering, solid lines to scattering in an electric field $\varepsilon = 16$ kV/cm.

Eq. (7.13) immediately reveals that if the potential energy surface is governed by terms with κ even, parity-conserving transitions, $f \to f$, will dominate for Δj even, while parity-changing transitions, $f \to e$, will dominate for Δj odd. This propensity can be seen in Fig. 7.2. It was explained previously in Ref. [306] by a rather involved analysis of the close-coupling matrix elements.

The qualitative features of the scattering in an electric field can also be readily explained by the Fraunhofer model. If the field is present and the target molecule oriented, both even and odd Δj's in the curly brackets of Eq. (7.12) contribute to the scattering for any value of κ. For a potential energy surface governed by even-κ terms, the electric field will enhance the parity-conserving transitions for Δj odd, and suppress them for Δj even; parity-breaking collisions will prevail for Δj even and subside for Δj odd.
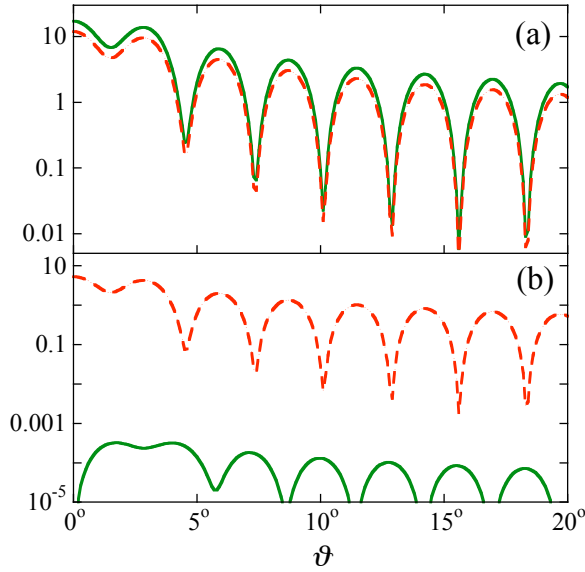
Figure 7.3: Differential cross sections for the excitation of $NO(j = |\Omega| = \frac{1}{2}, f)$ in collisions with Ar to the $j' = \frac{5}{2}, \Omega = \frac{1}{2}$ state. Panels (a) and (b) pertain, respectively, to parity-conserving and parity-breaking Ar-NO collisions. Green lines pertain to field-free scattering, red lines to scattering in an electric field $\varepsilon = 16$ kV/cm.

From Fig. 7.2 one could see that for $\Delta j > 2$ the Fraunhofer model yields an integral cross section which is significantly smaller than the one obtained from a close-coupling calculation. This is supported by the work of Aoiz *et al.* [307], who found that the diffractive contribution to the differential cross sections of Ar-NO collisions is much greater for $\Delta j = 2$ than for $\Delta j = 3$.

Eqs. (7.12) and (7.13) also reveal the angular dependence of the scattering. In particular, by making use of the asymptotic forms of the Bessel functions [295], we see that for a potential energy surface governed either by even- or odd-κ terms, the differential cross sections for parity-conserving and parity-breaking transitions will be out of phase.

This is illustrated for scattering from $|j = \frac{1}{2}, |\Omega| = \frac{1}{2}, f\rangle$ to $|j' = \frac{5}{2}, |\Omega| = \frac{1}{2}, e/f\rangle$ states in Fig. 7.3 (full curves). We also note that the parity-breaking cross section is much smaller than the parity-conserving one, since the Ar–NO potential is dominated by even κ-terms, cf. Table 8.1. When the field is on, the initial parity is no longer defined. Moreover, both even and odd Bessel functions $J_{|\rho|}(kR_0\vartheta)$ contribute to the cross section. As a result, the differential cross sections corresponding to the final e and f states (dashed curves) become similar to one another.

We see that the field-free differential cross sections, presented in Fig. 7.3, are qualitatively similar to the results of close-coupling calculations presented in Fig. 4 of Ref. [308], which also show a phase shift between parity-changing and parity conserving cross sections. When the field is turned on, the close coupling calculations

also reveal that the cross sections corresponding to final e-states exhibit a phase shift and become similar to the cross sections for the final f-states, see Fig. 8 of Ref. [308].

Since the Fraunhofer model accounts only for small-angle scattering, it leads to integral cross sections much smaller than in exact calculations, see Fig. 7.2. Nevertheless, model cross sections and their field-dependence are in qualitative agreement with exact results.

8 Collisions of closed-shell molecules with closed-shell atoms in electric fields

> It can change as much as it likes. As long as it stays the same.
>
> Adrian Mourby

In this chapter we study collisions of closed-shell atoms with closed-shell molecules in electrostatic and laser fields, using the Fraunhofer scattering model described in Chapter 5. While an electrostatic field orients a polar molecule in the space fixed frame, a nonresonant laser field aligns the molecular axis due to induced-dipole interaction. In both cases the effective shape of the molecular target alters in the scattering frame, resulting in changes in magnitude and shape of the differential cross sections. On the other hand, an electrostatic or radiative field hybridizes rotational states of a molecule, affecting the collision dynamics: some of the selection rules become relaxed in a field. We exemplify our theory with collisions of Ne with $\text{OCS}(X^1\Sigma)$, and of Na^+ ion with $\text{N}_2(X^1\Sigma)$.

8.1 Collisions of $^1\Sigma$ molecules with ^1S atoms in an electrostatic field

When a polar $^1\Sigma$ molecule enters an electrostatic field, its rotational states undergo *hybridization* (coherent linear superposition), induced by the interaction of the molecule's

body-fixed electric dipole moment, $\boldsymbol{\mu}$, with the electric field, $\boldsymbol{\varepsilon}$ [115], [116]. Because of the cylindrical symmetry about the electric field vector, the permanent-dipole interaction couples free-rotor basis states, $|j, m\rangle$, with a fixed value of the good quantum number, m, but a range of j's. Thus the hybrid wavefunctions take the general form

$$|\tilde{j}, m, \omega\rangle = \sum_j a_{jm}^{\tilde{j}}(\omega)|j, m\rangle, \tag{8.1}$$

where the expansion coefficients $a_{jm}^{\tilde{j}}$ depend solely on a dimensionless interaction parameter,

$$\omega \equiv \mu\varepsilon/B, \tag{8.2}$$

which measures the maximum potential energy, $\mu\varepsilon$, of the dipole in terms of the molecule's rotational constant, B. The symbol $\tilde{j}$ denotes the nominal value of j that pertains to the field-free rotational state which adiabatically correlates with the hybrid state,

$$|\tilde{j}, m, \omega \to 0\rangle \to |j, m\rangle, \tag{8.3}$$

and $\mu \equiv |\boldsymbol{\mu}|$, $\varepsilon \equiv |\boldsymbol{\varepsilon}|$.

The free-rotor states in the field-fixed coordinate system $X^\sharp Y^\sharp Z^\sharp$ are thus given by spherical harmonics whose arguments are the angles $\theta^\sharp$ and $\varphi^\sharp$ in the field-fixed frame,

$$|j, m\rangle = Y_{jm}(\theta^\sharp, \varphi^\sharp) \tag{8.4}$$

Apart from possessing a *sui generis* energy level pattern, the $|\tilde{j}, m, \omega\rangle$ eigenstates have an indefinite (mixed) parity and are directional, exhibiting a varying degree of orientation, which depends on the values of $\tilde{j}$, m, and ω. In the oriented states, the body-fixed dipole (and thus the internuclear axis) librates about the field direction like a pendulum, and so the hybrid states are referred to as *pendular*. It is the directionality of the pendular states along with their mixed parity that enters the field-dependent Fraunhofer model and distinguishes it from the field-free model, which assumes an
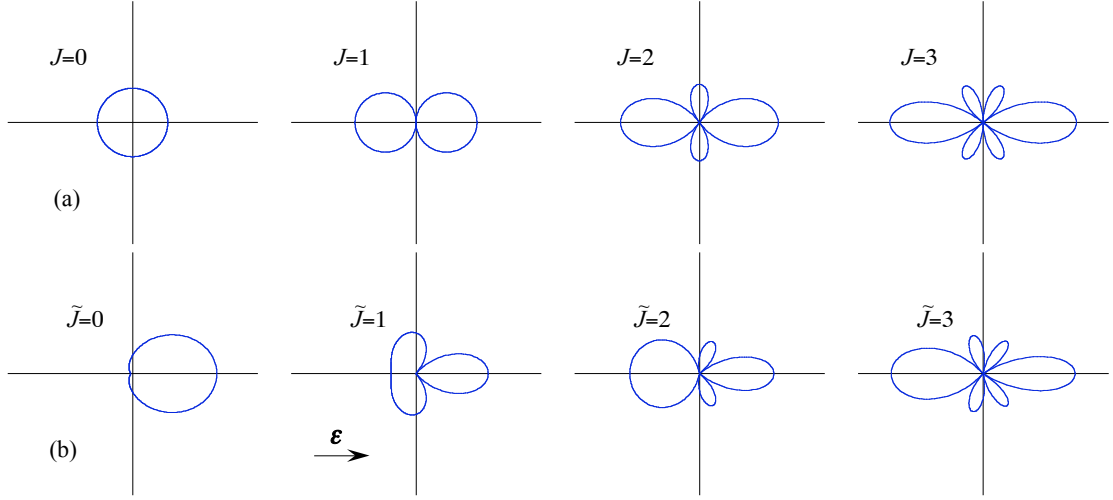
Figure 8.1: A comparison of the moduli of the free rotor wavefunctions $\big||j, m = 0\rangle\big|$, panel (a), with the moduli of the pendular wavefunctions $\big||\tilde{j}, m = 0, \omega = 5\rangle\big|$, panel (b). Also shown is the direction of the electric field vector, $\boldsymbol{\varepsilon}$.

isotropic distribution of the molecular axes and a definite parity. The directional properties of pendular states are exemplified in Fig. 8.1, which shows polar diagrams of the field-free and pendular wave functions at $\omega = 5$.

Hence the scattering process in the field comprises the following steps: A molecule in a free-rotor state $|j, m\rangle$ enters adiabatically the field where it is transformed into a pendular state $|\tilde{j}, m, \omega\rangle$. This pendular state may be changed by the collision in the field into another pendular state, $|\tilde{j'}, m', \omega\rangle$. As the molecule leaves the field, the latter pendular state is adiabatically transformed into a free-rotor state $|j', m'\rangle$. Thus the net result is, in general, a rotationally inelastic collision, $|j, m\rangle \to |j', m'\rangle$.

In order to be able to apply Eq. (5.42) to collisions in the electrostatic field, we transform Eq. (8.1) to the space-fixed frame XYZ. If the electric field vector is specified by the Euler angles $(\varphi_\varepsilon, \theta_\varepsilon, 0)$ in the XYZ frame, the initial and final pendular states take the form

$$|\mathfrak{i}\rangle \equiv |\tilde{j}, m, \omega\rangle = \sum_j a_{jm}^{\tilde{j}}(\omega) \sum_\xi \mathscr{D}_{\xi m}^{j}(\varphi_\varepsilon, \theta_\varepsilon, 0) Y_{j\xi}(\theta, \varphi), \tag{8.5}$$

$$\langle \mathfrak{f}| \equiv \langle \tilde{j'}, m', \omega| = \sum_{j'} b_{j'm'}^{\tilde{j'}*}(\omega) \sum_{\xi'} \mathscr{D}_{\xi' m'}^{j'*}(\varphi_\varepsilon, \theta_\varepsilon, 0) Y_{j'\xi'}^{*}(\theta, \varphi), \tag{8.6}$$

which is seen to depend solely on the angles θ and φ (and not the angles $\theta^\sharp$ and $\varphi^\sharp$ pertaining to the field-fixed frame).

On substituting from Eqs. (8.5) and (8.6) into Eq. (5.42) and its integration, we obtain a general expression for the Fraunhofer scattering amplitude in the field,

$$f_{i\to f}^{\omega}(\vartheta) = \frac{ikR_0}{2\pi} \sum_{\substack{\kappa\rho \\ \kappa\neq 0 \\ \kappa+\rho \text{ even}}} \mathscr{D}_{-\rho,\Delta m}^{\kappa*}(\varphi_\varepsilon,\theta_\varepsilon,0)\Xi_{\kappa 0}F_{\kappa\rho}J_{|\rho|}(kR_0\vartheta)$$

$$\times \sum_{jj'} a_{jm}^{\tilde{j}}(\omega)b_{j'm'}^{\tilde{j}'*}(\omega)\sqrt{\frac{2j+1}{2j'+1}}C(j\kappa j';000)C(j\kappa j';m\Delta m m'), \quad (8.7)$$

where $\Delta m \equiv m'-m$ and $C(j_1,j_2,j_3;m_1,m_2,m_3)$ are Clebsch-Gordan coeffients [283]. Since the atom-linear molecule potential is axially symmetric, only the $\Xi_{\kappa 0}$ coefficients contribute to the scattering amplitude.

Eq. (8.7) can be simplified by limiting our considerations to special cases. A first such simplification arises when we let the initial free-rotor state to be the ground state, $|j,m\rangle \equiv |0,0\rangle$. A second simplification is achieved by restricting the orientation of the electric field in the space-fixed frame to a particular geometry.

(i) For an electric field *parallel* to the initial wave vector, $\boldsymbol{\varepsilon} \uparrow\uparrow \mathbf{k}$, we have $\theta_\varepsilon \to 0$, $\varphi_\varepsilon \to 0$. As as result, the Wigner matrix becomes $\mathscr{D}_{-\rho,\Delta m}^{\kappa*}(0,0,0)$, which equals a Kronecker delta, $\delta_{-\rho\Delta m}$. Hence only the $\rho = -\Delta m'$ term yields a nonvanishing contribution to the scattering amplitude of Eq. (8.7),

$$f_{0,0\to\tilde{j}',m'}^{\omega,\|}(\vartheta) = J_{|m'|}(kR_0\vartheta)\frac{ikR_0}{2\pi} \sum_{\substack{\kappa\neq 0 \\ \kappa+m' \text{ even}}} \Xi_{\kappa 0}F_{\kappa m'}$$

$$\times \sum_{jj'} a_{j0}^{0}(\omega)b_{j'm'}^{\tilde{j}'*}(\omega)\sqrt{\frac{2j+1}{2j'+1}}C(j\kappa j';000)C(j\kappa j';0m'm') \quad (8.8)$$

We see that the angular dependence of the scattering amplitude for the parallel case is simple, given by a single Bessel function, $J_{|m'|}$.

(ii) For an electric field *perpendicular* to the initial wave vector, $\boldsymbol{\varepsilon} \perp \mathbf{k}$, we have

$\theta_\varepsilon \rightarrow \frac{\pi}{2}$, $\varphi_\varepsilon \rightarrow 0$. Hence

$$f_{0,0\rightarrow\tilde{j}',m'}^{\omega,\perp}(\vartheta) = \frac{ikR_0}{2\pi} \sum_{\substack{\kappa\rho \\ \kappa\neq 0 \\ \kappa+\rho \text{ even}}} d_{-\rho,m'}^\kappa\left(\frac{\pi}{2}\right) \Xi_{\kappa 0} F_{\kappa\rho} J_{|\rho|}(kR_0\vartheta)$$

$$\times \sum_{jj'} a_{j0}^0(\omega) b_{j'm'}^{\tilde{j}'*}(\omega) \sqrt{\frac{2j+1}{2j'+1}} C(j\kappa j'; 000) C(j\kappa j'; 0m'm'), \quad (8.9)$$

where $d_{-\rho,m'}^\kappa(\theta)$ are the real Wigner rotation matrices. Since the summation mixes different Bessel functions (for a range of ρ's), the angular dependence of the scattering amplitude in the perpendicular case is more involved than in the parallel case.

We note that, unfortunately, the Fraunhofer model does not distinguish between the parallel and antiparallel orientations of the field with respect to the initial wave vector, as can be seen by substituting $\mathscr{D}_{-\rho,\Delta m}^{\kappa*}(0,\pi,0) = \delta_{\rho\Delta m}(-1)^{\kappa-\rho}$ into Eq. (8.7). This defect is inherent to the Fraunhofer model, since the diffraction occurs on a two-dimensional obstacle in the XY plane, which looks the same from either side of the plane, no matter whether $\boldsymbol{\varepsilon} \uparrow\uparrow \mathbf{k}$ or $\boldsymbol{\varepsilon} \uparrow\downarrow \mathbf{k}$.

8.2 Results for Ne–OCS($^1\Sigma, j = 0 \rightarrow j'$) scattering in an electrostatic field

We now proceed with the presentation of the collisional model with a concrete collision system in mind, namely Ne–OCS($^1\Sigma, j = 0 \rightarrow j'$). The OCS molecule has been widely used in experiments with helium nanodroplets [309]. The electric dipole moment $\mu = 0.709$ D, rotational constant $B = 0.2039$ cm^{-1}, and spectroscopic amicability make the OCS molecule a suitable candidate for an experiment to test the field-dependent Fraunhofer model for a $^1\Sigma$ molecule.

According to Ref. [310], the ground-state Ne–OCS potential energy surface has a global minimum of a depth of -81.26 cm^{-1}. In order to diminish the effect of this attractive well in the collision, we choose a collision energy $E_{\text{coll}} = 500$ cm^{-1}, which

corresponds to a wave number $k = 21.09$ Å^{-1}. The "hard shell" of the potential energy surface at this collision energy, shown in Fig. 8.2, we found by a fit to Eq. (5.34) for $\kappa \leq 6$. The coefficients $\Xi_{\kappa 0}$ obtained from the fit are listed in the Table 8.1. According to Eq. (5.36), the Ξ_{00} coefficient determines the hard-sphere radius R_0, which is responsible for elastic scattering.

We start by analyzing the *field-free* state-to-state differential cross section, which is given by

$$\mathcal{I}^{\text{f-f}}_{0,0 \to j',m'}(\vartheta) = |f_{0,0 \to j',m'}(\vartheta)|^2 = \Phi_{j'|m'|}\Xi^2_{j'0}J^2_{|m'|}(kR_0\vartheta), \qquad (8.10)$$

with

$$\Phi_{j'|m'|} = \begin{cases} \frac{(kR_0)^2}{4\pi} \frac{\sqrt{(j'+|m'|)!(j'-|m'|)!}}{(j'+|m'|)!!(j'-|m'|)!!} & \text{for } j' + |m'| \text{ even,} \\ \\ 0 & \text{otherwise,} \end{cases} \qquad (8.11)$$

see Eq. (5.42) and Ref. [195]. We see that the state-to-state differential cross section is proportional to the square of the $\Xi_{j'0}$ coefficient, which means that the shape of the repulsive potential provides a direct information about the relative probabilities of the field-free transitions and *vice versa*. For the Ne-OCS system, the $\Xi_{2,0}$ coefficient dominates the anisotropic part of the potential, see Table 8.1. As a result, the corresponding $j = 0 \to j' = 2$ transition is expected to dominate the inelastic cross section.

Recalling the properties of the Bessel functions [295], we see that for $kR_0\vartheta \gtrsim \frac{\pi j'}{2}$ (which corresponds to $\vartheta \gtrsim j'$ degrees for the system under investigation), the differential cross-section has the following angular dependence:

$$\mathcal{I}^{\text{f-f}}_{0,0 \to j',m'}(\vartheta) \sim \begin{cases} \cos^2\left(kR_0\vartheta - \frac{\pi}{4}\right) & \text{for } m' \text{ even,} \\ \\ \sin^2\left(kR_0\vartheta - \frac{\pi}{4}\right) & \text{for } m' \text{ odd} \end{cases} \qquad (8.12)$$

By averaging over m' and taking into account that $\Phi_{j'|m'|}$ vanishes for $j' + |m'|$ odd, we

obtain the angular dependence of the differential cross-section for a $0 \to j'$ transition:

$$\mathcal{I}_{0\to j'}^{\text{f-f}}(\vartheta) \sim \begin{cases} \cos^2\left(kR_0\vartheta - \frac{\pi}{4}\right) & \text{for } j' \text{ even,} \\ \\ \sin^2\left(kR_0\vartheta - \frac{\pi}{4}\right) & \text{for } j' \text{ odd} \end{cases} \tag{8.13}$$

The "phase shift" of $\frac{\pi}{2}$ predicted by Eq. (8.13) for the oscillations in the differential cross sections corresponding to even and odd field-free transitions is shown in Fig. 8.3.

The elastic scattering amplitude, given by Eq. (5.20), has a $\sin^2\left(kR_0\vartheta - \frac{\pi}{4}\right)$ asymptote, and so is out of phase with even-j'-transitions. This latter effect, which is known as the "Blair phase rule," can be also seen in Fig. 8.3.

Table 8.1: Hard-shell Legendre moments $\Xi_{\kappa 0}$ for the Ne–OCS potential at a collision energy of 500 cm^{-1} and for the Ar–NO potential at a collision energy of 442 cm^{-1}.

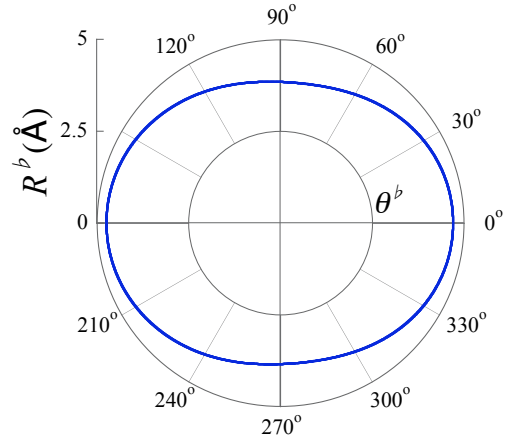|	$\Xi_{\kappa 0}$ (Å)	
κ	Ne-OCS	Ar-NO
0	14.7043	11.0407
1	-0.0968	0.1744
2	0.9455	0.5757
3	0.0540	0.0040
4	-0.0384	-0.0713
5	-0.0131	-0.0013
6	0.0012	0.0106

Figure 8.2: Equipotential line $R^\flat(\theta^\flat)$ for the Ne–OCS potential energy surface at a collision energy of 500 cm^{-1}. We note that the equipotential line for the Ar–NO collision system looks similar and is not shown. The Legendre moments for either potential energy surface are listed in Table 8.1.

The state-to-state differential cross sections for scattering in a field parallel ($\parallel$) and perpendicular ($\perp$) to $\mathbf{k}$ are given by

$$\mathcal{I}_{0 \to j'}^{\omega,(\parallel,\perp)}(\vartheta) = \sum_{m'} \mathcal{I}_{0,0 \to j',m'}^{\omega,(\parallel,\perp)}(\vartheta), \tag{8.14}$$

with

$$\mathcal{I}_{0,0 \to j',m'}^{\omega,(\parallel,\perp)}(\vartheta) = \left| f_{0,0 \to \tilde{j}',m'}^{\omega,(\parallel,\perp)}(\vartheta) \right|^2, \tag{8.15}$$

and are shown for the Ne–OCS collisions at $\varepsilon = 50$ and 100 kV/cm in Fig. 8.3. The figure reveals that an electrostatic field on the order of 10 kV/cm dramatically alters the cross-sections. (i) For a *parallel field*, $\boldsymbol{\varepsilon} \parallel \mathbf{k}$, the differential cross section, Eq. (8.15), has the same explicit angular dependence as for the field-free case, Eq. (8.12). However, the field suppresses the selection rule (8.11) and so the summation in Eq. (8.14) comprises all m'-states. Therefore, the resulting cross section is a field-dependent mixture of the sine- and cosine-contributions given by Eq. (8.12). The angular dependence of the differential cross sections in the left panel of Fig. 8.3 can be gleaned from Eq. (8.8). The first sum in Eq. (8.8) extends over even κ for even m', and over odd κ for odd m'. Therefore, the $\Xi_{\kappa 0}$ coefficients, Table 8.1, determine not only the relative contributions of different j' states, but also of different m' states in Eq. (8.14). Since the Ξ_{20} coefficient eclipses the others, transitions to even m' states dominate whenever the field is high enough, and the field-free cross-section (8.13) has a $\cos^2 \vartheta$ asymptote. This can be clearly seen in the left panel of Fig. 8.3: for odd j', there is a field-induced phase shift of the differential cross section, which is absent for transitions to even j'.

(ii) For a *perpendicular field*, $\boldsymbol{\varepsilon} \perp \mathbf{k}$, several Bessel functions contribute to the scattering amplitude. However, since the summation in Eq. (8.9) requires that $\kappa + \rho$ be even, it is the even Bessel functions which, like in the case of a parallel field, can be expected to dominate the cross section. Indeed, the cross sections shown in Fig. 8.3 for parallel and perpendicular fields are, for $j' = 1, 2, 3$, similar to one another. However, the $j = 0 \to j' = 4$ differential cross section in the perpendicular field exhibits an additional phase shift. This cross section represents a special case
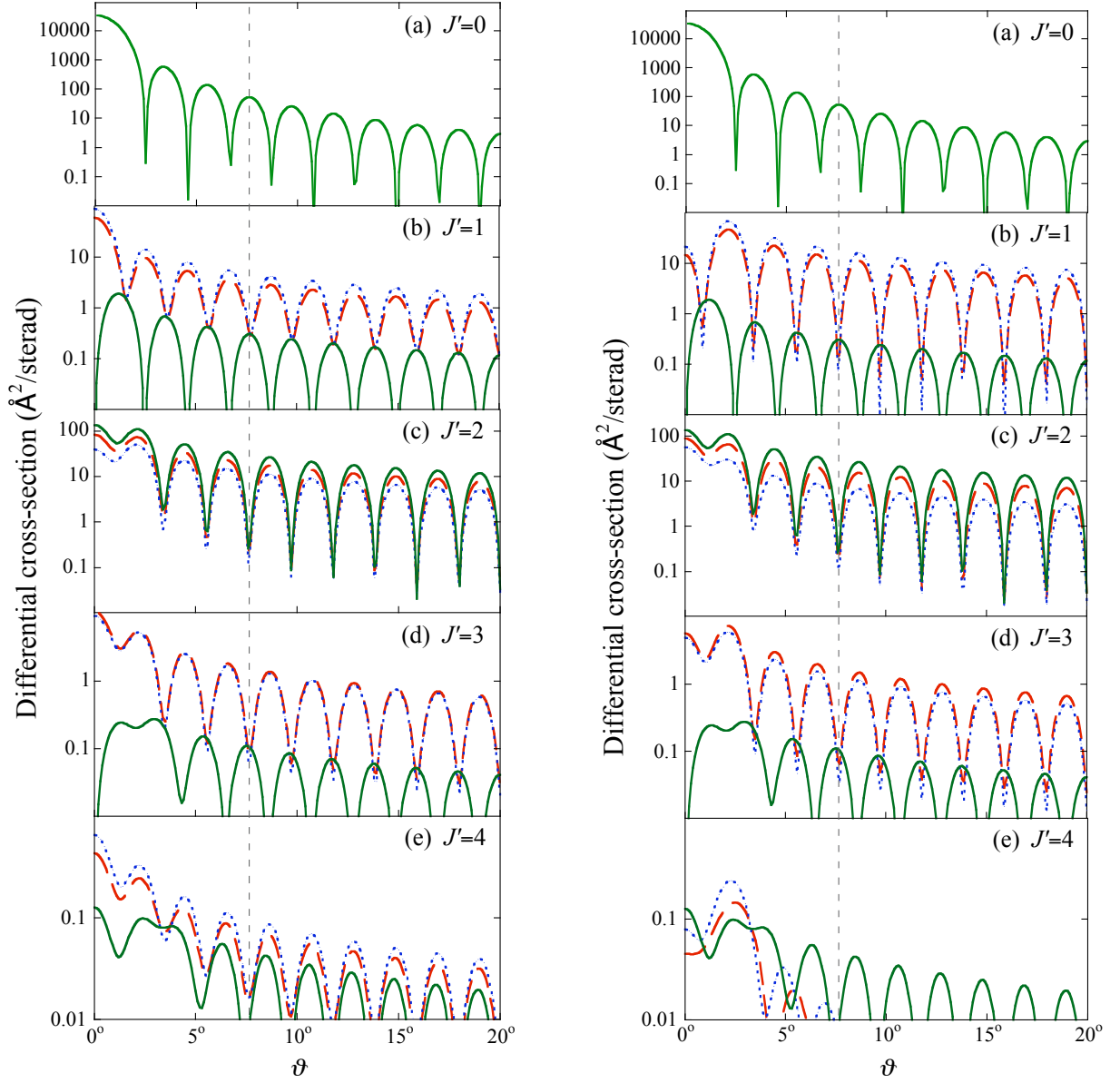
Figure 8.3: Differential cross sections for the Ne–OCS ($j = 0 \rightarrow j'$) collisions in an electrostatic field ε=50 kV/cm (red dashed line) and 100 kV/cm (blue dotted line), *parallel* (left) and *perpendicular* (right) to the relative velocity vector. The field-free cross sections are shown by the green solid line. The dashed vertical line serves to guide the eye in discerning the angular shifts of the partial cross sections.

as it is not dominated by the Ξ_{20} coefficient. The Ξ_{20} coefficient fails to dominate the $j = 0 \to j' = 4$ cross section because of the selection rule, $j' = j; j \pm 2$, that the Clebsch-Gordon coefficients $C(j2j', 000)$ impose on the $\kappa = 2$ term. However, the products of the hybridization coefficients, $a_{j0}^0(\omega)b_{j0}^{\tilde{4}*}(\omega)$ and $a_{j0}^0(\omega)b_{j\pm2,0}^{\tilde{4}*}(\omega)$ that occur in the term are very small, due to a tiny overlap of the $a_{j0}^0(\omega)$ and $b_{j'0}^{\tilde{4}*}(\omega)$ hybridization coefficents. Therefore, a superposition of both even and odd Bessel functions contributes to the $j = 0 \to j' = 4$ differential cross section. A more detailed discussion of the overlaps of the hybridization coefficients is given in Ref. [196].

8.3   Collisions of $^1\Sigma$ molecules with ^1S atoms and ions in a laser field

When subject to an external electric field, the electronic distribution of any molecule becomes polarized to some extent. This interaction, governed by the molecular polarizability, results in an induced dipole moment. While for the experimentally feasible static fields such induced moments are very weak, sizable dipole moments can be induced by a radiative field. If the induced-dipole interaction is anisotropic and sufficiently strong, the molecular rotational states undergo *hybridization* (coherent linear superposition) which aligns the molecular axis along the field vector [311, 312, 313]. The strength of the interaction is characterized by a dimensionless parameter $\Delta\omega$,

$$\Delta\omega \equiv \frac{2\pi\Delta\alpha I}{Bc} = \frac{\Delta\alpha\varepsilon^2}{4B}, \qquad (8.16)$$

with $\Delta\alpha = \alpha_\parallel - \alpha_\perp$ the polarizability anisotropy, $\alpha_{\parallel,\perp}$ the polarizability components parallel and perpendicular to the molecular axis, B the rotational constant of the molecule, I the radiation intensity, and ε the amplitude of the corresponding oscillating electric field. The induced-dipole interaction couples states of the free-rotor basis set with same m but with j's that differ by $0, \pm 2$. Thus the resulting hybrid states take

the form:

$$|\tilde{j}, m; \Delta\omega\rangle = \sum_{j=2n} a_{jm}^{\tilde{j}}(\Delta\omega)|j, m\rangle \qquad \text{for } \tilde{j} \text{ even,} \qquad (8.17)$$

$$|\tilde{j}, m; \Delta\omega\rangle = \sum_{j=2n+1} a_{jm}^{\tilde{j}}(\Delta\omega)|j, m\rangle \quad \text{for } \tilde{j} \text{ odd,} \qquad (8.18)$$

where $2n = m + |m|$ and $2n + 1 = m + |m|$ with m either $0, 2, 4\ldots$ or $1, 3, 5\ldots$. The hybridization coefficients $a_{jm}^{\tilde{j}}(\Delta\omega)$ depend solely on the interaction parameter $\Delta\omega$. The symbol $\tilde{j}$ denotes the nominal value of j that pertains to the field-free rotational state which adiabatically correlates with the hybrid state,

$$|\tilde{j}, m, \Delta\omega \to 0\rangle \to |j, m\rangle \qquad (8.19)$$

Since the hybrid wavefunctions, Eqs. (8.17) and (8.18), comprise either even or odd j's, the states have *definite parity*, $(-1)^{\tilde{j}}$.

Apart from possessing a particular energy level pattern, the $|\tilde{j}, m, \Delta\omega\rangle$ eigenstates are aligned along the electric field vector, $\boldsymbol{\varepsilon}$. The degree of alignment depends on the values of $\tilde{j}$, m, and $\Delta\omega$.

In such states, the molecular axis librates about the field direction like a pendulum, and so the hybrid states are referred to as *pendular*. It is the directionality of the pendular states that enters the field-dependent Fraunhofer model and distinguishes it from the field-free model, which assumes an isotropic distribution of the molecular axes. The directional properties of pendular states are exemplified in Fig. 8.4, which shows polar diagrams of both field-free and pendular wave functions at $\Delta\omega = 25$.

The scattering process in the field consists of the following steps: A molecule in a free-rotor state $|j, m\rangle$ enters adiabatically the radiative field where it is transformed into a pendular state $|\tilde{j}, m, \Delta\omega\rangle$. This pendular state may be changed by the collision in the field into another pendular state, $|\tilde{j}', m', \Delta\omega\rangle$. As the molecule leaves the field, the latter pendular state is adiabatically transformed into a free-rotor state $|j', m'\rangle$. Thus the net result is, in general, a rotationally inelastic collision, $|j, m\rangle \to |j', m'\rangle$.
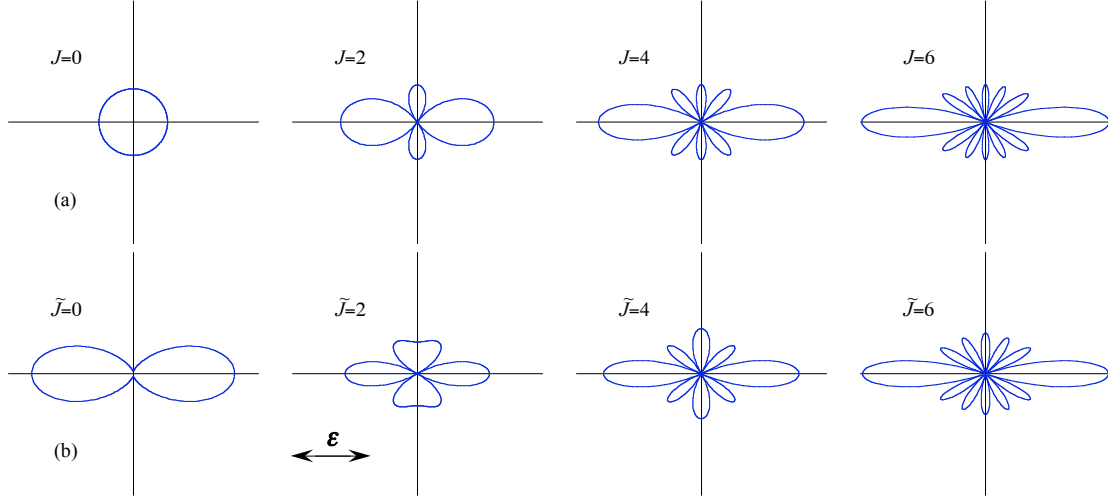
Figure 8.4: A comparison of the moduli of the free rotor wavefunctions $|j, m = 0\rangle$, panel (a), with the moduli of the pendular wavefunctions $|\tilde{j}, m = 0; \Delta\omega = 25\rangle$, panel (b). The polarization vector $\boldsymbol{\varepsilon}$ of the radiative field is also shown.

In order to be able to apply Eq. (5.42) to collisions in the radiative field, we have to transform Eqs. (8.17) and (8.18) to the space-fixed frame XYZ. If the electric field vector is specified by the Euler angles $(\varphi_\varepsilon, \theta_\varepsilon, 0)$ in the XYZ frame, the initial and final pendular states take the form:

$$|\mathfrak{i}\rangle \equiv |\tilde{j}, m; \Delta\omega\rangle = \sum_j a_{jm}^{\tilde{j}}(\Delta\omega) \sum_\xi \mathscr{D}_{\xi m}^j(\varphi_\varepsilon, \theta_\varepsilon, 0) Y_{j\xi}(\theta, \varphi), \qquad (8.20)$$

$$\langle\mathfrak{f}| \equiv \langle\tilde{j}', m'; \Delta\omega| = \sum_{j'} b_{j'm'}^{\tilde{j}'*}(\Delta\omega) \sum_{\xi'} \mathscr{D}_{\xi'm'}^{j'*}(\varphi_\varepsilon, \theta_\varepsilon, 0) Y_{j'\xi'}^*(\theta, \varphi), \qquad (8.21)$$

which is seen to depend solely on the angles θ and φ.

On substituting from Eqs. (8.20) and (8.21) into Eq. (5.42) and its integration, we obtain a general expression for the Fraunhofer scattering amplitude in the field,

$$f_{i \to f}^{\omega}(\vartheta) = \frac{ikR_0}{2\pi} \sum_{\substack{\kappa,\rho \\ \kappa \neq 0 \\ \kappa+\rho \text{ even}}} \mathscr{D}_{-\rho,\Delta m}^{\kappa*}(\varphi_\varepsilon, \theta_\varepsilon, 0) \Xi_{\kappa 0} F_{\kappa\rho} J_{|\rho|}(kR_0\vartheta)$$

$$\times \sum_{jj'} a_{jm}^{\tilde{j}}(\Delta\omega) b_{j'm'}^{\tilde{j}'*}(\Delta\omega) \sqrt{\frac{2j+1}{2j'+1}} C(j\kappa j'; 000) C(j\kappa j'; m\Delta m m'), \quad (8.22)$$

where $\Delta m \equiv m' - m$ and $C(j_1, j_2, j_3; m_1, m_2, m_3)$ are Clebsch-Gordan coeffients [283]. Since the ion-linear molecule potential is axially symmetric, only the $\Xi_{\kappa 0}$ coefficients contribute to the scattering amplitude.

Eq. (8.22) simplifies for special cases. If we limit our considerations to homonuclear diatomics, only the $\Xi_{\kappa 0}$ coefficients for even κ contribute to the expansion, Eq. (5.35), and, consequently, to the scattering amplitude, Eq. (8.22). Furthermore, if we fix the initial molecular state to the ground state, $|j, m\rangle \equiv |0, 0\rangle$, and restrict the polarization of the radiation in the space-fixed frame to a particular geometry, the problem simplifies as follows:

(i) For a polarization vector *collinear* with the initial wave vector, $\boldsymbol{\varepsilon} \parallel \mathbf{k}$, we have $\theta_\varepsilon \to 0$, $\varphi_\varepsilon \to 0$. As as result, only the $\rho = -\Delta m'$ term yields a nonvanishing contribution and so

$$f_{0,0 \to \tilde{j}',m'}^{\omega,\parallel}(\vartheta) = J_{|m'|}(kR_0\vartheta) \frac{ikR_0}{2\pi} \sum_{\substack{\kappa \text{ even} \\ \kappa \neq 0}} \Xi_{\kappa 0} F_{\kappa m'}$$

$$\times \sum_{jj'} a_{j0}^{0}(\omega) b_{j'm'}^{\tilde{j}'*}(\omega) \sqrt{\frac{2j+1}{2j'+1}} C(j\kappa j'; 000) C(j\kappa j'; 0m'm') \quad (8.23)$$

We see that the angular dependence of the scattering amplitude for the parallel case is simple, given by a single Bessel function, $J_{|m'|}$.

(ii) If the polarization vector is *perpendicular* to the initial wave vector, $\boldsymbol{\varepsilon} \perp \mathbf{k}$, we have $\theta_\varepsilon \to \frac{\pi}{2}$, $\varphi_\varepsilon \to 0$.

Hence

$$
f_{0,0\to\tilde{j}',m'}^{\omega,\perp}(\vartheta) = \frac{ikR_0}{2\pi} \sum_{\substack{\kappa,\rho \text{ even} \\ \kappa\neq 0}} d_{-\rho,m'}^{\kappa}\left(\frac{\pi}{2}\right) \Xi_{\kappa 0} F_{\kappa\rho} J_{|\rho|}(kR_0\vartheta)
$$

$$
\times \sum_{jj'} a_{j0}^0(\omega) b_{j'm'}^{\tilde{j}'*}(\omega) \sqrt{\frac{2j+1}{2j'+1}} C(j\kappa j';000) C(j\kappa j';0m'm'), \quad (8.24)
$$

where $d_{-\rho,m'}^{\kappa}$ are the real Wigner rotation matrices. Since the summation mixes different Bessel functions (for a range of ρ's), the angular dependence of the scattering amplitude in the perpendicular case is more involved than in the parallel case.

The Clebsch-Gordan coefficient $C(j\kappa j';000)$ in Eqs. (8.23) and (8.24) is nonzero only if $j + j'$ is even, since the summation includes only even-κ terms. Moreover, given the definite parity of the pendular states, we see that only parity-conserving transitions are allowed, namely $j = 0 \to j' = 2, 4, 6, \ldots$ for our choice of the initial state.

We can also see that, for either geometry, only the partial cross sections for the $j = 0, m = 0 \to j', m'$ collisions with m' even contribute to the scattering. This is particularly clear in the $\boldsymbol{\varepsilon} \parallel \mathbf{k}$ case, where the $F_{\kappa m'}$ coefficients vanish for m' odd. In the $\boldsymbol{\varepsilon} \perp \mathbf{k}$ case, a summation over ρ arises. Since for κ even and m' odd the real Wigner matrices obey the relation $d_{-\rho,m'}^{\kappa}\left(\frac{\pi}{2}\right) = -d_{\rho,m'}^{\kappa}\left(\frac{\pi}{2}\right)$, the sum over ρ is zero and so are the partial cross sections with m' odd.

8.4 Rotationally inelastic Na$^+$–N$_2$ collisions in a radiative field

Here we apply the model to the Na$^+$–N$_2(j = 0 \to j')$ collisions. The polarization anisotropy $\Delta\alpha = 0.93$ Å^3 and rotational constant $B = 1.9982$ cm^{-1} make the N$_2$ molecule a suitable candidate for an experiment on laser-assisted ion-molecule collisions.

Table 8.2: Hard shell Legendre moments $\Xi_{\kappa 0}$, Eq. (5.35), for the Na$^+ -$ N$_2$ potential at a collision energy of 5 eV. All odd moments are zero.

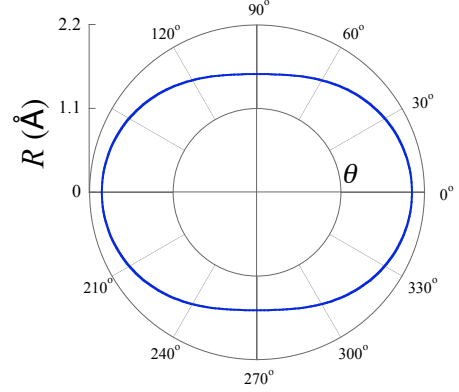| κ	$\Xi_{\kappa 0}$ (Å)
0	6.1221
2	0.5301
4	-0.0359
6	0.0022
8	0.0002

Figure 8.5: Equipotential line $R(\theta)$ for the Na$^+$– N$_2$ potential energy surface at a collision energy of 5 eV. The Legendre moments, Eq. (5.35), of the potential energy surface are listed in Table 8.2.

According to Ref. [314], the ground-state Na$^+$–N$_2$ potential energy surface has a global minimum -2712 cm^{-1} deep. The effect of this attractive well is negligible for low-energy collisions; we chose a collision energy of 5 eV, which corresponds to a wave number $k = 173.8$ Å^{-1}. The "hard shell" of the potential energy surface at this collision energy is shown in Fig. 8.5. We found it by a fit to Eq. (5.35). The $\Xi_{\kappa 0}$ coefficients are listed in Table 8.2. Due to the D_{2v} symmetry of the potential energy surface, only even-κ terms arise. According to Eq. (5.36), the Ξ_{00} coefficient determines the hard-sphere radius R_0, responsible for elastic scattering.

The *field-free* state-to-state differential cross section,

$$\mathcal{I}_{0,0\to j',m'}^{\text{f-f}}(\vartheta) = |f_{0,0\to j',m'}(\vartheta)|^2, \tag{8.25}$$

see Eq. (5.42), is proportional to $\Xi_{j'0}^2$, which means that the shape of the repulsive potential provides direct information about the relative probabilities of the field-free transitions and *vice versa*. Since for the Na$^+$–N$_2$ system the $\Xi_{2,0}$ coefficient dominates the anisotropic part of the potential, see Table 8.2, the corresponding $j = 0 \to j' = 2$ collisions are expected to dominate the inelastic cross section. Because

of the D_{2h} symmetry, there are no parity-breaking $j = 0 \rightarrow$ odd j' collisions in the $\text{Na}^+\text{--}\text{N}_2(j = 0 \rightarrow j')$ system.

After averaging over m' and invoking the asymptotic properties of the Bessel functions [295], we obtain for the parity-conserving $j = 0 \rightarrow$ even j' collisions:

$$\mathcal{I}_{0 \rightarrow j'}^{\text{f-f}}(\vartheta) \sim \cos^2\left(kR_0\vartheta - \frac{\pi}{4}\right) \tag{8.26}$$

The elastic differential scattering cross section, cf. Eq. (5.20), has a $\sin^2\left(kR_0\vartheta - \frac{\pi}{4}\right)$ asymptote, and so is seen to be shifted with respect to the differential cross sections for even-j' transitions by a quarter of a wavelength. Known as the "Blair phase rule," the shift is a conspicuous feature of Fig. 8.6.

The state-to-state differential cross sections for scattering in a radiative field parallel ($\boldsymbol{\varepsilon} \parallel \mathbf{k}$) and perpendicular ($\boldsymbol{\varepsilon} \perp \mathbf{k}$) to the initial wave vector are given by

$$\mathcal{I}_{0 \rightarrow j'}^{\omega,(\parallel,\perp)}(\vartheta) = \sum_{m'} \mathcal{I}_{0,0 \rightarrow j',m'}^{\omega,(\parallel,\perp)}(\vartheta), \tag{8.27}$$

with

$$\mathcal{I}_{0,0 \rightarrow j',m'}^{\omega,(\parallel,\perp)}(\vartheta) = \left| f_{0,0 \rightarrow \tilde{j}',m'}^{\omega,(\parallel,\perp)}(\vartheta) \right|^2 \tag{8.28}$$

The differential cross sections for the $\text{Na}^+\text{--}\text{N}_2$ collisions are presented in Fig. 8.6 for an interaction parameter $\Delta\omega = 10$ and 25, corresponding to laser intensities of 2.15×10^{12} W/cm^2 and 5.37×10^{12} W/cm^2, respectively. The figures show that a radiative field on the order of 10^{12} W/cm^2 dramatically alters the magnitudes of the differential cross sections, but does not produce any "phase shift" of the angular oscillations. Such a "phase shift" is absent because only even Bessel functions, which have a $\cos^2\left(kR_0\vartheta - \frac{\pi}{4}\right)$ asymptote, contribute to the scattering at any field strength, see Eqs. (8.23) and (8.24).
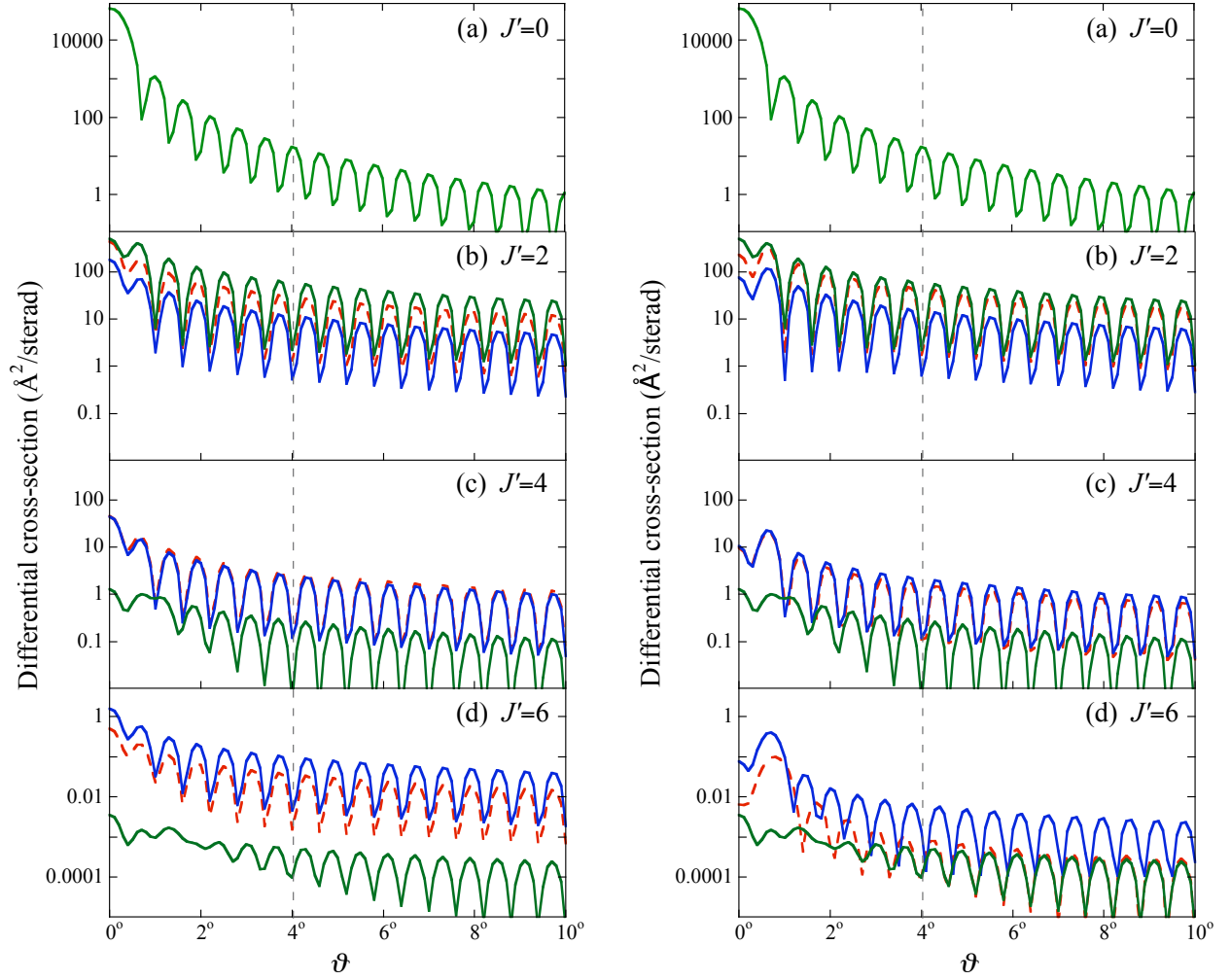
Figure 8.6: Differential cross sections for the $Na^+ + N_2$ ($j = 0 \rightarrow j'$) collisions in a radiative field for $\Delta\omega = 10$ (red dashed line) and $\Delta\omega = 25$ (blue solid line), *parallel* (left) and *perpendicular* (right) to the initial wave vector. The field-free cross sections are shown by the green solid line.

9 Effect of a magnetic field on differential cross sections

> A grocer is attracted to his business by a magnetic force as great as the repulsion which renders it odious to artists.
>
> Honoré de Balzac

In this chapter we apply the Fraunhofer model described in Chapter 5 to treat collisions of closed-shell atoms with open-shell molecules in $^2\Sigma$, $^3\Sigma$ and $^2\Pi$ electronic states, whose magnetic moment is on the order of 1 Bohr magneton. The magnetic field affects the collision dynamics by aligning the molecular axis with respect to the relative velocity vector, and thereby changing the effective shape of the target. Also, the field hybridizes different rotational states of a molecule, which alters collision dynamics by relaxing some of the selection rules. We exemplify our theory by investigating collisions of $CaH(X^2\Sigma^+)$, $O_2(X^3\Sigma^-)$, and $OH(X^2\Pi_\Omega)$ with a helium atom, which is a favorite buffer gas, used to thermalize molecules and radicals produced by laser ablation and other entrainment techniques [315].

9.1 Scattering of $^2\Sigma$ molecules by closed-shell atoms in a magnetic field

9.1.1 A $^2\Sigma$ molecule in a magnetic field

The field-free Hamiltonian of a rigid $^2\Sigma$ molecule,

$$H_0 = BN^2 + \gamma \mathbf{N} \cdot \mathbf{S}, \tag{9.1}$$

is represented by a 2×2 matrix, diagonal in the Hund's case (b) basis, $|N, j, m\rangle$. Here $\mathbf{N}$ and $\mathbf{S}$ are the rotational and (electronic) spin angular momenta, B is the rotational constant and γ the spin-rotation constant. Its eigenfunctions,

$$\Psi_\pm(j, m) = \frac{1}{\sqrt{2}} \left[\left|S, \tfrac{1}{2}\right\rangle |j, \Omega, m\rangle \pm \left|S, -\tfrac{1}{2}\right\rangle |j, -\Omega, m\rangle \right], \tag{9.2}$$

are combinations of (electronic) spin functions $|S, m_S\rangle$ with Hund's case (a) (i.e., symmetric top) functions $|j, \Omega, m\rangle$ pertaining to the total angular momentum $\mathbf{j} = \mathbf{N} + \mathbf{S}$, whose projections on the space- and body-fixed axes are m and $\Omega = \pm\tfrac{1}{2}$, respectively. The Hund's case (a) wavefunctions are given by:

$$|j, m, \Omega\rangle = \sqrt{\frac{2j+1}{4\pi}} \mathscr{D}^{j*}_{m\Omega}(\varphi, \theta, \gamma = 0) \tag{9.3}$$

The Ψ_+ and Ψ_- states are conventionally designated as F_1 and F_2 states, for which the rotational quantum number $N = j - \tfrac{1}{2}$ and $N = j + \tfrac{1}{2}$, respectively. Equation (9.2) can be recast in terms of N instead of j:

$$|\Psi_\epsilon(N, m)\rangle = \frac{1}{\sqrt{2}} \left[\left|S, \tfrac{1}{2}\right\rangle \left|N + \tfrac{\epsilon}{2}, \Omega, m\right\rangle + \epsilon \left|S, -\tfrac{1}{2}\right\rangle \left|N + \tfrac{\epsilon}{2}, -\Omega, m\right\rangle \right], \tag{9.4}$$

with $\epsilon = \pm 1$. The eigenvalues corresponding to states F_1 and F_2 are given by:

$$E_+\left(N + \tfrac{1}{2}, m; F_1\right) = BN(N+1) + \frac{\gamma}{2}N, \tag{9.5}$$

$$E_-\left(N - \tfrac{1}{2}, m; F_2\right) = BN(N+1) - \frac{\gamma}{2}(N+1), \tag{9.6}$$

whence we see that the spin-rotation interaction splits each rotational level into a doublet separated by $\Delta E \equiv E_+ - E_- = \gamma(N + \tfrac{1}{2})$.

In a static magnetic field, $\mathscr{H}$, directed along the space-fixed Z axis, the Hamiltonian acquires a magnetic dipole potential which is proportional to the projection, S_Z, of $\mathbf{S}$ on the Z axis,

$$V_{\mathrm{m}} = S_Z \omega_{\mathrm{m}} B, \tag{9.7}$$

with

$$\omega_{\mathrm{m}} \equiv \frac{g_S \mu_B \mathscr{H}}{2B}, \tag{9.8}$$

a dimensionless interaction parameter involving the electron gyromagnetic ratio $g_S \simeq 2.0023$, the Bohr magneton μ_B, and the rotational constant B.

The Zeeman eigenproperties of a $^2\Sigma$ molecule can be readily obtained in closed form, since the V_{m} operator couples states that differ in N by 0 or ± 2 and, therefore, the Hamiltonian matrix, $H = H_0 + V_{\mathrm{m}}$, factors into 2×2 blocks for each N:

$$H = -\omega_{\mathrm{m}} B \begin{pmatrix} -\frac{m}{2N+1} + \frac{E_-}{\omega_{\mathrm{m}} B} & \frac{1}{2}[1 - \frac{m^2}{(N+1/2)^2}]^{\frac{1}{2}} \\ \\ \frac{1}{2}[1 - \frac{m^2}{(N+1/2)^2}]^{\frac{1}{2}} & \frac{m}{2N+1} + \frac{E_+}{\omega_{\mathrm{m}} B} \end{pmatrix} \tag{9.9}$$

As a result, the Zeeman eigenfunctions of a $^2\Sigma$ molecule are given by a linear combination of the field-free wavefunctions (9.4),

$$\psi(\tilde{N}, \tilde{j}, m; \omega_{\mathrm{m}}) = a(\omega_{\mathrm{m}})\big|\Psi_-(N, m)\big\rangle + b(\omega_{\mathrm{m}})\big|\Psi_+(N, m)\big\rangle, \tag{9.10}$$

with the hybridization coefficients $a(\omega_{\mathrm{m}})$ and $b(\omega_{\mathrm{m}})$ obtained by diagonalizing Hamiltonian (9.9). Although N and j are no longer good quantum numbers in the magnetic field, they can be employed as adiabatic labels of the states: we use $\tilde{N}$ and $\tilde{j}$ to denote the angular momentum quantum numbers of the field-free state that adiabatically correlates with the given state in the field.
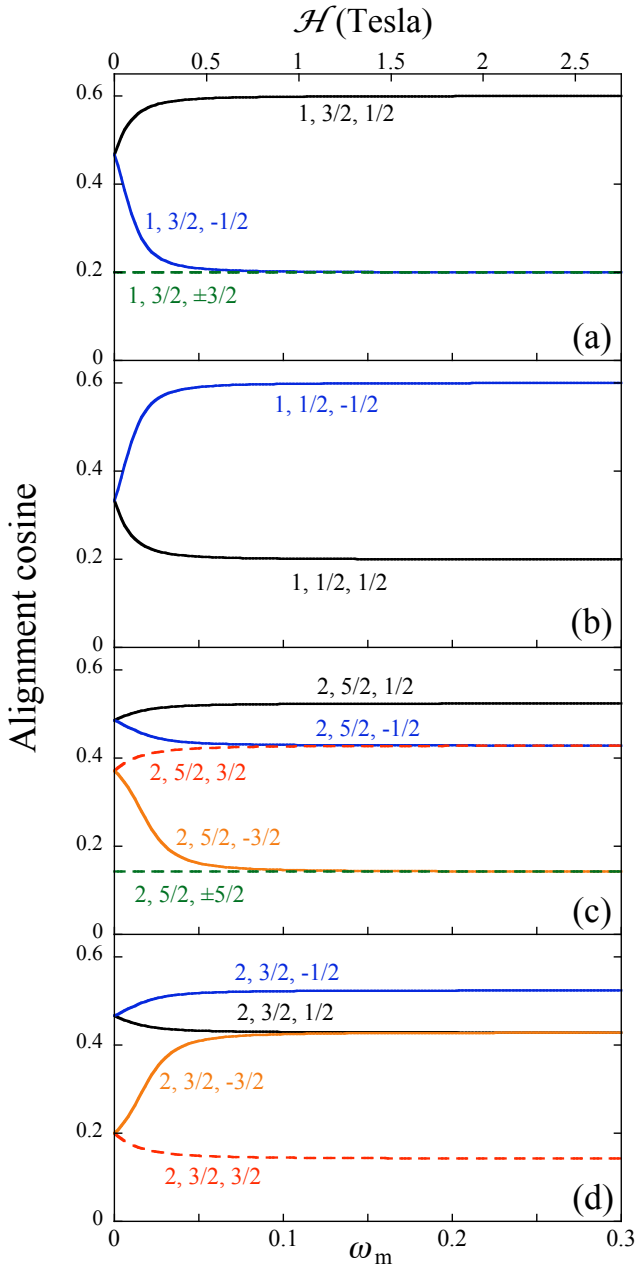
Figure 9.1: Expectation values of the alignment cosine $\langle \cos^2 \theta \rangle$ for the Zeeman states of $CaH(X^2\Sigma^+)$ as a function of the magnetic field strength parameter ω_m. States are labeled as $\tilde{N}, \tilde{j}, m$, see text.

Since the Zeeman eigenfunction comprises rotational states with either N even or N odd, the parity of the eigenstates remains definite even in the presence of the magnetic field; it is given by $(-1)^{\tilde{N}}$.

The degree of mixing of the Hund's case (b) states that make up a $^2\Sigma$ Zeeman eigenfunction is determined by the splitting of the rotational levels measured in terms of the rotational constant, $\Delta E/B$: for $\omega_m \leq \Delta E/B$ the mixing (hybridization) is incomplete, while it is perfect in the high-field limit, $\omega_m \gg \Delta E/B$. We note that in the high-field limit, the eignevectors can be found from matrix (9.9) with $E_\pm/\omega_m B \to 0$. As an example, Table 9.1 lists the values of the hybridization coefficients $a(\omega_m)$ and $b(\omega_m)$ for the $N = 2, j = \frac{5}{2}, m$ states of the CaH molecule in the high-field limit, which is attained at $\omega_m \gg 0.025$.

The degree of molecular axis alignment is given by the alignment cosine, $\langle \cos^2 \theta \rangle$, which, in the $^2\Sigma$ case, can be obtained in closed form. To the best of our knowledge, this result has not been

presented in the literature before; therefore, we give it in Appendix 16.2. The dependence of the alignment cosine on the magnetic field strength parameter ω_m is

Table 9.1: The hybridization coefficients $a(\omega_{\mathrm{m}})$ and $b(\omega_{\mathrm{m}})$ for the $N = 2, j = \frac{5}{2}, m$ state in the high-field limit, $\omega_{\mathrm{m}} \gg \Delta E/B$, which arises for $\omega_{\mathrm{m}} \gg 0.025$ for the $N = 2$ level of the $\mathrm{CaH}(X^2\Sigma^+)$ molecule. See text.

m	$a(\omega_{\mathrm{m}})$	$b(\omega_{\mathrm{m}})$
$\frac{1}{2}$	$\sqrt{\frac{2}{5}}$	$\sqrt{\frac{3}{5}}$
$-\frac{1}{2}$	$\sqrt{\frac{3}{5}}$	$\sqrt{\frac{2}{5}}$
$\frac{3}{2}$	$\frac{1}{\sqrt{5}}$	$\frac{2}{\sqrt{5}}$
$-\frac{3}{2}$	$\frac{2}{\sqrt{5}}$	$\frac{1}{\sqrt{5}}$
$\pm\frac{5}{2}$	0	1

shown in Fig. 9.1 for the two lowest N states of the CaH molecule. One can see that for $\omega_{\mathrm{m}} \gg \Delta E/B$, the alignment cosine smoothly approaches a constant value, corresponding to as good an alignment as the uncertainty principle allows.

9.1.2 The field-dependent scattering amplitude

In what follows, we consider scattering from the $N = 0, j = 1/2$ state to some N', j' state in a magnetic field. Since the $N = 0$ state of a $^2\Sigma$ molecule is not aligned, the effects of the magnetic field on the scattering arise solely from the alignment of the final state.

In order to account for an arbitrary direction of the electric field with respect to the initial wave vector $\mathbf{k}$, we introduce a field-fixed coordinate system $X^\sharp Y^\sharp Z^\sharp$, whose $Z^\sharp$-axis is defined by the direction of the electric field vector $\boldsymbol{\varepsilon}$. By making use of the relation

$$\mathscr{D}^{j*}_{m\Omega}(\varphi^\sharp, \theta^\sharp, 0) = \sum_\xi \mathscr{D}^j_{\xi m}(\varphi_\varepsilon, \theta_\varepsilon, 0)\mathscr{D}^{j*}_{\xi\Omega}(\varphi, \theta, 0) \tag{9.11}$$

we transform the wavefunctions (9.10) to the space-fixed frame. For the initial and

the final states we have:

$$
|\mathfrak{i}(N,m)\rangle = \frac{1}{\sqrt{4\pi}} \sum_{\xi} \left\{ a(\omega_{\mathrm{m}})\sqrt{N}\, \mathscr{D}_{\xi m}^{N-\frac{1}{2}}(\varphi_{\varepsilon},\theta_{\varepsilon},0) \left[\mathscr{D}_{\xi\Omega}^{N-\frac{1}{2}*}(\varphi,\theta,0) - \mathscr{D}_{\xi-\Omega}^{N-\frac{1}{2}*}(\varphi,\theta,0) \right] \right.
$$
$$
\left. + b(\omega_{\mathrm{m}})\sqrt{N+1}\, \mathscr{D}_{\xi m}^{N+\frac{1}{2}}(\varphi_{\varepsilon},\theta_{\varepsilon},0) \left[\mathscr{D}_{\xi\Omega}^{N+\frac{1}{2}*}(\varphi,\theta,0) - \mathscr{D}_{\xi-\Omega}^{N+\frac{1}{2}*}(\varphi,\theta,0) \right] \right\}, \quad (9.12)
$$

$$
\langle \mathfrak{f}(N',m')| = \frac{1}{\sqrt{4\pi}} \sum_{\xi'} \left\{ a'(\omega_{\mathrm{m}})\sqrt{N'}\, \mathscr{D}_{\xi'm'}^{N'-\frac{1}{2}}(\varphi_{\varepsilon},\theta_{\varepsilon},0) \left[\mathscr{D}_{\xi'\Omega}^{N'-\frac{1}{2}*}(\varphi,\theta,0) - \mathscr{D}_{\xi'-\Omega}^{N'-\frac{1}{2}*}(\varphi,\theta,0) \right] \right.
$$
$$
\left. + b'(\omega_{\mathrm{m}})\sqrt{N'+1}\, \mathscr{D}_{\xi'm'}^{N'+\frac{1}{2}}(\varphi_{\varepsilon},\theta_{\varepsilon},0) \left[\mathscr{D}_{\xi'\Omega}^{N'+\frac{1}{2}*}(\varphi,\theta,0) - \mathscr{D}_{\xi'-\Omega}^{N'+\frac{1}{2}*}(\varphi,\theta,0) \right] \right\}, \quad (9.13)
$$

where $\Omega = \frac{1}{2}$ for a $^2\Sigma$ molecule.

By substituting from Eqs. (9.12) and (9.13) into Eq. (5.42), we finally obtain the scattering amplitude for inelastic collisions of $^2\Sigma$ molecules with closed-shell atoms in a magnetic field:

$$
f_{\mathfrak{i}\to\mathfrak{f}}^{\omega_{\mathrm{m}}}(\vartheta) = \frac{ikR_0}{4\pi} \sum_{\substack{\kappa\rho \\ \kappa\neq 0 \\ \kappa+\rho\ \mathrm{even}}} \Xi_{\kappa 0}\, \mathscr{D}_{-\rho,\Delta m}^{\kappa*}(\varphi_{\varepsilon},\theta_{\varepsilon},0) F_{\kappa\rho} J_{|\rho|}(kR_0\vartheta) \left[(-1)^{\kappa} + (-1)^{\Delta N} \right]
$$
$$
\times \left\{ a(\omega_{\mathrm{m}})a'(\omega_{\mathrm{m}})\sqrt{\frac{N}{N'}}\, C\!\left(N-\tfrac{1}{2},\kappa,N'-\tfrac{1}{2};\Omega 0\Omega\right) C\!\left(N-\tfrac{1}{2},\kappa,N'-\tfrac{1}{2};m\Delta mm'\right) \right.
$$
$$
+ a(\omega_{\mathrm{m}})b'(\omega_{\mathrm{m}})\sqrt{\frac{N}{N'+1}}\, C\!\left(N-\tfrac{1}{2},\kappa,N'+\tfrac{1}{2};\Omega 0\Omega\right) C\!\left(N-\tfrac{1}{2},\kappa,N'+\tfrac{1}{2};m\Delta mm'\right)
$$
$$
+ a'(\omega_{\mathrm{m}})b(\omega_{\mathrm{m}})\sqrt{\frac{N+1}{N'}}\, C\!\left(N+\tfrac{1}{2},\kappa,N'-\tfrac{1}{2};\Omega 0\Omega\right) C\!\left(N+\tfrac{1}{2},\kappa,N'-\tfrac{1}{2};m\Delta mm'\right)
$$
$$
\left. + b(\omega_{\mathrm{m}})b'(\omega_{\mathrm{m}})\sqrt{\frac{N+1}{N'+1}}\, C\!\left(N+\tfrac{1}{2},\kappa,N'+\tfrac{1}{2};\Omega 0\Omega\right) C\!\left(N+\tfrac{1}{2},\kappa,N'+\tfrac{1}{2};m\Delta mm'\right) \right\}
$$
$$
(9.14)
$$

As noted above, there is no hybridization of the initial state for the $N = 0, j = \frac{1}{2} \to N', j'$ collisions, i.e., $a(\omega_{\mathrm{m}}) = 0$, $b(\omega_{\mathrm{m}}) = 1$ in Eq. (9.14). By making use of

the properties of the Clebsch-Gordan coefficients [283],[284], the expression for the scattering amplitude from the $N = 0, j = \frac{1}{2}, m = \pm\frac{1}{2}$ state to an N', j', m' state simplifies to

$$f^{\omega_{\mathrm{m}}}_{0,\frac{1}{2},\pm\frac{1}{2} \to N',j',m'}(\vartheta) = \frac{ikR_0}{2\pi} \frac{\Xi_{N'0}}{2N'+1} \mathcal{X}_{N'm'}(\omega_{\mathrm{m}}) \sum_{\substack{\rho \\ \rho+N'\text{even}}} d^{N'}_{-\rho,\Delta m}(\theta_\varepsilon) F_{N'\rho} J_{|\rho|}(kR_0\vartheta),$$

$$(9.15)$$

with the field-dependent coefficient,

$$\mathcal{X}_{N'm'}(\omega_{\mathrm{m}}) = \pm a'(\omega_{\mathrm{m}})\sqrt{N' \mp m' + \tfrac{1}{2}} + b'(\omega_{\mathrm{m}})\sqrt{N' \pm m' + \tfrac{1}{2}} \qquad (9.16)$$

The amplitude is seen to be directly proportional to the $\Xi_{N'0}$ Legendre moment. We note that the cross section for the $N, j, m \to N', j', m'$ transition differs from that for the $N, j, -m \to N', j', -m'$ scattering. This is because the magnetic field completely lifts the degeneracy of the m states, in contrast to the electric field case [196].

9.1.3 Results for He–CaH$(X^2\Sigma, j = 1/2 \to j')$ scattering in a magnetic field

Here we apply the analytic model scattering to the He–CaH$(^2\Sigma^+, j = \frac{1}{2} \to j')$ collision system. The CaH molecule, employed previously in thermalization experiments with a He buffer gas [316], [317], has a rotational constant $B = 4.2766$ cm^{-1} and a spin-rotational interaction parameter $\gamma = 0.0430$ cm^{-1} [318]. Such values of molecular constants result in an essentially perfect mixing (and alignment) of the molecular states for field strengths $\mathscr{H} \geq 0.1$ Tesla, see Sec. 9.1.1.

According to Ref. [243], the ground-state He–CaH potential energy surface has a global minimum of -10.6 cm^{-1}. Such a weak attractive well can be neglected at a collision energy as low as 200 cm^{-1} (which corresponds to a wave number $k = 6.58$ Å^{-1}). The corresponding value of the Massey parameter, $\xi \approx 0.5$, warrants the validity of the sudden approximation to the He–CaH collision system from this collision energy on.

Table 9.2: Hard-shell Legendre moments $\Xi_{\kappa 0}$ for He–CaH ($X^2\Sigma^+$) and He–O$_2$ ($X^3\Sigma^-$) potential energy surfaces at a collision energy of 200 cm^{-1}, and for He–OH ($X^2\Pi_{\frac{3}{2}}$) potential at 1000 cm^{-1}.

	$\Xi_{\kappa 0}$ (Å)		
κ	He–CaH	He–O$_2$	He–OH
0	13.3207	9.5987	7.7941
1	-0.4397	0	0.1380
2	1.0140	0.5672	0.1625
3	0.6147	0	0.0961
4	0.0337	-0.1320	0.01789
5	-0.1475	0	-0.0032
6	-0.0653	0.0250	-0.0034
7	0.0265	0	-0.0008
8	0.0277	-0.0060	0.0002
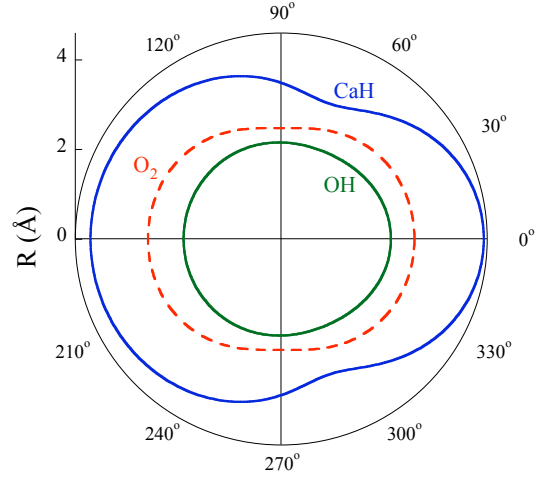
Figure 9.2: Equipotential lines $R(\theta)$ for the He–CaH ($X^2\Sigma^+$) and He–O$_2$ ($X^3\Sigma^-$) potential energy surfaces at a collision energy of 200 cm^{-1}, and for the He–OH ($X^2\Pi_\Omega$) potential at 1000 cm^{-1}. The Legendre moments for the potential energy surfaces are listed in Table 9.2.

The "hard shell" of the potential energy surface was found by a fit to Eq. (5.35) for $\kappa \leq 8$, and is shown in Fig. 9.2. The coefficients $\Xi_{\kappa 0}$ obtained from the fit are listed in Table 9.2. According to Eq. (5.36), the Ξ_{00} coefficient determines the hard-sphere radius R_0, which is responsible for elastic scattering.

The state-to-state differential cross sections for scattering in a field parallel ($\parallel$) and perpendicular ($\perp$) to $\mathbf{k}$ are given by:

$$\mathcal{I}_{0\to j'}^{\omega_{\mathrm{m}},(\parallel,\perp)}(\vartheta) = \sum_{m'} \mathcal{I}_{0,0\to j',m'}^{\omega_{\mathrm{m}},(\parallel,\perp)}(\vartheta), \ \ \text{with} \ \ \mathcal{I}_{0,0\to j',m'}^{\omega_{\mathrm{m}},(\parallel,\perp)}(\vartheta) = \left| f_{0,0\to \tilde{j}',m'}^{\omega_{\mathrm{m}},(\parallel,\perp)}(\vartheta) \right|^2 \tag{9.17}$$

They are presented in Fig. 9.3 for He–CaH collisions at zero field, $\omega_{\mathrm{m}} = 0$, as well as at high field, $\omega_{\mathrm{m}} = 0.3$ (corresponding to $\mathscr{H}$=2.75 T for CaH), where the hybridization and alignment are as complete as they can get.

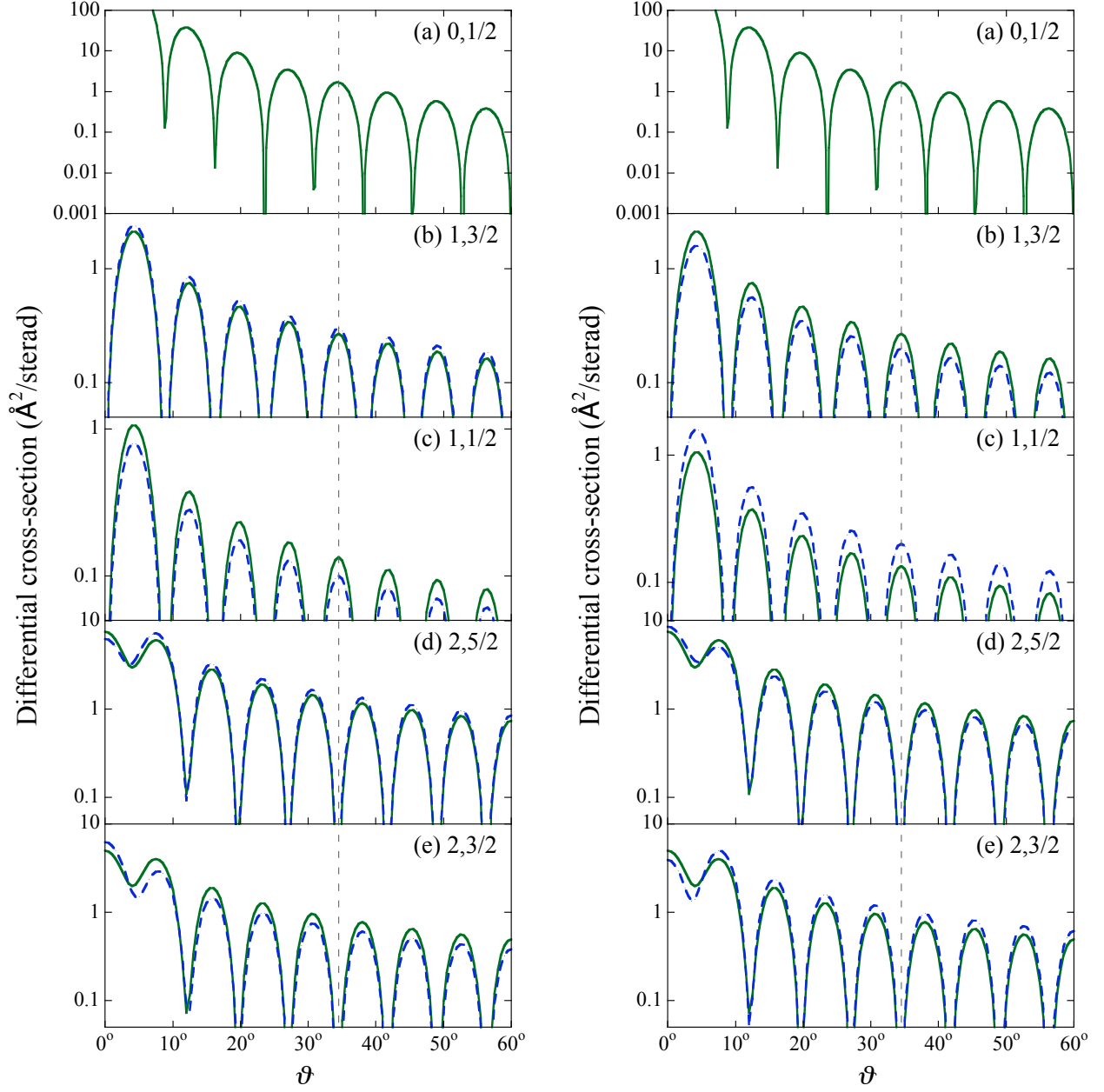Figure 9.3: Differential cross sections for the He–CaH ($N = 0, j = \frac{1}{2} \rightarrow N', j'$) collisions in a magnetic field $\omega_{\mathrm{m}} = 0.3$ (blue dashed line) parallel to the relative velocity vector, $\mathscr{H} \parallel \mathbf{k}$ (left) and perpendicular to the relative velocity vector, $\mathscr{H} \perp \mathbf{k}$ (right). The field-free cross sections are shown by the green solid line. The collision energy is 200 cm^{-1}. The dashed vertical line serves to guide the eye in discerning the angular shifts of the partial cross sections.

From Eq. (9.15) for the scattering amplitude, we see that the differential cross section for the $N = 0 \to N'$ transitions is proportional to the $\Xi_{N'0}$ Legendre moment. According to Table 9.2, the Legendre expansion of the He–CaH potential energy surface is dominated by Ξ_{20}. Therefore, the transition $N = 0 \to N' = 2$ provides the largest contribution to the cross section.

The field dependence of the scattering amplitude, Eq. (9.15), is encapsulated in the coefficients $a'(\omega_{\mathrm{m}})$ and $b'(\omega_{\mathrm{m}})$, whose values cannot affect the angular dependence, as this is determined solely by the Bessel functions, $J_{|\rho|}(kR_0\vartheta)$. Furthermore, the summation in Eq. (9.15) includes only even ρ for even N', and odd ρ for odd N'. From the asymptotic properties of Bessel functions [295], we have for large angles such that $\vartheta \gg \pi\rho/2kR_0$:

$$
J_{|\rho|}(kR_0\vartheta) \sim
\begin{cases}
\cos\left(kR_0\vartheta - \frac{\pi}{4}\right) & \text{for } \rho \text{ even,} \\[2mm]
\sin\left(kR_0\vartheta - \frac{\pi}{4}\right) & \text{for } \rho \text{ odd}
\end{cases}
\tag{9.18}
$$

For the He–CaH system, the phase shift between the J_0 and J_2 Bessel functions, which contribute to the $N = 0 \to N' = 1, 2$ transitions, is negligibly small at angles up to about 30°. Therefore there is no field-induced phase shift, neither in the parallel nor in the perpendicular case, as illustrated by Fig. 9.3.

Fig. 9.3 shows that the magnetic field induces only small changes in the amplitudes of the cross sections, without shifting their oscillations. The amplitude variation is so small because the magnetic field fails to mix contributions from the different $\Xi_{\kappa,0}$ Legendre moments, in contrast to scattering in electrostatic [196] and radiative [197] fields. The changes in the amplitudes of the differential cross sections are closely related to the field dependence of the partial integral cross sections, which are analyzed in Ref. [198].

9.2 Scattering of $^3\Sigma$ molecules by closed-shell atoms in a magnetic field

9.2.1 A $^3\Sigma$ molecule in a magnetic field

The field-free Hamiltonian of a $^3\Sigma$ electronic state consists of rotational, spin-rotation, and spin-spin terms:

$$H_0 = BN^2 + \gamma \mathbf{N} \cdot \mathbf{S} + \tfrac{2}{3}\lambda(3S_z^2 - S^2), \tag{9.19}$$

where γ and λ are the spin-rotation and spin-spin constants, respectively. In the Hund's case (b) basis, the field-free Hamiltonian (9.19) consists of 3×3 matrices pertaining to different j values (except for $j{=}0$). The matrix elements of Hamiltonian (9.19) can be found, e.g., in Ref. [319] (see also [320] and [321, 322]). The eigenenergies of H_0 are (in units of the rotational constant B):

$$E_1(j)/B = j(j+1) + 1 - \frac{3\gamma'}{2} - \frac{\lambda'}{3} - X,$$

$$E_2(j)/B = j(j+1) - \gamma' + \frac{2\lambda'}{3}, \tag{9.20}$$

$$E_3(j)/B = j(j+1) + 1 - \frac{3\gamma'}{2} - \frac{\lambda'}{3} + X,$$

with

$$X \equiv \left[j(j+1)(\gamma'-2)^2 + \left(\frac{\gamma' + 2\lambda' - 2}{2}\right)^2 \right]^{1/2}, \quad \gamma' \equiv \gamma/B, \ \ \lambda' \equiv \lambda/B$$

The eigenenergies (9.20) correspond to the three ways of combining rotational and electronic spin angular momenta $\mathbf{N}$ and $\mathbf{S}$ for $S = 1$ into a total angular momentum $\mathbf{j}$; the total angular momentum quantum number takes values $j = N + 1$, $j = N$, and $j = N - 1$ for states which are conventionally designated as F_1, F_2, and F_3, respectively.
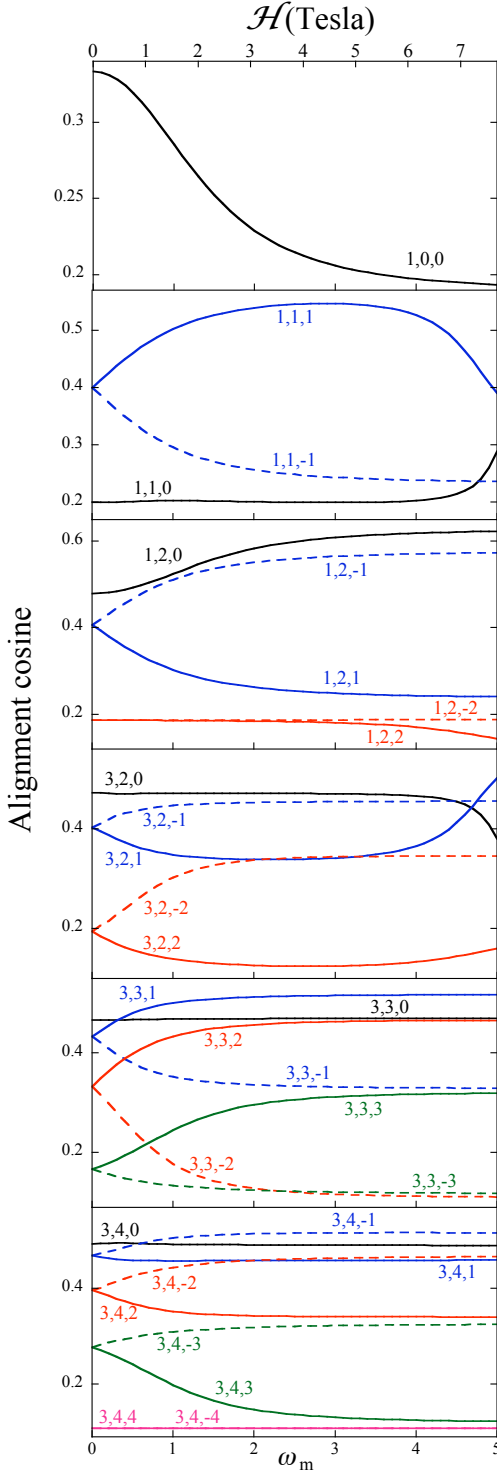
Figure 9.4: Expectation values of the alignment cosine $\langle \cos^2 \theta \rangle$ for the lowest Zeeman states of $^{16}O_2(X^3\Sigma^-)$ as a function of the magnetic field strength parameter ω_m. States are labeled by $\tilde{N}, \tilde{j}, m$.

For the case when $N = 1$, $j = 0$, the sign of the X term should be reversed [323]. The parity of the states is $(-1)^N$.

The interaction of a $^3\Sigma$ molecule with a magnetic field $\mathcal{H}$ is given by Eq. (9.7) with a dimensionless parameter characterizing the strength of the Zeeman interaction given by:

$$\omega_m \equiv \frac{g_S \mu_B \mathcal{H}}{B}, \tag{9.21}$$

cf. Eq. (9.8). We evaluated the Zeeman effect in Hund's case (b) basis,

$$|N, j, m\rangle = c^1_{Nj}|j, 1, m\rangle$$
$$+ c^0_{Nj}|j, 0, m\rangle + c^{-1}_{Nj}|j, -1, m\rangle, \tag{9.22}$$

using the matrix elements of the S_Z operator as given in Appendix 16.3.

The Zeeman eigenfunctions are hybrids of the Hund's case (b) basis functions (9.22):

$$\left| \tilde{N}, \tilde{j}, m; \omega_m \right\rangle = \sum_{Nj} a^{\tilde{N}\tilde{j}}_{Nj}(\omega_m) \left| N, j, m \right\rangle \tag{9.23}$$

and are labeled by $\tilde{N}$ and $\tilde{j}$, which are the angular momentum quantum numbers of the field-free state that adiabatically correlates with a given state in the field. Since V_m couples Hund's case (b) states that differ in N by 0 or ± 2, the parity remains definite in the

presence of a magnetic field, and is given by $(-1)^{\tilde{N}}$. However, the Zeeman matrix for a $^3\Sigma$ molecule is no longer finite, unlike the 2×2 Zeeman matrix for a $^2\Sigma$ state. Using the Hund's case (b) rather than Hund's case (a) basis set makes it possible to directly relate the field-free states and the Zeeman states, via the hybridization coefficients $a^{\tilde{N}\tilde{j}}_{Nj}$.

The alignment cosine, $\langle \cos^2 \theta \rangle$, of the Zeeman states can be evaluated from the matrix elements of Appendix 16.4. The dependence of $\langle \cos^2 \theta \rangle$ on the magnetic field strength parameter ω_{m} is exemplified in Fig. 9.4 for $\tilde{N} = 1, 3$ Zeeman states of the $^{16}O_2$ molecule.

9.2.2 The field-dependent scattering amplitude

We consider scattering from an initial N, j state to a final N', j' state. We transform the wavefunctions (9.23) to the space-fixed frame by making use of Eq. (9.11) – cf. Section 9.1.2. As a result, the initial and final states become:

$$|\mathfrak{i}\rangle \equiv \left|\tilde{N}, \tilde{j}, m, \omega_{\mathrm{m}}\right\rangle = \sum_{Nj} \sqrt{\frac{2j+1}{4\pi}} a^{\tilde{N}\tilde{j}}_{Nj}(\omega_{\mathrm{m}}) \sum_{\Omega} c^{\Omega}_{Nj} \sum_{\xi} \mathscr{D}^j_{\xi m}(\varphi_\varepsilon, \theta_\varepsilon, 0) \mathscr{D}^{j*}_{\xi\Omega}(\varphi, \theta, 0),$$
(9.24)

$$\langle\mathfrak{f}| \equiv \langle\tilde{N}', \tilde{j}', m', \omega_{\mathrm{m}}| = \sum_{N'j'} \sqrt{\frac{2j'+1}{4\pi}} b^{\tilde{N}'\tilde{j}'}_{N'j'}(\omega_{\mathrm{m}}) \sum_{\Omega'} c^{\Omega'}_{N'j'} \sum_{\xi'} \mathscr{D}^{j'}_{\xi'm'}(\varphi_\varepsilon, \theta_\varepsilon, 0) \mathscr{D}^{j'*}_{\xi'\Omega'}(\varphi, \theta, 0)$$
(9.25)

On substituting from Eqs. (9.24) and (9.25) into Eq. (5.42) and some angular momentum algebra, we obtain a general expression for the scattering amplitude:

$$f^{\omega_{\mathrm{m}}}_{\mathfrak{i}\to\mathfrak{f}}(\vartheta) = \frac{ikR_0}{4\pi} \sum_{\substack{\kappa\rho \\ \kappa\neq 0 \\ \kappa+\rho \text{ even}}} \Xi_{\kappa 0} \mathscr{D}^{\kappa*}_{-\rho,\Delta m}(\varphi_\varepsilon, \theta_\varepsilon, 0) F_{\kappa\rho} J_{|\rho|}(kR_0\vartheta) \mathcal{Y}^{\tilde{N}',\tilde{j}',m';\kappa}_{\tilde{N},\tilde{j},m}(\omega_{\mathrm{m}}), \quad (9.26)$$

where the field-dependent part is

$$\mathcal{Y}_{\tilde{N},\tilde{j},m}^{\tilde{N}',\tilde{j}',m';\kappa}(\omega_{\mathrm{m}}) = \sum_{\substack{Nj \\ N'j'}} \sqrt{\frac{2j+1}{2j'+1}} a_{Nj}^{\tilde{N}\tilde{j}}(\omega_{\mathrm{m}}) b_{N'j'}^{\tilde{N}'\tilde{j}'}(\omega_{\mathrm{m}}) C(j\kappa j'; m\Delta mm') \sum_{\Omega} c_{Nj}^{\Omega} c_{N'j'}^{\Omega} C(j\kappa j'; \Omega 0\Omega)$$

(9.27)

9.2.3 Results for He–O$_2$($X^3\Sigma$, $N = 0, j = 1 \to N', j'$) scattering in a magnetic field

The ^{16}O$_2$($^3\Sigma^-$) molecule has a rotational constant $B = 1.4377$ cm^{-1}, a spin-rotation constant $\gamma = -0.0084$ cm^{-1}, and a spin-spin constant $\lambda = 1.9848$ cm^{-1} [324]. According to Ref. [325], the ground state He–O$_2$ potential energy surface has a global minimum of -27.90 cm^{-1}, which can be neglected at a collision energy 200 cm^{-1} (corresponding to a wave number $k = 6.49$ Å^{-1}). A small value of the massey parameter, $\xi \approx 0.1$, ensures the validity of the sudden approximation. The "hard shell" of the potential energy surface at this collision energy is shown in Fig. 9.2, and the Legendre moments $\Xi_{\kappa 0}$, obtained from a fit to the potential energy surface of Ref. [325], are listed in Table 9.2. Since the He–O$_2$ potential is of D$_{2\mathrm{h}}$ symmetry, only even Legendre moments are nonzero.

Furthermore, since the nuclear spin of ^{16}O is zero and the electronic ground state antisymmetric (a $^3\Sigma_g^-$ state), only rotational states with an odd rotational quantum number N are allowed. We will assume that the O$_2$ molecule is initially in its rotational ground state, $|N = 1, j = 0, m = 0\rangle$.

Expression (9.26) for the scattering amplitude further simplifies for particular geometries. In what follows, we will consider two such geometries.

(i) Magnetic field *parallel* to the initial wave vector, $\mathscr{H} \parallel \mathbf{k}$, in which case the scattering amplitude becomes:

$$f_{1,0,0 \to N',j',m'}^{\omega_{\mathrm{m}},\parallel}(\vartheta) = \frac{ikR_0}{4\pi} J_{|m'|}(kR_0\vartheta) \sum_{\substack{\kappa \neq 0 \\ \kappa \text{ even}}} \Xi_{\kappa 0} F_{\kappa m'} \mathcal{Y}_{1,0,0}^{\tilde{N}',\tilde{j}',m';\kappa}(\omega_{\mathrm{m}})$$

(9.28)

(ii) Magnetic field *perpendicular* to the initial wave vector, $\mathscr{H} \perp \mathbf{k}$, in which case Eq. (9.26) simplifies to:

$$f_{1,0,0 \rightarrow N',j',m'}^{\omega_\mathrm{m},\perp}(\vartheta) = \frac{ikR_0}{4\pi} \sum_{\substack{\kappa,\rho \text{ even} \\ \kappa \neq 0}} \Xi_{\kappa 0} \, d_{-\rho,m'}^{\kappa}(\tfrac{\pi}{2}) F_{\kappa\rho} J_{|\rho|}(kR_0\vartheta) \mathcal{Y}_{1,0,0}^{\tilde{N}',\tilde{j}',m';\kappa}(\omega_\mathrm{m}) \qquad (9.29)$$

Eqs. (9.28) and (9.29) imply that for either geometry, only partial cross sections for the $N = 1, j = 0, m = 0 \rightarrow N', j', m'$ collisions with m' even can contribute to the scattering. This is particularly easy to see in the $\mathscr{H} \parallel \mathbf{k}$ case, where the $F_{\kappa m'}$ coefficients vanish for m' odd as $F_{\kappa\rho}$ vanishes for odd $\kappa + \rho$. In the $\mathscr{H} \perp \mathbf{k}$ case, a summation over ρ arises. Since for κ even and m' odd the real Wigner matrices obey the relation $d_{-\rho,m'}^{\kappa}\left(\frac{\pi}{2}\right) = -d_{\rho,m'}^{\kappa}\left(\frac{\pi}{2}\right)$, the sum over ρ vanishes and so do the partial cross sections for m' odd.

The differential cross sections of the He–O$_2$ ($N = 1, j = 0 \rightarrow N', j'$) collisions, calculated from Eq. (9.17), are presented in Fig. 9.5. Also shown is the elastic cross section, obtained from the scattering amplitude (5.20). The differential cross sections are shown for the field-free case, $\omega_\mathrm{m} = 0$, as well as for $\omega_\mathrm{m} = 5$, which for O$_2$ corresponds to a magnetic field $\mathscr{H} = 7.7$ T.

The angular dependence of the differential cross sections is determined by the Bessel functions appearing in the scattering amplitudes (9.28) and (9.29). In the parallel case, the angular dependence is given expressly by $J_{|m'|}(kR_0\vartheta)$, and is not affected by the magnetic field. Since only even-κ terms contribute to the sum in the scattering amplitude and the coefficients $F_{\kappa\rho}$ vanish for $\kappa + \rho$ odd, the differential cross sections are given solely by even Bessel functions. This is the case for both parallel and perpendicular geometries. As the elastic scattering amplitude is given by an odd Bessel function, Eq. (5.20), the elastic and rotationally inelastic differential cross sections oscillate with an opposite phase.

According to the general properties of Bessel functions [295], at large angles the phase shift between different even Bessel functions disappears and their asymptotic
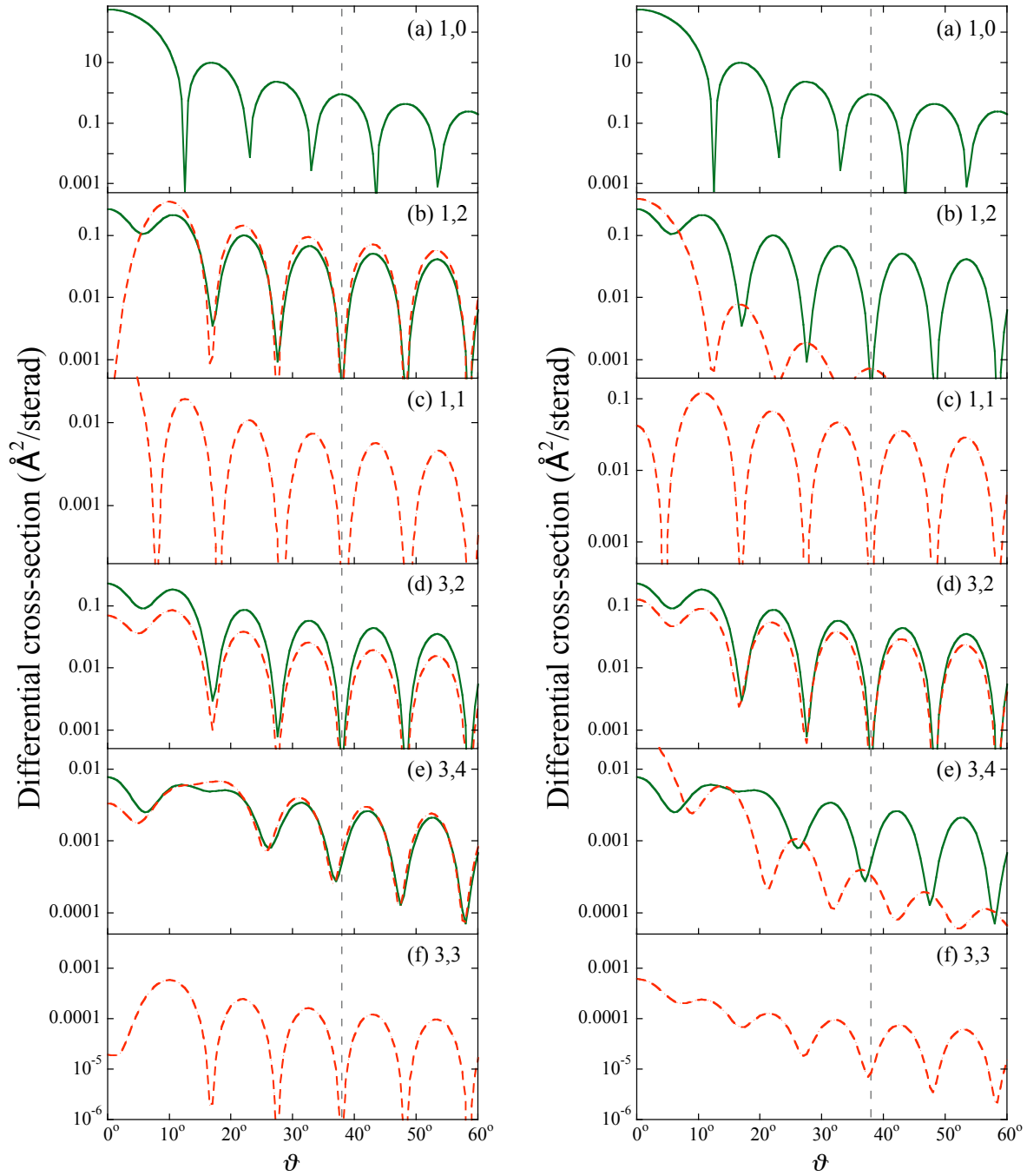
Figure 9.5: Differential cross sections for the He–O$_2$ ($N = 1, j = 0 \rightarrow N', j'$) collisions in a magnetic field $\omega_{\mathrm{m}} = 5$ (red dashed line) parallel to the relative velocity vector, $\mathscr{H} \parallel \mathbf{k}$ (left) and perpendicular to the relative velocity vector, $\mathscr{H} \perp \mathbf{k}$ (right). The field-free cross sections are shown by the green solid line. The collision energy is 200 cm^{-1}. The dashed vertical line serves to guide the eye in discerning the angular shifts of the partial cross sections. The field-free cross sections for the scattering to final states with $j' = N'$ vanish, see text.

form is given by Eq. (9.18). For the system under consideration, the phase shift between $J_0(kR_0\vartheta)$ and $J_2(kR_0\vartheta)$ functions becomes negligibly small at angles about $40°$, while the shift between $J_4(kR_0\vartheta)$ and either $J_0(kR_0\vartheta)$ or $J_2(kR_0\vartheta)$ can only be neglected at angles about $120°$. Therefore, if the cross section is comprised only of J_0 and J_2 contributions, it will not be shifted with respect to the field-free case, while there may appear a field-iduced phase shift if the J_4 Bessel function also contributes. Indeed, in the parallel case, the $1,0 \to 3,4$ cross section, presented in the left panel of Fig. 9.5 (e), exhibits a slight phase shift. In the perpendicular case, the Bessel functions $J_{|\rho|}(kR_0\vartheta)$ for a range of ρ's are mixed, see Eq. (9.29), which results in a field-induced phase shift for both the $1,0 \to 1,2$ and $1,0 \to 3,4$ transitions. Fig. 9.5 shows the differential cross sections only up to $60°$, since this angular range dominates the integral cross sections. However, the phase shifts disappear only at larger angles, of about $120°$.

The most dramatic feature of the magnetic field dependence of the differential cross sections is the onset of inelastic scattering for channels that are closed in the absence of the field: these involve the transitions $N = 1, j = 0 \to N', j'$ with $j' = N'$. That these channels are closed in the field-free case can be gleaned from the scattering amplitude (9.28) for $\omega_m = 0$, which reduces to

$$f_{1,0,0 \to N',j',m'}^{FF}(\vartheta) = \frac{ikR_0}{4\pi} J_{|m'|}(kR_0\vartheta) \frac{\Xi_{j'0}}{\sqrt{2j'+1}} F_{j'm'} c_{N'j'}^0 \qquad (9.30)$$

This field-free amplitude vanishes because the $c_{N'j'}^0$ coefficients are zero for $N' = j'$, as can be shown by the diagonalization of the field-free Hamiltonian (9.19). As a result, the field-free cross sections for the transitions to $1,1$ and $3,3$ states vanish. The hybridization by a magnetic field brings in coefficients $c_{N'j'}^{\pm 1}$ which are nonvanishing for $N' = j'$. The feature manifests itself in the integral cross sections as well.

9.3 Scattering of $^2\Pi$ molecules by closed-shell atoms in magnetic fields

9.3.1 The $^2\Pi$ molecule in magnetic field

In this Section, we consider a Hund's case (a) molecule, equivalent to a linear symmetric top. A good example of such a molecules is the OH radical in its electronic ground state, $X^2\Pi_\Omega$, whose electronic spin and orbital angular momenta are strongly coupled to the molecular axis. Each rotational state within the $^2\Pi_\Omega$ ground state is equivalent to a symmetric-top state $|j, \Omega, m\rangle$ with projections Ω and m of the total angular momentum $\mathbf{j}$ on the body- and space-fixed axes, respectively. Due to a coupling of the Π state with a nearby Σ state [326], the levels with the same Ω are split into nearly-degenerate doublets whose members have opposite parities. The Ω doubling of the $^2\Pi_{\frac{3}{2}}$ state of OH increases as j^3, whereas that of the $^2\Pi_{\frac{1}{2}}$ state increases linearly with j [283]. In our study, we used the values of the Ω doubling listed in Table 8.24 of Ref. [326].

The definite-parity rotational states of a Hund's case (a) molecule can be written as:

$$|j, m, \Omega, \epsilon\rangle = \frac{1}{\sqrt{2}}\left[|j, m, \Omega\rangle + \epsilon|j, m, -\Omega\rangle\right], \qquad (9.31)$$

where the symmetry index ϵ distinguishes between the members of a given Ω doublet. Here and below we use the definition $\Omega \equiv |\Omega|$. The symmetry index takes the value of $+1$ or -1 for e or f levels, respectively. The parity of wave function (9.31) is equal to $\epsilon(-1)^{j-\frac{1}{2}}$ [299]. The rotational energy level structure of the OH radical in its $X^2\Pi_\Omega$ state is reviewed in Sec. 2.1.4 of Ref. [327].

When subject to a magnetic field, a Hund's case (a) molecule acquires a Zeeman potential,

$$V_{\mathrm{m}} = j_Z \omega_{\mathrm{m}} B, \qquad (9.32)$$

with j_Z the Z component of the total angular momentum (apart from nuclear spin),
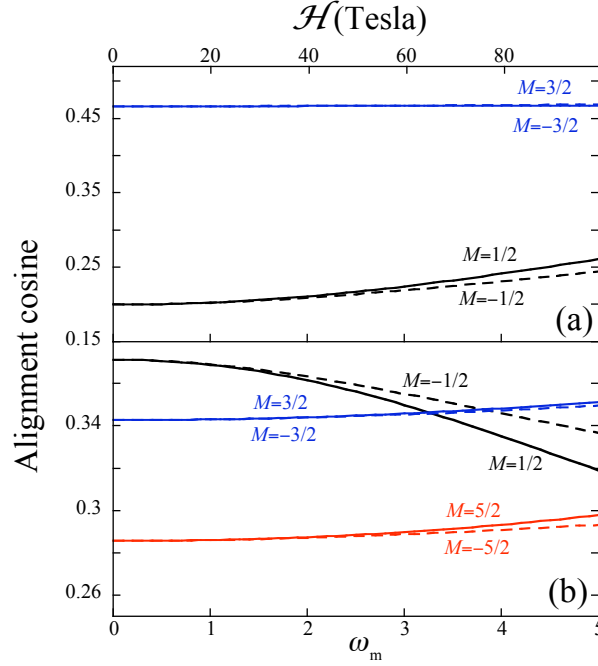
$\mathcal{H}$(Tesla)

Figure 9.6: Expectation values of the alignment cosine $\langle \cos^2 \theta \rangle$ for the $3/2, f$ (a) and $5/2, f$ (b) states of the OH molecule, as a function of the magnetic field strength parameter ω_m.

$\mathbf{j}$, and

$$\omega_\mathrm{m} \equiv (g_L \Lambda + g_S \Sigma) \mu_B \mathcal{H}/B \tag{9.33}$$

Here Λ and Σ are projections of the orbital, $\mathbf{L}$, and spin, $\mathbf{S}$, electronic angular momenta on the molecular axis, and $g_L = 1$ is the electronic orbital gyromagnetic ratio, cf. Eqs. (9.8) and (9.21). The matrix elements of Hamiltonian (9.32) in the definite-parity basis (9.31) are

$$\langle j'm'\epsilon'|V_\mathrm{m}|jm\epsilon \rangle = \omega_\mathrm{m} B \left(\frac{1 + \epsilon\epsilon'(-1)^{j+j'+2\Omega}}{2} \right) (-1)^{j+j'+m-1/2}$$

$$\times \sqrt{(2j+1)(2j'+1)} \begin{pmatrix} j & 1 & j' \\ -\Omega & 0 & \Omega' \end{pmatrix} \begin{pmatrix} j' & 1 & j \\ m & 0 & -m' \end{pmatrix}, \tag{9.34}$$

where the last two factors are $3j$-symbols [283], [284]. The matrix elements (9.34) are

a generalization of Eqs. (16.13)–(16.18), and were presented, e.g., in Ref. [328]. For an OH molecule in its ground $^2\Pi_{3/2}$ state, the parity factor, $(1 + \epsilon\epsilon'(-1)^{j+j'+2\Omega})/2$, reduces to $\delta_{\epsilon\epsilon'}$, which means that the Zeeman interaction preserves parity. The Zeeman eigenstates are hybrids of the field-free states (9.31):

$$\left|\tilde{j}, m, \Omega, \epsilon; \omega_{\mathrm{m}}\right\rangle = \sum_j a_{jm}^{\tilde{j}}(\omega_{\mathrm{m}})|j, m, \Omega, \epsilon\rangle, \tag{9.35}$$

where $\tilde{j}$ designates the angular momentum quantum number of the field-free state that adiabatically correlates with a given state in the field. The coefficients $a_{jm}^{\tilde{j}}(\omega_{\mathrm{m}})$ can be obtained by the diagonalization of the Hamiltonian (9.32) in the basis (9.31).

The dependence of the alignment cosine, $\langle\cos^2\theta\rangle$, on the field strength parameter ω_{m} is shown in Fig. 9.6 for the $3/2, f$ and $5/2, f$ states of the OH molecule. The matrix elements of the $\langle\cos^2\theta\rangle$ operator are listed in Appendix 16.4.

9.3.2 The field-dependent scattering amplitude

We consider scattering from the initial $j = 3/2, e$ state to some $j', e/f$ state. As in the previous Sections, we use Eq. (9.11) to transform the wavefunctions (9.31). Considering only the Ω-conserving transitions ($\Omega' = \Omega$), the initial and final states are:

$$|\mathfrak{i}\rangle \equiv \left|\tilde{j}, m, \Omega, \epsilon, \omega_{\mathrm{m}}\right\rangle$$
$$= \frac{1}{\sqrt{2}} \sum_j \sqrt{\frac{2j+1}{4\pi}} a_{jm}^{\tilde{j}}(\omega_{\mathrm{m}}) \sum_\xi \mathscr{D}_{\xi m}^j(\varphi_\varepsilon, \theta_\varepsilon, 0) \left[\mathscr{D}_{\xi\Omega}^{j*}(\varphi, \theta, 0) + \epsilon\mathscr{D}_{\xi-\Omega}^{j*}(\varphi, \theta, 0)\right], \tag{9.36}$$

$$\langle\mathfrak{f}| \equiv \left\langle\tilde{j}', m', \Omega, \epsilon', \omega_{\mathrm{m}}\right|$$
$$= \frac{1}{\sqrt{2}} \sum_{j'} \sqrt{\frac{2j'+1}{4\pi}} b_{j'm'}^{\tilde{j}'}(\omega_{\mathrm{m}}) \sum_{\xi'} \mathscr{D}_{\xi'm'}^{j'*}(\varphi_\varepsilon, \theta_\varepsilon, 0) \left[\mathscr{D}_{\xi'\Omega'}^{j'}(\varphi, \theta, 0) + \epsilon'\mathscr{D}_{\xi'-\Omega'}^{j'}(\varphi, \theta, 0)\right] \tag{9.37}$$

By substituting Eqs. (9.36) and (9.37) into Eq. (5.42), we obtain a closed expression for the scattering amplitude:

$$f_{i\to f}^{\omega_m}(\vartheta) = \frac{ikR_0}{4\pi} \sum_{\substack{\kappa\rho \\ \kappa\neq 0 \\ \kappa+\rho \text{ even}}} \Xi_{\kappa 0} \mathscr{D}_{-\rho,\Delta m}^{\kappa*}(\varphi_\varepsilon, \theta_\varepsilon, 0) F_{\kappa\rho} J_{|\rho|}(kR_0\vartheta) \mathcal{Z}_{\tilde{j},m,\epsilon;\Omega}^{\tilde{j}',m',\epsilon';\kappa}(\omega_m), \qquad (9.38)$$

where

$$\mathcal{Z}_{\tilde{j},m,\epsilon;\Omega}^{\tilde{j}',m',\epsilon';\kappa}(\omega_m) = \sum_{jj'} \sqrt{\frac{2j+1}{2j'+1}} a_{jm}^{\tilde{j}}(\omega_m) b_{j'm'}^{\tilde{j}'}(\omega_m)$$

$$\times C(j\kappa j'; m\Delta mm') C(j\kappa j'; \Omega 0\Omega) \left[1 + \epsilon\epsilon'(-1)^{\kappa+\Delta j} \right] \quad (9.39)$$

Eq. (9.38) simplifies for parallel or perpendicular orientations of the magnetic field with respect to the relative velocity vector.

(i) For $\mathscr{H} \parallel \mathbf{k}$ we have:

$$f_{i\to f}^{\omega_m,\parallel}(\vartheta) = \frac{ikR_0}{4\pi} J_{|\Delta m|}(kR_0\vartheta) \sum_{\substack{\kappa\neq 0 \\ \kappa+\Delta m \text{ even}}} \Xi_{\kappa 0} F_{\kappa\Delta m} \mathcal{Z}_{\tilde{j},m,\epsilon;\Omega}^{\tilde{j}',m',\epsilon';\kappa}(\omega_m), \qquad (9.40)$$

(ii) and for $\mathscr{H} \perp \mathbf{k}$ we obtain:

$$f_{i\to f}^{\omega_m,\perp}(\vartheta) = \frac{ikR_0}{4\pi} \sum_{\substack{\kappa\rho \\ \kappa\neq 0 \\ \kappa+\rho \text{ even}}} \Xi_{\kappa 0} d_{-\rho,\Delta m}^{\kappa*}(\tfrac{\pi}{2}) F_{\kappa\rho} J_{|\rho|}(kR_0\vartheta) \mathcal{Z}_{\tilde{j},m,\epsilon;\Omega}^{\tilde{j}',m',\epsilon';\kappa}(\omega_m) \qquad (9.41)$$

9.3.3 Results for He–OH($X^2\Pi_{\frac{3}{2}}, j = \frac{3}{2}, f \to j', e/f$) scattering in a magnetic field

According to Ref. [329], the ground state He–OH potential energy surface has a global minimum of -30.02 cm^{-1}, which could be considered negligible with respect to a collision energy on the order of 100 cm^{-1}, as for the He–CaH and He–O$_2$ systems treated above. However, the OH molecule has a large rotational constant,

$B = 18.5348$ cm^{-1}, and so the Massey parameter (5.21) becomes significantly smaller than unity only at higher energies. Therefore, in order to ensure the validity of the sudden approximation, we had to work with a collision energy of 1000 cm^{-1} ($k = 13.86$ Å^{-1}; Massey parameter $\xi \approx 0.5$). The corresponding equipotential line of the He–OH ($^2\Pi$) potential energy surface is shown in Fig. 9.2, and the Legendre moments, $\Xi_{\kappa 0}$, obtained by fitting the surface, are listed in Table 9.2.

Because of the negative spin-orbit constant, $A = -139.051$ cm^{-1} [326], the Ω doublet of the OH($X^2\Pi_\Omega$) molecule is inverted, with the paramagnetic $^2\Pi_{3/2}$ state as its ground state. Since $|A| \gg |B|$, we can see why the OH molecule can be well described by the Hund's case (a) coupling scheme.

In what follows, we consider OH ($^2\Pi$) radicals prepared in the $v = 0, \Omega = \frac{3}{2}, j = \frac{3}{2}, f$ state by hexapole state selection, like, e.g., in Ref. [107]. The molecules enter a magnetic field region where they collide with ^{4}He atoms. The scattered molecules are state-sensitively detected in a field-free region.

We note that due to a large rotational constant, the Zeeman effect in the case of the OH radical is very weak, and so are the field-induced changes of the scattering. The differential cross sections for the He–OH collisions, as obtained from Eq. (9.17), are shown in Fig. 9.7, together with the elastic scattering cross section obtained from Eq. (5.20). The differential cross sections are presented for the field-free case, $\omega_{\mathrm{m}} = 0$, as well as for $\omega_{\mathrm{m}} = 5$, which for the OH radical corresponds to an extreme field strength of $\mathscr{H} = 99.2$ T. First, let us consider the field-free scattering amplitude

$$
\begin{aligned}
f_{\mathrm{i} \to \mathrm{f}}^{w=0}(\vartheta) = {} & \sqrt{\frac{2j+1}{2j'+1}} J_{|\Delta m|}(kR_0\vartheta) \\
& \times \sum_{\substack{\kappa \neq 0 \\ \kappa + \Delta m \text{ even}}} \Xi_{\kappa 0} F_{\kappa, \Delta m} C(j\kappa j'; m\Delta m m') C(j\kappa j'; \Omega 0\Omega) \left[1 + \epsilon\epsilon'(-1)^{\kappa+\Delta j}\right]
\end{aligned} \quad (9.42)
$$

We see that the angular dependence of the amplitude is given by the Bessel function $J_{|\Delta m|}$. The term in the square brackets and the $F_{\kappa,\Delta m}$ coefficient provide a selection rule: $\Delta m + \Delta j$ must be even for parity conserving ($f \to f$) transitions, and odd for parity breaking ($f \to e$) transitions.
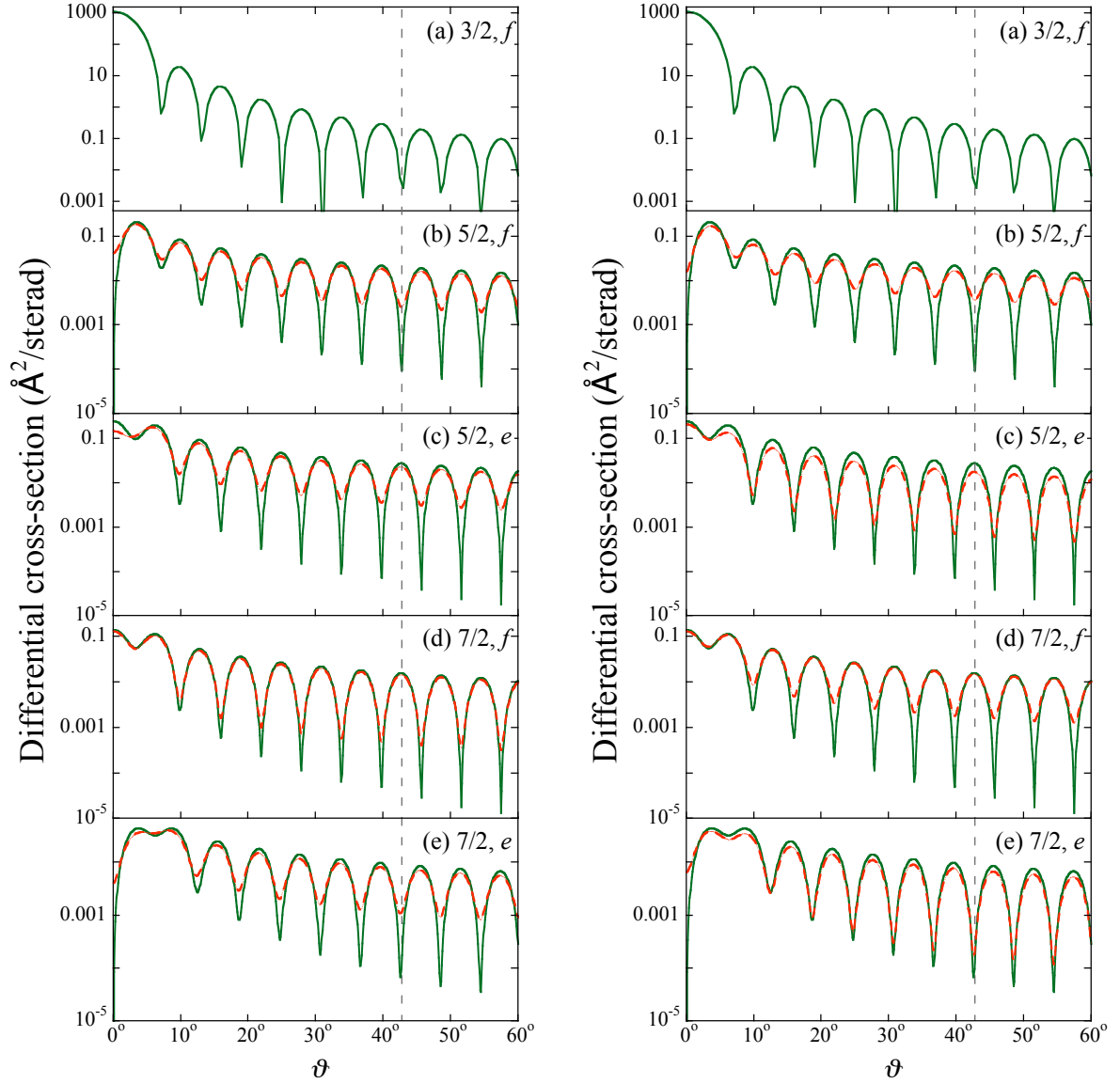
Figure 9.7: Differential cross sections for the He–OH ($j = 3/2, f \to j', e/f$) collisions in a magnetic field $\omega_{\mathrm{m}} = 5$ (red dashed line) parallel to the relative velocity vector, $\mathscr{H} \parallel \mathbf{k}$ (left) and perpendicular to the relative velocity vector, $\mathscr{H} \perp \mathbf{k}$ (right). The field-free cross sections are shown by the green solid line. The collision energy is 1000 cm^{-1}. The dashed vertical line serves to guide the eye in discerning the angular shifts of the partial cross sections. See text.

The effect of this selection rule can be seen in Fig. 9.7. The elastic cross section, Fig. 9.7 (a), is proportional to an odd Bessel function, cf. Eq. (5.20). Therefore, it is in phase with the $3/2, f \to 5/2, f$ and $3/2, f \to 7/2, e$ cross sections, but out of phase with $3/2, f \to 5/2, e$ and $3/2, f \to 7/2, f$ cross sections.

For a magnetic field parallel to the relative velocity, $\mathscr{H} \parallel \mathbf{k}$, the angular dependence is given explicitly by $J_{|\Delta m|}(kR_0\vartheta)$, and is seen to be independent of the field, cf. Eq. (9.40). Therefore, as the left panel of Fig. 9.7 shows, no field-induced phase shift of the differential cross sections takes place. For $\mathscr{H} \perp \mathbf{k}$, a mix of Bessel functions, $J_{|\rho|}(kR_0\vartheta)$, contribute to the sum. However, since the Zeeman effect is so weak for the OH molecule, it is the $a_{jm}^{\tilde{j}}(\omega_\mathrm{m})$, $b_{j'm'}^{\tilde{j}'}(\omega_\mathrm{m})$ hybridization coefficients with $j = \tilde{j}$ which provide the main contribution to the sum, even at $\omega_\mathrm{m} \approx 5$. As a result, no contributions from higher Bessel functions are drawn in, and so no significant field-induced phase shift is observed for the perpendicular case either.

10 The $\mathbf{k} - \mathbf{k}' - \mathbf{j}'$ vector correlation in Ar–NO($X^2\Pi$) collisions

10.1 Alignment moments: comparison with experiment and exact theory

In this section we apply the Fraunhofer model of vector correlations, Sec. 6, to the investigation of inelastic collisions of closed-shell atoms with rotationally polarized symmetric-top-equivalent linear molecules.

For this case study, we chose the $\mathbf{k} - \mathbf{k}' - \mathbf{j}'$ three-vector correlation in the Ar–NO ($j = \Omega = 1/2 \to j', \Omega' = 1/2$) collisions, as this can be compared with the results of experiments and close-coupling calculations of Wade *et al.* [93]. We restrict our considerations to the two lowest rotational channels, $j' = 9/2$ and $17/2$, reported in Ref. [93], and average over the e/f parity states as these have not been resolved in the experiment. We take into account the energy spread of the molecular beams, $E_{\mathrm{coll}} = 520 \pm 70$ cm^{-1}, by averaging our results over three collision energies corresponding to the most probable energy and to energies at half-maximum of an essentially Gaussian collision energy distribution. In determining the Ar–NO potential, we rely on the most recent potential energy surface (PES) obtained by Sumiyoshi *et al.* [305] and make use of only the average potential, V_{sum}, since the differential and depolarization cross sections are found to be only weakly affected by the difference PES, V_{dif} [307, 330].

Table 10.1: The physical meaning and range of the $a_0^2(\mathbf{j}')$ and $a_{2+}^2(\mathbf{j}')$ alignment polarization moments. The Z axis points along the initial relative velocity $\mathbf{k}$. The final relative velocity $\mathbf{k}'$ lies in the $X > 0$ half of the XZ plane. The $a_0^2(\mathbf{j}')$ moment accounts for alignment of $\mathbf{j}'$ with respect to $\mathbf{k}$. Positive (negative) values of $a_0^2(\mathbf{j}')$ correspond to $\mathbf{j}' \parallel \mathbf{k}$ ($\mathbf{j}' \perp \mathbf{k}$, in which case $\mathbf{j}'$ lies in the XY plane). The positive (negative) values of the $a_{2+}^2(\mathbf{j}')$ moment correspond to alignment of $\mathbf{j}'$ along the X-axis (Y-axis). The $a_{2-}^2(\mathbf{j}')$ moment vanishes identically. The indicated ranges of the moments correspond to the high-j limit.

Moment	$a_0^2(\mathbf{j}')$	$a_{2+}^2(\mathbf{j}')$
Meaning	$\mathbf{j}'$ along Z	$\mathbf{j}'$ along Y or X
Range	$\mathbf{j}' \perp Z \;\rightarrow\; -1/2$	$\mathbf{j}' \parallel Y \;\rightarrow\; -\sqrt{3}/2$
	$\mathbf{j}' \parallel Z \;\rightarrow\; 1$	$\mathbf{j}' \parallel X \;\rightarrow\; \sqrt{3}/2$

The PES of Ref. [305] comes close to that of Alexander [308] and both PES's yield essentially the same polarization moments.

In order to characterize the $\mathbf{k} - \mathbf{k}' - \mathbf{j}'$ three-vector correlation, we make use of the alignment moments $a_0^2(\mathbf{j}')$ and $a_{2+}^2(\mathbf{j}')$ of the diatomic's final rotational angular momentum $\mathbf{j}'$ with respect to the XY plane. The $a_0^2(\mathbf{j}')$ moment accounts for alignment of $\mathbf{j}'$ with respect to the initial relative velocity $\mathbf{k}$ and, in the high-j' limit, ranges between $-1/2$ and 1. Positive (negative) values of $a_0^2(\mathbf{j}')$ correspond to $\mathbf{j}' \parallel \mathbf{k}$ ($\mathbf{j}' \perp \mathbf{k}$, in which case $\mathbf{j}'$ lies in the XY plane). The $a_{2+}^2(\mathbf{j}')$ moment varies from $-\sqrt{3}/2$ to $\sqrt{3}/2$ (in the high-j' limit). Its positive (negative) values correspond to alignment of $\mathbf{j}'$ along the X-axis (Y-axis). This is summarized in Table 10.1.

Figure 10.1 display the $a_0^2(\mathbf{j}')$ and $a_{2+}^2(\mathbf{j}')$ moments obtained in analytic form from the Fraunhofer model along with the results of experiment and close-coupling calculations of Wade *et al.* [93]. The agreement between the Fraunhofer model and the close-coupling calculation is compelling.

Unfortunately, only two experimental points are available for the scattering angles concerned. Therefore, it is not clear whether the oscillatory behavior at small-angles would indeed show up in an experiment. We hope that the present work will inspire an experiment whose resolution will suffice to clarify this issue.

One can see that for zero scattering angle, $\vartheta = 0$, $a_0^2 = -1/2$ and $a_{2+}^2 = 0$. The
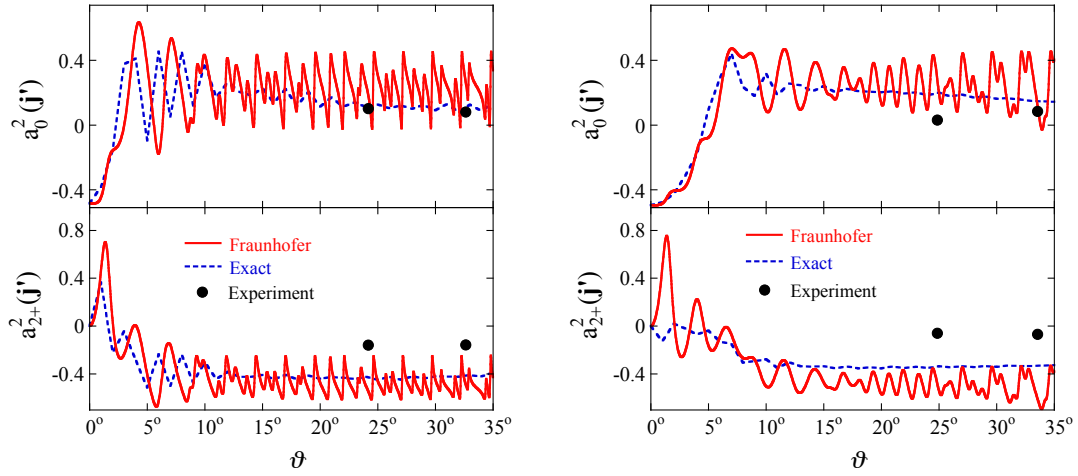
Figure 10.1: Polarization moments pertaining to the $\mathbf{k} - \mathbf{k'} - \mathbf{j'}$ three-vector correlation in Ar–NO ($j = \Omega = 1/2, \rightarrow j', \Omega' = 1/2$) collisions at 520 ± 70 cm^{-1}, for $j' = 9/2$ (left) and $j' = 17/2$ (right). The analytic results furnished by the Fraunhofer model (red solid line) are compared with the experiment (black dots) and close-coupling calculations (blue dashed line) of Ref. [93].
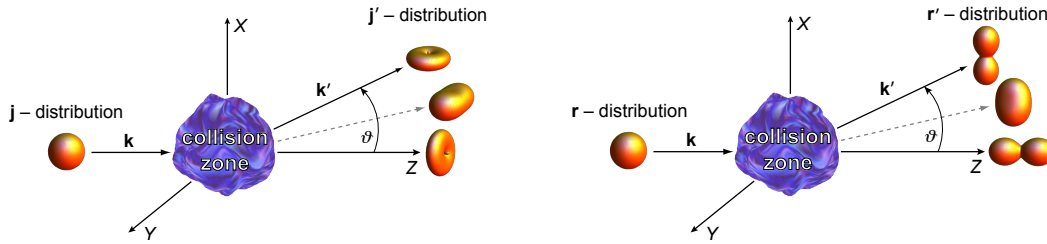

Figure 10.2: Distribution of final angular momentum vector, $\mathbf{j'}$, and internuclear axes, $\mathbf{r'}$, when the initial distributions of $\mathbf{j}$ and $\mathbf{r}$ are unpolarized, illustrating the $\mathbf{k} - \mathbf{k'} - \mathbf{j'}$ three-vector correlation.

reason is geometric: in pure forward scattering, the $\mathbf{j'}$ vector must be perpendicular to $\mathbf{k}$. Also, since $\mathbf{k}$ is roughly parallel to $\mathbf{k'}$ for very small ϑ, the $\mathbf{j'}$ vector is approximately perpendicular to $\mathbf{k'}$. For small but nonzero scattering angles, $\vartheta \sim 5°$, the a_0^2 moment becomes positive, both for $j' = 9/2$ and $17/2$, indicating that $\mathbf{j'}$ tends to align along $\mathbf{k}$.

The a_{2+}^2 moment, on the other hand, exhibits narrow positive oscillations at very small angles ($\vartheta \approx 1°$), but is in general negative, which corresponds to alignment of $\mathbf{j'}$ along the Y-axis.

Figure 10.2 shows the distribution of the $\mathbf{j'}$ and $\mathbf{r'}$ vectors of the NO molecule after

a collision with Ar, obtained with Eq. (4.20), (4.21).

Interestingly, the polarization moments presented in this paper are in a quantitative agreement with the accurate, close-coupling calculations, while the differential cross sections for the Ar–NO scattering, presented in Chapter 7, agree only qualitatively. From this we draw the conclusion that the polarization moments are mainly due to the hard-core part of the potential. This conclusion is also supported by purely classical arguments based on the conservation of the projection of angular momentum on the collision's kinematic apse, see, e.g., Ref. [275]. The phase shift of the moment's oscillations as derived from the model with respect to those obtained from the close-coupling calculation is likely due to the non-diffractive contributions to scattering, attractive part of the Ar–NO potential, and breakdown of the sudden approximation.

The alignment moments of Fig. 10.1 were normalized by the differential cross sections obtained from the Fraunhofer model. Since the Fraunhofer differential cross sections decrease faster with the scattering angle than their close-coupling counterparts [196], the oscillations of the analytic polarization moments are left relatively undamped at large scattering angles.

The Fraunhofer model readily explains the above results: the analytic scattering amplitudes are proportional to the Bessel functions, which is a signature feature of diffraction. It is thus a diffractive oscillatory pattern that determines the angular dependence of the polarization moments. While the shape and frequency of the angular oscillations are entirely determined by the hard core of the PES, their position is somewhat influenced by the PES's attractive branch and non-diffractive contributions to the scattering, neglected within the model. The Clebsch-Gordan coefficients that appear in the scattering amplitude bring about selection rules that constrain the final parity of the states and the projections of the angular momentum $\mathbf{j}'$ on $\mathbf{k}$. Within the model, the shape of the scatterer enters through the Legendre moments of a series expansion of the hard-core PES in terms of Legendre polynomials, $P_\kappa(\cos\theta)$. The angular momentum algebra that the model entails gives rise to additional selection rules which allow for nonzero contributions to the polarization moments to arise only

from Legendre moments of order $\kappa \geq j' - j$. Therefore, the vector correlations for the $j = 1/2,\ 3/2 \rightarrow j' = 9/2$ channels are governed by the Legendre moment with $\kappa = 4$, whereas the $\kappa = 8$ Legendre moment governs the polarization moments of the $j = 1/2,\ 3/2 \rightarrow j' = 17/2$ channels.

Moreover, since the Fraunhofer model can account for collisions in an electrostatic field [196, 199], we investigated the effect of the field on the polarization moments. A field of 16 kV/cm, sufficient to significantly orient the NO molecule in the space-fixed frame, was found to cause only a tiny difference in the parity-resolved polarization moments as compared with the field-free ones. Upon averaging over the e/f states, the effect of the field was found to be altogether negligible.

In summary, we made use of the Fraunhofer model of direct rotationally inelastic atom–diatom collisions to study vector correlations in such collisions analytically. The vector correlations obtained from the model closely reproduce those extracted from close-coupling calculations which, in turn, agree well with experiment. The Fraunhofer model of vector correlations demonstrates that the stereodynamics of the Ar–NO rotationally inelastic collisions is contained solely in the diffractive part of the scattering amplitude which is governed by a single Legendre moment characterizing the anisotropy of the hard-core part of the system's PES. Given the "geometric" origin of this behavior – ordained by the angular momentum algebra – we expect to find a similar behavior in other systems.

10.2   Influence of higher-order polarization moments

The left panel of Fig. 10.3 shows the $a_{q\pm}^4(\mathbf{j}')$ moments to the $\mathbf{k} - \mathbf{k}' - \mathbf{j}'$ three-vector correlation in Ar–NO ($j = \Omega = 1/2, \rightarrow j', \Omega' = 1/2$) collisions at 520 cm^{-1}. All the moments oscillate about zero, with $a_0^4(\mathbf{j}')$ and $a_{4+}^4(\mathbf{j}')$ being in general slightly positive, and $a_{2+}^4(\mathbf{j}')$ slightly negative. Although the values of these moments are small, taking them into account in Eqs. (4.20), (4.21) slightly changes the distributions of $\mathbf{j}'$ and $\mathbf{r}'$ vectors shown in Fig. 10.4, the $\mathbf{j}'$ distribution becomes peaked in Y and Z directions at larger scattering angles. The right panel of Fig. 10.3 shows the $a_{q\pm}^6(\mathbf{j}')$ moments describing the $\mathbf{k} - \mathbf{k}' - \mathbf{j}'$ three-vector correlation. The average values of these moments are very small and they don't alter the distributions of $\mathbf{j}'$ and $\mathbf{r}'$ vectors presented in Fig. 10.4.
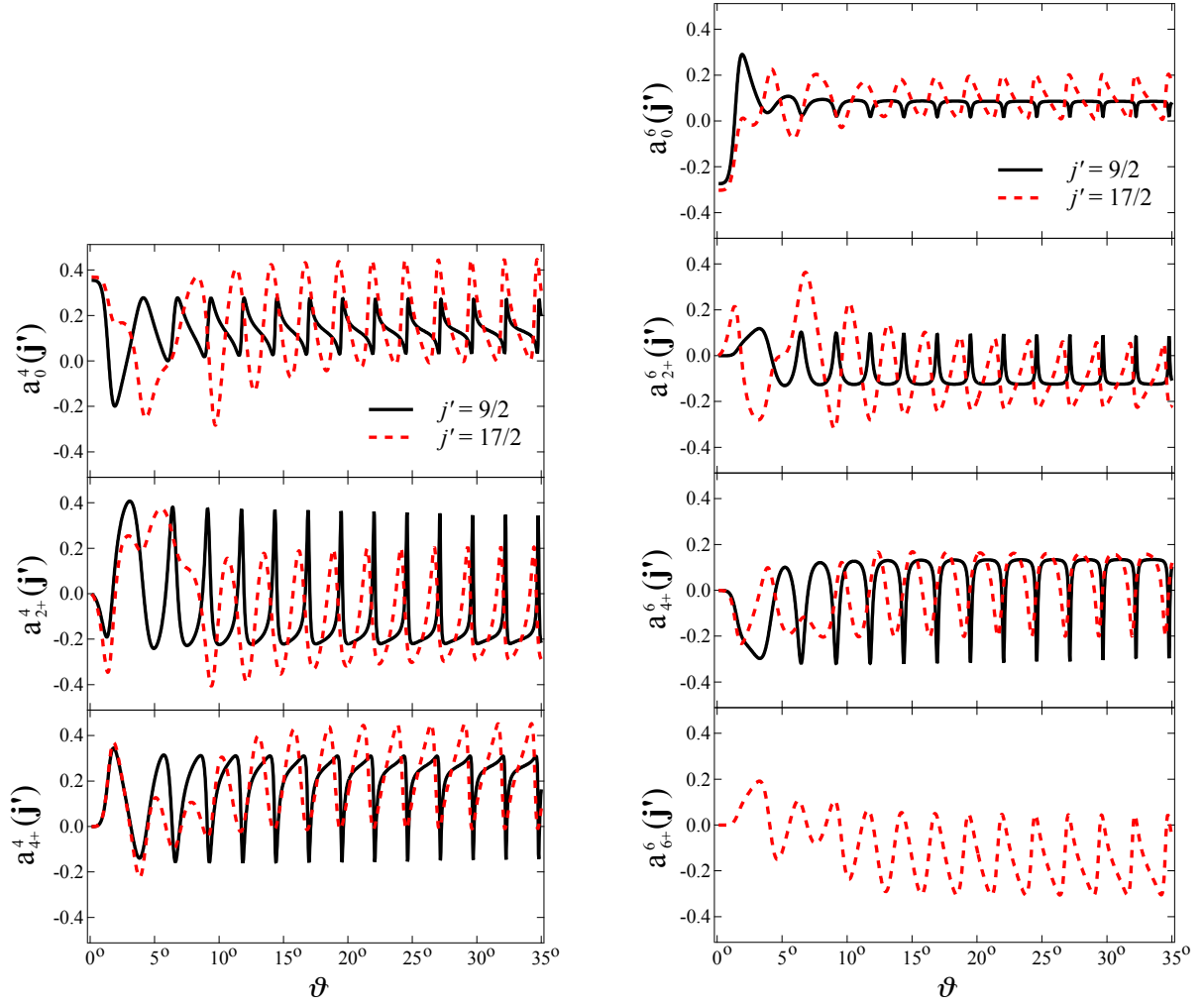
Figure 10.3: Polarization moments $a_{q\pm}^4(\mathbf{j}')$ and $a_{q\pm}^6(\mathbf{j}')$ pertaining to the $\mathbf{k} - \mathbf{k}' - \mathbf{j}'$ three-vector correlation in Ar–NO ($j = \Omega = 1/2, \rightarrow j', \Omega' = 1/2$) collisions at 520 cm^{-1}. There is no $a_{6+}^6(\mathbf{j}')$ moment for $j' = 9/2$.
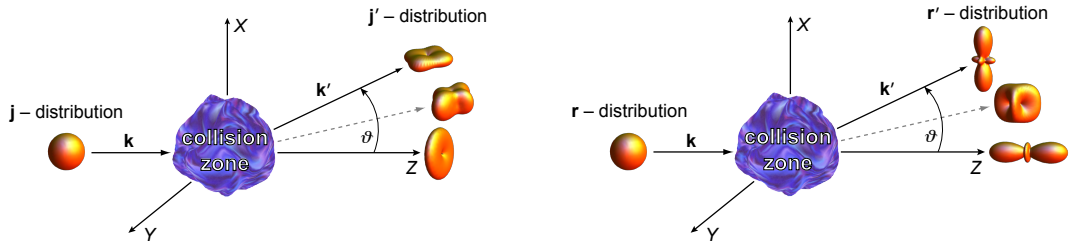
Figure 10.4: Distribution of final angular momentum vector, $\mathbf{j}'$, and internuclear axes, $\mathbf{r}'$, when the initial distributions of $\mathbf{j}$ and $\mathbf{r}$ are unpolarized, as in Fig. 10.2, but with $a_{q\pm}^4(\mathbf{j}')$ moments included.

11 The $\mathbf{k} - \mathbf{k'} - \mathbf{j'}$ vector correlation in other systems: the fingerprints of diffraction

> The moment of glory comes with the discovery
> of a new theory that does not solve any of the
> old problems, but renders them irrelevant.
>
> Gian-Carlo Rota, "Indiscrete thoughts"

Here we follow the previous line of research for Ar–NO to investigate the $\mathbf{k} - \mathbf{k'} - \mathbf{j'}$ three-vector correlation in collisions of He with NO, O_2, OH, and CaH, which allows us to identify the form factors ("fingerprints") of diffraction-driven stereodynamics.

First, we focus on vector correlations in the He–NO system, for different scattering channels and collision energies. We compare analytic model results with fully quantum close-coupling calculations performed using the HIBRIDON suite of computer codes [331] on the PES of Kłos et $al.$ [332] by Pablo Jambrina and Marcelo de Miranda. As before, in order to characterize the $\mathbf{k} - \mathbf{k'} - \mathbf{j'}$ three-vector correlation, we make use of the alignment moments $a_0^2(\mathbf{j'})$ and $a_{2+}^2(\mathbf{j'})$, which physical meaning and range moments is given in Table 10.1.

Figure 11.1 shows the $a_0^2(\mathbf{j'})$ and $a_{2+}^2(\mathbf{j'})$ moments for different channels of the He–NO ($j = \Omega = 1/2 \rightarrow j', \Omega' = 1/2$) system at a collision energy of 520 cm^{-1}. All the alignment moments we present below were obtained for unresolved initial and final lambda-doublet states. The compelling agreement of the Fraunhofer model with the exact calculations for the He–NO as well as for Ar–NO [200] systems attests to the predominant role of diffraction in shaping the stereodynamics of rotationally inelastic
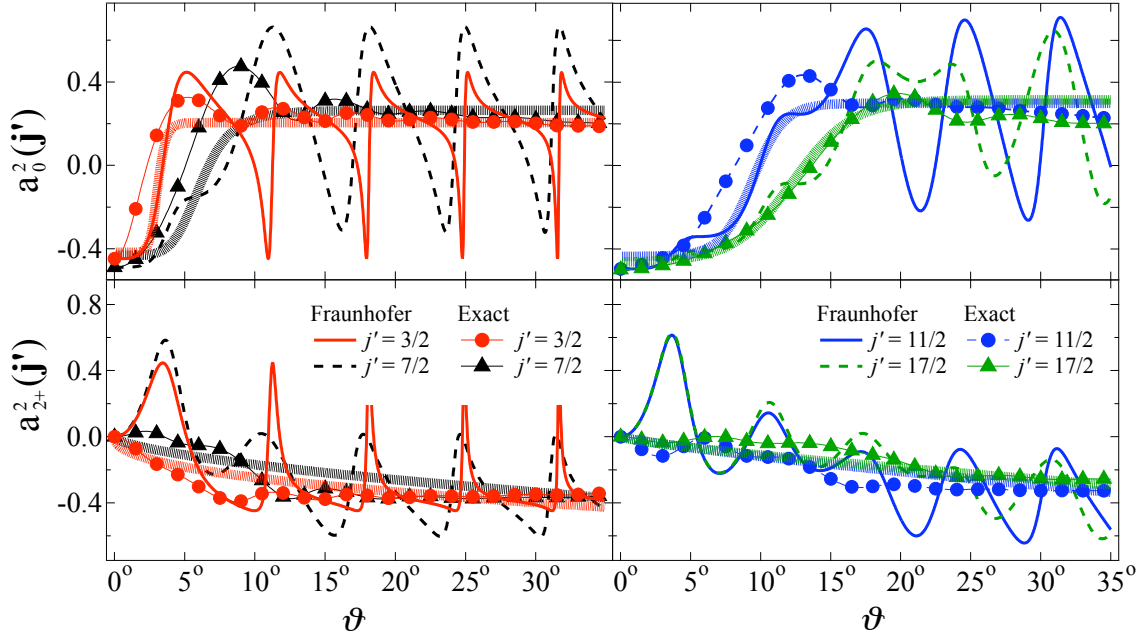
Figure 11.1: Polarization moments pertaining to the He–NO ($j = \Omega = 1/2 \to j', \Omega' = 1/2$) system at 520 cm^{-1}. Model results are shown by lines, exact computations – by symbols. Form factors of the alignment moments are shown by thick semitransparent lines.

collisions at thermal and hyperthermal energies. Furthermore, the agreement with the model shows that what matters the most – as far as the PES is concerned – is the 2D contour of its repulsive core. Save for the moments' oscillatory structure, which differs for different final states (as these arise due to different sets of the PES's Legendre moments), the diffraction manifests itself in the same way in all the scattering channels, i.e., it leaves behind the same fingerprints, shown in Fig. 11.1 by the thick semi-transparent lines: whereas the a_0^2 moments are negative for a purely forward scattering and increase at larger scattering angles where they approach a constant positive value, the a_{2+}^2 moments drop from a zero for forward scattering and tend to a constant negative value at larger scattering angles. This means that, due to geometric reasons, $\mathbf{j'}$ aligns perpendicular to $\mathbf{k}$ for a purely forward scattering. At larger scattering angles, $\mathbf{j'}$ aligns along the Z and Y axes, indicating that the molecular axis aligns preferentially in the X direction.
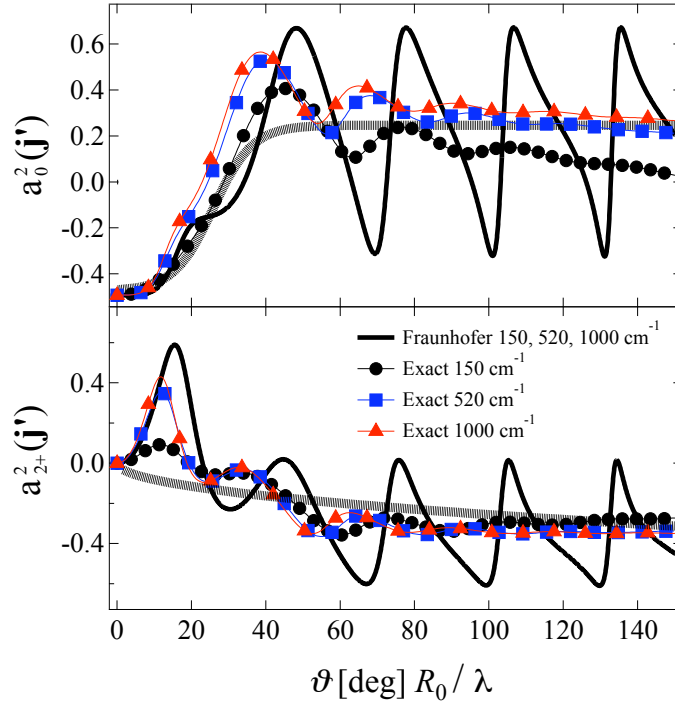
Figure 11.2: Polarization moments versus scaled scattering angle pertaining to the He–NO ($j = \Omega = 1/2 \to j' = 9/2, \Omega' = 1/2$) system at different collision energies. The Fraunhofer moments coincide exactly. Form factors of the alignment moments are shown by thick semitransparent lines. See text.

If the oscillations of the alignment moments are due to diffraction, they should scale with the de Broglie wavelength of the collision system and the size of the molecular scatterer, in analogy with the wavelength of light and the obstacle size in optics. Indeed, Figure 11.2 reveals such a scaling of the $a_0^2(\mathbf{j'})$ and $a_{2+}^2(\mathbf{j'})$ moments for the He–NO ($j = \Omega = 1/2 \to j' = 9/2, \Omega' = 1/2$) channel and a range of collision energies. The scaling was implemented by the transformation $\vartheta \to \vartheta R_0/\lambda$, where ϑ is the scattering angle, R_0 is the molecular size and λ is the de Broglie wavelength. Whereas the alignment moments furnished by the Fraunhofer model coincide exactly upon scaling in ϑ (black solid line), such a scaling brings the exact moments (filled circles, squares, and triangles) quite close to one another, but does not result in their exact matching. The remaining differences among the scaled exact moments corresponding to different collision energies attest to non-diffractive contributions to scattering, the influence of the attractive branch of the PES, and a breakdown of the
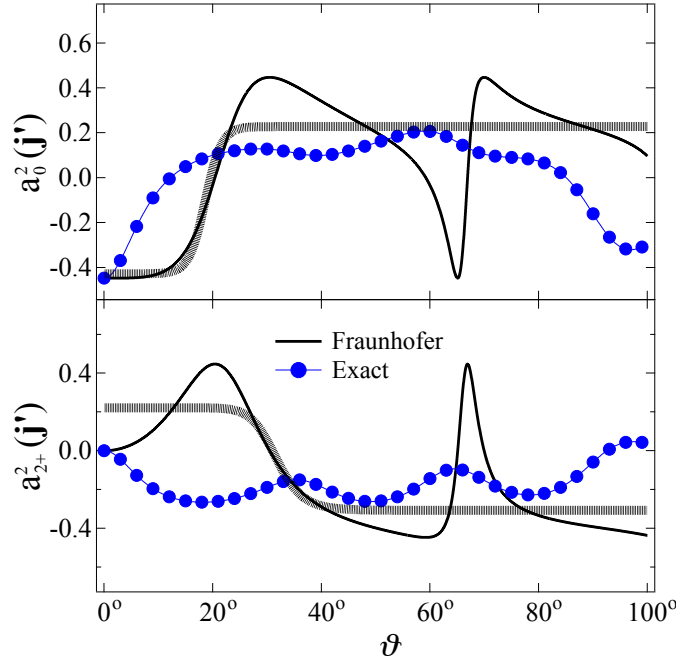
Figure 11.3: Polarization moments pertaining to the He–NO ($j = \Omega = 1/2 \to j' = 3/2, \Omega' = 1/2$) system at 10 cm^{-1}. Model results (black solid line) are compared with exact computation (blue circles). Form factors of the alignment moments are shown by thick semitransparent lines.

sudden approximation. For instance, the scaled exact moments corresponding to 520 and 1000 cm^{-1} come close to one another, while the oscillations for 150 cm^{-1} are quite off, especially for the $a_0^2(\mathbf{j'})$ moment. We ascribe this discrepancy to the potential well of 25 cm^{-1} [332] that brings about non-diffractive contributions to the stereodynamics while, at the same time, diminishing the role of the PES's "repulsive core." However, the form factor of the alignment moments (thick semitransparent line) is quite similar to the ones shown in Figure 11.1, indicating that diffraction leaves behind the same "fingerprint" for different collision energies and scattering channels. Interestingly, at low collision energies (10 cm^{-1}), the oscillations of the alignment moments fall further out of phase, but the form factors still remain in place. This is exemplified by Fig. 11.3 which shows the alignment moments for He–NO ($j = \Omega = 1/2 \to j' = 3/2, \Omega' = 1/2$) scattering at 10 cm^{-1}.

In order to see how the diffraction patterns change from one scattering system to another, we also examined the He–O$_2$, He–OH, and He–CaH systems at a collision
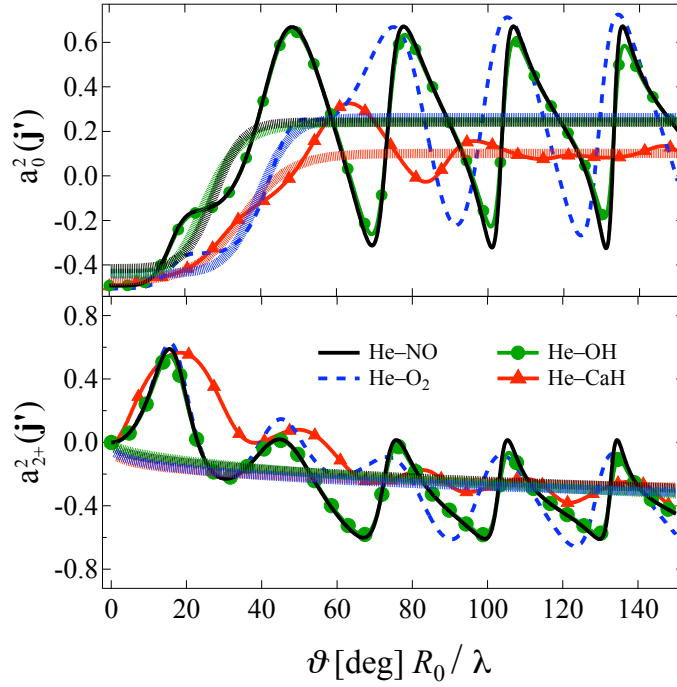
Figure 11.4: Polarization moments versus scaled scattering angle pertaining to the He–NO ($j = \Omega = 1/2 \to j' = 9/2, \Omega' = 1/2$), He–O$_2$ ($j = 0, N = 1, \to j' = 4, N' = 5$), He–OH ($j = \Omega = 1/2, \to j' = 9/2, \Omega' = 1/2$), and He–CaH ($j = 1/2, N = 0, \to j' = 11/2, N' = 6$) systems at 520 cm^{-1}. The moments were obtained using the Fraunhofer model. Form factors of the alignment moments are shown by thick semitransparent lines. See text.

energy of 520 cm^{-1} and similar channels, using potential energy surfaces of refs. [243, 325, 329].

Figure 11.4 shows the dependence of the polarization moments on the scaled scattering angle obtained from the Fraunhofer model, pertaining to the He–NO ($j = \Omega = 1/2 \to j' = 9/2, \Omega' = 1/2$), He–O$_2$ ($j = 0, N = 1, \to j' = 4, N' = 5$), He–OH ($j = \Omega = 1/2, \to j' = 9/2, \Omega' = 1/2$), and He–CaH ($j = 1/2, N = 0, \to j' = 11/2, N' = 6$) systems. One can see that the shape of the oscillations differs for different collision partners. Going from the most symmetric scatterer, O$_2$, through NO and OH to the most asymmetric one, CaH, one can see that the oscillations become increasingly asymmetric too, and their amplitudes decrease. This suggests relating the asymmetry and amplitude of the oscillations to the asymmetry of the repulsive core of the PES. However, the form factors (shown by the semi-transparent curves) that capture the

alignment moments are very similar to one another, indicating that the "fingerprints" of diffraction barely depend on the collision system.

In summary, in order to gain insight into the stereodynamics of rotationally inelastic atom-molecule collisions, we compared polarization moments obtained from an analytic model with those extracted from exact close-coupling calculations for the He–NO collisions. The model alignment moments were found to come as close to exact results as for the previously examined Ar–NO system, which reveals that the collision stereodynamics in question is governed by diffraction of matter waves from a 2D contour of the repulsive core of the potential (flat sharp-edged obstacle). The oscillatory patterns of the alignment moments due to diffraction scale with the de Broglie wavelength and the molecular size. Therefore, deviations from such patterns single out other contributions to the scattering which are mainly non-diffractive. Furthermore, diffraction leaves behind the same fingerprints for different channels and collision energies for a range of systems, including He–NO, He–O_2, He–OH, and He–CaH. These fingerprints can be used to identify diffraction-driven stereodynamics in future experiments and exact computations.

12 The $\mathbf{k} - \mathbf{k}' - \mathbf{j}'$ vector correlation in Ne–NO($A^2\Sigma$) collisions

> It's not enough that we do our best; sometimes
> we have to do what's required.
>
> Winston Churchill

12.1 Comparison of model and exact results

In experiment with ground state molecules, forward scattered species are hardly distinguishable from unscattered molecular beam coming through. As presented in Chapter 10, at small scattering angles very few points could be extracted from measurements of Wade *et al.* of the $\mathbf{j}'$-alignment in Ar–NO($X^2\Pi$) collisions. This problem might be overcame by colliding molecules preliminary excited into a higher electronic state. Recently Kay *et al.* performed accurate measurements of the $\mathbf{k} - \mathbf{k}' - \mathbf{j}'$ vector correlation in Ne–NO(A^Σ) collisions. In the experiment, the pump laser populates the $A^2\Sigma, N = 0, J = 1/2$ molecular states, that are then rotationally excited to $N' = 4, 5, 7, 9$ due to collisions with Ne. Two probe lasers are used to excite the scattering products into the $E^2\Sigma$ state and subsequently ionize the molecules. Velocity-mapped ion imaging measurements for different polarizations of the probe laser (within or perpendicular to the collision plane) allow to reveal the $a_0^2(\mathbf{j}')$, $a_{2+}^2(\mathbf{j}')$ alignment moments pertaining to the $\mathbf{k} - \mathbf{k}' - \mathbf{j}'$ vector correlation [94]. In this section we compare analytic alignment moments furnished by the Fraunhofer model with exact computations for the collision energies and channels relevant to the experiment of Kay *et al.*

Figures 12.1, 12.2 show differential cross sections and $a_0^2(\mathbf{j}')$, $a_{2+}^2(\mathbf{j}')$, $a_0^4(\mathbf{j}')$ polarization moments for Ne–NO ($A^2\Sigma; N = 0, J = 1/2 \to N'$) collisions with the values of $N' = 4, 5, 7, 9$ relevant to experiment of Kay *et al.*

Exact computations were performed by Jacek Kłos and Millard Alexander using the HIBRIDON package [331]. The DCS's and polarization moments were averaged over the spin-rotation splitting, $J' = N' \pm 1/2$, not resolved in experiment, and the spread of molecular beam, which was $\pm 7\%$ of the center-of-mass collision energy.

The Fraunhofer model takes accounts only for diffractive contributions, therefore the magnitudes of model DCS's are systematically smaller than exact ones. Also, since diffraction takes place only in the forward-scattering region, the agreement becomes worse for larger angles. One can see that the model alignment moments are in good agreement with the exact ones, for $N' = 4$ and 5, but the agreement is worse for higher N', especially for the $a_0^2(\mathbf{j}')$ moment.

To figure out the origin of this disagreement in Figure 12.3 we compare model and exact $a_0^2(\mathbf{j}')$ moments computed for $N' = 1 \ldots 8$ at the experimental energy of 470 cm^{-1}. One can see that the larger rotational transfer the worse is the agreement with exact results. We attribute this effect to the breakdown of the sudden approximation for higher N's. Indeed, model alignment moments, computed at higher energy of 1000 cm^{-1} are in much better agreement with exact computations, cf. Fig. 12.4.
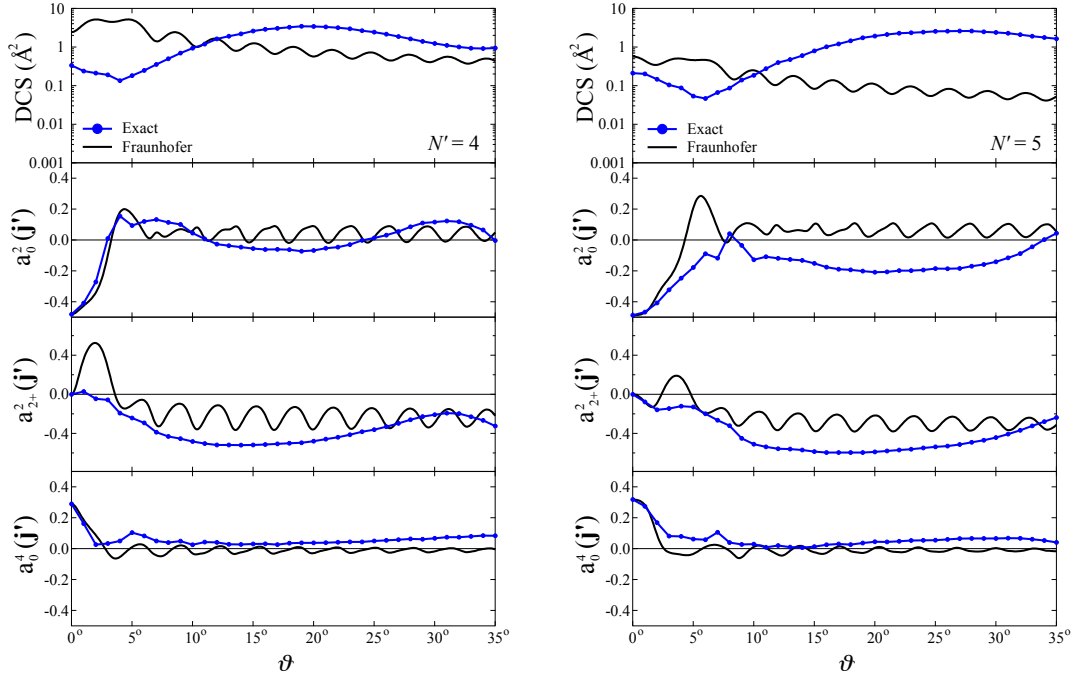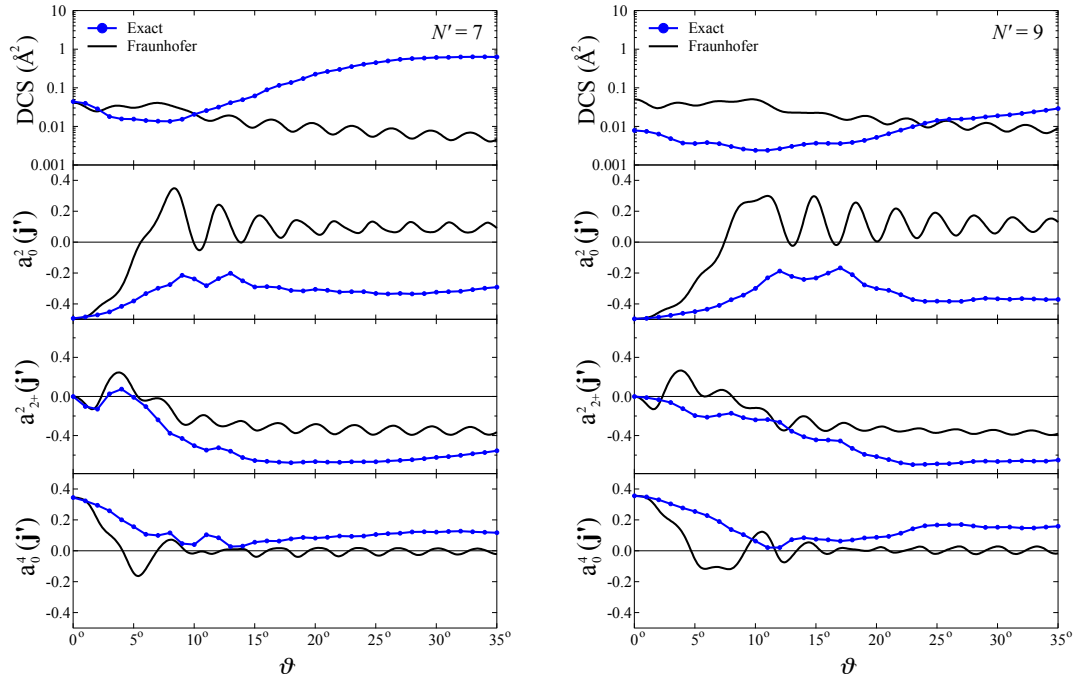
Figure 12.1: Differential cross sections and polarization moments pertaining to the $\mathbf{k} - \mathbf{k}' - \mathbf{j}'$ three-vector correlation in Ne–NO ($A^2\Sigma; N = 0, J = 1/2 \rightarrow N' = 4, 5$) collisions at 470 ± 33 cm^{-1}. The analytic results furnished by the Fraunhofer model (black solid line) are compared with close-coupling calculations (blue dots).
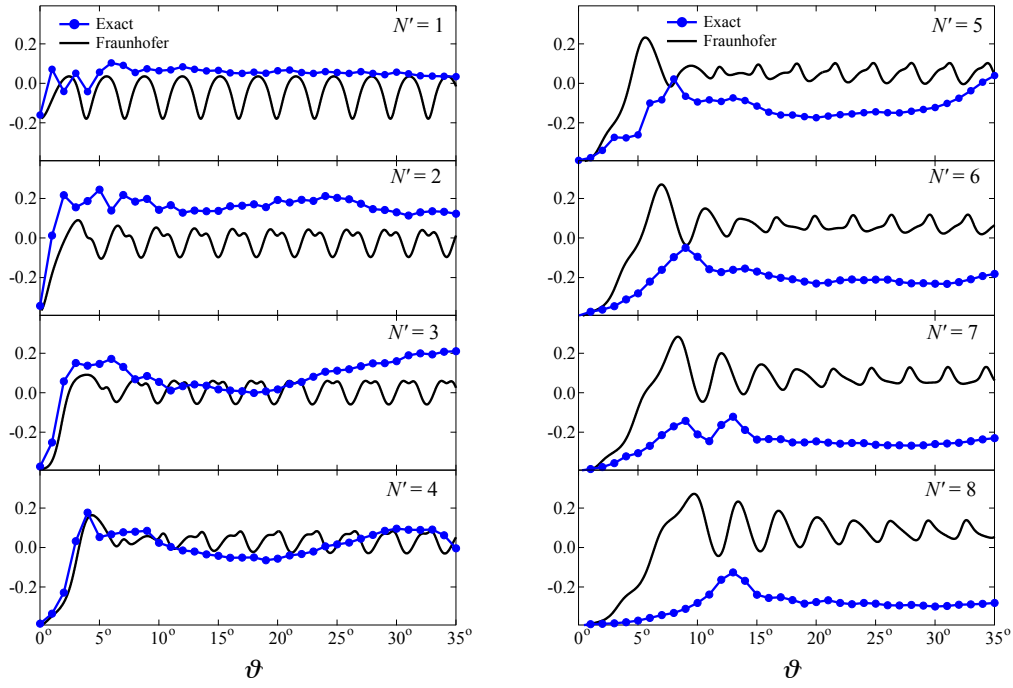

Figure 12.2: Differential cross sections and polarization moments pertaining to the $\mathbf{k} - \mathbf{k}' - \mathbf{j}'$ three-vector correlation in Ne–NO ($A^2\Sigma; N = 0, J = 1/2 \rightarrow N' = 7, 9$) collisions at 470 ± 33 cm^{-1}. The analytic results furnished by the Fraunhofer model (black solid line) are compared with close-coupling calculations (blue dots).
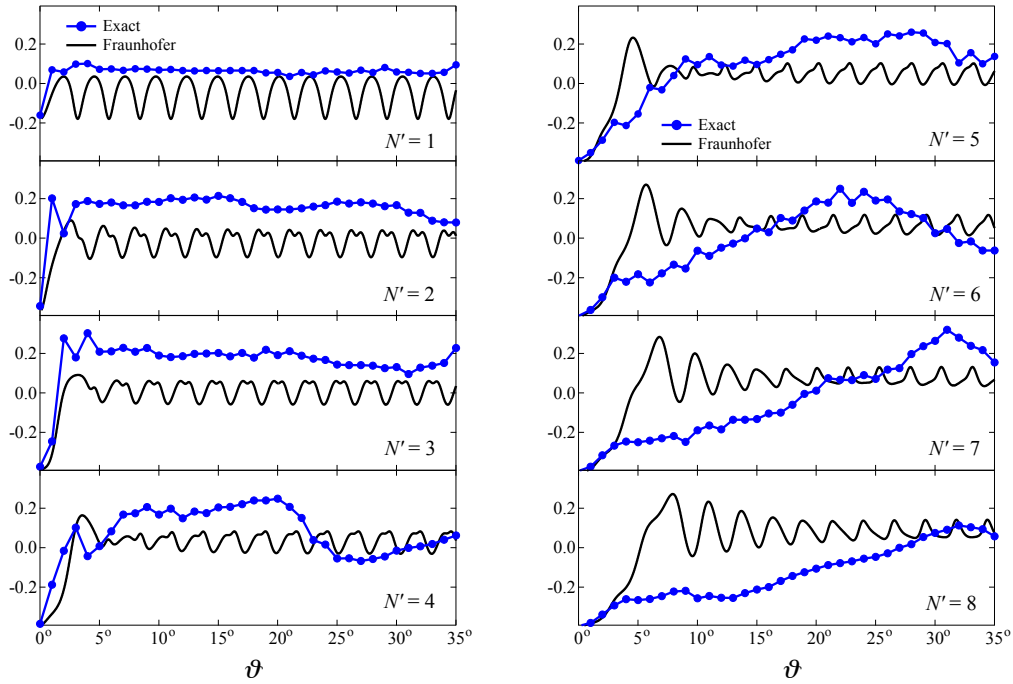
Figure 12.3: The $a_0^2(\mathbf{j}')$ polarization moments pertaining to the $\mathbf{k} - \mathbf{k}' - \mathbf{j}'$ three-vector correlation in Ne–NO ($A^2\Sigma; N = 0, J = 1/2 \to N'$) collisions at 470 cm^{-1}. The analytic results furnished by the Fraunhofer model (black solid line) are compared with close-coupling calculations (blue dots).

Figure 12.4: The $a_0^2(\mathbf{j}')$ polarization moments pertaining to the $\mathbf{k} - \mathbf{k}' - \mathbf{j}'$ three-vector correlation in Ne–NO ($A^2\Sigma; N = 0, J = 1/2 \to N'$) collisions at 1000 cm^{-1}. The analytic results furnished by the Fraunhofer model (black solid line) are compared with close-coupling calculations (blue dots).

12.2 Effect of a magnetic field

The Fraunhofer model allows to easily account for the effect of external fields. In this section we investigate the effect of a magnetic field on differential cross sections and alignment moments of Ne–NO ($A^2\Sigma; N = 0, J = 1/2 \rightarrow N'$) collisions. Here we employ the theory for collisions of closed-shell atoms with $^2\Sigma$ molecules in magnetic fields, described in detail in Chapter 9.

Figure 12.5 shows the comparison of cross sections and alignment moments for the field-free and field-dressed cases, for the field strength of 1 Tesla. One can see that the magnitudes of the DCS's show quite strong field dependence, that will affect integral cross sections, more easily measurable experimentally. At the same time, the alignment moments characterizing the $\mathbf{k} - \mathbf{k}' - \mathbf{j}'$ vector correlation are not influenced by the field.
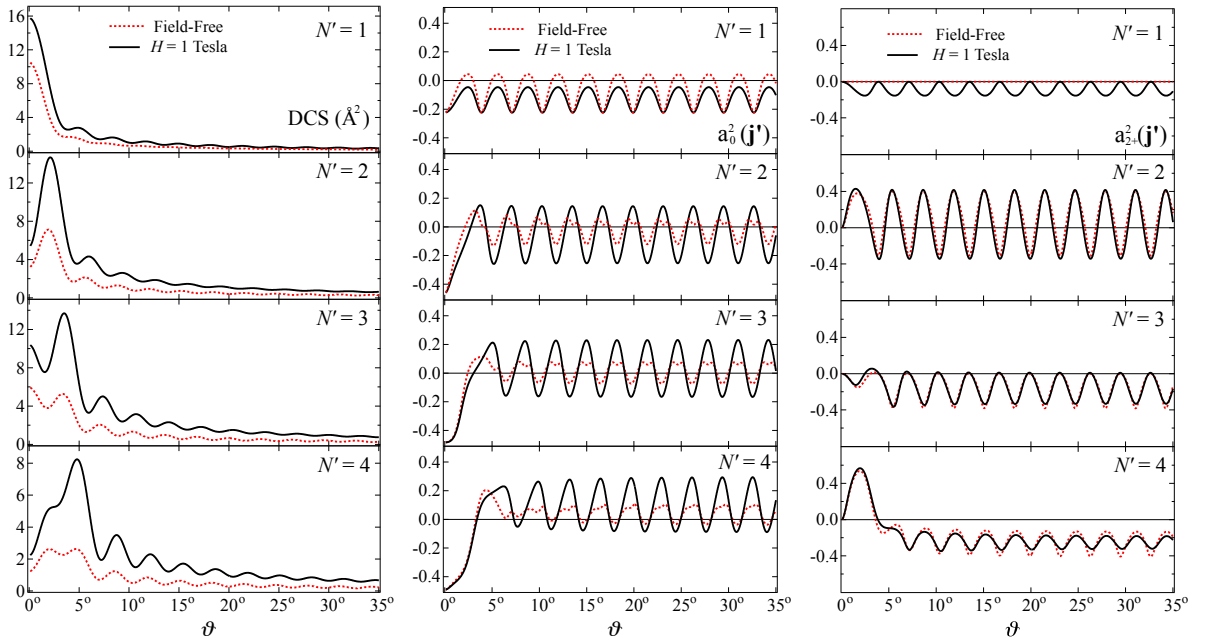

Figure 12.5: Differential cross sections and the $a_0^2(\mathbf{j}')$, $a_{2+}^2(\mathbf{j}')$ polarization moments for Ne–NO ($A^2\Sigma; N = 0, J = 1/2 \rightarrow N'$) collisions at 470 cm^{-1}. Field free model results (red dotted line are compared) with the collisions in a magnetic field of 1 Tesla (black solid line).

13 The $\mathbf{k} - \mathbf{j} - \mathbf{k}'$ and $\mathbf{k} - \mathbf{j} - \mathbf{k}' - \mathbf{j}'$ vector correlations

These parts of the work should be called:
"a best means for getting a headache!" [sic]

Lenin, Conspectus of Hegel's Logic (1914)

Here we illustrate the scope of the model by treating the $\mathbf{k} - \mathbf{j} - \mathbf{k}'$ and $\mathbf{k} - \mathbf{j} - \mathbf{k}' - \mathbf{j}'$ correlations in the Ar–NO ($X^2\Pi, j = \Omega = 3/2 \to j', \Omega' = 3/2$) scattering which, to date, have not been measured or evaluated. Since the $\mathbf{j}$ vector with $j = 1/2$ can only be oriented but not aligned, the only-to-alignment-sensitive Fraunhofer model cannot handle vector correlations involving the $\mathbf{j}$-vector with $j = 1/2$.
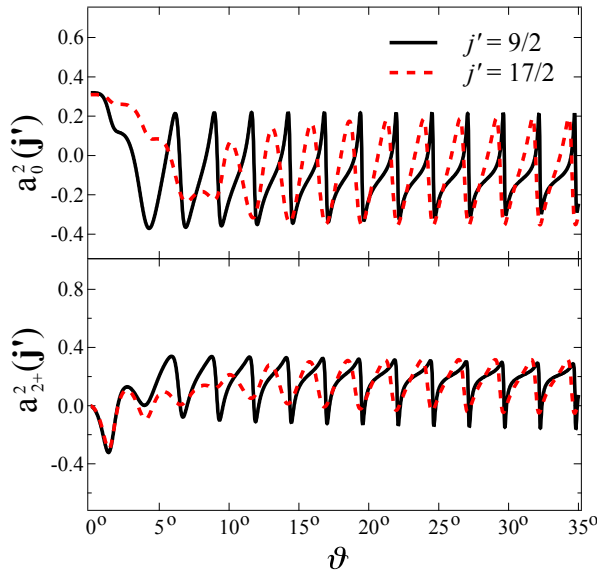

Figure 13.1: Polarization moments pertaining to the $\mathbf{k} - \mathbf{j} - \mathbf{k}'$ three-vector correlation in Ar–NO ($j = \Omega = 3/2, \to j', \Omega' = 3/2$) collisions at 520 cm^{-1} obtained from the Fraunhofer model.

However, since the $\mathbf{j}$ vector with $j = 3/2$ can be aligned, we worked out the $\mathbf{k} - \mathbf{j} - \mathbf{k}'$ and $\mathbf{k} - \mathbf{j} - \mathbf{k}' - \mathbf{j}'$ vector correlations for the Ar – NO ($X^2\Pi, j = 3/2, \Omega, \to j', \Omega$) scattering within the $\Omega = 3/2$ manifold

Figure 13.1 displays the $a_0^2(\mathbf{j})$ polarization moment for the $\mathbf{k} - \mathbf{j} - \mathbf{k}'$ three-vector correlation. One can see that the small-angle scattering is favored by positive values of the $a_0^2(\mathbf{j})$ moment, which corresponds to $\mathbf{j} \parallel \mathbf{k}$, i.e., to a "broadside" approach of NO with respect to $\mathbf{k}$, which enhances the scattering cross sec-

tion. However, for larger scattering angles, the $a_0^2(\mathbf{j})$ moment becomes slightly negative, attesting to a preference for an "edge-on" approach with $\mathbf{j} \perp \mathbf{k}$.

Figure 13.2 exemplifies the $\mathbf{k} - \mathbf{j} - \mathbf{k}' - \mathbf{j}'$ four-vector correlation in terms of the alignment moment $a_0^2(\mathbf{j}')$ of the final $\mathbf{j}'$ for different polarizations $a_0^2(\mathbf{j})$ of the initial $\mathbf{j}$. For an unpolarized initial state (black line), $\mathbf{j}'$ tends to align perpendicular to $\mathbf{k}$ ("broadside" recoil) for very small ϑ, but reverses to a slight alignment in the parallel direction ("edge-on" recoil) for larger scattering angles. Initial polarization of NO such that $\mathbf{j} \perp \mathbf{k}$ is seen to result in only small changes of the final alignment (blue dashed line). However, in the case of a "broadside" approach, $\mathbf{j} \parallel \mathbf{k}$, the stereodynamics changes significantly (red dotted line). The $a_0^2(\mathbf{j}')$ moment remains slightly negative throughout the range of scattering angles, indicating a propensity for an "edge-on" recoil, with $\mathbf{j}' \perp \mathbf{k}$.

Although the $\mathbf{k} - \mathbf{j} - \mathbf{k}'$ and $\mathbf{k} - \mathbf{j} - \mathbf{k}' - \mathbf{j}'$ vector correlations in rotationally inelastic scattering of Ar–NO have not been revealed in up-to-date experiments, such measurements are possible by preparing polarized reagents in a supersonic expansion or by electronic excitation of the NO molecules with polarized laser light which results in the unequal population of the rotational m states due to selection rules.
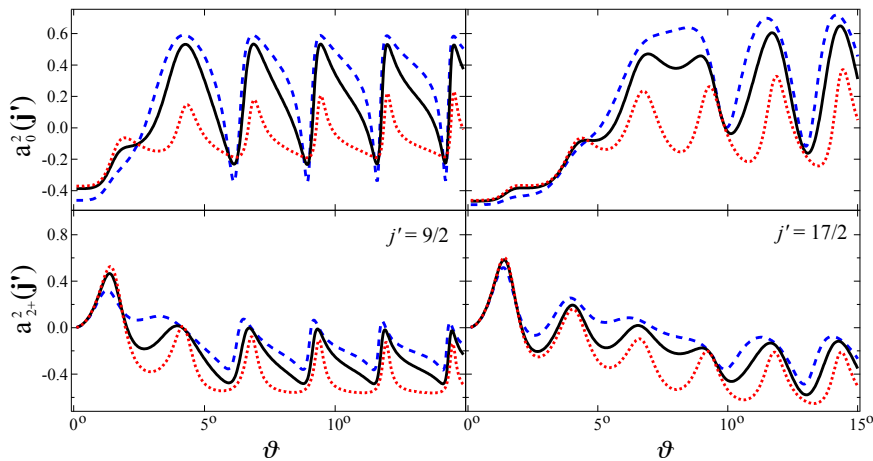

Figure 13.2: The $\mathbf{k} - \mathbf{j} - \mathbf{k}' - \mathbf{j}'$ four-vector correlation in the Ar–NO ($j = \Omega = 3/2, \rightarrow j', \Omega' = 3/2$) collisions at 520 cm^{-1} in terms of the dependence of the final polarization moments $a_0^2(\mathbf{j}')$, $a_{2+}^2(\mathbf{j}')$ on the initial alignment $a_0^2(\mathbf{j}) = 0$ (black line), $a_0^2(\mathbf{j}) = -0.4$ (blue dashed line), and $a_0^2(\mathbf{j}) = 0.4$ (red dotted line), with $a_{2+}^2(\mathbf{j}) = 0$ in each case. Obtained analytically from the Fraunhofer model.

14 Extensions of the Fraunhofer model: multiple scattering of matter waves

> A physicist is just an atom's way of looking at itself.
>
> Niels Bohr

Multiple scattering of matter waves arises in a broad variety of contexts, ranging from gas transport [333] to the scattering of subatomic particles by atoms or molecules [334, 335] to cosmic ray showers [336]. Inherent to the concept of multiple matter wave scattering is the notion of a refractive index, n, which, by the optical theorem [293], is proportional to the forward scattering amplitude, $f(0)$. While $\mathrm{Im}[f(0)]$ and thus $\mathrm{Im}[n]$ are related to the total integral scattering cross section and so can be measured in a standard beam scattering experiment, $\mathrm{Re}[f(0)]$ and thus $\mathrm{Re}[n]$ reflect the change of the wave's phase velocity and can only be accessed by matter wave interferometry. The first such interferometric measurement was carried out in 1995 by Schmiedmayer *et al.* [337, 338], who determined both the attenuation and the phase velocity change of sodium atom waves propagating through a number of gases. Subsequently, the Pritchard group was able to observe glory-type oscillations in the dependence of the refractive index on the sodium beam velocity [339, 340, 341]. In 2007, Jacquey *et al.* [342] implemented an improved, Mach-Zehnder type of an atom interferometer and measured the index of refraction of lithium waves passing through noble gases. In 2008, Champenois *et al.* [343] and, independently, Hornberger and Vaccini [344], provided an analysis of how the motion of the scatterers affects the measured refractive index. This work showed that the formulae used to extract the

refractive index from the experimental data [338, 345] and in the related theoretical treatments [346, 347, 348, 349] lacked consistency with the Beer-Lambert law and thus were incorrect.

According to the scenario of Ref. [343], an atomic or ionic beam of "projectiles" p of mass m_p and the laboratory velocity $\mathbf{v}_p$ propagates through a gas of density N_t made out of "target" particles t of mass m_t and laboratory velocity $\mathbf{v}_t$. For plane matter waves, the velocities $\mathbf{v}_{p,t}$ are related to the laboratory wave vectors $\mathbf{k}_{p,t}$ by $\hbar\mathbf{k}_{p,t} = m_{p,t}\mathbf{v}_{p,t}$. The relative motion of the target and projectile particles is described by the relative wave vector $\mathbf{k}_r = \mu\mathbf{v}_r/\hbar$, where $\mathbf{v}_r = \mathbf{v}_p - \mathbf{v}_t$ is the relative velocity, and $\mu = m_p m_t/(m_p + m_t)$ the reduced mass. Taking this scenario into account, Champenois *et al.* [343] derived a new formula for the refractive index of a matter wave propagating through a dilute gas:

$$n = 1 + 2\pi N_t \frac{m_p + m_t}{m_t} \frac{\langle f(k_r, 0)\rangle}{k_p^2}, \tag{14.1}$$

where $f(k_r, 0) \equiv f(0)$ is the forward scattering amplitude pertaining to the scattering angle $\vartheta = 0$. The averaging in Eq. (14.1) is carried out over the relative wave vectors, k_r, corresponding to a normalized relative velocity distribution [343], see below.

Previous theoretical treatments of the refractive index of atomic waves, surveyed in Ref. [343], were based on WKB [338] or eikonal [341, 350] approximations, which become analytic only if the repulsive, short-range interaction, is neglected, cf. also Refs. [338, 343]. In this Chapter, we combine the WKB treatment of scattering for the long-range attraction with the Fraunhofer approximation for the short-range repulsion and thereby obtain an analytic model of the refractive index which accounts for both short- and long-range multiple matter-wave scattering. The resulting analytic refractive index provides an additional insight into multiple scattering and facilitates data analysis.

After briefly introducing the model, we apply it to the refractive index of Li atom waves propagating through Ar, Kr, and Xe gases and compare the results with the measurements of Jacquey *et al.* [342]. In addition, we exemplify the model's scope by

examining the refraction of a Na^+ ionic beam passing through a dilute N_2 gas.

14.1 Model of matter-wave refraction

In the model introduced herein, we consider the scattering amplitude to consist of two parts:

$$f(k_r, 0) = f_{\text{short}}(k_r, 0) + f_{\text{long}}(k_r, 0) \tag{14.2}$$

The short range part, $f_{\text{short}}(k_r, 0)$, arises from the scattering by the "hard core," repulsive branch of the potential, and can be evaluated in closed form within the Fraunhofer model of matter wave scattering. The Fraunhofer model was introduced by Drozdov [193] and generalized by Blair [194] in the late 1950s to treat inelastic nuclear scattering, and adapted by Faubel [195] to account for rotationally inelastic thermal collisions between helium atoms and N_2 and CH_4 molecules. Recently, we generalized the Fraunhofer model to treat atom-molecule collisions in electric [196, 199], magnetic [198], and laser fields [197], and also to gain insight into the stereodynamics of molecular collisions [200, 201].

Within the Fraunhofer model, the hard core part of the potential amounts to a two-dimensional, impenetrable obstacle with sharp boundaries. The elastic scattering amplitude is given by the amplitude for the Fraunhofer diffraction of matter waves by such an obstacle [196],

$$f_{\text{short}}(k_r, \vartheta) = ik_r R_0^2(k_r) \frac{J_1[k_r R_0(k_r)\vartheta]}{k_r R_0(k_r)\vartheta}, \tag{14.3}$$

where J_1 is the Bessel function [295] and R_0 is the radius of the interaction which, for an atom-atom potential, is given by the solution of the equation $V(R_0) = \hbar^2 k_r^2/(2\mu)$, with $V(r)$ the interaction potential. For forward scattering, the amplitude of Eq. (14.3) becomes:

$$f_{\text{short}}(k_r, 0) = \frac{ik_r R_0^2(k_r)}{2} \tag{14.4}$$

Hence the Fraunhofer amplitude is purely imaginary and, therefore, contributes only

to the imaginary part of the refractive index.

In order to account for the long-range part of the scattering amplitude, $f_{\text{long}}(k_r, 0)$, we make use of the WKB approximation, which is accurate for thermal collisions dominated by partial waves with large angular momenta l. We consider the general case of the inverse-power long-range potential,

$$V_{\text{long}}(r) = -\frac{C_\beta}{r^\beta}, \tag{14.5}$$

with $C_\beta > 0$ and $\beta > 3$. For an atom-atom interaction, $\beta = 6$, while $\beta = 4$ for an ion interacting with an atom or molecule. For the potential of Eq. (14.5), the WKB phase shift for the l-th partial wave is given by [293]:

$$\delta_l^{(\beta)} = \frac{\mu C_\beta k_r^{\beta-2}}{2\hbar^2 l^{\beta-1}} \frac{\Gamma(\frac{1}{2})\Gamma(\frac{\beta-1}{2})}{\Gamma(\frac{\beta}{2})} \tag{14.6}$$

The WKB forward scattering amplitude [293],

$$f_{\text{WKB}}^{(\beta)}(k_r, 0) = \frac{1}{ik_r} \int_0^\infty l \left(e^{2i\delta_l^{(\beta)}} - 1 \right) dl, \tag{14.7}$$

then becomes, on substituting from Eq. (14.6):

$$f_{\text{long}}^{(\beta)}(k_r, 0) = k_r^{\frac{\beta-3}{\beta-1}} \left(\frac{\sqrt{\pi}}{2} \right)^{\frac{\beta+1}{\beta-1}} \left[\frac{\mu C_\beta}{\hbar^2} \frac{\Gamma(\frac{\beta-1}{2})}{\Gamma(\frac{\beta}{2})} \right]^{\frac{2}{\beta-1}} \left[\frac{\Gamma(\frac{3-\beta}{2-2\beta})}{\Gamma(\frac{1}{1-\beta})} + i\frac{\Gamma(\frac{\beta-2}{\beta-1})}{\Gamma(\frac{\beta+1}{2\beta-2})} \right] \tag{14.8}$$

14.2   Refraction of atom matter waves

In the case of an atom beam passing through an atomic gas, $\beta = 6$ and the forward scattering amplitude becomes

$$f_{\text{atom}}(k_r, 0) = f_{\text{short}}(k_r, 0) + f_{\text{long}}^{(6)}(k_r, 0)$$
$$= \frac{ik_r R_0^2(k_r)}{2} + \left(\frac{ik_r}{2} \right)^{3/5} \Gamma\left(\frac{3}{5} \right) \left(\frac{3\pi}{16} \frac{\mu C_6}{\hbar^2} \right)^{2/5} \tag{14.9}$$
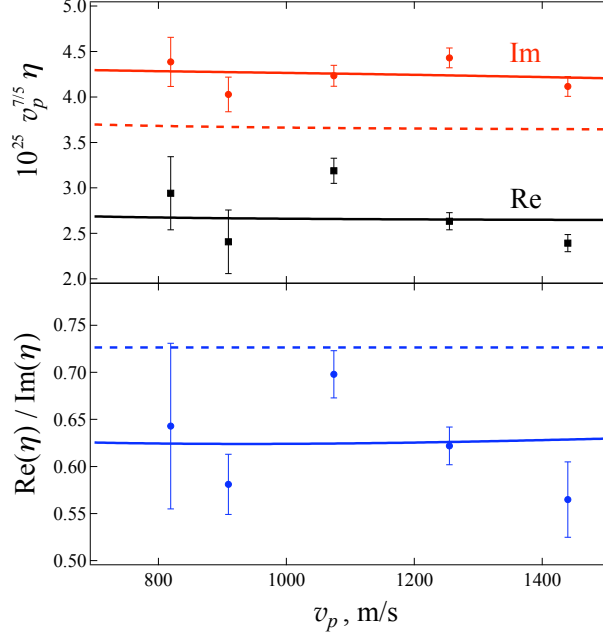
Figure 14.1: Upper panel shows the real and imaginary parts of the reduced refractive index $\eta \equiv (n-1)/N_t$ [m³] multiplied by $10^{25} v_p^{7/5}$ for Li beam propagating through Xe gas, in dependence of the beam velocity v_p. Lower panel shows the corresponding ratio Re(η)/Im(η). Model results (solid curves) are compared with experimental data of Ref. [342]. Dashed curves show the results of the model with the short-range potential excluded.

By substituting from Eq. (14.9) into Eq. (14.1) and making use of the distribution function given by Eq. (A3) of Ref. [343],

$$P(v_r) = \frac{2v_r}{\pi^{1/2}\alpha v_p} \exp\left[-\frac{v_p^2 + v_r^2}{\alpha^2}\right] \sinh\left[\frac{2v_p v_r}{\alpha^2}\right], \tag{14.10}$$

with $\alpha = \sqrt{2k_B T/m_t}$, k_B Boltzmann's constant, and T the temperature, we obtain the following expression for the reduced index of refraction,

$$\eta_{\text{atom}} \equiv \frac{n-1}{N_t} = \frac{2\pi\hbar}{m_p v_p^2}\left[i\langle v_r\rangle R_0^2 + \langle v_r^{3/5}\rangle \left(\frac{i}{2}\right)^{3/5} \Gamma\left(\frac{3}{5}\right)\left(\frac{3\pi}{16}\frac{C_6}{\hbar}\right)^{2/5}\right], \tag{14.11}$$

where the velocity averages are given by

$$\langle v_r\rangle = \int_0^\infty v_r P(v_r)dv_r; \quad \langle v_r^{3/5}\rangle = \int_0^\infty v_r^{3/5} P(v_r)dv_r \tag{14.12}$$

139

Table 14.1: Reduced index of refraction, $\eta \equiv (n-1)/N_t$ [m^3], for a Li beam propagating through different noble gases with a mean velocity $v_p = 1075$ m/s.

	Experiment of Ref. [342]	Model	Model $f_{\text{short}}(k_r, 0) \equiv 0$
Ar			
$10^{29}\text{Re}(\eta)$	1.20 ± 0.11	0.97	0.97
$10^{29}\text{Im}(\eta)$	2.11 ± 0.06	1.65	1.33
$\text{Re}(\eta)/\text{Im}(\eta)$	0.56 ± 0.05	0.58	0.73
Kr			
$10^{29}\text{Re}(\eta)$	1.57 ± 0.10	1.25	1.25
$10^{29}\text{Im}(\eta)$	1.99 ± 0.07	2.04	1.71
$\text{Re}(\eta)/\text{Im}(\eta)$	0.78 ± 0.04	0.61	0.73
Xe			
$10^{29}\text{Re}(\eta)$	1.82 ± 0.07	1.52	1.52
$10^{29}\text{Im}(\eta)$	2.40 ± 0.06	2.42	2.08
$\text{Re}(\eta)/\text{Im}(\eta)$	0.70 ± 0.03	0.62	0.72

In general, the R_0 value depends on the relative velocity v_r, but for narrow velocity distributions, such as those implemented in the experiments of Jacquey *et al.* [342], the dependence is found to be negligible. We could thus simplify the resulting expression by fixing $R_0(v_r)$ to a constant value pertaining to the mean relative velocity, $R_0 \equiv R_0(\langle v_r \rangle)$.

While Table 14.1 compares the experimental values of η_{atom} obtained by Jacquey *et al.* [342] with our model results for Li matter waves propagating through Ar, Kr, and Xe gases, Figure 1 singles out the Li–Xe system and compares the experimental and theoretical dependence of the refractive index on the Li velocity. As an input for the analytic model we used potential energy curves of Ahokas *et al.* [351]. The analytic refractive index is seen to be in a compelling agreement with the experiment. Also presented in both Table 14.1 and Figure 1 are the values of the refractive index

for the long range potential included but the short-range interaction excluded, i.e., for $f(k_r, 0) = f_{\text{long}}(k_r, 0)$, cf. Eq. (14.2). One can see that in such a case the imaginary part of the refractive index is substantially less than in the experiment.

In the limit of a cold atomic gas, i.e., for $T \to 0$, the velocity distribution (14.10) becomes a δ-function, which simplifies Eq. (14.11), since then $\langle v_r \rangle \to v_p$ and $\langle v_r^{3/5} \rangle \to v_p^{3/5}$. In this case, $\text{Re}[\eta_{\text{atom}}]$ is proportional to $v_p^{-7/5}$, while $\text{Im}[\eta_{\text{atom}}]$ is proportional to both v_p^{-1} and $v_p^{-7/5}$. However, since the v_p^{-1} term arises from the diffraction of matter waves from the hard core of the potential, it dominates $\text{Im}\,[\eta_{\text{atom}}]$ at large collision energies at the expense of the $v_p^{-7/5}$ term, which arises from the long-range attraction.

14.3 Refraction of ion matter waves

For an ion beam passing through an atomic or molecular gas, $\beta = 4$ and the scattering amplitude becomes

$$
\begin{aligned}
f_{\text{ion}}(k_r, 0) &= f_{\text{short}}(k_r, 0) + f_{\text{long}}^{(4)}(k_r, 0) \\
&= \frac{ik_r R_0^2(k_r)}{2} + \left(\frac{ik_r}{2}\right)^{1/3} \Gamma\left(\frac{1}{3}\right) \left(\frac{\pi}{4}\frac{\mu C_4}{\hbar^2}\right)^{2/3} \quad (14.13)
\end{aligned}
$$

leading to a reduced refractive index for an ionic beam:

$$
\begin{aligned}
\eta_{\text{ion}} &\equiv \frac{n-1}{N_t} \\
&= 2\pi \frac{\hbar}{m_p v_p^2} \left[i\langle v_r \rangle R_0^2 + \langle v_r^{1/3} \rangle \left(\frac{i}{2}\right)^{1/3} \Gamma\left(\frac{1}{3}\right) \left(\frac{\pi}{4}\frac{C_4}{\hbar}\right)^{2/3} \right], \quad (14.14)
\end{aligned}
$$

with

$$
\langle v_r^{1/3} \rangle = \int_0^\infty v_r^{1/3} P(v_r) dv_r \quad (14.15)
$$

We note that in the case of an anisotropic interaction of, say, an ion or atom with a linear molecule given by a potential $V(r, \theta)$, the R_0 value is given by the spherical part of the hard core of the potential [196]. In order to extract R_0, we first solve the

Table 14.2: Reduced index of refraction, $\eta \equiv (n-1)/N_t$ [m³], for a Na⁺ beam propagating through N₂ gas with a mean velocity $v_p = 5000$ m/s.

	Model	Model $f_{\text{short}}(k_r, 0) \equiv 0$
$10^{29}\text{Re}(\eta)$	0.25	0.25
$10^{29}\text{Im}(\eta)$	0.16	0.14
$\text{Re}(\eta)/\text{Im}(\eta)$	1.60	1.73

equation $V(R(\theta), \theta) = \hbar^2 k_r^2/(2\mu)$ to obtain the hard core shape $R(\theta)$, which we then expand in a Legendre series,

$$R(\theta) = R_0 P_0(\cos\theta) + R_1 P_1(\cos\theta) + R_2 P_2(\cos\theta) + \dots, \qquad (14.16)$$

from which we deduce the R_0 value.

The values of the refractive index for an ion beam passing through a molecular gas, as exemplified by the Na⁺–N₂ system, are listed in Table 14.2 at an ion projectile velocity $v_p = 5000$ m/s. The requisite value of R_0 was extracted from the potential energy surface of Ref. [244]. We see that the refractive index is less affected by switching off the repulsive part of the potential for the ion–molecule system than for the atom–atom system, cf. section 14.2. This is due to the greater strength of the $-C_4 r^{-4}$ interaction compared with that of the $-C_6 r^{-6}$ potential and the more dominant role it thus plays in determining n.

We note that in the limit of zero temperature, $v_r \to v_p$, the real part of the refractive index (14.14) becomes proportional to $v_p^{-5/3}$. The imaginary part of the refractive index is determined by two terms, one of which is proportional to v_p^{-1} and the other to $v_p^{-5/3}$.

15 Summary and outlook

> Everybody knows that a tomato consists of 99%
> of water and only one percent of tomato!
>
> Ray Magliozzi, the NPR Car Talk show

In this thesis we presented an analytic model that furnishes scalar and vector properties of molecular collisions, both field-free and in fields. The model is based on the sudden approximation and treats molecular scattering as the Fraunhofer diffraction of matter waves from the hard-core part of the potential. As described in Chapters 5, 6, the theory has no fitting parameters and is inherently quantum, rendering fully state- and energy-resolved scattering amplitudes and all the quantities that unfold from them in analytic form. This allows to obtain complex polarization moments inherent to quantum stereodynamics, and account for interference and other non-classical effects. The simplicity and analyticity of the model paves the way to understanding the origin of the features observed in experiment and exact computations, such as the angular oscillations in the state-to-state differential cross sections and polarization moments, the rotational-state dependent variation of the integral cross sections, and change of these quantities as a function of the applied field.

In Chapter 7 we used the Fraunhofer model to derive analytic expressions for differential and integral cross sections for collisions of $^2\Pi$ molecules with closed-shell atoms, and applied them to the case of Ar–NO($X^2\Pi$). Analyzing the closed-form expressions for the scattering amplitudes we were able to explain the changes of differential and integral cross sections in dependence of the parity-resolved final rotational state and the strength of the electrostatic field.

Chapter 8 studied the effect of nonresonant electric fields on collisions of $^1\Sigma$ molecules with closed-shell atoms and ions. We focused on the $\mathbf{k} - \mathbf{k}'$ vector correlation,

i.e. the differential cross section, in collisions of Ne with OCS($X^1\Sigma$) in an electrostatic field and Na$^+$ with N$_2$($X^1\Sigma$) in a laser field. In the case of Ne–OCS, the model provided an easy explanation for the "phase shifts" of the differential cross sections due to the external field. Although no such shifts take place for Na$^+$–N$_2$, even a small field-induced alignment of the molecules was shown to cause a large alteration of the magnitudes of the differential cross-sections.

Chapter 9 dealt with collisions of closed-shell atoms with paramagnetic molecules in a magnetic field. We considered the cases of $^2\Sigma$, $^3\Sigma$, and $^2\Pi$ species that exhibit significantly different rotational-level structure due to spin-rotation, spin-orbit, and spin-spin terms in the Hamiltonian, which results in distinct mechanisms of the molecule-field interaction. We applied the model to the He–CaH($^2\Sigma, j = 1/2 \to j'$), He–O$_2$($X^3\Sigma, N = 0, j = 1 \to N', j'$), and He–OH($X^2\Pi, J = 3/2, f \to j', e/f$) systems. The CaH molecule has a non-magnetic ground state and, therefore, all the field-induced changes of the He–CaH scattering are due to the Zeeman effect in the final state, which leads to weak variations of the cross sections between the zero-field and field-dressed regimes. In contrast to the $^2\Sigma$ case, where a magnetic field couples only the members of the spin-rotation doublet, the Hamiltonian matrices of the $^3\Sigma$ and $^2\Pi$ molecules in a magnetic field are in principle infinite, resulting in a stronger field-effect. The He–O$_2$ collision system exhibits a dramatic feature: in the absence of a magnetic field, the scattering vanishes for channels leading to the F_2 manifold, i.e., final states with $j' = N'$. However, in the presence of the field, such transitions become allowed, and, although weak, should be observable. The OH molecule has a large rotational constant and is, therefore, only weakly aligned by the magnetic field. As a result, the field-induced changes of the scattering cross sections are tiny. Unlike the He–CaH and He–O$_2$ systems, the hard core of the He–OH potential energy surface is dominated by odd Legendre moments, which gives rise to scattering features which are qualitatively different from those of the other systems. Among all the three systems studied, the strongest field-induced changes of the differential cross sections – such as angular shifts of their oscillations – were found for the $N = 1, j = 0 \to N' = 1, j' = 2$ and

$N = 1, j = 0 \rightarrow N' = 3, j' = 4$ transitions in He–O$_2$. These occur for scattering in a magnetic field perpendicular to the relative velocity vector, and are due to a field-induced mixing of terms containing higher Bessel-functions into the scattering amplitude.

It was the goal of Chapter 10 to merge the Fraunhofer model with the quantum theory of vector correlations, described in Chapter 4, in order to study a more complicated case of the $\mathbf{k} - \mathbf{k'} - \mathbf{j'}$ three-vector correlation. We used the model to obtain the alignment moments describing the polarization of the $\mathbf{j'}$ vector and compare them with experiment and exact computations. The $a_0^2(\mathbf{j'})$ and $a_{2+}^2(\mathbf{j'})$ moments were found to be in excellent agreement with experimental and exact results, which lead us to conclude that the stereodynamics of the Ar–NO rotationally inelastic collisions is contained solely in the diffractive part of the scattering amplitude which is governed by a single Legendre moment characterizing the anisotropy of the hard-core part of the system's PES. At the same time, the contribution of the higher $a_{q\pm}^4(\mathbf{j'})$ and $a_{q\pm}^6(\mathbf{j'})$ moments to stereodynamical portraits was found to be negligible. A field of 16 kV/cm, sufficient to significantly orient the NO molecule in the space-fixed frame, was found to cause a very small effect both on the parity-resolved and averaged polarization moments.

In Chapter 11 we investigated vector correlations in He–NO($X^2\Pi$), He–OH($X^2\Pi$), He–O$_2$($X^3\Sigma$), and He–CaH($X^2\Sigma$) collisions. The model alignment moments for He–NO were found to come as close to exact results as for the previously examined Ar–NO system which revealed that the collision stereodynamics in question is governed by diffraction of matter waves from a 2D contour of the repulsive core of the potential. Scaling of the oscillatory patterns of the alignment moments with the de Broglie wavelength and the molecular size allowed to single out non-diffractive contributions to the exact results. Interestingly, the form-factors of the model alignment moments look very similar for all the studied systems. This allowed us to identify the fingerprints of diffraction, which can be used to determine diffraction-driven stereodynamics in future experiments and exact computations.

In Chapter 12 we looked into the polarization of angular momentum of the electronically excited $NO(A^2\Sigma)$ molecule due to collisions with Ne. By comparing our results with exact computations, we showed that the physical mechanisms behind the stereodynamics of the ground-state and excited-state NO molecules are substantially different. At the collision energy of 470 cm^{-1} the model results were found to be in compelling agreement with the exact theory in the case of a small rotational transfer, $N = 0 \rightarrow N' = 1 \dots 4$, while the agreement became worse for $N = 0 \rightarrow N' > 4$ transitions. We found out that such a discrepancy is due to the breakdown of the sudden approximation, which holds much better at higher collision energy of 1000 cm^{-1}. We also investigated the effect of a magnetic field on the stereodynamics of Ne–NO($A^2\Sigma$) collisions. We found that a field of 1 Tesla causes significant changes in the magnitudes of differential cross sections, but has a negligible effect on $a_0^2(\mathbf{j}')$ and $a_{2+}^2(\mathbf{j}')$ alignment moments.

In Chapter 13 we applied the Fraunhofer theory to look into other types of vector correlations, considering the $\mathbf{k} - \mathbf{j} - \mathbf{k}'$ and $\mathbf{k} - \mathbf{j} - \mathbf{k}' - \mathbf{j}'$ correlations in rotationally inelastic Ar–NO ($X^2\Pi$) scattering as an example. It was shown that preparing the reagents with polarized angular momentum $\mathbf{j}$ makes it possible to significantly alter the collision dynamics and stereodynamics. Although the $\mathbf{k} - \mathbf{j} - \mathbf{k}'$ and $\mathbf{k} - \mathbf{j} - \mathbf{k}' - \mathbf{j}'$ vector correlations in Ar–NO have not been determined in experiment yet, such measurements are possible by preparing polarized reagents in a supersonic expansion or by electronic excitation of the NO molecules with polarized laser light.

In Chapter 14 we presented an analytic model of the refraction of atom or ion matter waves passing through atomic or molecular gases, based on the extension of the Fraunhofer model of molecular collisions described in Chapter 5. The values of the refractive index furnished by the model were found to be in good agreement with experiment. Our analysis has shown that in order to appraise the imaginary part of the refractive index correctly, we need to account for the diffraction by the repulsive hard core part of the interaction potential. This was achieved by combining the WKB treatment of the scattering by the attractive branch of the potential with

the Fraunhofer model applied to the hard core part, which preserves the analyticity of the theory. Since the refractive index depends on the elastic scattering amplitude, given by the spherical part of the potential, it is independent on external fields in the model treatment.

The strength of the analytic model lies in its ability to separate dynamical and geometrical effects and to qualitatively explain the resulting scattering features. In the face of the absence of any other analytic model of vector correlations in molecular collisions, the Fraunhofer model is apt at providing a touchstone for understanding collisional stereodynamics and developing new ways of controlling scattering outcomes by means of external fields. We hope that the results presented in this thesis will inspire new experiments on vector correlations in molecular collisions, and manipulation of collisional stereodynamics with nonresonant fields.

16 Appendices

> You know, I love angular momentum. I even
> blame my parents for not naming me "Angular
> momentum"!
>
> Dudley Herschbach,
> Faraday Discussions 142:
> Cold and Ultracold molecules

16.1 Different conventions used to define alignment moments

Unfortunately, the density matrix normalization condition, Eq. (4.5), has not been universally adopted. Other normalization conventions include, for instance:

$$\mathrm{Tr}(\rho) \equiv 2j + 1 \tag{16.1}$$

$$\mathrm{Tr}(\rho) \equiv \frac{d\sigma}{d\omega} \tag{16.2}$$

$$\mathrm{Tr}(\rho) \equiv \frac{2\pi}{\sigma}\frac{d\sigma}{d\omega} \tag{16.3}$$

Here σ and $d\sigma/d\omega$ represent respectively a collision's integral and differential cross sections. When comparing two sets of polarization moments, one must ensure that they refer to density matrices defined within the same normalization convention.

There are various ways in which one can expand a density matrix in terms of its multipolar components. The variations relate to the following: (i) whether the expansion is covariant or contravariant, (ii) how the multipoles are normalized.

Unfortunately, there is no widely adopted convention. Here we present the relations between the convention that we use and the one of Zare [180, 283]. The expansion used in Zare's book [283] is:

$$
\rho_{m_1 m_2} = \sum_{k=0}^{2j} \sum_{q=-k}^{k} \rho_{kq} \langle jm_1 | \hat{T}_{kq} | jm_2 \rangle \tag{16.4}
$$

$$
= \sum_{kq} \rho_{kq} (-1)^{j-m_2} C(jjk, m_1 - m_2 q) \tag{16.5}
$$

$$
= \sum_{kq} \rho_{kq} (-1)^{j-m_2} (-1)^{j-m_2} \left(\frac{2k+1}{2j+1} \right)^{1/2} C(jkj, m_2 q m_1) \tag{16.6}
$$

$$
= \sum_{kq} \rho_{kq} \left(\frac{2k+1}{2j+1} \right)^{1/2} C(jkj, m_2 k m_1), \tag{16.7}
$$

where ρ_{kq} are Zare's polarization moments and the $\hat{T}_{kq}$ are Fano's multipole operators [285].

Since the expansion of Eq. (16.4) is written in terms of multipole operators, the expansion is contravariant. This means that if Zare's polarization moments are rotated to a different reference frame, they don't change in the same way as the $|jm\rangle$ basis states. Instead, they transform in what can be seen as the opposite way, hence the "contravariance". The multipoles in Eq. (16.4) are as defined by Fano. Inversion of Eq. (16.4) leads to:

$$
\rho_{kq} = \sum_{m_1 m_2} \left(\frac{2k+1}{2j+1} \right)^{1/2} \rho_{m_1 m_2} C(jkj, m_2 q m_1), \tag{16.8}
$$

and the fact that $C(j0j, m_2 0 m_1) = \delta_{m_1 m_2}$ implies:

$$
\rho_{00} = \frac{1}{\sqrt{2j+1}} \sum_m \rho_{mm} = \frac{\mathrm{Tr}(\rho)}{\sqrt{2j+1}} \tag{16.9}
$$

Ref. [162] contains a table showing the relations between sets of polarization moments defined according to various conventions.

16.2 The alignment cosine of a $^2\Sigma$ molecule in a magnetic field

Within the Hund's (b) basis functions, Eq. (9.4), the expectation value of the alignment cosine takes the form:

$$
\langle\cos^2\theta\rangle = a^2(\omega_\mathrm{m})\langle N-\tfrac{1}{2},\Omega,m\big|\cos^2\theta\big|N-\tfrac{1}{2},\Omega,m\rangle
$$
$$
+b^2(\omega_\mathrm{m})\langle N+\tfrac{1}{2},\Omega,m\big|\cos^2\theta\big|N+\tfrac{1}{2},\Omega,m\rangle+2a(\omega_\mathrm{m})b(\omega_\mathrm{m})\langle N-\tfrac{1}{2},\Omega,m\big|\cos^2\theta\big|N+\tfrac{1}{2},\Omega,m\rangle,
$$

$$(16.10)$$

where the matrix elements of the $\cos^2\theta$ operator in the Hund's case (a) basis can be obtained from (16.20) and (16.22):

$$
\langle j,\Omega,m\big|\cos^2\theta\big|j,\Omega,m\rangle = \frac{1}{3} + \frac{2}{3}\frac{[j(j+1)-3m^2]\,[j(j+1)-3\Omega^2]}{j(j+1)(2j-1)(2j+3)} \tag{16.11}
$$

$$
\langle j,\Omega,m\big|\cos^2\theta\big|j+1,\Omega,m\rangle = 2\Omega m\frac{\sqrt{[(j+1)^2-m^2]\,[(j+1)^2-\Omega^2]}}{j(j+1)(j+2)\sqrt{(2j+1)(2j+3)}} \tag{16.12}
$$

The coefficients $a(\omega_\mathrm{m})$ and $b(\omega_\mathrm{m})$ are given by the solution of the Zeeman problem, Eqs. (9.9)–(9.10).

16.3 Matrix elements of the j_Z operator

In general, the Zeeman operator is proportional to the projection, j_Z, of the total electronic angular momentum, $\mathbf{j}$, on the space-fixed field axis, Z, see e.g. Eq. (9.32). In this Appendix we present the matrix elements of the j_Z operator, employed in this work. For Σ electronic states, j_Z reduces to S_Z.

We transform the angular momentum projection operator from the body-fixed to the space-fixed coordinates using the direction cosines operator, Φ:

$$
j_Z = \tfrac{1}{2}\left(\Phi_Z^+ j^- + \Phi_Z^- j^+\right) + \Phi_Z^z j^z \tag{16.13}
$$

The matrix elements of the body-fixed spin operator in the Hund's case (a) basis, $|j, \Omega, m\rangle$, are given by the standard relations [293]:

$$\langle j, \Omega, m| \, j^{\pm} \, |j, \Omega \mp 1, m\rangle = \sqrt{(j \pm \Omega)(j \mp \Omega + 1)} \tag{16.14}$$

$$\langle j, \Omega, m| \, j^{z} \, |j, \Omega, m\rangle = \Omega \tag{16.15}$$

The matrix elements of the direction cosine operator can be obtained from Table 6 of Ref. [352]. Some of them are also given in Refs. [321, 322]. Here we list all non-vanishing matrix elements for $m' = m$:

$$\langle j', \Omega, m|\Phi_Z^z|j, \Omega, m\rangle = \begin{cases} \dfrac{\Omega m}{j(j+1)} & j' = j \\[4ex] \dfrac{\sqrt{(j+\Omega+1)(j-\Omega+1)(j+m+1)(j-m+1)}}{(j+1)\sqrt{(2j+1)(2j+3)}} & j' = j+1 \\[4ex] \dfrac{\sqrt{(j+\Omega)(j-\Omega)(j+m)(j-m)}}{j\sqrt{(2j+1)(2j-1)}} & j' = j-1 \end{cases} \tag{16.16}$$

$$\langle j', \Omega-1, m|\Phi_Z^+|j, \Omega, m\rangle = \begin{cases} \dfrac{m\sqrt{(j+\Omega)(j-\Omega+1)}}{j(j+1)} & j' = j \\[4ex] \dfrac{\sqrt{(j-\Omega+1)(j-\Omega+2)(j+m+1)(j-m+1)}}{(j+1)\sqrt{(2j+1)(2j+3)}} & j' = j+1 \\[4ex] -\dfrac{\sqrt{(j+\Omega)(j+\Omega-1)(j+m)(j-m)}}{j\sqrt{(2j+1)(2j-1)}} & j' = j-1 \end{cases} \tag{16.17}$$

$$\langle j', \Omega+1, m|\Phi_Z^-|j, \Omega, m\rangle = \begin{cases} \dfrac{m\sqrt{(j-\Omega)(j+\Omega+1)}}{j(j+1)} & j' = j \\[4ex] -\dfrac{\sqrt{(j+\Omega+1)(j+\Omega+2)(j+m+1)(j-m+1)}}{(j+1)\sqrt{(2j+1)(2j+3)}} & j' = j+1 \\[4ex] \dfrac{\sqrt{(j-\Omega)(j-\Omega-1)(j+m)(j-m)}}{j\sqrt{(2j+1)(2j-1)}} & j' = j-1 \end{cases} \tag{16.18}$$

16.4 Matrix elements of the $(\Phi_Z^z)^2$ operator

The matrix elements of the alignment cosine can be reduced to the matrix elements of the Φ_Z^z operator by means of the full basis set:

$$\langle \cos^2 \theta \rangle = \langle j', \Omega, m|(\Phi_Z^z)^2|j, \Omega, m\rangle = \sum_{j''} \langle j', \Omega, m|\Phi_Z^z|j'', \Omega, m\rangle \langle j'', \Omega, m|\Phi_Z^z|j, \Omega, m\rangle \tag{16.19}$$

By taking into account that the matrix elements (16.16) are nonzero only for $\Delta j = 0, \pm 1$, we obtain the matrix elements of the direction cosine operator:

$$\langle j, \Omega, m|(\Phi_Z^z)^2|j, \Omega, m\rangle = |\langle j - 1, \Omega, m|\Phi_Z^z|j, \Omega, m\rangle|^2$$
$$+ |\langle j, \Omega, m|\Phi_Z^z|j, \Omega, m\rangle|^2 + |\langle j + 1, \Omega, m|\Phi_Z^z|j, \Omega, m\rangle|^2 \tag{16.20}$$

$$\langle j - 1, \Omega, m|(\Phi_Z^z)^2|j, \Omega, m\rangle = \langle j - 1, \Omega, m|\Phi_Z^z|j, \Omega, m\rangle \Big\{ \langle j, \Omega, m|\Phi_Z^z|j, \Omega, m\rangle$$
$$+ \langle j - 1, \Omega, m|\Phi_Z^z|j - 1, \Omega, m\rangle \Big\} \tag{16.21}$$

$$\langle j + 1, \Omega, m|(\Phi_Z^z)^2|j, \Omega, m\rangle = \langle j + 1, \Omega, m|\Phi_Z^z|j, \Omega, m\rangle \Big\{ \langle j, \Omega, m|\Phi_Z^z|j, \Omega, m\rangle$$
$$+ \langle j + 1, \Omega, m|\Phi_Z^z|j + 1, \Omega, m\rangle \Big\} \tag{16.22}$$

$$\langle j - 2, \Omega, m|(\Phi_Z^z)^2|j, \Omega, m\rangle = \langle j - 2, \Omega, m|\Phi_Z^z|j - 1, \Omega, m\rangle \langle j - 1, \Omega, m|\Phi_Z^z|j, \Omega, m\rangle \tag{16.23}$$

$$\langle j + 2, \Omega, m|(\Phi_Z^z)^2|j, \Omega, m\rangle = \langle j + 2, \Omega, m|\Phi_Z^z|j + 1, \Omega, m\rangle \langle j + 1, \Omega, m|\Phi_Z^z|j, \Omega, m\rangle \tag{16.24}$$

Bibliography

[1] J. V. Dunworth, *Review of Scientific Instruments* **11**, 167 (1940).

[2] D. R. Hamilton, *Physical Review* **58**, 122 (1940).

[3] S. Kikuchi, Y. Watase, and J. Itoh, *Zeitschrift für Physik* **119**, 185 (1942).

[4] R. Beringer, *Physical Review* **63**, 23 (1943).

[5] W. M. Good, *Physical Review* **70**, 978 (1946).

[6] E. L. Brady and M. Deutsch, *Physical Review* **72**, 870 (1947).

[7] G. Goertzel, *Physical Review* **70**, 897 (1946).

[8] I. Zinnes, *Physical Review* **80**, 386 (1950).

[9] D. R. Hamilton, *Physical Review* **74**, 782 (1948).

[10] J. W. Gardner, *Proceedings of the Physical Society (London) A* **62**, 763 (1949).

[11] J. W. Gardner, *Proceedings of the Physical Society (London) A* **63**, 238 (1951).

[12] D. L. Falkoff, *Physical Review* **73**, 518 (1948).

[13] D. S. Ling and D. L. Falkoff, *Physical Review* **76**, 1639 (1949).

[14] D. L. Falkoff and G. E. Uhlenbeck, *Physical Review* **79**, 323 (1950).

[15] G. Racah, *Physical Review* **84**, 910 (1951).

[16] E. U. Condon and G. H. Shortley, *Theory of Atomic Spectra*, Cambridge University Press, 1935.

[17] G. Racah, *Physical Review* **62**, 438 (1942).

[18] S. P. Lloyd, *Physical Review* **85**, 904 (1952).

[19] U. Fano, *Physical Review* **90**, 577 (1953).

[20] L. Biedenharn and M. Rose, *Reviews of Modern Physics* **25**, 729 (1953).

[21] A. Abragam and R. V. Pound, *Physical Review* **92**, 943 (1953).

[22] R. M. Steffen, *Advances in Physics* **4**, 293 (1955).

[23] F. Coester, *Physical Review* **93**, 1304 (1954).

[24] G. R. Satchler, *Physical Review* **94**, 1304 (1954).

[25] H. J. Rose and D. M. Brink, *Reviews of Modern Physics* **39**, 306 (1967).

[26] L. C. Biedenharn, Angular Correlations in Nuclear Spectroscopy, in *Nuclear Spectroscopy B*, edited by F. Azjenberg-Selove, p. 732, Academic Press, 1960.

[27] J. Blatt and L. Biedenharn, *Reviews of Modern Physics* **24**, 258 (1952).

[28] A. Simon and T. A. Welton, *Physical Review* **90**, 1036 (1953).

[29] A. Simon, *Physical Review* **92**, 1050 (1953).

[30] G. R. Satchler, *Proceedings of the Physical Society (London) A* **68**, 1041 (1955).

[31] J. M. Kennedy and W. T. Sharp, *Physical Review* **95**, 440 (1954).

[32] M. Jacob and G. C. Wick, *Annals of Physics* **7**, 404 (1959).

[33] J. M. DANIELS and J. GOLDEMBERG, *Reports on Progress in Physics* **25**, 1 (1962).

[34] E. SHELDON, *Reviews of Modern Physics* **35**, 795 (1963).

[35] G. G. OHLSEN, *Reports on Progress in Physics* **35**, 717 (1972).

[36] C. GLASHAUSSER, *Annual Review of Nuclear and Particle Sciences* **29**, 33 (1979).

[37] H. E. CONZETT, *Reports on Progress in Physics* **57**, 1 (1994).

[38] U. FANO and J. H. MACEK, *Reviews of Modern Physics* **45**, 553 (1973).

[39] N. ANDERSEN, J. W. GALLAGHER, and I. V. HERTEL, *Physics Reports* **165**, 1 (1988).

[40] N. ANDERSEN, J. T. BROAD, E. E. B. CAMPBELL, J. W. GALLAGHER, and I. V. HERTEL, *Physics Reports* **278**, 107 (1997).

[41] N. ANDERSEN, K. BARTSCHAT, J. T. BROAD, and I. V. HERTEL, *Physics Reports* **279**, 251 (1997).

[42] K. BLUM and H. KLEINPOPPEN, *Physics Reports* **96**, 251 (1983).

[43] I. V. HERTEL, H. SCHMIDT, A. BAHRING, and E. MEYER, *Reports on Progress in Physics* **48**, 375 (1985).

[44] S. R. LEONE, *Accounts of Chemical Research* **25**, 71 (1992).

[45] K. BLUM and H. KLEINPOPPEN, *Physics Reports* **52**, 203 (1979).

[46] W. R. GENTRY, in *Atomic and Molecular Beam Methods*, edited by G. SCOLES, chapter 3, p. 54, Oxford University Press, Oxford, 1988.

[47] P. CASAVECCHIA, *Reports on Progress in Physics* **63**, 355 (2000).

[48] T. H. BULL and P. B. MOON, *Disscusions of the Faraday Society* **17**, 54 (1954).

[49] E. H. TAYLOR and S. DATZ, *Journal of Chemical Physics* **23**, 1711 (1955).

[50] J. ROSS, editor, *Molecular beams*, volume 10 of *Advances in Chemical Physics*, Wiley, New York, 1966.

[51] Y. T. LEE, J. T. MCDONALD, P. R. LEBRETON, and D. R. HERSCHBACH, *Review of Scientific Instruments* **40**, 1402 (1969).

[52] D. R. HERSCHBACH, *Angewandte Chemie International Edition* **26**, 1221 (1987).

[53] J. M. FARRAR and Y. T. LEE, *Annual Review of Physical Chemistry* **25**, 357 (1974).

[54] D. R. HERSCHBACH, *Faraday Discussions of the Chemical Society* **55**, 233 (1973).

[55] C. MALTZ, N. D. WEINSTEIN, and D. R. HERSCHBACH, *Molecular Physics* **24**, 133 (1972).

[56] D. S. Y. HSU, N. D. WEINSTEIN, and D. R. HERSCHBACH, *Molecular Physics* **29**, 257 (1975).

[57] D. S. Y. HSU, G. M. MCCLELLAND, and D. R. HERSCHBACH, *Journal of Chemical Physics* **61**, 4927 (1974).

[58] D. A. CASE and D. R. HERSCHBACH, *Molecular Physics* **30**, 1537 (1975).

[59] M. H. HIJAZI and J. C. POLANYI, *Chemical Physics* **11**, 1 (1975).

[60] J. D. BARNWELL, J. G. LOESER, and D. R. HERSCHBACH, *Journal of Physical Chemistry* **87**, 2781 (1983).

[61] D. A. CASE and D. R. HERSCHBACH, *Journal of Chemical Physics* **64**, 4212 (1976).

[62] G. M. McCLELLAND and D. R. HERSCHBACH, *Journal of Physical Chemistry* **83**, 1445 (1979).

[63] D. A. CASE and D. R. HERSCHBACH, *Journal of Chemical Physics* **69**, 150 (1978).

[64] G. H. KWEI and D. R. HERSCHBACH, *Journal of Physical Chemistry* **83**, 1550 (1979).

[65] G. M. McCLELLAND and D. R. HERSCHBACH, *Journal of Physical Chemistry* **91**, 5509 (1987).

[66] S. K. KIM and D. R. HERSCHBACH, *Faraday Discussions of the Chemical Society* **84**, 159 (1987).

[67] D. A. CASE, G. M. McCLELLAND, and D. R. HERSCHBACH, *Molecular Physics* **35**, 541 (1978).

[68] M. BROUARD, I. BURAK, S. MARINAKIS, L. R. LAGO, P. TAMPKINS, and C. VALLANCE, *Journal of Chemical Physics* **121**, 10426 (2004).

[69] M. BROUARD, S. P. DUXON, P. A. ENRIQUEZ, and J. P. SIMONS, *Journal of Chemical Physics* **97**, 7414 (1992).

[70] H. L. KIM, M. A. WICKRAMAARATCHI, X. ZHENG, and G. E. HALL, *Journal of Chemical Physics* **101**, 2033 (1994).

[71] M. BROUARD, S. DUXON, P. ENRIQUEZ, and J. SIMONS, *Journal of Chemical Society Faraday Transactions* **89**, 1435 (1993).

[72] M. BROUARD, H. M. LAMBERT, J. SHORT, and J. P. SIMONS, *Journal of Physical Chemistry* **99**, 13571 (1995).

[73] M. Brouard, H. M. Lambert, S. Rayner, and J. P. Simons, *Molecular Physics* **89**, 403 (1996).

[74] M. Brouard, I. Burak, D. W. Hughes, K. S. Kalogerakis, J. P. Simons, and V. Stavros, *Journal of Chemical Physics* **113**, 3173 (2001).

[75] A. J. Orr-Ewing, W. R. Simpson, T. P. Rakitzis, S. A. Kandel, and R. N. Zare, *Journal of Chemical Physics* **106**, 5961 (1997).

[76] T. P. Rakitzis, S. A. Kandel, and R. N. Zare, *Journal of Chemical Physics* **107**, 9382 (1997).

[77] T. P. Rakitzis, S. A. Kandel, T. Lev-On, and R. N. Zare, *Journal of Chemical Physics* **107**, 9392 (1997).

[78] T. L. D. Collins, A. J. McCaffery, and M. J. Wynn, *Physical Review Letters* **66**, 137 (1991).

[79] T. L. D. Collins, A. J. McCaffery, and M. J. Wynn, *Faraday Discussions* **91**, 91 (1991).

[80] P. L. Houston, *Journal of Physical Chemistry* **100**, 12757 (1996).

[81] M. N. R. Ashfold, N. H. Nahler, A. J. Orr-Ewing, O. P. J. Vieuxmaire, R. L. Toomes, T. N. Kitsopoulos, I. A. Garcia, D. A. Chestakov, S.-M. Wu, and D. H. Parker, *Physical Chemistry Chemical Physics* **8**, 26 (2006).

[82] T. N. Kitsopoulos, M. A. Buntine, D. P. Baldwin, R. N. Zare, and D. W. Chandler, *Science* **260**, 1605 (1993).

[83] M. Ahmed, D. S. Peterka, and A. G. Suits, *Chemical Physics Letters* **301**, 372 (1999).

[84] R. L. Toomes and T. N. Kitsopoulos, *Physical Chemistry Chemical Physics* **5**, 2481 (2003).

[85] K. Lorenz, D. Chandler, and G. McBane, *Journal of Physical Chemistry A* **106**, 1144 (2002).

[86] J. J. Kay, S. Y. T. van de Meerakker, E. A. Wade, K. E. Strecker, and D. W. Chandler, *Journal of Physical Chemistry A* **113**, 14800 (2009).

[87] E. Wade, K. Lorenz, J. Springfield, and D. Chandler, *Journal of Physical Chemistry A* **107**, 4976 (2003).

[88] A. Suits, L. Bontuyan, P. Houston, and B. Whitaker, *Journal of Chemical Physics* **96**, 8618 (1992).

[89] H. Kohguchi, T. Suzuki, and M. Alexander, *Science* (2001).

[90] M. Elioff and D. Chandler, *Journal of Chemical Physics* **117**, 6455 (2002).

[91] K. Lorenz, D. Chandler, J. Barr, W. Chen, G. Barnes, and J. I. Cline, *Science* **293**, 2063 (2001).

[92] J. Cline, K. Lorenz, E. Wade, J. Barr, and D. Chandler, *Journal of Chemical Physics* **115**, 6277 (2001).

[93] E. Wade, K. T. Lorenz, D. Chandler, and J. Barr, *Chemical Physics* **301**, 261 (2004).

[94] J. J. Kay, G. Paterson, M. Lemeshko, E.Wade, B. Friedrich, M. L. Costen, K. E. Strecker, K. G. McKendrick, and D. W. Chandler, *in preparation* (2011).

[95] J. J. Lin, W. Shiu, and K. Liu, *Review of Scientific Instruments* **74**, 2495 (2003).

[96] J. J. Lin, J. Zhou, W. Shiu, and K. Liu, *Science* **300**, 966 (2003).

[97] D. Parker and R. B. Bernstein, *Annual Review of Physical Chemistry* **40**, 561 (1989).

[98] P. R. Brooks, *International Reviews in Physical Chemistry* **14**, 327 (1995).

[99] P. R. Brooks and E. M. Jones, *Journal of Chemical Physics* **45**, 3449 (1966).

[100] R. J. Beuhler, R. B. Bernstein, and K. H. Kramer, *Journal of the American Chemical Society* **88**, 5331 (1966).

[101] D. H. Parker, K. K. Chakravorty, and R. B. Bernstein, *Chemical Physics Letters* **82**, 113 (1982).

[102] P. R. Brooks, *Journal of Chemical Physics* **50**, 5031 (1969).

[103] R. Vetter and J. Vigué, editors, *Recent Advances in Molecular Reaction Dynamics*, Paris: Editions du CNRS, 1987.

[104] M. H. M. Janssen, D. H. Parker, and S. Stolte, *Journal of Physical Chemistry* **95**, 8142 (1991).

[105] D. van den Ende and S. Stolte, *Chemical Physics* **45**, 55 (1980).

[106] D. H. Parker, H. Jalink, and S. Stolte, *Journal of Physical Chemistry* **91**, 5427 (1987).

[107] M. C. van Beek, J. J. ter Meulen, and M. H. Alexander, *Journal of Chemical Physics* **113**, 628 (2000).

[108] M. van Beek, G. Berden, H. Bethlem, and J. ter Meulen, *Physical Review Letters* **86**, 4001 (2001).

[109] M. J. L. de Lange, S. Stolte, C. A. Taatjes, J. Kłos, G. C. Groenenboom, and A. van der Avoird, *Journal of Chemical Physics* **121**, 11691 (2004).

[110] A. Gijsbertsen, H. Linnartz, J. Kłos, and S. Stolte, *Physica Scripta* **72**, C1 (2005).

[111] A. Gijsbertsen, H. Linnartz, G. Rus, A. E. Wiskerke, S. Stolte, D. W. Chandler, and J. Kłos, *Journal of Chemical Physics* **123**, 224305 (2005).

[112] A. Gijsbertsen, H. Linnartz, and S. Stolte, *Journal of Chemical Physics* **125**, 133112 (2006).

[113] R. B. Bernstein, D. R. Herschbach, and R. D. Levine, *Journal of Physical Chemistry* **91**, 5365 (1987).

[114] P. R. Brooks, *Science* **193**, 4247 (1976).

[115] H. J. Loesch and A. Remsheid, *Journal of Chemical Physics* **93**, 4779 (1990).

[116] B. Friedrich and D. Herschbach, *Nature* (1991).

[117] J. J. van Leuken, J. Bulthuis, S. Stolte, and H. J. Loesch, *Journal of Physical Chemistry* **99**, 13582 (1995).

[118] H. J. Loesch and J. Möller, *Journal of Physical Chemistry* **97**, 2158 (1993).

[119] H. J. Loesch and F. Stienkemeier, *Journal of Chemical Physics* **98**, 9570 (1993).

[120] H. J. Loesch and J. Moller, *Journal of Physical Chemistry A* **101**, 7534 (1997).

[121] H. J. Loesch, *Annual Review of Physical Chemistry* **46**, 555 (1995).

[122] B. Friedrich, H. Rubahn, and N. Sathyamurthy, *Physical Review Letters* **69**, 2487 (1992).

[123] R. N. Zare, *Ber. Bunsenges. Phys. Chem.* **86**, 422 (1982).

[124] H. J. Loesch and F. Stienkemeier, *Journal of Chemical Physics* **100**, 740, 4308 (1994).

[125] W. R. Simpson, T. P. Rakitzis, S. A. Kandel, A. J. Orr-Ewing, and R. N. Zare, *Journal of Chemical Physics* **103**, 7313 (1995).

[126] M. S. DE VRIES, V. I. SRDANOV, C. P. HANRAHAN, and R. M. MARTIN, *Journal of Chemical Physics* **78**, 5582 (1983).

[127] H. SENFTLEBEN, *Physikalische Zeitschrift* **31**, 822 (1930).

[128] C. J. GORTER, *Naturwissenschaften* **26**, 140 (1938).

[129] N. F. RAMSEY, *Physical Review* **98**, 1853 (1955).

[130] M. P. SINHA, C. D. CALDWELL, and R. N. ZARE, *Journal of Chemical Physics* **61**, 491 (1974).

[131] H.-G. RUBAHN and J. P. TOENNIES, *Journal of Chemical Physics* **89**, 287 (1988).

[132] A. G. VISSER, J. P. BEKOOY, L. K. VAN DER MEIJ, C. DE VREUGD, and J. KORVING, *Chemical Physics* **20**, 391 (1977).

[133] D. P. PULLMAN, B. FRIEDRICH, and D. R. HERSCHBACH, *Journal of Chemical Physics* **93**, 3224 (1990).

[134] M. J. WEIDA and D. J. NESBITT, *Journal of Chemical Physics* **100**, 6372 (1994).

[135] D. PULLMAN, B. FRIEDRICH, and D. HERSCHBACH, *Journal of Physical Chemistry* **99**, 7407 (1995).

[136] V. AQUILANTI, D. ASCENZI, D. CAPPELLETTI, and F. PIRANI, *Nature* **371**, 399 (1994).

[137] V. AQUILANTI, M. BARTOLOMEI, F. PIRANI, D. CAPPELLETTI, F. VECCHIO-CATTIVI, Y. SHIMIZU, and T. KASAI, *Physical Chemistry Chemical Physics* **7**, 291 (2005).

[138] K. G. MCKENDRICK, *Journal of Chemical Society Faraday Transactions* **94**, 1921 (1998).

[139] M. Brouard, H. Chadwick, Y. Chang, R. Cireasa, and C. J. Eyles, *Physica Scripta* **80**, 048120 (2009).

[140] M. Brouard, H. Chadwick, Y.-P. Chang, R. Cireasa, C. J. Eyles, A. O. L. Via, N. Screen, F. J. Aoiz, and J. Kłos, *Journal of Chemical Physics* **131**, 4307 (2009).

[141] M. Brouard, A. Bryant, I. Burak, S. Marinakis, F. Quadrini, I. Garcia, and C. Vallance, *Molecular Physics* **103**, 1693 (2005).

[142] M. Brouard, A. Bryant, Y.-P. Chang, R. Cireasa, C. J. Eyles, A. M. Green, S. Marinakis, F. J. Aoiz, and J. Kłos, *Journal of Chemical Physics* **130**, 4306 (2009).

[143] M. L. Costen, R. Livingstone, K. G. McKendrick, G. Paterson, M. Brouard, H. Chadwick, Y.-P. Chang, C. J. Eyles, F. J. Aoiz, and J. Kłos, *Journal of Physical Chemistry A* **113**, 15156 (2009).

[144] F. J. Aoiz, M. Brouard, C. J. Eyles, J. Kłos, and M. P. de Miranda, *Journal of Chemical Physics* **130**, 4305 (2009).

[145] M. P. de Miranda and D. C. Clary, *Journal of Chemical Physics* **106**, 4509 (1997).

[146] M. P. de Miranda, D. C. Clary, J. F. Castillo, and D. E. Manolopoulos, *Journal of Chemical Physics* **108**, 3142 (1998).

[147] J. Aldegunde, J. M. Alvarino, B. K. Kendrick, V. S. Rubanos, M. P. de Miranda, and F. J. Aoiz, *Physical Chemistry Chemical Physics* **8**, 4881 (2006).

[148] M. de Miranda and R. Gargano, *Chemical Physics Letters* **309**, 257 (1999).

[149] M. de Miranda, S. Crocchianti, and A. Laganà, *Journal of Physical Chemistry A* **103**, 10776 (1999).

[150] M. P. DE MIRANDA, S. K. POGREBNYA, and D. C. CLARY, *Faraday Discussions* **113**, 119 (1999).

[151] J. ALDEGUNDE, J. M. ALVARIÑO, M. P. D. MIRANDA, V. SÁEZ-RÁBANOS, and F. J. AOIZ, *Journal of Chemical Physics* **125**, 3104 (2006).

[152] J. ALDEGUNDE, F. J. AOIZ, V. SÁEZ-RÁBANOS, B. K. KENDRICK, and M. P. DE MIRANDA, *Physical Chemistry Chemical Physics* **9**, 5794 (2007).

[153] F. AOIZ, M. BROUARD, and P. ENRIQUEZ, *Journal of Chemical Physics* **105**, 4964 (1996).

[154] F. AOIZ, M. BROUARD, V. HERRERO, V. RABANOS, and K. STARK, *Chemical Physics Letters* **264**, 487 (1997).

[155] A. ALEXANDER, F. AOIZ, L. BANARES, M. BROUARD, J. SHORT, and J. SIMONS, *Journal of Physical Chemistry A* **101**, 7544 (1997).

[156] S. KANDEL, A. ALEXANDER, Z. KIM, R. ZARE, F. AOIZ, L. BAÑARES, J. CASTILLO, and V. RÁBANOS, *Journal of Chemical Physics* **112**, 670 (2000).

[157] J. CASTILLO, F. AOIZ, L. BANARES, and J. SANTAMARIA, *Chemical Physics Letters* **329**, 517 (2000).

[158] A. ALEXANDER, F. AOIZ, L. BANARES, M. BROUARD, and J. SIMONS, *Physical Chemistry Chemical Physics* **2**, 571 (2000).

[159] F. J. AOIZ, L. BAÑARES, J. F. CASTILLO, B. MARTÍNEZ-HAYA, and M. P. DE MIRANDA, *Journal of Chemical Physics* **114**, 8328 (2001).

[160] F. AOIZ, M. MARTÍNEZ, and V. SÁEZ-RÁBANOS, *Journal of Chemical Physics* **114**, 8880 (2001).

[161] F. AOIZ, B. FRIEDRICH, V. HERRERO, and V. S. RÁBANOS, *Chemical Physics Letters* **289**, 132 (1998).

[162] M. DE MIRANDA, F. AOIZ, L. BAÑARES, and V. SÁEZ-RÁBANOS, *Journal of Chemical Physics* **111**, 5368 (1999).

[163] M. DE MIRANDA and F. AOIZ, *Physical Review Letters* **93**, 083201 (2004).

[164] M. P. DE MIRANDA, F. J. AOIZ, V. SÁEZ-RÁBANOS, and M. BROUARD, *Journal of Chemical Physics* **121**, 9830 (2004).

[165] J. ALDEGUNDE, M. DE MIRANDA, J. HAIGH, B. KENDRICK, V. SÁEZ-RÁBANOS, and F. AOIZ, *Journal of Physical Chemistry A* **109**, 6200 (2005).

[166] J. ALDEGUNDE, F. J. AOIZ, and M. P. DE MIRANDA, *Physical Chemistry Chemical Physics* **10**, 1139 (2008).

[167] M. P. DE MIRANDA and B. K. KENDRICK, *Journal of Physical Chemistry A* **113**, 14943 (2009).

[168] R. N. ZARE and D. R. HERSCHBACH, *Proceedings of the IEEE* **51**, 173 (1983).

[169] R. J. VAN BRUNT and R. N. ZARE, *Journal of Chemical Physics* **48**, 4304 (1968).

[170] K.-H. GERICKE, S. KLEE, F. J. COMES, and R. N. DIXON, *Journal of Chemical Physics* **85**, 4463 (1986).

[171] M. P. DOCKER, A. HODGSON, and J. P. SIMONS, *Chemical Physics Letters* **128**, 264 (1986).

[172] G. E. HALL, N. SIVAKUMAR, P. L. HOUSTON, and I. BURAK, *Physical Review Letters* **56**, 1671 (1986).

[173] M. DUBS, U. BRUEHLMANN, and J. R. HUBER, *Journal of Chemical Physics* **84**, 3106 (1986).

[174] M. WU, R. J. BEMISH, and R. E. MILLER, *Journal of Chemical Physics* **101**, 9447 (1994).

[175] R. J. Bemish, E. J. Bohac, M. Wu, and R. E. Miller, *Journal of Chemical Physics* **101**, 9457 (1994).

[176] L. Oudejans and R. E. Miller, *Journal of Physical Chemistry* **99**, 13670 (1995).

[177] M. H. M. Janssen, J. W. G. Mastenbroek, and S. Stolte, *Journal of Physical Chemistry A* **101**, 7605 (1997).

[178] M. Brouard, P. O'Keeffe, and C. Vallance, *Journal of Physical Chemistry A* **106**, 3629 (2002).

[179] A. J. Alexander, M. Brouard, K. S. Kalogerakis, and J. P. Simons, *Chemical Society Reviews* **27**, 405 (1998).

[180] A. J. Orr-Ewing and R. N. Zare, *Annual Review of Physical Chemistry* **45**, 315 (1994).

[181] D. R. Herschbach, *European Physical Journal D* **38**, 3 (2006).

[182] F. J. Aoiz and M. P. de Miranda, Stereodynamics: Orientation and Alignment in Chemistry, in *Tutorials in Molecular Reaction Dynamics*, edited by M. Brouard and C. Vallance, Royal Society of Chemistry, 2010.

[183] M. L. Costen, S. Marinakis, and K. G. McKendrick, *Chemical Society Reviews* **37**, 732 (2008).

[184] *Special issue on Stereodynamics of Chemical Reactions, Journal of Physical Chemistry A* **101** (1997).

[185] A. J. Orr-Ewing, *Journal of Chemical Society Faraday Transactions* **92**, 881 (1996).

[186] R. V. Krems, *International Reviews in Physical Chemistry* **24**, 99 (2005).

[187] A. G. Suits and O. S. Vasyutinskii, *Chemical Reviews* **108**, 3706 (2008).

[188] A. P. CLARK, M. BROUARD, F. QUADRINI, and C. VALLANCE, *Physical Chemistry Chemical Physics* **8**, 5591 (2006).

[189] L. J. BUTLER and D. M. NEUMARK, *Journal of Physical Chemistry* **100**, 12801 (1996).

[190] R. SCHINKE, *Photodissociation Dynamics*, volume 1 of *Cambridge Monographs on Atomic, Molecular and Chemical Physics*, Cambridge University Press, Cambridge, England, 1993.

[191] G. E. HALL and P. L. HOUSTON, *Annual Review of Physical Chemistry* **40**, 375 (1989).

[192] C. H. GREENE and R. N. ZARE, *Annual Review of Physical Chemistry* **33**, 119 (1982).

[193] S. I. DROZDOV, *Soviet Physics JETP* **1**, 588, 591 (1955).

[194] J. S. BLAIR, Scattering of Strongly Absorbed Particles, in *Lectures in Theoretical Physics VIII C – Nuclear Structure Physics*, edited by P. D. KUNZ, D. A. LIND, and W. E. BRITTIN, pp. 343–444, The University of Colorado Press, Boulder, 1965.

[195] M. FAUBEL, *Journal of Chemical Physics* **81**, 5559 (1984).

[196] M. LEMESHKO and B. FRIEDRICH, *Journal of Chemical Physics* **129**, 4301 (2008).

[197] M. LEMESHKO and B. FRIEDRICH, *International Journal of Mass Spectrometry* **280**, 19 (2009).

[198] M. LEMESHKO and B. FRIEDRICH, *Physical Review A* **79**, 012718 (2009).

[199] M. LEMESHKO and B. FRIEDRICH, *Journal of Physical Chemistry A* **113**, 15055 (2009).

[200] M. LEMESHKO and B. FRIEDRICH, *Physical Chemistry Chemical Physics* **12**, 1038 (2010).

[201] M. LEMESHKO, P. G. JAMBRINA, M. P. DE MIRANDA, and B. FRIEDRICH, *Journal of Chemical Physics* **132**, 161102 (2010).

[202] J. P. TOENNIES, *Zeitschrift für Physik* **182**, 257 (1964).

[203] W. R. GENTRY and C. F. GIESE, *Journal of Chemical Physics* **67**, 5389 (1977).

[204] P. A. BARRASS, P. SHARKEY, and I. W. M. SMITH, *Physical Chemistry Chemical Physics* **5**, 1400 (2003).

[205] J. W. HUDGENS, in *Advances in Multi-Photon Processes and Spectroscopy*, edited by S. H. LIN, chapter 4, p. 171, World Scientific Publications, Singapore, 1988.

[206] M. N. R. ASHFOLD and J. D. HOWE, *Annual Review of Physical Chemistry* **45**, 57 (1994).

[207] L. SCHNIEDER, K. SEEKAMP-RAHN, E. WREDE, and K. H. WELGE, *Journal of Chemical Physics* **107**, 6175 (1997).

[208] D. W. CHANDLER and P. L. HOUSTON, *Journal of Chemical Physics* **87**, 1445 (1987).

[209] S. Y. T. VAN DE MEERAKKER, H. L. BETHLEM, and G. MEIJER, *Nature Physics* **4**, 595 (2008).

[210] J. J. GILIJAMSE, S. HOEKSTRA, S. Y. T. VAN DE MEERAKKER, G. C. GROENENBOOM, and G. MEIJER, *Science* **313**, 1617 (2006).

[211] L. SCHARFENBERG, J. KŁOS, P. J. DAGDIGIAN, M. H. ALEXANDER, G. MEIJER, and S. Y. T. VAN DE MEERAKKER, *Physical Chemistry Chemical Physics* **12**, 10660 (2010).

[212] M. Kirste, L. Scharfenberg, J. Kłos, F. Lique, M. H. Alexander, G. Meijer, and S. Y. T. van de Meerakker, *Physical Review A* **82**, 042717 (2010).

[213] R. N. Zare, *Science* **279**, 1875 (1998).

[214] M. Brouard, S. P. Duxon, P. A. Enriques, R. Sayos, and J. P. Simons, *Journal of Physical Chemistry* **95**, 8169 (1991).

[215] J. P. Simons, *Journal of the Chemical Society Faraday Transactions* **93**, 4095 (1997).

[216] F. Green, G. Hancock, A. J. Orr-Ewing, M. Brouard, S. P. Duxon, P. A. Enriquez, R. Sayos, and J. P. Simons, *Chemical Physics Letters* **182**, 568 (1991).

[217] D. F. Varley and P. J. Dagdigian, *Journal of Physical Chemistry* **99**, 9843 (1995).

[218] N. E. Shafer, A. J. Orr-Ewing, W. R. Simpson, H. Xu, and R. N. Zare, *Chemical Physics Letters* **212**, 155 (1993).

[219] A. J. Orr-Ewing and R. N. Zare, in *Chemical Dynamics and Kinetics of Small Radicals*, edited by A. Wagner and K. Liu, World Scientific Publications, Singapore, 1995.

[220] F. Aoiz, M. Brouard, P. Enriquez, and R. Sayos, *Journal of Chemical Society Faraday Transactions* **89** (1993).

[221] N. E. Shafer-Ray, A. J. Orr-Ewing, and R. N. Zare, *Journal of Physical Chemistry* **99**, 7591 (1995).

[222] W. R. Simpson, A. J. Orr-Ewing, T. P. Rakitzis, S. A. Kandel, and R. N. Zare, *Journal of Chemical Physics* **103**, 7299 (1995).

[223] W. R. Simpson, A. J. Orr-Ewing, and R. N. Zare, *Chemical Physics Letters* **212**, 163 (1993).

[224] M. Brouard, E. K. Campbell, A. J. Johnsen, C. Vallance, W. H. Yuen, and A. Nomerotski, *Review of Scientific Instruments* **79**, 3115 (2008).

[225] A. D. Rudert, J. Martin, W.-B. Gao, J. B. Halpern, and H. Zacharias, *Journal of Chemical Physics* **111**, 9549 (1999).

[226] G. O. Sitz and R. L. Farrow, *Journal of Chemical Physics* **101**, 4682 (1994).

[227] S. Mukamel, *Principles of Nonlinear Optics Spectroscopy*, Oxford University Press, Oxford, 1995.

[228] M. L. Costen, H. J. Crichton, and K. G. McKendrick, *Journal of Chemical Physics* **120**, 7910 (2004).

[229] S. Marinakis, G. Paterson, J. Kłos, M. L. Costen, and K. G. McKendrick, *Physical Chemistry Chemical Physics* **9**, 4414 (2007).

[230] G. Paterson, S. Marinakis, M. L. Costen, K. G. McKendrick, J. Kłos, and R. Tobola, *Journal of Chemical Physics* **129**, 074304 (2008).

[231] G. Paterson, S. Marinakis, M. L. Costen, and K. G. McKendrick, *Physica Scripta* **80**, 8111 (2009).

[232] A. Alagappan, I. Ballingall, M. L. Costen, and K. G. Mckendrick, *Journal of Chemical Physics* **126**, 1103 (2007).

[233] M. Brouard and J. P. Simons, in *Chemical Dynamics and Kinetics of Small Radicals*, edited by A. Wagner and K. Liu, World Scientific Publications, Singapore, 1995.

[234] J. P. Simons, *Faraday Discussions* **113**, 1 (1999).

[235] M. BROUARD, P. O'KEEFFE, and C. VALLANCE, *Journal of Physical Chemistry A* **106**, 3629 (2002).

[236] E. HACK and J. R. HUBER, *International Reviews in Physical Chemistry* **10**, 287 (1991).

[237] R. T. CARTER and J. R. HUBER, *Chemical Society Reviews* **29**, 305 (2000).

[238] F. LONDON, *Zeitschrift für Elektrochemie und Angewandte Physikalische Chemie* **35**, 552 (1929).

[239] H. EYRING and M. POLANYI, *Zeitschrift für Physikaliche Chemie B* **12**, 279 (1931).

[240] J. HIRSCHFELDER, H. EYRING, and B. TOPLEY, *Journal of Chemical Physics* **4**, 170 (1936).

[241] F. J. AOIZ, L. BAÑARES, and V. J. HERRERO, *International Reviews in Physical Chemistry* **24**, 119 (2005).

[242] J. KŁOS, F. J. AOIZ, R. CIREASA, and J. J. TER MEULEN, *Physical Chemistry Chemical Physics* **6**, 4968 (2004).

[243] G. C. GROENENBOOM and N. BALAKRISHNAN, *Journal of Chemical Physics* **118**, 7380 (2003).

[244] P. SOLDÁN, V. SPIRKO, E. LEE, and T. WRIGHT, *Journal of Chemical Physics* **111**, 3420 (1999).

[245] *Faraday Discussions* **110**, 1 (1998).

[246] A. LAGANÀ, J. M. ALVARIÑO, M. L. HERNANDEZ, P. PALMIERI, E. GARCÍA, and T. MARTINEZ, *Journal of Chemical Physics* **106**, 10222 (1997).

[247] C. O. DE ASPURU and D. C. CLARY, *Journal of Physical Chemistry A* **102**, 9631 (1998).

[248] T. Hollebeek, T.-S. Ho, and H. Rabitz, *Annual Review of Physical Chemistry* **50**, 537 (1999).

[249] R. B. Bernstein, editor, *Atom-Molecule Collision Theory*, Plenum, New York, 1979.

[250] A. Volpi and J. L. Bohn, *Physical Review A* **65**, 052712 (2002).

[251] R. V. Krems and A. Dalgarno, *Journal of Chemical Physics* **120**, 2296 (2004).

[252] R. V. Krems and A. Dalgarno, in *Fundamental World of Quantum Chemistry*, edited by E. J. Brändas and E. S. Kryachko, volume 3, p. 273, Kluwer, 2004.

[253] H. Cybulski, R. V. Krems, H. R. Sadeghpour, A. Dalgarno, J. Kłos, G. C. Groenenboom, A. van der Avoird, D. Zgid, and G. Chałasiński, *Journal of Chemical Physics* **122**, 4307 (2005).

[254] T. V. Tscherbul and R. V. Krems, *Journal of Chemical Physics* **125**, 4311 (2006).

[255] E. Abrahamsson, T. V. Tscherbul, and R. V. Krems, *Journal of Chemical Physics* **127**, 4302 (2007).

[256] T. V. Tscherbul, G. C. Groenenboom, R. V. Krems, and A. Dalgarno, *Faraday Discussions of the Chemical Society* **142**, 127 (2009).

[257] S. V. Alyabyshev, T. V. Tscherbul, and R. V. Krems, *Physical Review A* **79**, 060703(R) (2009).

[258] K. P. Lawley and J. Ross, *Journal of Chemical Physics* **43**, 2930 (1965).

[259] R. J. Cross and R. G. Gordon, *Journal of Chemical Physics* **45**, 3571 (1966).

[260] R. J. Cross, *Journal of Chemical Physics* **55**, 510 (1971).

[261] H. A. RABITZ and T. G. GORDON, *Journal of Chemical Physics* **53**, 1815; 1831 (1970).

[262] E. A. GISLASON and D. R. HERSCHBACH, *Journal of Chemical Physics* **64**, 2133 (1976).

[263] M. KARPLUS, R. N. PORTER, and R. D. SHARMA, *Journal of Chemical Physics* **43**, 3259 (1965).

[264] H. R. MAYNE, in *Dynamics of Molecules and Chemical Reactions*, edited by R. E. WYATT and J. Z. H. ZHANG, p. 589, Marcel Dekker, New York, 1996.

[265] F. J. AOIZ, L. BANARES, and V. J. HERRERO, *Journal of Chemical Society Faraday Transactions* **94**, 2483 (1998).

[266] F. AOIZ, L. BANARES, V. HERRERO, B. MARTINEZ-HAYA, M. MENENDEZ, P. QUINTANA, I. TANARRO, and E. VERDASCO, *Journal of Physical Chemistry A* **105**, 6976 (2001).

[267] F. J. AOIZ, L. BAÑARES, V. J. HERRERO, B. MARTÌNEZ-HAYA, M. MENÈNDEZ, P. QUINTANA, I. TANARRO, and E. VERDASCO, *Chemical Physics Letters* **367**, 500 (2003).

[268] G. AMARAL, F. AOIZ, L. BAÑARES, J. BARR, V. J. HERRERO, B. MARTINEZ-HAYA, M. MENENDEZ, G. PINO, I. TANARRO, I. TORRES, and J. VERDASCO, *Journal of Physical Chemistry A* **109**, 9402 (2005).

[269] F. AOIZ, V. HERRERO, V. SÁEZ-RÁBANOS, and J. VERDASCO, *Physical Chemistry Chemical Physics* **6**, 4407 (2004).

[270] H. J. KORSCH and R. SCHINKE, *Journal of Chemical Physics* **73**, 1222 (1980).

[271] H. J. KORSCH and R. SCHINKE, *Journal of Chemical Physics* **75**, 3850 (1981).

[272] S. BOSANAC, *Physical Review A* **22**, 2617 (1980).

[273] S. Bosanac and U. Buck, *Chemical Physics Letters* **81**, 315 (1981).

[274] C. J. Eyles, *An Experimental and Theoretical Study of the Dynamics of Atom-Molecule Scattering*, PhD thesis, University of Oxford, 2010.

[275] V. Khare, D. J. Kouri, and D. K. Hoffman, *Journal of Chemical Physics* **74**, 2275 (1981).

[276] A. Gijsbertsen, H. Linnartz, C. A. Taatjes, and S. Stolte, *Journal of the American Chemical Society* **128**, 8777 (2006).

[277] C. A. Taatjes, A. Gijsbertsen, M. J. L. deLange, and S. Stolte, *Journal of Chemical Physics* **111**, 7631 (2007).

[278] C. A. Taatjes, A. Gijsbertsen, M. J. L. D. Lange, and S. Stolte, *Journal of Physical Chemistry A* **111**, 7631 (2007).

[279] A. J. McCaffery, *Physical Chemistry Chemical Physics* **6**, 1637 (2004).

[280] F. J. Aoiz, J. E. Verdasco, M. Brouard, J. Kłos, S. Marinakis, and S. Stolte, *Journal of Physical Chemistry A* **113**, 14636 (2009).

[281] K. Blum, *Density Matrix Theory and Applications*, Plenum, New York, 1996.

[282] M. P. de Miranda, F. J. Aoiz, L. Bañares, and V. Sáez-Rábanos, *Journal of Chemical Physics* **111**, 5368 (1999).

[283] R. N. Zare, *Angular momentum: Understanding spatial aspects in chemistry and physics*, Wiley, New York, 1988.

[284] D. A. Varshalovich, A. N. Moskalev, and V. K. Khersonski, *Quantum theory of angular momentum*, World Scientific Publications, Singapore and Teaneck, N.J., 1988.

[285] U. Fano, *Reviews of Modern Physics* **29**, 74 (1957).

[286] A. Busalla and K. Blum, *Journal of Physical Chemistry A* **101**, 7476 (1997).

[287] D. Beck, U. Ross, and W. Schepper, *Zeitschrift für Physik A* **293**, 107 (1979).

[288] A. Ichimura and M. Nakamura, *Physical Review A* **69**, 022716 (2004).

[289] M. Nakamura and A. Ichimura, *Physical Review A* **71**, 062701 (2005).

[290] A. J. Marks, *Journal of Chemical Society Faraday Transactions* **90**, 2857 (1994).

[291] S. Bosanac, *Physical Review A* **26**, 282 (1982).

[292] M. Born and E. Wolf, *Principles of Optics*, Cambridge University Press, 7th edition, 1997.

[293] L. D. Landau and E. M. Lifshitz, *Quantum Mechanics, Non-Relativistic Theory*, Oxford: Pergamon, 1977.

[294] J. S. Blair, *Physical Review* **115**, 928 (1965).

[295] G. N. Watson, *Theory of Bessel Functions*, Cambridge University Press, Cambridge, 1922.

[296] A. I. Maergoiz, E. E. Nikitin, J. Troe, and V. G. Ushakov, *Journal of Chemical Physics* **105**, 6263 (1996).

[297] E. E. Nikitin, *Theory of Elementary Atomic and Molecular Processes in Gases*, Clarendon, Oxford, 1974.

[298] A. R. Edmonds, *Angular momenum in quantum mechanics*, Princeton University, Princeton, 1960.

[299] J. M. Brown, J. T. Hougen, K.-P. Huber, J. W. C. Johns, I. Kopp, H. Lefebvre-Brion, A. J. Merer, D. A. Ramsay, J. Rostas, and R. N. Zare, *Journal of Molecular Spectroscopy* **55**, 500 (1975).

[300] M. H. Alexander, *Chemical Physics* **92**, 337 (1985).

[301] J. J. van Leuken, J. Bulthuis, S. Stolte, and J. G. Snijders, *Chemical Physics Letters* **260**, 595 (1996).

[302] M. J. L. de Lange, M. Drabbels, P. T. Griffiths, J. Bulthuis, S. Stolte, and J. G. Snijders, *Chemical Physics Letters* **313**, 491 (1999).

[303] M. H. Alexander, *Journal of Chemical Physics* **99**, 7723 (1993).

[304] J. J. van Leuken, F. H. W. van Amerom, J. Bulthuis, J. G. Snijders, and S. Stolte, *Journal of Physical Chemistry* **99**, 15573 (1995).

[305] Y. Sumiyoshi and Y. Endo, *Journal of Chemical Physics* **127**, 4309 (2007).

[306] A. D. Esposti, A. Berning, and H. Werner, *Journal of Chemical Physics* **103**, 2067 (1995).

[307] F. Aoiz, J. Verdasco, V. Herrero, and V. Rábanos, *Journal of Chemical Physics* **119**, 5860 (2003).

[308] M. H. Alexander, *Faraday Discussions* **113**, 437 (1999).

[309] J. Toennies and A. Vilesov, *Angewandte Chemie International Edition* **43**, 2622 (2004).

[310] H. Zhu, Y. Zhou, and D. Xie, *Journal of Chemical Physics* **122**, 4312 (2005).

[311] B. Friedrich and D. Herschbach, *Physical Review Letters* **74**, 4623 (1995).

[312] B. Friedrich and D. Herschbach, *Journal of Physical Chemistry* **99**, 15686 (1995).

[313] B. Friedrich and D. Herschbach, *Chemical Physics Letters* **262**, 41 (1996).

[314] P. Soldan, V. Spirko, E. Lee, and T. Wright, *Journal of Chemical Physics* **111**, 3420 (1999).

[315] W. C. CAMBELL and J. M. DOYLE, in *Cold molecules: theory, experiment, applications*, edited by R. V. KREMS, W. C. STWALLEY, and B. FRIEDRICH, Taylor&Francis/CRC, Boca Raton, FL, 2009.

[316] J. D. WEINSTEIN, R. DECARVALHO, T. GUILLET, B. FRIEDRICH, and J. M. DOYLE, *Nature* **395**, 148 (1998).

[317] B. FRIEDRICH, J. WEINSTEIN, R. DECARVALHO, and J. DOYLE, *Journal of Chemical Physics* **110**, 2376 (1999).

[318] H. MARTIN, *Journal of Molecular Spectroscopy* **108**, 66 (1984).

[319] C. AMIOT and J. VERGES, *Canadian Journal of Physics* **59**, 1391 (1981).

[320] A. BOCA and B. FRIEDRICH, *Journal of Chemical Physics* **112**, 3609 (2000).

[321] H. LEFEBVRE-BRION and R. W. FIELD, *Perturbations in the Spectra of Diatomic Molecules*, Academic Press, New York, 1986.

[322] H. LEFEBVRE-BRION and R. W. FIELD, *The Spectra and Dynamics of Diatomic Molecules*, Elsevier, New York, 2004.

[323] G. HERZBERG, *Spectra of Diatomic Molecules*, Van Nostrand, Princeton, 1950.

[324] L. TOMUTA, M. MIZUSHIMA, C. J. HOWARD, and K. M. EVENSON, *Physical Review A* **12**, 974 (1975).

[325] G. C. GROENENBOOM and I. M. STRUNIEWICZ, *Journal of Chemical Physics* **113**, 9562 (2000).

[326] J. M. BROWN and A. CARRINGTON, *Rotational Spectroscopy of Diatomic Molecules*, Cambridge University Press, Cambridge, England, 2003.

[327] K. GUBBELS, *Dynamics of Stark Acceleration/Deceleration: Molecules Riding Waves*, MSc thesis, Radboud University, Nijmegen, 2006.

[328] C. TICKNOR and J. L. BOHN, *Physical Review A* **71**, 022709 (2005).

[329] H.-S. Lee, A. B. McCoy, R. R. Toszyłowski, and C. M. Cybulski, *Journal of Chemical Physics* **113**, 5736 (2000).

[330] P. J. Dagdigian and M. H. Alexander, *Journal of Chemical Physics* **130**, 204304 (2009).

[331] *HIBRIDON - a package of programs for the time-independent quantum treatment of inelastic collisions and photodissociation written by M. H. Alexander, D. E. Manolopoulos, H.-J. Werner and B. Follmeg, with contributions by P. F. Vohralik, D. Lemoine, G. Corey, R. Gordon, B. Johnson, T. Orlikowski, A. Berning, A. Degli-Esposti, C. Rist, P. Dagdigian, B. Pouilly, G. van der Sanden, M. Yang, and F. de Weerd.*

[332] J. Kłos, G. Chałasiński, M. T. Berry, R. Bukovski, and S. M. Cybulski, *Journal of Chemical Physics* **112**, 2195 (2000).

[333] A. D. Cronin, J. Schmiedmayer, and D. E. Pritchard, *Reviews of Modern Physics* **81**, 1051 (2009).

[334] H. Rauch, in *Advances in Quantum Phenomena*, edited by E. G. Beltrametti and J.-M. Lévy-Leblond, volume 347 of *NATO Advanced Science Institutes, Series B. Physics*, p. 113, Plenum, New York, 1995.

[335] A. F. Borghesani, *IEEE Transactions on Dielectrics and Electrical Insulations* **13**, 492 (2006).

[336] L. Anchordoqui, M. T. Dova, A. Mariazzi, T. McCauley, T. Paul, S. Reucroft, and J. Swain, *Annals of Physics* **314**, 145 (2004).

[337] J. Schmiedmayer, C. R. Ekstrom, M. S. Chapman, T. R. Hammond, and D. E. Pritchard, in *Fundamentals of Quantum Optics III*, edited by F. Ehlotzky, Lecture Notes In Physics No. 420, p. 21, Springer, Berlin, 1993.

[338] J. Schmiedmayer, M. S. Chapman, C. R. Ekstrom, T. D. Hammond, S. Wehinger, and D. E. Pritchard, *Physical Review Letters* **74**, 1043 (1995).

[339] J. Schmiedmayer, M. S. Chapman, C. R. Ekstrom, T. D. Hammond, D. A. Kokorowski, A. Lenef, R. A. Rubenstein, E. T. Smith, and D. E. Pritchard, in *Atom Interferometry*, edited by P. R. Berman, p. 1, Academic Press, New York, 1997.

[340] T. D. Hammond, M. S. Chapman, A. Lenef, J. Schmiedmayer, E. T. Smith, R. A. Rubenstein, D. A. Kokorowski, and D. E. Pritchard, *Brazilian Journal of Physics* **27**, 193 (1997).

[341] T. D. Roberts, A. D. Cronin, D. A. Kokorowski, and D. E. Pritchard, *Physical Review Letters* **89**, 200406 (2002).

[342] M. Jacquey, M. Büchner, G. Trénec, and J. Vigué, *Physical Review Letters* **98**, 240405 (2007).

[343] C. Champenois, M. Jacquey, S. Lepoutre, M. Büchner, G. Trénec, and J. Vigué, *Physical Review A* **77**, 13621 (2008).

[344] K. Hornberger and B. Vacchini, *Physical Review A* **77**, 22112 (2008).

[345] J. Vigué, *Physical Review A* **52**, 3973 (1995).

[346] R. C. Forrey, L. You, V. Kharchenko, and A. Dalgarno, *Physical Review A* **54**, 2180 (1996).

[347] C. Champenois, E. Audouard, P. Duplàa, and J. Vigué, *Journal de Physique II* **7**, 523 (1997).

[348] V. Kharchenko and A. Dalgarno, *Physical Review A* **63**, 23615 (2001).

[349] R. C. Forrey, V. Kharchenko, and A. Dalgarno, *Journal of Physics B* **35**, L261 (2002).

[350] S. Blanchard, D. Civello, and R. C. Forrey, *Physical Review A* **67**, 13604 (2003).

[351] J. Ahokas, T. Kiljunen, J. Eloranta, and H. Kunttu, *Journal of Chemical Physics* **112**, 2420 (2000).

[352] J. T. Hougen, *The Calculation of Rotational Energy Levels and Rotational Line Intensities in Diatomic Molecules*, NIST, 1970.

Acknowledgements

> Whatever is worth saying can be stated in fifty words or less.
>
> Stan Ulam

I am indebted to Stan Ulam for the excellent epigraph, but I somehow doubt that I'll be able to make it in fifty words. First of all, I am extremely grateful to my thesis advisor, Bretislav Friedrich, without whose help the completion of this thesis would have not been possible. Bretislav, working with you was a wonderful time and a great experience for me. You gave me everything a PhD student could dream of, proposing thrilling research directions and giving me the freedom to develop my own ideas. Thank you for your enthusiasm and encouragement, for always being there for my questions, and for not sharing my pessimism when I was stuck. Of course, I still believe that pessimism is the only way to deal with reality (because it always works, you know), but being healthily balanced with your optimism it made the whole thing work very efficiently.

I am grateful to Gerard Meijer for giving me the opportunity to work in his department; for numerous discussions and criticism; and for supporting me in this weird story of Elsevier, an Egyptian science freak, a blog post, and a lawsuit.

During my PhD I had the pleasure to collaborate with a number of theorists and experimentalists from the vector correlations community. Discussions with Elena Dashevskaya, Evgueni Nikitin, Steven Stolte, and Hans ter Meulen were of great help in the development of the Fraunhofer model of field-dressed molecular collisions. I thank Marcelo de Miranda, Pablo Jambrina, and Javier Aoiz for collaborating with me on vector correlations and for the hospitality during my visits to Leeds and Madrid.

Lebenslauf

	Mikhail Lemeshko, geboren am 15. April 1985 in Rostow-am-Don, Sowjetunion
09.1991–06.2001	Besuch des Klassischen Gymnasiums 45, Rostow-am-Don, Russland
09.2001–06.2005	Physikstudium an der Staatliche Universität Rostow, Russland. B.Sc. dissertation zum Thema "Study of X-ray absorption spectra of weakly packed crystals containing covalent groups of closely located atoms" unter Anleitung durch Prof. Dr. Rostislav Vedrinskii
06.2005	B.Sc. in Physik
09.2005–06.2007	Masterarbeit zum Thema "Study of local atomic structure of solid solutions $K_xNa_{1-x}NbO_3$ by x-ray absorption spectroscopy" unter Anleitung durch Prof. Dr. Rostislav Vedrinskii
06.2007	M.Sc. in Festkörperphysik
09.2007-04.2011	Anfertigung der Dissertation "Vector correlations in rotationally inelastic molecular collisions" unter Anleitung durch Prof. Dr. B. Friedrich am Fritz-Haber-Institut der Max-Planck-Gesellschaft, Berlin

List of publications

1. M. Lemeshko, M. Mustafa, S.Kais, B. Friedrich. *Supersymmetry identifies molecular Stark states whose eigenproperties can be obtained analytically*, submitted (2011).

2. M. Lemeshko, M. Mustafa, S.Kais, B. Friedrich. *Supersymmetric factorization yields exact solutions to the molecular Stark effect problem for "stretched" states*, submitted (2010).

3. M. Lemeshko, B. Friedrich. *Fine-tuning molecular energy levels by nonresonant laser pulses*, J. Phys. Chem. A **114**, 9848 (2010).

4. M. Lemeshko, B. Friedrich. *Multiple scattering of matter waves: an analytic model of the refractive index for atomic and molecular gases*,
Phys. Rev. A **82**, 022711 (2010).

5. M. Lemeshko, P. G. Jambrina, M P. de Miranda, B. Friedrich.
When diffraction rules the stereodynamics of rotationally inelastic collisions,
J. Chem. Phys. **132**, 161102 (2010).

6. M. Lemeshko, B. Friedrich. *Rotational structure of weakly bound molecular ions*,
J. At. Mol. Sci. **1**, 39 (2009).

7. M. Lemeshko, B. Friedrich. *An analytic model of the stereodynamics of rotationally inelastic molecular collisions*,
Phys. Chem. Chem. Phys. **12**, 1038 (2010).

8. M. Lemeshko, B. Friedrich. *A model analysis of rotationally inelastic $Ar+H_2O$ scattering in an electric field*, J. Phys. Chem. A **113**, 15055-15063 (2009).

9. M. Lemeshko, B. Friedrich. *Probing weakly bound molecules with nonresonant light*, Phys. Rev. Lett. **103**, 053003 (2009).

10. M. Lemeshko, B. Friedrich. *Rotational and rotationless states of weakly bound molecules*, Phys. Rev. A **79**, 050501(R) (2009).

11. M. Lemeshko, B. Friedrich. *Collisions of paramagnetic molecules in magnetic fields: an analytic model based on Fraunhofer diffraction of matter waves*,
Phys. Rev. A **79**, 012718 (2009).

12. M. Lemeshko, B. Friedrich. *The effect of a nonresonant radiative field on low-energy rotationally inelastic $Na^+ + N_2$ collisions,*
Int. J. Mass. Spec. **280**, 19 (2009).

13. M. Lemeshko, B. Friedrich. *Quantum Zeno effect,*
Chem. Listy. **102**, 880 (2008) (in Czech).

14. M. Lemeshko, B. Friedrich. *An analytic model of rotationally inelastic collisions of polar molecules in electric fields,*
J. Chem. Phys. **129**, 024301 (2008).

15. G. S. Pokrovski, J. Roux, J.-L. Hazemann, A. Yu. Borisova, A. A. Gonchar, M. P. Lemeshko. *In situ X-ray absorption spectroscopy measurement of vapor-brine fractionation of antimony at hydrothermal conditions,* Mineralogical Magazine, **72**, 667 (2008).

16. R. V. Vedrinskii, V. L. Kraizman, M. P. Lemeshko, E. S. Nazarenko, A. A. Novakovich, L. A. Reznichenko, V. N. Fokin, V. A. Shuvaeva. *Local atomic structure of niobates and titanates from X-ray absorption spectroscopic data,*
Physics of the Solid State, **51**, 1394 (2009).

17. M. P. Lemeshko, E. S. Nazarenko, A. A. Gonchar, L. A. Reznichenko, A. A. Novakovich, O. Mathon, Y. Joly, R. V. Vedrinskii. *XAFS studies of the local atomic structure of the lead-free piezoelectric ceramics $K_x Na_{1-x} NbO_3$ over the temperature range 10-1023 K,* Phys. Rev. B. **76**, 134106 (2007).

18. M. P. Lemeshko, E. S. Nazarenko, A. A. Gonchar, L. A. Reznichenko, O. Mathon, Y. Joly, R. V. Vedrinskii. *Phase transitions in lead-free piezoelectric ceramics: study of local atomic structure,*
Europhys. Lett. **77**, 26003 (2007).

19. R. V. Vedrinskii, E. S. Nazarenko, M. P. Lemeshko, V. Nassif, O. Proux, A. A. Novakovich, Y. Joly. *Temperature dependent XAFS studies of local atomic structure for the perovskite-type zirconates,*
Phys. Rev. B **73**, 134109 (2006).

20. A. Ehresmann, L. Werner, S. Klumpp, Ph. V. Demekhin, M. P. Lemeshko, V. L. Sukhorukov, K.-H. Schartner, H. Schmoranzer. *Predissociation of the $N_2^+(C^2\Sigma_u^+)$ state observed via $C\ ^2\Sigma_u^+ \to X\ ^2\Sigma_g^+$ fluorescence after $1s - 1\pi^*$ excitation of N_2 molecule,*
J. Phys. B.: At. Mol. Opt. Phys. **39**, L119-L126 (2006).

21. A. Ehresmann, L. Werner, S. Klumpp, S. Lucht, H. Schmoranzer, S. Mickat, R. Shill, K.-H. Schartner, Ph. V. Demekhin, M. P. Lemeshko, V. L. Sukhorukov. *Studying the $N_2^+\ C\ ^2\Sigma_u^+ \to X\ ^2\Sigma_g^+$ fluorescence excited via the $1s - 1\pi^*$ resonance,*
J. Phys. B.: At. Mol. Opt. Phys. **39**, 283-304 (2006).

Eidesstattliche Versicherung

Ich versichere an Eides statt, dass ich die von mir vorgelegte Dissertation selbstständig angefertigt und alle benutzten Quellen und Hilfsmittel vollständig angegeben habe. Die Zusammenarbeit mit anderen Wissenschaftlern habe ich kenntlich gemacht. Diese Personen haben alle bereits ihr Promotionsverfahren abgeschlossen.

Berlin, den 13. April 2011   Mikhail Lemeshko

Erklärung

Teile dieser Arbeit sind bereits veröffentlicht oder zur Veröffentlichung eingereicht.

- M. Lemeshko, B. Friedrich. *An analytic model of rotationally inelastic collisions of polar molecules in electric fields*, J. Chem. Phys. **129**, 024301 (2008).

- M. Lemeshko, B. Friedrich. *The effect of a nonresonant radiative field on low-energy rotationally inelastic $Na^+ + N_2$ collisions*,
  Int. J. Mass. Spec. **280**, 19 (2009).

- M. Lemeshko, B. Friedrich. *Collisions of paramagnetic molecules in magnetic fields: an analytic model based on Fraunhofer diffraction of matter waves*,
  Phys. Rev. A **79**, 012718 (2009).

- M. Lemeshko, B. Friedrich. *An analytic model of the stereodynamics of rotationally inelastic molecular collisions*,
  Phys. Chem. Chem. Phys. **12**, 1038 (2010).

- M. Lemeshko, P. G. Jambrina, M. P. de Miranda, B. Friedrich.
  When diffraction rules the stereodynamics of rotationally inelastic collisions,
  J. Chem. Phys. **132**, 161102 (2010).

- M. Lemeshko, B. Friedrich. *Multiple scattering of matter waves: an analytic model of the refractive index for atomic and molecular gases*,
  Phys. Rev. A **82**, 022711 (2010).

Kein Teil dieser Arbeit wurde bisher für eine Dissertation verwendet. Eine Anmeldung der Promotionsabsicht habe ich an keiner anderen Fakultät oder Hochschule beantragt.

Berlin, den 13. April 2011   Mikhail Lemeshko